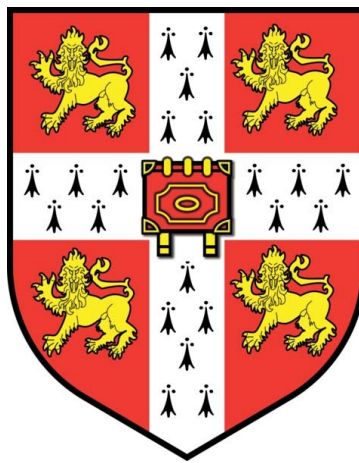


**CYCLIC BEHAVIOUR OF MONOPILE
FOUNDATIONS FOR OFFSHORE WIND
TURBINES IN CLAY**



A dissertation submitted for the degree of Doctor of Philosophy
at the University of Cambridge

Ben Hong, Lau

Churchill College

March 2015

DECLARATION

I hereby declare that, except where reference is made to the work of others, the contents of this dissertation are a result of my own work and include nothing which is the outcome of work done in collaboration. This dissertation has not been submitted in whole or part for consideration for any other degree, diploma or other qualification to this University or any other institution, except where cited specifically.

This dissertation contains no more than 65,000 words, inclusive of appendices, references, footnotes, tables and equations, and has less than 150 figures.

Ben Hong, Lau

March 2015

ACKNOWLEDGEMENTS

I would like to express my sincere gratitude to my supervisor, Dr Stuart Haigh, for his guidance and assistance throughout my time in Cambridge. I would not be writing this thesis if not for his support, knowledge, and wisdom. Many thanks go to my advisor, Dr Gopal Madabhushi who advised me regarding soil mechanics and centrifuge experiments, encouraged me to actively move forward, and at times worked into the wee hours of the morning to help run the centrifuge. I also would like to thank Professor Malcolm Bolton for the insightful advice he provided whenever complex issues arose throughout the research project.

A big thank you goes to the technicians of Schofield Centre that include John Chandler, Kristian Pether, Mark Smith, Richard Adams, Chris McGinnie, Ewan Cameron, and David Yates for their invaluable assistance, technical support, and insightful advice. I also would like to thank Anama Lowday for running the Schofield Centre smoothly and for arranging the test schedule to meet everyone's needs.

I would like to express my gratitude to my fellow researchers at Schofield Centre for their advice, help, and most importantly, their friendship. These include Sidney Lam, Aliasger Haiderali, Yuchen Li, Crystal Xue, Junkan Wang, Chang Ye Gue, Mei Yin, Takaaki Kobayashi, and Peter Kirkwood. A special thank you goes to Sidney Lam who showed me the ropes, guided me throughout my first two years, and continued to provide both moral and technical support even after leaving for Perth. A big thank you goes to Aliasger Haiderali who worked together with me on the analysis of my results and assisted me to further improve my Literature Review.

This PhD was made possible with the financial support I received from the EPSRC, Churchill College, the Cambridge University Engineering Department, and the Cambridge Philosophical Society.

Finally, I would like to thank my parents and my sister for their warm love and undying support over the past years. I would not have gotten this far if it were not for them.

ABSTRACT

Investment into offshore wind farms has been growing to address the growing threat of climate change. The majority of offshore wind turbines (both current and planned) are founded on monopiles, large circular steel pipe piles ranging from 4.0 m – 7.5 m in diameter. Based on available borehole records, most planned wind turbines in the UK will be founded in overconsolidated clay deposits. Monopile design is done via usage of the well established p - y curves. However, there are issues with the usage of the p - y curves. Firstly, the curves may be unsuitable to model the monopile's behaviour as it is expected to behave similarly to a rigid pile rather than flexibly. Secondly, the curves may not accurately estimate the initial pile-soil stiffness. Thirdly, the curves are not comprehensive enough to account for the accumulated strain and stiffness changes resulting from cyclic loading. Considering these issues, research was carried out to improve the current design of monopiles in clay by carrying out displacement controlled monotonic and load controlled cyclic load tests in a centrifuge.

Results from monotonic tests suggest that the DNV (2014) design methodology to construct p - y curves in clay based on Matlock's (1970) soft clay criterion significantly underestimate stiffness. Findings suggested that the experimental p - y curves could be characterised through modification of the criterion. Modification of the criterion produced estimates that matched the 3.83 m monopile experimental curves. Pile toe shear force was observed to contribute little to ultimate lateral resistance and stiffness. Despite the marginal contribution, an effort was made to characterise the pile toe shear force. Estimates of the modified criterion on the 7.62 m monopile did not match the observations, indicating that further research should be carried out to improve the modified criterion.

The cyclic tests displayed two distinct regimes; the stiffening regime and the softening regime. Results suggests that cyclic loads of different characteristics influence the locked in stress conditions of the soil which in turn influence the excess pore pressure behaviour, hence dictating whether the stiffening or softening regime takes place. Suggestions were made regarding the conditions that dictated whether the stiffening or softening regime would take place. In the stiffening regime, the stiffening rate decreased with increasing strain while as the accumulated rotation rate increased with vertical load for the same cyclic load magnitude. The softening regime was determined to be extremely detrimental as the high rates of softening and accumulated rotations could cause failure of the system in the short-term. Recommendations were made to estimate the cyclic stiffness and accumulated rotations resulting from both stiffening and softening regime.

TABLE OF CONTENTS

DECLARATION	i
ACKNOWLEDGEMENTS	iii
ABSTRACT	v
TABLE OF CONTENTS	vii
LIST OF FIGURES	xi
LIST OF TABLES	xvii
LIST OF NOTATIONS	xix
1. INTRODUCTION	1
1.1 Background	1
1.2 Objective and Research Scope	2
1.3 Outline of Thesis	3
2. LITERATURE REVIEW	4
2.1 Introduction	4
2.2 Monopile	5
2.3 Offshore Wind Farm Loads	9
2.4 Offshore Soil Conditions	12
2.5 Design Methods for Laterally Loaded Piles	14
2.6 p-y Method	17
2.6.1 Soft Clay Criterion (Matlock, 1970)	24
2.6.2 Stiff Clay Criterion below the Water Table (Reese et al., 1975)	27
2.6.3 Unified Clay Criterion (Sullivan et al., 1980)	30
2.6.4 Integrated Clay Criterion (Gazioglu and O'Neill, 1984)	33
2.6.5 Use of Bezier Curves (Kodikara et al., 2010)	37
2.7 Issues with Current Methodology	40
2.7.1 Rigid Pile Behaviour vs. Flexible Pile Behaviour	40
2.7.2 Estimation of Initial Pile-Soil Stiffness	42
2.7.3 Cyclic Loading Design	49
2.8 Summary and Research Objectives	67

3. METHODOLOGY	69
3.1 Introduction	69
3.2 Research Approach	69
3.3 Principles of Centrifuge Modelling	70
3.4 Centrifuge Facilities at University of Cambridge	73
3.4.1 Turner Beam Centrifuge at Schofield Centre	73
3.4.2 2D-Actuator	73
3.4.3 Data Acquisition	74
3.5 Experimental Programme	74
3.6 Experiment Instrumentation	77
3.6.1 PPTs	80
3.6.2 Lasers and MEMS Accelerometers	80
3.6.3 LVDT	81
3.6.4 T-bar	81
3.6.5 Seismic Cone Penetrometer	83
3.6.6 Strain-gauged Monopile, V-H Load Cell, and Pile Assembly	85
3.6.7 Web Cameras	89
3.7 Model Preparation & Experimental Procedure	89
3.7.1 Soil Preparation	90
3.7.2 PPT Installation into Tub	93
3.7.3 Model Making	94
3.7.4 Centrifuge Testing Procedure	94
3.7.5 Test Problems	98
3.8 Triaxial Testing	99
4. MONOTONIC TESTS RESULTS	102
4.1 Introduction	102
4.2 Soil Strength Profile for Uniform Preconsolidated Soils	102
4.2.1 T-bar Measurements	103
4.2.2 SCPT Measurements	106
4.3 Analysis of Bending Moments	109
4.3.1 Calculation of Soil Reaction	109
4.3.2 Estimation of Rotation Depth	111
4.3.3 Calculation of Pile Displacement	112

4.4	p-y Curves	114
4.4.1	Comparison between Experimental and DNV Design <i>p-y</i> Curves	114
4.4.2	Experiment vs. DNV Design Load-Displacement Comparison	123
4.4.3	Characterising Monopile <i>p-y</i> Curves	126
4.4.4	Comparison to Other Criteria for Constructing <i>p-y</i> Curves for Clay	132
4.4.5	Recommendations for <i>p-y</i> Curve Construction for Static Loading	135
4.5	Pile Toe Shear Force	135
4.5.1	The Effect of Pile Toe Shear Force on Pile Lateral Behaviour	135
4.5.2	Characterising the Pile Toe Shear Force	137
4.5.3	Recommendations for Constructing Pile Toe Shear Force Curve	140
4.6	Summary	141
5.	CYCLIC TESTS RESULTS	143
5.1	Introduction	143
5.2	Soil Strength Profile for Cyclic Experiments	143
5.3	Analysis Conditions	145
5.3.1	Filter Frequency Parameters	145
5.3.2	Vertical and Horizontal Load Conditions	145
5.4	Verification of OWF 09 Vertical Load Condition and Applicability of Suggested <i>p-y</i> Curves	148
5.5	Cyclic Stiffness Regimes	153
5.5.1	Investigating Cyclic Stiffness	153
5.5.2	Stiffening Regime	157
5.5.2.1	$\xi_c \approx 0$	157
5.5.2.2	$\xi_c \approx -0.35$	165
5.5.3	Softening Regime	172
5.5.3.1	$\xi_c \approx -0.25$	172
5.5.4	Factors and Conditions to Stiffening & Softening Regimes	176
5.6	Estimating Cyclic Stiffness	181
5.6.1	Secant Stiffness over <i>p-y</i> Curve Stiffness	181
5.6.2	Estimating Cyclic Stiffness of Stiffening Regime	183
5.6.3	Estimating Cyclic Stiffness of Softening Regime	195
5.6.4	Recommendation to Estimate Cyclic Stiffness	197
5.7	Estimating Accumulated Rotations	198

5.7.1	Estimating Accumulated Rotations in Stiffening Regime	198
5.7.2	Estimating Accumulated Rotations in Softening Regime	206
5.7.3	Recommendation to Estimate Cyclic Accumulated Rotations	207
5.8	Ground Surface Disturbance	208
5.9	Summary	211
6.	CONCLUSION	214
6.1	Introduction	214
6.2	Static Loading	214
6.2.1	Analysis of Bending Moments	214
6.2.2	<i>p-y</i> Curves	215
6.2.3	Pile Toe Shear Force	216
6.2.4	Effect of Pile Diameter	216
6.3	Cyclic Loading	217
6.3.1	Cyclic Stiffness Regimes	217
6.3.2	Estimating Cyclic Stiffness	218
6.3.3	Estimating Accumulated Rotations	218
6.3.4	Implications of Stiffness Changes	219
6.3.5	Ground Surface Disturbance	219
6.4	Recommendations for Further Research	219
	REFERENCES	223

LIST OF FIGURES

Figure 2.1	Wind Turbine Size Comparison and Foundation Options	6
Figure 2.2	Offshore Wind Turbine Current and Future Trend (Doherty et al., 2011).	7
Figure 2.3	6.5 m Monopile for Baltic 2 Offshore Wind Farm (Offshore Wind Industry, 2013).....	8
Figure 2.4	Difference between Load Conditions for an Offshore Wind Turbine and Oil & Gas Jack-up Rig (Byrne and Houlsby, 2003)	9
Figure 2.5	Typical Excitation Ranges of a Modern Offshore Wind Turbine (adapted from LeBlanc, 2009).....	11
Figure 2.6	Generalised Soil Provinces in the North Sea (Thomas, 1989).....	13
Figure 2.7	Round 3 Offshore Wind Zones (adapted from The Crown Estate, 2013)	14
Figure 2.8	Distribution of Stresses against a Pile before and after Lateral Deflection (Brødbæk et al., 2009)	17
Figure 2.9	Model for a Pile under Lateral Loading with p - y Curves (Reese and Van Impe, 2001).....	18
Figure 2.10	Element from Beam-Column (adapted from Reese and Van Impe, 2001)	18
Figure 2.11	Adopted Sign Convention (adapted from Reese and Van Impe, 2001) .	21
Figure 2.12	Complete Solution Results (adapted from Reese and Van Impe, 2001)	21
Figure 2.13	Undrained Stiffness to Undrained Shear Strengths for Clays with Low Plasticity (Reese and Van Impe, 2001).....	22
Figure 2.14	Arrangement for Field Tests using Restrained-Head Lateral Loading carried out by Matlock (1970)	24
Figure 2.15	Characteristic Shapes of p - y Curves for Soft Clay (a) Static Loading (b) Cyclic Loading (c) After Cyclic Loading (DNV, 1992).....	26
Figure 2.16	Field Test Setup for 0.61 m Diameter Test Piles by Reese et al. (1975)	27
Figure 2.17	Static Load p - y Curve for Stiff Clay below Water Table (adapted from Reese et al., 1975).....	28
Figure 2.18	Values of Constants A_s and A_c Table (adapted from Reese et al., 1975)	29
Figure 2.19	Cyclic Load p - y curve for Stiff Clay below Water Table (adapted from Reese et al., 1975).....	29
Figure 2.20	Static Load p - y Curve for Unified Clay Criterion (adapted from Sullivan et al., 1980)	31
Figure 2.21	Cyclic Load p - y Curve for Unified Clay Criterion (adapted from Sullivan et al., 1980).....	33
Figure 2.22	p - y Curve for Integrated Clay Criterion (Gazioglu and O'Neill, 1984)..	36

Figure 2.23 Typical Representations of p - y Curve (Bransby, 1996) and Bezier technique (Kodikara et al., 2010).....	37
Figure 2.24 Variation in p_u/c_uD with s_i/s_u (adapted from Kodikara et al., 2010)	39
Figure 2.25 Rigid vs. Flexible Pile Behaviour (Brødbæk et al., 2009).....	40
Figure 2.26 Mobilised Horizontal Stresses for a 7.5 m Monopile in 30 m Dense Sand (Abdel-Rahman and Achmus, 2005)	42
Figure 2.27 Comparison of Finite Element Results with p - y Results (Abdel-Rahman and Achmus, 2005).....	43
Figure 2.28 Ratio of Numerically Derived Pile Head Displacements to Displacements from p - y Method relative to Sand Relative Density and Pile Diameter (Achmus et al., 2011).....	44
Figure 2.29 Lely Wind Farm (a) Layout of Wind Turbines (b) Typical Soil Profile	46
Figure 2.30 Clay Stress-Strain Curve from Cyclic Constant-Volume Equivalent Undrained Direct Simple-Shear Test (Matasović and Vucetic, 1995)	50
Figure 2.31 Secant Shear Modulus Reduction vs. Cyclic Shear Strain for Fully Saturated Soils (adapted from Vucetic, 1994)	51
Figure 2.32 Variation of Degradation Parameter t_{dgrd} with γ_c and Overconsolidation Ratio (OCR) for Four Venezuelan Offshore Clays (adapted from Vucetic and Dobry, 1988)	52
Figure 2.33 Strains Measureable by Different Laboratory Tests (Rattley, 2011)	53
Figure 2.34 Pore-Water Pressure Variation during Cyclic Loading (Dobry and Vucetic, 1987).....	54
Figure 2.35 Lombardi et al. (2013) Model Cyclic Test Setup.....	57
Figure 2.36 Comparison of Load Test and Calculated Ultimate Capacity (Zhang et al., 2011)	59
Figure 2.37 T-bar Resistance Degradation Factor (Zhang et al., 2011)	61
Figure 2.38 Normalised Stiffness Degradation (Zhang et al., 2011).....	61
Figure 2.39 Experiment Setup of Su et al. (2014)	62
Figure 2.40 Pile Head Displacement (a) Time History of Unidirectional Cyclic Test (b) Time History of Unidirectional Irregular Test (c) Path for Cross Test (d) Path for Eight-Shape Test (e) Path for Multidirectional Irregular Test (Su et al., 2014).....	63
Figure 2.41 Displacement Path Influence on Resistance Degradation (Su et al., 2014)	64
Figure 2.42 Comparison between Estimates of Heidari et al. (2014) and Measurements of Pender-Pranjoto (Pender and Pranjoto, 1996, Pranjoto and Pender, 2003)	65
Figure 2.43 Load Displacement Comparison between Estimates of Heidari et al. (2014) and Measurements of Tuladhar et al. (2008) for Different Models	65
Figure 3.1 Soil Behaviour Difference between Model and Prototype (adapted from Madabhushi, 2014)	70

Figure 3.2	Principle of Centrifuge Modelling (adapted from Madabhushi, 2014)....	71
Figure 3.3	Turner Beam Centrifuge at Cambridge (Madabhushi, 2014).....	73
Figure 3.4	Schematic of Experiment Setup, Not to Scale (a) Plan View of the 850 mm Tub with Location of Monopile and CPT (b) Cross Section of Setup	76
Figure 3.5	(a) Instrumentation Plan (b) Experimental Setup for Experiments OWF 01 (First Run with No Counterweight) to OWF 03	78
Figure 3.6	(a) Instrumentation Plan (b) SCPT Setup for Experiments OWF 01 (Second Run) and OWF 05 to 09.....	79
Figure 3.7	Laser and MEMS behind Monopile	80
Figure 3.8	T-bar (a) Column Section (b) Cylindrical Section (c) Fully Assembled..	82
Figure 3.9	Seismic Cone Penetrometer (a) Design Details (b) Assembly (c) SCPT Head Submerged in Silicone Fluid	84
Figure 3.10	38.3 mm Diameter Monopile	86
Figure 3.11	76.2 mm Diameter Monopile	88
Figure 3.12	Top of Pile Assembly (a) General Assembly Schematic (b) OWF 02 and OWF 03 Assembly (c) OWF 05 to OWF 08 Assembly	89
Figure 3.13	Sample Preparation Procedure	90
Figure 3.14	Installation of PPTs	93
Figure 3.15	Preparation of the Clay	94
Figure 3.16	Dissipation of Excess Pore Water Pressure.....	95
Figure 3.17	Excess Pore Pressure Isochrones during Reconsolidation	96
Figure 4.1	OCR Profile at 90% Reconsolidation	102
Figure 4.2	s_u Comparison for Uniform Pre-consolidated Soils	103
Figure 4.3	Idealised Behaviour associated with Shallow and Deep T-bar Penetration (a) Variation in Bearing Factor Depth (b) Shallow and Deep Failure Mechanisms (adapted from White et al., 2010)	104
Figure 4.4	Soil Surface at T-bar after Spin-down.....	106
Figure 4.5	Fitting of Triaxial Test Data (adapted from Vardanega et al., 2012).....	106
Figure 4.6	SHANSEP s_u Comparison for Different m Values.....	107
Figure 4.7	OWF 03 Measured Bending Moment	109
Figure 4.8	Comparison of Results from MATLAB Fitting Functions	110
Figure 4.9	Rotation Depth from Point of Zero Soil Reaction.....	111
Figure 4.10	Linear Extrapolation of Bending Moment above Soil Surface	113
Figure 4.11	OWF 03 Pile Displacement Curves.....	114
Figure 4.12	Experimental vs. DNV Design p - y Curves of OWF 03 – 180 kPa Preconsolidated	118
Figure 4.13	Experimental vs. DNV Design p - y Curves of OWF 01 – 300 kPa Preconsolidated	120

Figure 4.14 Experimental vs. DNV Design p - y Curves of OWF 02 – 500 kPa Preconsolidated	122
Figure 4.15 LPILE Analysis Setup	123
Figure 4.16 Free Body Diagram of Centrifuge Test	124
Figure 4.17 Load Cell Force vs. Moment at Soil Surface	124
Figure 4.18 OWF 02 Bending Moment Comparison between Experiment and DNV Design in Prototype Scale	125
Figure 4.19 Load-Displacement and Stiffness Comparison between Experiment and DNV Design	126
Figure 4.20 Logarithmic Plot of p - y Curves for OWF 02	127
Figure 4.21 Experimental vs. Modified DNV Design p - y Curves of OWF 03 – 180 kPa Preconsolidated	128
Figure 4.22 Experimental vs. Modified DNV Design p - y Curves of OWF 01 – 300 kPa Preconsolidated	129
Figure 4.23 Experimental vs. Modified DNV Design p - y Curves of OWF 02 – 500 kPa Preconsolidated	130
Figure 4.24 Horizontal Load vs. Mudline Displacement Comparison between Experiment and Modified DNV Design	131
Figure 4.25 OWF 02 Bending Moment Comparison between Experiment and Modified DNV Design in Prototype Scale	132
Figure 4.26 Smooth Pile Comparison between EMSD and Finite Difference Method for Truncated Power Law (Klar and Osman, 2008)	134
Figure 4.27 Load-Displacement and Stiffness Comparison between Experiment, DNV Design and DNV Design with Pile Toe Shear Force	136
Figure 4.28 OWF 01 Soil Comparison between DNV and DNV + Shear Force	137
Figure 4.29 OWF 03 Bending Moment Curves at 18 m Depth showing Different Exponential Powers and Displacements for Shear Force Mobilisation	138
Figure 4.30 OWF 01 Bending Moment Curves at 17 m Depth Comparison for Shear Force with Different Exponential Powers at $32y_c$ Full Mobilisation	139
Figure 4.31 OWF 02 Bending Moment Curves at 18 m Depth Comparison for Shear Force with Different Exponential Powers at $55y_c$ Full Mobilisation	139
Figure 4.32 Experimental Pile Toe Normalised p - y Curves	140
Figure 5.1 Undrained Shear Strength Comparison for Cyclic Experiments	144
Figure 5.2 Cyclic Loading Characteristic Defined in Terms of ξ_b and ξ_c (adapted from LeBlanc et al., 2010b)	146
Figure 5.3 OWF 09 Vertical Load Condition for (a) Experimental Assembly (b) LPILE Modified Matching Bending Moment Condition	148
Figure 5.4 OWF 09 Peak Load Rotation Depth	149
Figure 5.5 OWF 08 Stage 4 Rotation Depth Difference between Soil Reaction Estimate and Laser & MEMs Estimate	149

Figure 5.6 Rotation Depth Comparison between 3.83 m and 7.62 m Monopile in 500 kPa Preconsolidated Speswhite Kaolin for F_{shear} of Different Exponents.....	150
Figure 5.7 OWF 09 Horizontal Load vs. Actuator Displacement Comparison between Experiment and LPILE Estimates	152
Figure 5.8 Method to Determine Stiffness for (a) $\xi_c \approx 0$ (b) $\xi_c < 0$	153
Figure 5.9 Layout of PPTs	154
Figure 5.10 Plotting of ES (Effective Stress) and TS (Total Stress) on $s' - t$ Space for Biaxial Lateral Compression and Lateral Expansion.....	156
Figure 5.11 OWF 08 Stage 4 $\xi_b = 0.57$, $\xi_c = 0.10$ (a) Prototype Scale Bending Moment at Zero Load (b) Prototype Rotational Stiffness	157
Figure 5.12 OWF 08 Stage 3 $\xi_b = 0.41$, $\xi_c = 0.05$ p - y Curve above Rotation Point Stiffness Quantification	158
Figure 5.13 OWF 08 Stage 3 $\xi_b = 0.41$, $\xi_c = 0.05$ p - y Curve below Rotation Point Stiffness Quantification	159
Figure 5.14 OWF 08 Stage 4 $\xi_b = 0.57$, $\xi_c = 0.10$ Excess Pore Pressure Behaviour	160
Figure 5.15 OWF 09 Location 1 to 3 Excess Pore Comparison with Horizontal Force	162
Figure 5.16 OWF 09 Stage 3 $\xi_b = 0.28$, $\xi_c = 0.03$ Excess Pore Pressure Behaviour	164
Figure 5.17 OWF 07 Stage 3 $\xi_b = 0.28$, $\xi_c = -0.35$ (a) Bending Moment at Zero Load (b) Rotational Stiffness (c) Stiffness relative to Marginal Actuator Displacement ..	166
Figure 5.18 OWF 09 Stage 6 $\xi_b = 0.40$, $\xi_c = -0.39$ Secant Stiffness	166
Figure 5.19 OWF 07 Stage 2 $\xi_b = 0.16$, $\xi_c = 0.06$ Bending Moment at Zero Load.	167
Figure 5.20 OWF 07 Stage 3 $\xi_b = 0.28$, $\xi_c = -0.35$ p - y Curve above Rotation Point Stiffness.....	168
Figure 5.21 OWF 07 Stage 3 $\xi_b = 0.28$, $\xi_c = -0.35$ p - y Curve below Rotation Point Stiffness.....	168
Figure 5.22 OWF 07 Stage 3 $\xi_b = 0.28$, $\xi_c = -0.35$ Excess Pore Pressure Behaviour	170
Figure 5.23 OWF 09 Stage 6 $\xi_b = 0.40$, $\xi_c = -0.39$ Excess Pore Pressure Behaviour	171
Figure 5.24 OWF 08 Stage 5 $\xi_b = 0.62$, $\xi_c = -0.25$ (a) Prototype Scale Bending Moment at Zero Load (b) Prototype Rotational Stiffness	172
Figure 5.25 OWF 08 Stage 5 $\xi_b = 0.62$, $\xi_c = -0.25$ p - y Curve above Rotation Point Stiffness.....	173
Figure 5.26 OWF 08 Stage 5 $\xi_b = 0.62$, $\xi_c = -0.25$ p - y Curve below Rotation Point Stiffness.....	173
Figure 5.27 OWF 08 Stage 5 $\xi_b = 0.62$, $\xi_c = -0.25$ Excess Pore Pressure Behaviour	174

Figure 5.28	OWF 07 Soil Reaction at Trough for Different Stages	176
Figure 5.29	OWF 08 Stage 7 Monotonic Soil Reaction	177
Figure 5.30	OWF 07 Soil Reaction Change at 12m Depth.....	178
Figure 5.31	Cyclic Load Conditions Dictating Stiffening and Softening Regime ..	179
Figure 5.32	Summarised Observations and ξ_c Uncertainty Range Dictating Cyclic Stiffness Regime for $\xi_b \geq \xi_{b\text{ prv}}$	180
Figure 5.33	Values of K_b and K_c as a Function of Relative Density, R_d , and the Characteristics of the Cyclic Load in terms of ξ_b and ξ_c (LeBlanc et al., 2010b)	184
Figure 5.34	Measured Non-Dimensional Stiffness Results of LeBlanc et al. (2010b)	185
Figure 5.35	Secant Stiffness Logarithmic Fits of Cyclic Experiments.....	186
Figure 5.36	Marginal Strain Comparison between OWF 06 and OWF 09	187
Figure 5.37	Power Function Fitting to (a) A_k/k_o vs. $\Delta\varepsilon_{pile}$ (b) A_k/k_o vs. $\Delta\theta$	188
Figure 5.38	Behaviour Comparison between Pile With and Without Vertical Load	189
Figure 5.39	OWF 08 Stage 4 $\xi_b = 0.57$, $\xi_c = 0.10$ Monopile Secant Stiffness from Mudline Displacement Comparison between Changing and Constant Rotation Depth	192
Figure 5.40	Fitted Secant Stiffness and Measured Secant Stiffness at Cycle 1.....	192
Figure 5.41	Secant Stiffness Comparison between Equation Derived vs. Experiment	194
Figure 5.42	OWF 09 Stage 6 $\xi_b = 0.40$, $\xi_c = -0.39$ Secant Stiffness Comparison between Equation Derived vs. Experiment.....	195
Figure 5.43	Stiffness Change Relative to 1 st Cycle for Softening Regime.....	196
Figure 5.44	Accumulated Rotation Definition (adapted from LeBlanc et al., 2010b)	198
Figure 5.45	Functions Relating T_b and T_c to R_d , ξ_b , and ξ_c (LeBlanc et al., 2010b).	199
Figure 5.46	B as a Function of ξ_b	200
Figure 5.47	j Fittings as a Function of ξ_b for Respective Experiments	202
Figure 5.48	j Fittings as a Function of ξ_b by Pile Diameter.....	203
Figure 5.49	Accumulated Rotation Comparison between Equation Derived vs. Experiment.....	205
Figure 5.50	OWF 09 Stage 5 $\xi_b = 0.44$, $\xi_c = -0.27$ θ_N/θ_o vs. Cycles	206
Figure 5.51	OWF 08 Stage 2 to 4 $\xi_c \approx 0$ Soil Deformation behind Monopile.....	209
Figure 5.52	OWF 07 Stage 3 $\xi_b = 0.28$, $\xi_c = -0.35$ Soil Deformation behind Monopile.....	210
Figure 5.53	OWF 08 Stage 5 $\xi_b = 0.62$, $\xi_c = -0.25$ Soil Deformation behind Monopile.....	210

LIST OF TABLES

Table 2.1 Recommended Values for k_s for Stiff Clays (Reese and Van Impe, 2001)	28
Table 2.2 Recommended k_s Values for Clays for Different s_u (Sullivan et al., 1980)	32
Table 2.3 Curve Parameters for Unified Clay Criterion (Sullivan et al., 1980)	32
Table 2.4 Soil Degradability Factor, F (Gazioglu and O'Neill, 1984)	34
Table 2.5 Soil Modulus vs. Undrained Shear Strength for Integrated Clay Criterion (adapted from Gazioglu and O'Neill, 1984)	34
Table 2.6 Results of A' -Factor Optimisation Study (adapted from Gazioglu and O'Neill, 1984)	35
Table 2.7 Values of Constants α , β , B and C for Tension and No-Tension Failure of Soils (adapted from Kodikara et al., 2010)	39
Table 2.8 Chronological List of Research on Diameter Effect on Secant and Initial Stiffness of p - y curves (Brødbæk et al., 2009)	44
Table 2.9 Predicted and Measured Frequencies of Turbines in Lely Wind Farm (Delft University of Technology et al., 2003)	47
Table 2.10 Reference Deflection for 4 m Monopile for Soft Clay Criterion	48
Table 2.11 Reference Deflection for 4 m Monopile for Stiff Clay Criterion below Water Table	48
Table 2.12 Research Summary on Monopile Cyclic Lateral Load Behaviour in Sand	56
Table 3.1 Scaling Laws relevant to Centrifuge Modelling of Monopile	72
Table 3.2 Performance Specification of 2D-Actuator (Haigh et al., 2010)	74
Table 3.3 Experimental Programme in Prototype Scale	75
Table 3.4 Site Specifications	75
Table 3.5 Details of Distance Sensor Lasers Utilised	81
Table 3.6 Published Properties of Speswhite Kaolin Clay	91
Table 3.7 Measured Properties of Speswhite Kaolin Clay	92
Table 3.8 Comparison between Undrained Shear Strength Profile Estimates	93
Table 3.9 Cyclic Experiment Loading Details in Model Scale	96
Table 3.10 Experimental Troubles and Issues	98
Table 5.1 Monotonic Load Capacity of Experiments OWF 07 & OWF 08	146
Table 5.2 Cyclic Load Characteristics of Experiment OWF 06 to OWF 09	147
Table 5.3 Rotation Depth of 35 m Long Monopile (Haiderali, 2012)	151
Table 5.4 LPILE p - y Curve Stiffness Change Study Cases	181

Table 5.5	p - y Curve Final Stiffness Ratio Relative to First Cycle.....	182
Table 5.6	LPILE Rotation Depth Comparison between Study Cases	182
Table 5.7	Rotation Depth at Peak Load from Experiment Soil Reaction Curves....	183
Table 5.8	A_k Comparison between Stiffening and Softening Regimes for Similar ξ_b	196
Table 5.9	j Comparison between $\xi_c \approx 0$ and $\xi_c \approx -0.25$ for Similar ξ_b	206

LIST OF NOTATIONS

Roman

A	Coefficient to define shape of p - y curve for Unified Clay criterion
A'	Coefficient to define shape of p - y curve for Integrated Clay criterion
A_c	Constant to construct cyclic p - y curves for Stiff Clay criterion below Water Table
A_{comb}	Combined cross-sectional area of monopile and enclosed soil plug
A_k	Rate of pile cyclic secant stiffness increase
$A_{k\ soft}$	Rate of pile cyclic secant stiffness decrease
A_s	Constant to construct static p - y curves for Stiff Clay criterion below Water Table
B	Dimensionless constant to quantify accumulated rotation exponentially
C_{as}	Secondary swelling index
C_s	Swelling index
D	Pile diameter
D_{cone}	Cone diameter
E_{py}^*	Initial pile-soil stiffness
E_p	Pile elastic modulus
E_{py}	Reaction modulus of pile under lateral loading or modulus of subgrade reaction (secant modulus p/y)
E_s	Soil elastic modulus
ES	Effective stress
E_{sec}	Secant soil stiffness at half the deviator stress at failure in UU triaxial compression
$(E_s)_{max}$	Limiting maximum value of soil modulus on p - y curve for Unified Clay criterion
F	Soil degradability factor
F_1	Resistance in first cycle
F_c	Soil degradability factor for cyclic loading
$F_{capacity}$	Monotonic load capacity
F_{max}	Maximum horizontal force acting at top of pile
F_{min}	Minimum horizontal force acting at top of pile
F_N	Resistance in N th cycle

FOS	Factor of safety
F_s	Soil degradability factor for static loading
F_{shear}	Pile toe shear force
F_x	Horizontal force acting at top of pile
F_{zero}	Horizontal force at time of zero lateral load
G	Soil shear modulus
$G_{max N}$	Maximum initial shear modulus at small strains
G_s	Specific gravity
G_{sN}	Secant shear modulus at cycle N
I_p	Pile area moment of inertia
J	Dimensionless empirical constant to construct p - y curves for Soft Clay criterion
K_b	Dimensionless function dependent on load magnitude to determine dimensionless monopile stiffness of 1 st cycle
K_c	Dimensionless function dependent on cyclic load characteristic to determine dimensionless monopile stiffness of 1 st cycle.
L	Pile embedded length
L_c	Critical pile length
LI	Liquidity Index
LL	Moisture content at liquid limit (%)
M	Bending moment in pile
M_{CSL}	Slope of critical state line in q' - p plane
M_{max}	Maximum applied bending moment
M_{min}	Minimum applied bending moment
M_{soil}	Soil surface bending moment
M_y	Pile yield moment
M_{zero}	Bending moment at time of zero lateral load
N	Number of cycles
N_b	T-bar bar factor
NC	Normally consolidated
N_{CL}	Intercept of isotropic consolidation line at $p' = 1$ kPa
N_{kt}	Cone factor
N_p	Ultimate lateral soil resistance coefficient
N_s	Scaling factor
N_T	Bearing factor
N_{T-bar}	T-bar cycle number

N_{T-deep}	Bearing factor at which deep flow mechanism takes place
$N_{T-shallow}$	Bearing factor at which shallow flow mechanism takes place
OC	Overconsolidated
OCR	Overconsolidation ratio
P	Force per unit length acting on cylinder
PI	Plasticity index
PL	Moisture content at plastic limit (%)
P_x	Axial force in pile
R^2	Coefficient of determination
R_d	Relative density
S	Shearing force in pile
S_t	Sensitivity
T_b	Dimensionless function to estimate accumulated rotation in sand that is dependent on cyclic load ratio to monotonic capacity and relative density
T_c	Dimensionless functions to estimate accumulated rotation in sand that is dependent on minimum cyclic load magnitude to maximum cyclic load magnitude ratio
TS	Total stress
V	Dimensionless penetration rate
W_{c-w}	Counterweight force
W_{pile}	Pile self weight
X	Depth below soil surface
X_{cr}	Critical depth
X_R	Transition depth to construct p - y curves for Soft Clay criterion
$1P$	Wind turbine first excitation frequency
$3P$	Three-bladed wind turbine blade passing frequency
a	Cone area ratio
b	Constant to resolve for double integration of bending moment curve
c	Second constant to resolve for double integration of bending moment curve
c_v	Coefficient of consolidation
d	Diameter of T-bar cylinder
dof	Degrees of freedom for t-distribution calculation
d_{rot}	Monopile rotation depth

f	Factor to calculate accumulated plastic strains
f_1	First natural frequency of the tower-foundation system
f_N	Natural frequency after N cycles
g	Earth's gravity
h	Height of force acting above soil surface
h_{pile}	Height above soil that pile self weight is acting
j	Dimensionless rate of accumulated rotation of stiffening regime
j_{soft}	Dimensionless rate of accumulated rotation of softening regime
k	Monopile secant stiffness
$k_{equation}$	Equation estimated monopile secant stiffness
$k_{experiment}$	Experimentally observed monopile secant stiffness
k_N	Monopile secant stiffness at N th cycle
\tilde{k}_N	Dimensionless monopile stiffness at N th cycle
k_o	Fitted monopile stiffness at 1 st cycle
\tilde{k}_o	Dimensionless first cycle pile stiffness
k_s	Subgrade reaction modulus to establish initial straight line portion of static and cyclic p - y curve for Stiff Clay criterion below Water Table
m	Soil parameter defining the relationship between normalized s_u values at different OCR levels
n	Number of data points used in regression
p	Lateral soil reaction
p_a	Atmospheric Pressure
p_u	Ultimate lateral soil reaction
p -value	The smallest level of significance that would lead to the rejection of the null hypothesis
q_c	Cone resistance
q_t	Corrected total cone resistance
q_{t-bar}	T-bar undrained penetration resistance
r	Square of the correlation coefficient
s	Plane strain mean stress
s_u	Undrained shear strength
$(s_u)_{avg}$	Average undrained shear strength above depth X
t	Plane-strain deviatoric stress
$tails$	Number of tails in Student t-distribution
t_{dgrd}	Degradation parameter
t_{st}	Test statistic for Student's t-distribution

Δu	Excess pore pressure
u_2	Pore pressure acting behind the cone
v	Cone penetration rate
w_{deep}	Depth at which deep failure flow mechanism takes place
x	Position along the pile axis
y	Pile lateral displacement
y_{act}	2D-actuator displacement
y_c	Reference deflection to construct p - y curves where half the maximum lateral soil reaction is mobilised
y_{int}	Pile lateral displacement from double integration
y_{max}	Maximum pile lateral displacement
y_p	Deflection to construct cyclic p - y curves for Stiff Clay criterion below Water Table
$y_{shear\ full}$	Deflection where pile toe shear force is fully mobilised
$y_{shear\ ref}$	Arbitrary reference deflection to construct pile toe shear force curve
z_{cr}	Height of unsupported excavation

Greek

α	Constant to calculate reference deflection of Modified DNV methodology
β	Exponential power to calculate pile toe shear force curve
χ	Constant to calculate displacement at which pile toe shear force is fully mobilised
δ	Degradation index
ε_c	Axial strain which occurs at one-half the maximum deviatoric stress in laboratory undrained compression tests of undisturbed soil samples
ε_{pile}	Monopile displacement strain
Γ	Intercept of csl at $p' = 1$ kPa
γ'	Effective unit weight
γ'_{avg}	Average effective unit weight from ground surface to depth at which p - y curves applies
γ_c	Cyclic shear strain amplitude
γ_{ll}	Linear cyclic threshold shear strain
γ_{lv}	Volumetric cyclic threshold shear strain
$\gamma_{M=2}$	Shear strain at half strength

η	Average exponential power to accumulated rotation fit
φ	Double differentiation of pile lateral displacement to depth
κ	Slope of unload-reload line
λ	Slope of normal consolidation line
$\theta_{equation}$	Equation estimated monopile accumulated rotation
$\theta_{experiment}$	Experimentally observed monopile accumulated rotation
θ_{max}	Monopile rotation at maximum horizontal force
θ_{min}	Monopile rotation at minimum horizontal force
θ_N	Monopile peak load rotation at N th cycle
θ_o	Monopile peak load rotation of 1 st cycle
θ_s	Static pile rotation from pushover test
θ_{zero}	Monopile rotation at zero load
σ'_h	Effective horizontal stress
σ_o	Initial compressive stress
σ_t	Soil tensile strength
σ'_v	Effective vertical stress
σ_{vo}	Total in-situ vertical stress
τ_{cN}	Cyclic shear stress amplitude at cycle N
ω	Constant to calculate softening rate of softening regime
ξ_b	Cyclic load ratio to monotonic capacity
$\xi_{b\,prv}$	Cyclic load ratio to monotonic capacity of previous stage
ξ_c	Minimum cyclic load magnitude to maximum cyclic load magnitude ratio
ψ	Constant to calculate rate of accumulated rotation due to softening regime

CHAPTER 1

1. INTRODUCTION

1.1 Background

Many countries throughout the world are investing in renewable sources of energy not only to reduce their reliance on imported fossil fuels, but also to address the global issue of climate change that threatens to endanger the stability of the world's climate, economy, and population. One promising source of renewable energy is offshore wind; i.e. the construction of wind farms in bodies of water to generate electricity from wind. Offshore wind farms have multiple advantages that include greater output due to stronger winds and greater consistency and efficiency due to less turbulence. Considering the advantages and benefits that offshore wind turbines have to offer, many countries throughout the world are investing heavily in offshore wind. The UK in particular is investing heavily as it aims to construct 7,000 turbines that are expected to generate 33 GW of energy by 2020 (McCarthy, 2008).

To ensure the viability of offshore wind turbines, the foundations have to be well designed to resist the harsh conditions at sea. Not only must the foundation be designed to resist large overturning moments, it must also be designed to resist millions of cycles of lateral loading and maintain its stiffness over its 25 year design lifetime. There are multiple foundation options that are utilised to support these offshore wind turbines that include monopod support structures such as gravity bases, suction caissons, and large single piles known as monopiles, and multipod support structures such as tripods, jackets, and tension leg with suction buckets. Out of the three monopod foundations, the monopile is the most widely applied concept in most recent offshore wind farm developments as it is relatively easy to fabricate in large quantities, handle, install, and design as the loads are normally more readily defined. Since most of the Round 3 offshore wind farms are situated in the northern and central parts of UK (The Crown Estate, 2013), it is likely that these wind farms will be founded on overconsolidated clay deposits (Thomas, 1989) .

Monopiles are designed according to the p - y curves (i.e. soil reaction – lateral displacement curves) specified in the design standards such as DNV (2014). Even though the p - y curves have been proven to be effective due to low failure rates of piles over several decades, there are multiple issues and limitations regarding their usage. This include the suitability of utilising p - y curves on short rigid monopiles, accurate estimation of initial pile-soil stiffness, the shortcomings of the p - y curves in cyclic loading design, and the lack of knowledge of how soil stiffness would change over the design lifetime when subjected to millions of cycles of load. Much research has been carried out for monopiles in sand. However, very little research has been done on monopiles in clay. Considering the need to construct monopiles in clay in the UK and the lack of knowledge in these areas, further research is required.

1.2 Objective and Research Scope

The main objective of this research is to optimise and improve the current design of monopiles in the UK by obtaining a better understanding of soil-monopile behaviour in overconsolidated clay under monotonic and cyclic loading through centrifuge testing. To achieve this objective:

1. Horizontal pushover tests on monopiles in overconsolidated speswhite kaolin subjected to different consolidation pressures were carried out to ascertain the suitability of the p - y curves recommended by the DNV. Evaluation of the p - y curves involved triaxial testing that provided stress-strain information of the soil and the utilisation of lateral pile response computer program LPILE to evaluate the monopile's lateral response. Findings from these tests provided the basis for suggestions to improve monopile design with regards to initial stiffness and ultimate capacity.
2. Cyclic lateral load tests involving lateral loads of varying characteristics (i.e. varying load to ultimate capacity ratios and cyclic load ratios) were carried out to study the monopile's long-term response to cyclic loading. Observations from these tests provided information regarding the monopile's behaviour under cyclic loading and enabled recommendations to improve cyclic design to be developed. Pore pressure measurements made during these tests provided insight on the

excess pore pressure behaviour along the length of the monopile and how it changed across the cyclic loading phase. Video recordings and photos taken during the tests enabled evaluation of the effects of cyclic loading at the monopile-soil interface at mudline.

1.3 Outline of Thesis

The thesis contains six chapters:

Chapter 1 describes the background, objectives, and scope of the work.

Chapter 2 provides a review of literature and outlines the background knowledge regarding monopiles that include the loading conditions, the design process, cyclic loading, and the issues and limitations pertaining to the usage of p - y curves for monopile design.

Chapter 3 provides background information behind centrifuge modelling and proceeds to detail the design of the overall project that include preparation of the model, the instruments and equipment utilised, the procedure of the centrifuge experiments, and the problems faced in each of the experiments. The triaxial testing procedure utilised to obtain the stress-strain behaviour of the tested soil is also described in chapter 3.

In chapter 4, the results of the monotonic lateral load tests are reported and discussed. Suggestions to improve the design procedure are also made in this chapter.

Chapter 5 discusses the results of the cyclic lateral load tests from different aspects and suggestions to improve cyclic design are provided.

Chapter 6 summarises the key findings of this research and provides suggestions on future research in this area.

CHAPTER 2

2. LITERATURE REVIEW

2.1 Introduction

According to the UK Department of Trade and Industry (2007), “climate change as a result of rising greenhouse gas emissions is a global issue of great significance that threatens the stability of the world’s climate, economy, and population”. Since the causes and consequences of climate change are global, a collective global effort is necessary to effectively address this issue. Inaction is detrimental to all. According to the review carried out by Stern (2007), climate change has to be addressed as the “economic risks of inaction in the face of climate change are very severe”. Though mitigation measures to reduce emissions may appear costly, the benefits of addressing climate change greatly outweigh the costs. One measure that is expected to contribute significantly to the reduction of emissions is renewable energy. According to the International Energy Agency’s 450 ppm scenario, renewable energy can contribute 20% of the world goal of greenhouse gas emission reductions by 2030 under accelerated environmental policies, contributing 2741 Mt (million tons) in reductions out of 13,800 Mt (Renewable Energy Focus, 2009).

In spring 2007, the European heads of state endorsed a plan and agreed to an Energy Policy for Europe that would address the issues of energy supply, climate change, and industrial development (European Commission, 2008). The “20:20:20” targets of the plan called for a 20% increase in energy efficiency, 20% reduction in greenhouse gas emissions, and 20% share of renewables in overall European Union (EU) energy consumption – all by 2020. Based on the report from the Carbon Trust (2008), the targets require that 15% of all energy in the United Kingdom (UK) comes from renewables. This can be achieved by introducing renewables into transport, gas heating, and electricity. However, there are significant challenges to biofuels and heat renewables as highlighted by the Carbon Trust (2008). Therefore, if the UK is to

achieve the EU renewable energy targets and to avoid the risk of trading with other countries, 40% of electricity would need to come from renewables by 2020.

Considering that the UK has 40% of Europe's wind resource, that offshore wind farms face less planning restrictions than onshore wind farms and that offshore wind farms offer a great reduction in carbon dioxide emissions (Ffrench et al., 2006), it can be seen that utilising offshore wind would probably be the most effective way to achieve these targets (Carter, 2007). As a result, the UK government announced that it aims to construct 7,000 turbines that are expected to generate 33 GW of energy, which will be about one-third of UK energy requirements (McCarthy, 2008). This in turn would place the UK as the world leader of offshore wind power generation by 2020 (Carbon Trust 2008). Therefore, offshore wind farms will play a major role in the future of renewable energy in the UK.

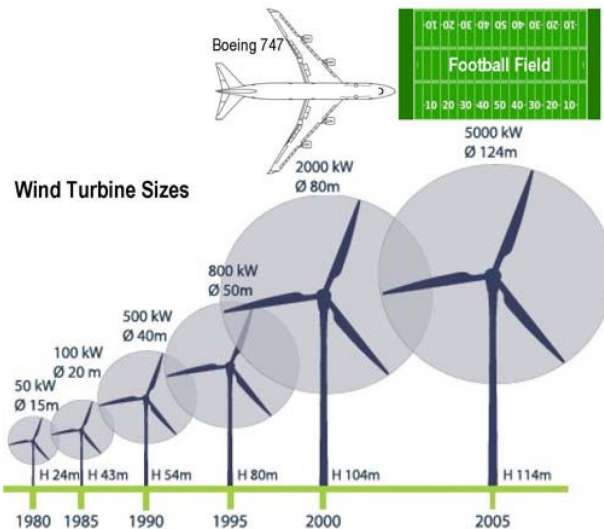
2.2 Monopile

Besides the fact that offshore wind farms face less planning restrictions relative to onshore wind farms (Ffrench et al., 2006), offshore wind farms have multiple advantages over onshore wind farms that make offshore wind the most effective way to achieve the renewable targets. According to Abdel-Rahman and Achmus (2005):

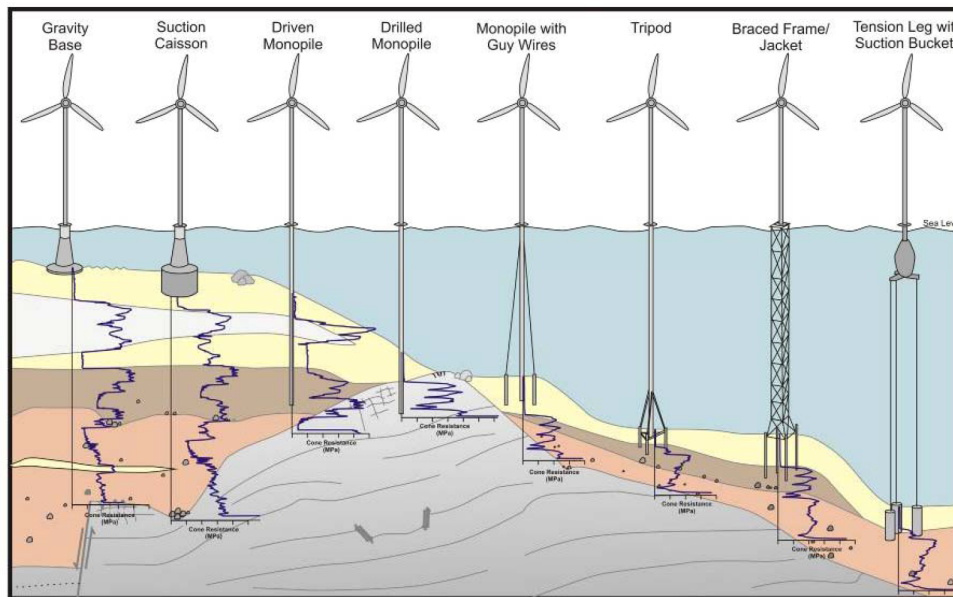
- Considering the availability of large continuous areas, larger wind turbines of greater height and rotor diameter can be constructed, allowing for a much greater output.
- Offshore winds tend to flow at higher speeds than onshore winds, thus allowing turbines to produce more electricity.
- As there is less turbulence offshore, the turbines can harvest energy more effectively and consistently, reducing the fatigue loads on the turbine.

Despite the advantages, foundation design for offshore wind turbines is more complicated compared to onshore wind. Based on the announcement that the UK government aims to construct 7,000 turbines that will generate 33 GW of energy (McCarthy, 2008), on average, each turbine would have to produce 5 MW of energy. It can be seen from Figure 2.1 (a) that both 5 MW and 2 MW turbines are massive

structures that have diameters of 80 m and 124 m respectively. Considering the size and significance of these structures, it is crucial that a suitable foundation is selected and is then designed to withstand the harsher conditions offshore, which would in turn ensure the long-term integrity of these structures.



(a) Size Comparison (Pao and Johnson, 2009)

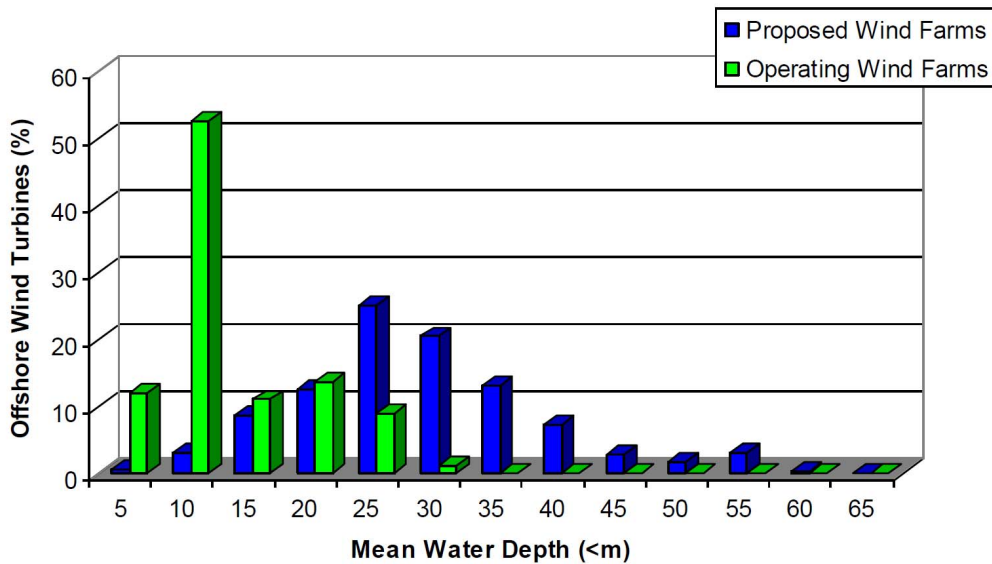


(b) Foundation Options (Rattley, 2011)

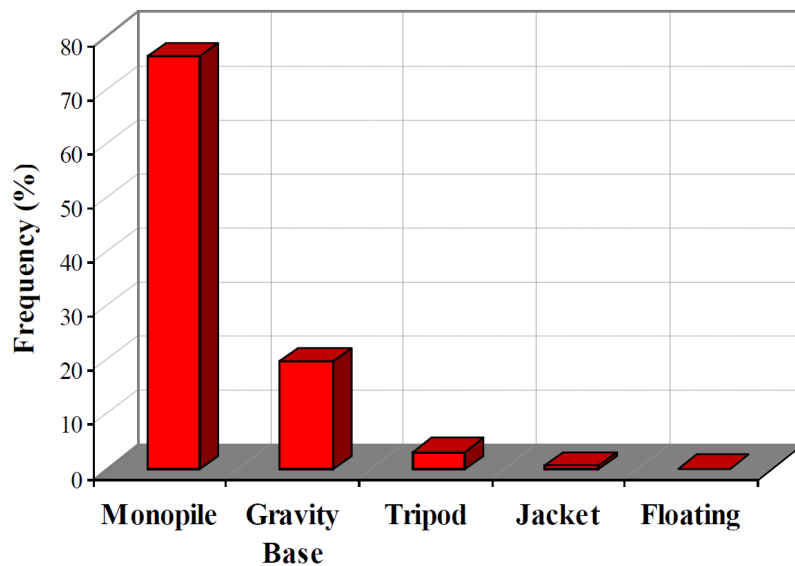
Figure 2.1 Wind Turbine Size Comparison and Foundation Options

There are multiple foundation options available to support offshore wind turbines as shown in Figure 2.1(b). In shallow waters with water depths ranging from 0 m – 25 m, gravity bases, suction caissons and monopiles can be utilised. Even though the Det Norske Veritas industry design code (DNV, 2014) suggests that monopiles are

suitable for water depths of up to approximately 25 m, recent wind farm construction has extended this limit to 35 m (Doherty et al., 2011). For deeper water depths ranging from 30 m – 70 m, multipod support structures such as tripods, jackets, and tension leg with suction buckets are typically utilised.



(a) Water Depth Comparison for Existing and Proposed Wind Turbines in Europe



(b) Foundation Breakdown of Current Turbines

Figure 2.2 Offshore Wind Turbine Current and Future Trend (Doherty et al., 2011)

Figure 2.2(a) shows that a majority of offshore wind turbines in Europe are currently sited in shallow water. Figure 2.2(b) shows that the monopile is by far the industry’s preferred option (~75%), followed by gravity bases (~20%). Considering that the

majority of the proposed offshore wind farms to be constructed in the next 10 to 15 years will be sited in water depths ranging from 25 m to 35 m (Figure 2.2(a)) and that the industry has extended the usage of monopiles to 35 m deep waters, it is highly likely that the industry will continue relying on monopiles as a proven foundation option.



Figure 2.3 6.5 m Monopile for Baltic 2 Offshore Wind Farm (Offshore Wind Industry, 2013)

As illustrated in Figure 2.3, monopiles are large diameter circular steel pipe piles that range from 4.0 m to 7.5 m in diameter (New Civil Engineer, 2014) and are drilled or driven 20 m to 30 m into the seabed, leading to a pile slenderness ratio (embedded length, L /diameter, D) of around 5 (LeBlanc et al., 2010b). Monopile wall thickness can range from a low of 40 mm for the Egmond aan Zee wind farm with 3 MW turbines founded on 4.6 m monopiles (Noordzee Wind et al., 2008) to a high of 150 mm (Hearn, 2009), depending on loading conditions. A review of the Horns Rev, Kentish Flats, and Eegmond aan Zee monopiles by Elkinton (2007) shows that the wall thickness is about 1.10% to 1.25% of the monopile diameter. As highlighted in Figure 2.2(b), the monopile is the preferred option of the construction industry. The reasons for this are:

- Installation is fast and highly automated with no prior preparation of the seabed (DNV and Risø National Laboratory, 2002). Duration for installation is short in locations where driving with a hydraulic hammer is sufficient (LeBlanc, 2009).

- Fabrication is simple (DNV and Risø National Laboratory, 2002) and suitable for batch production considering that future offshore wind farms will consist of more than 100 turbines (LeBlanc, 2009).
- Handling is relatively easy and many current jack-ups are capable of installing a monopile (LeBlanc, 2009).
- Loading due to wave, currents and ice are normally more readily defined due to the simple shape of the foundation.

2.3 Offshore Wind Farm Loads

Foundation design for offshore wind farms is different from that for typical oil and gas foundation design. As can be seen for the jack-up rig in Figure 2.4, the loading of typical oil and gas installations is often dominated by the huge self weight. Therefore, the structures are less exposed to dynamic excitation. However, offshore wind turbines are subjected to large moments at the seabed and strong cyclic loading as a result of both wind and wave forces. Load estimates for an anticipated 3.5 MW design offshore the UK are shown in Figure 2.4.

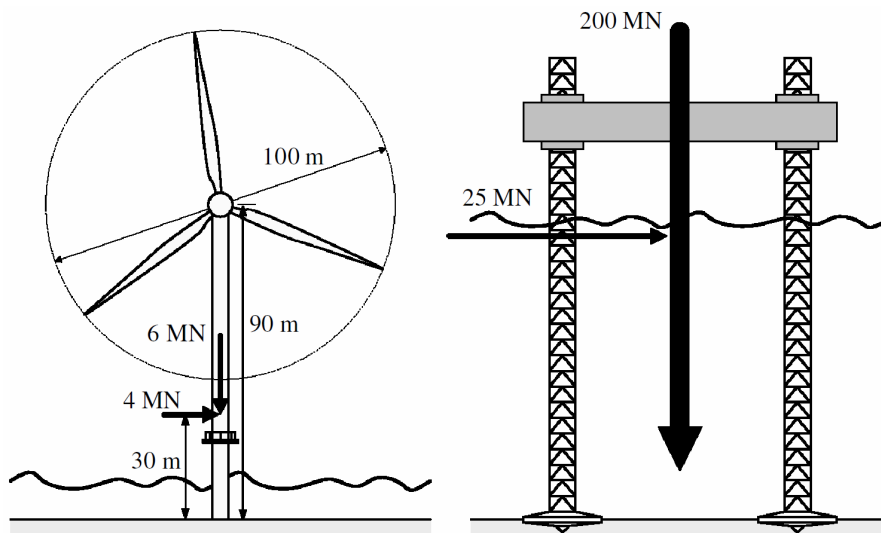


Figure 2.4 Difference between Load Conditions for an Offshore Wind Turbine and Oil & Gas Jack-up Rig (Byrne and Hously, 2003)

The vertical load from the self-weight of the turbine, tower, and foundation is of the order of 6 MN. The maximum horizontal load from both wind and waves is of the order of 4 MN. With the horizontal load acting approximately 30 m above the seabed, a large overturning moment of 120 MN m occurs at the seabed. Although wind

contributes to 25% of the horizontal load, it contributes to 75% of the overturning moment as it acts at a much higher height (Byrne and Houlsby, 2003). As a result, foundation design is primarily governed by the large moment at seabed level while the horizontal and vertical loads are comparably smaller (LeBlanc, 2009).

The cyclic loads experienced by an offshore wind turbine fluctuate rapidly as compared to typical offshore designs where loads are relatively constant. As shown by Figure 2.4, from Byrne and Houlsby (2003), the hub, approximately 90 m above the sea floor, will be subjected to a maximum operational wind load of 1 MN that is relatively constant over a long period of time. The current and wave loads might be $1 \text{ MN} \pm 2 \text{ MN}$ and are applied at a much lower level, depending on the water depth (say 10 m) and cycle at a period of 10 s, considerably faster than wind loads. This translates to a resultant horizontal load of $2 \text{ MN} \pm 2 \text{ MN}$ and a resultant moment of $100 \text{ MN m} \pm 20 \text{ MN m}$. Therefore, the ratio of moment to horizontal load fluctuates rapidly rather than remaining constant. In addition, wave directions that may not be coincident with the prevailing wind direction will result in loads (both moment and horizontal) that are non-coincident. The cyclic loads experienced by a wind turbine over its design lifetime of 25 years can add up to over 150 million cycles. As a result, foundation design is further complicated as cyclic loading is expected to provoke changes in soil behaviour that would most likely result in unallowable inclination or even loss of structural stability (Hinz et al., 2006). This is not made any easier by the maximum permanent monopile rotation requirement of 0.5° at mudline set in recent projects (Achmus et al., 2009).

Since the structure is flexible and can hence be excited dynamically by wind and wave loading, consideration of the driving frequencies of the turbines and blades is vital in foundation design to prevent resonance. There are two driving frequencies for three-bladed wind turbines producing power in the range of 2.0 – 3.6 MW, these being the rotor rotation frequency ($1P$) and the blade passing frequency ($3P$). The frequencies range from 0.17 – 0.33 Hz and 0.5 – 1 Hz respectively as shown by Figure 2.5. To prevent resonance, the first natural frequency, f_1 of the tower-foundation system has to be designed to avoid both $1P$ and $3P$. This can be achieved by designing the system as either a “soft-soft” system in which $f_1 < 1P$, a “soft-stiff” system in which $1P < f_1 < 3P$, or a “stiff-stiff” system in which $f_1 > 3P$.

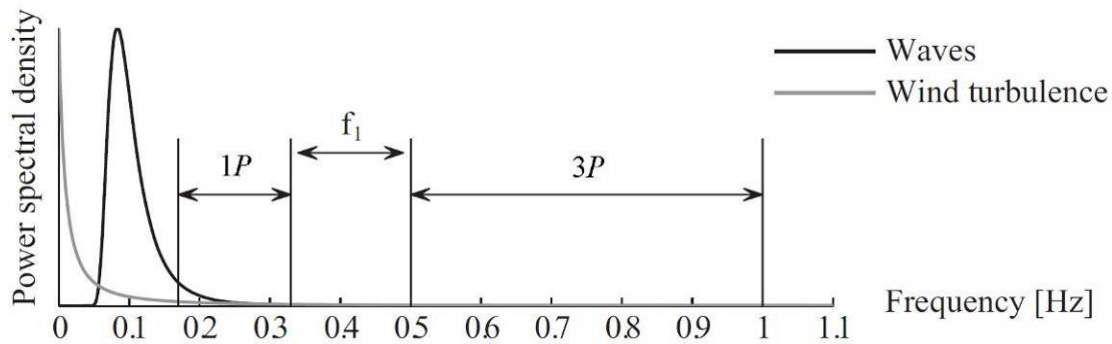


Figure 2.5 Typical Excitation Ranges of a Modern Offshore Wind Turbine (adapted from LeBlanc, 2009)

According to the Carbon Trust (2008), turbines make up 59% of the total costs of offshore wind farms. Following that, foundations and installation make up 17% and 8% of the total costs. Considering that both foundation and installation make up a significant portion of the total costs, cost-savings in these areas can be made to ensure profitability without sacrificing on structural integrity. A “stiff-stiff” design would result in much larger diameter and heavier monopiles relative to the other systems. This in turn significantly increases the costs of manufacturing, handling, and installation, making the “stiff-stiff” design extremely expensive and unpractical. The “soft-soft” system is the cheapest system relative to the others as it would result in a smaller diameter monopile that will experience less hydrodynamic loads due to the reduced size. However, “issues of fatigue and ultimate capacity may become dominant design drivers” as noted by LeBlanc (2009). Haigh (2014) carried out an assessment for a monopile supporting a 3.5 MW turbine that was designed as a “soft-soft” system and noted that even though significant cost savings were achieved due to reduced diameter, the system was unsuitable. Not only would a horizontal wind force of 1 MN produce excessive rotations at the top of the tower, there would also be great challenges in “ensuring sufficient ductility in the system to avoid structural failure” (Haigh, 2014). Despite the issues to implementing a “soft-soft” system, “soft-soft” systems are possible for smaller turbines. The 1.5 MW turbines at the Utgrunden wind farm in Sweden are designed as “soft-soft” systems due to the smaller weight of the nacelle (Kühn et al., 2005).

Since both “stiff-stiff” and “soft-soft” are not technically and economically viable, the “soft-stiff” approach is the only sensible approach. As a result, most systems are designed as “soft-stiff” systems. Despite being cost-effective and practical, the “soft-

stiff’ system has a drawback. Since the system natural frequency has to be designed within a very narrow band, the system is in turn very sensitive to changes in foundation stiffness. Changes in foundation stiffness due to cyclic loading may cause the natural frequency to enter either the $1P$ or $3P$ frequency bands. This will cause resonance that will lead to greater oscillation of the tower and foundation, causing a vicious cycle of continuing stiffening/softening and increased amplification until failure occurs (Haigh, 2014). Therefore, foundations for “soft-stiff” systems must not only be designed to resist the large overturning moments, but they must also maintain their stiffness over their 25 year design lifespan. During this time, a typical foundation may experience over 150 million load cycles.

2.4 Offshore Soil Conditions

Figure 2.6 shows how Thomas (1989) categorised the North Sea into four main provinces based upon the following generalised soil profiles:

- Province 1: Stiff to very stiff overconsolidated silty clays and clays
- Province 2: Very soft to soft normally consolidated clays and silty clays overlying stiff to very stiff overconsolidated silty clays
- Province 3: Stiff to very stiff overconsolidated silty clay and clays interbedded with dense fine sand
- Province 4: Fine to coarse sand with scattered seams and beds of soft to stiff silty clays

The first three profiles typically possess a thin surface unit of fine sand. Based on Figure 2.6, the soil profile varies significantly in the UK sector of the North Sea. The north consists mainly of stiff to very stiff overconsolidated clays, although in many areas they are interbedded with dense fine sand. The central parts are dominated by interbedded clays and sand whereas in the south stretching along the Belgian and Netherland coasts, there is a large tract of mainly fine to coarse sand. To verify the distribution of sands in the North Sea, Bond et al. (1997) examined 212 borehole records held by the British Geological Survey, BP International, and Shell UK. After examination, it was determined that sand generally made up less than 35% of the top

60 m below mudline in the northern and central parts of the North Sea whereas in the southern part, sand in the top 60 m was generally greater than 35%.

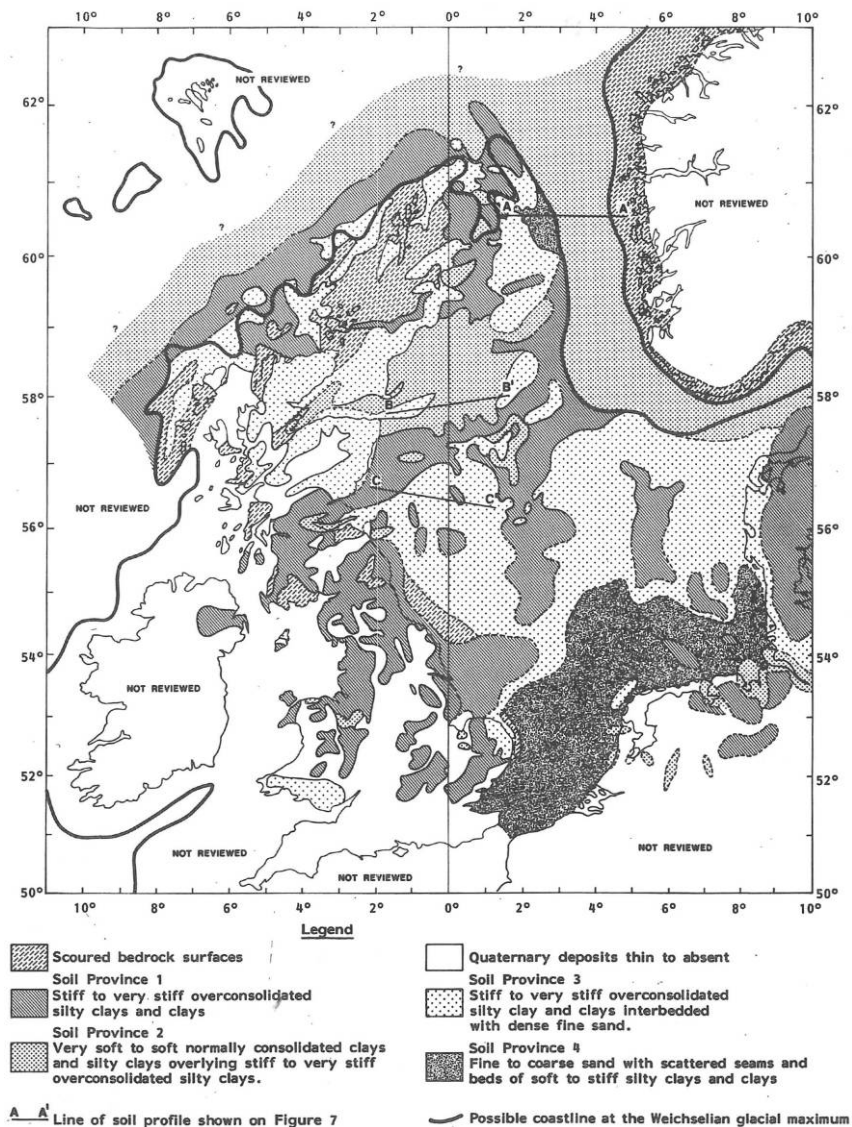


Figure 2.6 Generalised Soil Provinces in the North Sea (Thomas, 1989)

In June 2008, the Crown Estate announced the “round 3” leasing process that would provide 25 GW of energy, far bigger than the total capacity of rounds 1 and 2 of 8 GW (Carbon Trust 2008). Based on Figure 2.7, nine zones across the UK were identified by the Crown Estate. Comparisons between Figure 2.6 and Figure 2.7 indicate that most of the planned offshore wind farms will be founded in the northern and central parts of the North Sea. Therefore, most of the planned wind turbines will be founded in overconsolidated clay deposits.

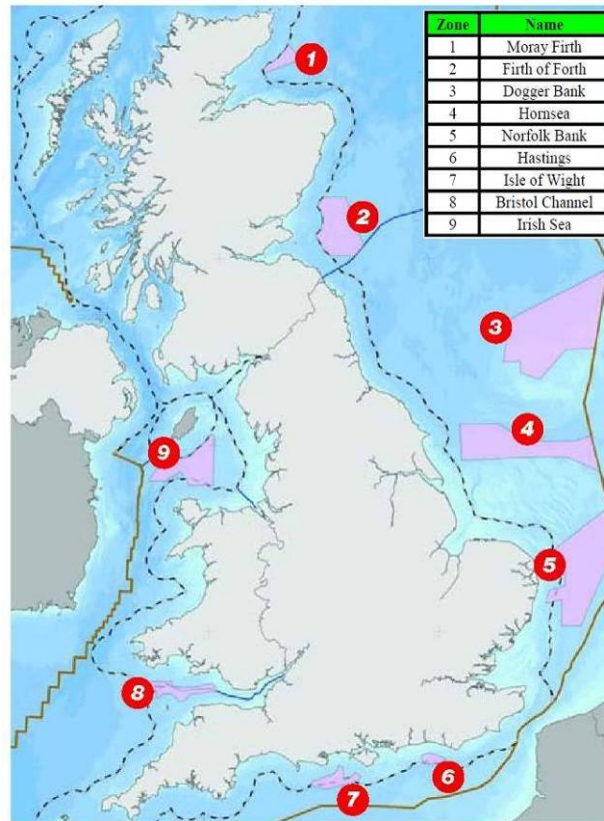


Figure 2.7 Round 3 Offshore Wind Zones (adapted from The Crown Estate, 2013)

2.5 Design Methods for Laterally Loaded Piles

According to the industry design standards established by DNV (2014), a monopile is required to have sufficient axial pile capacity to resist the weight of the system and to have sufficient lateral capacity to resist lateral loading, moment loading, and cyclic loading. Since design for offshore wind turbine foundations is primarily governed by the large overturning moment at seabed from horizontal wind and wave forces and cyclic lateral loads as highlighted in section 2.3, focus will be placed on the design of monopiles to resist lateral loads. In addition, focus will be placed on the design of monopiles in clay as most of the planned wind turbines in the UK over the next 10 to 15 years will be founded in overconsolidated clay deposits, as highlighted in section 2.4.

In the literature, several methods have been developed to design laterally loaded piles. According to Fan and Long (2005), these methods can be placed into five categories: (1) the limit states method; (2) the subgrade reaction method; (3) the p - y method; (4) the elasticity method; and (5) the finite element method. The limit states method

developed by Broms (1964a) for cohesive soils and cohesionless soils (Broms, 1964b) is the simplest method out of the five that provides a procedure (in the form of design charts and tables) for calculating the ultimate lateral load capacity and deflection of piles within the “working” load range (half of the computed ultimate load capacity (Meyer and Reese, 1979)). Though simple, the method has its limitations. For cohesive soils, the soil is assumed to be linearly elastic within the “working” load range when the soil is in fact not linearly elastic. Secondly, the subgrade modulus is assumed to be constant with depth. Thirdly, it is not possible to estimate pile response for a full range of loads, making it unsuitable for designs that have restrictions on allowable pile deflection. Finally, the method ignores the contribution of axial load, contributing to inaccuracies in calculations. Broms (1964a) compared his calculated deflection results with measured deflection results from load tests in cohesive soils. Based on the comparison, it was observed that the ratio of measured deflections to computed deflections ranged from 0.33 to 3.75. The value of 0.33 indicates that the method underestimated the actual deflection by 3.0. The values show that a simplified method is unsuitable to analyse a complex problem of a laterally loaded pile.

The subgrade reaction method (Reese and Matlock, 1956, Matlock and Reese, 1960) and p - y (in which p represents soil reaction and y represents pile lateral deflection) method both utilise the Winkler approach in which the pile is considered as a beam on an elastic foundation that is supported by a number of uncoupled springs. Since the springs are uncoupled, soil continuity is not taken into account. Despite being similar, the subgrade reaction method is inaccurate as it assumes soil resistance to be linearly dependent on pile deflection while the p - y method can assume a non-linear dependency between soil resistance and pile deflection and is therefore able to produce a more accurate solution. This method will be discussed in greater detail in section 2.6.

The elasticity method by Poulos (1971) is an elastic solution that assumes the soil to be an elastic, homogeneous, isotropic half-space with a constant Young's modulus and Poisson's ratio. Since the method includes soil continuity, Poulos argued that the Winkler model of using a series of discrete springs to model the soil behaviour is incorrect. To justify his claim, Poulos compared solutions from his model based on the theory of elasticity with solutions from the Winkler model and determined that the

deflections from the Winkler model were greater than his. However, the comparison of solutions between both models carried out by Vesic (1961) showed a small difference between the two methods for the case of an elastic material. This indicates that the subgrade reaction theory employing the Winkler assumption can be applied to the general case of nonlinear soil with a variable subgrade modulus while usage of the Poulos method is limited to materials which are linearly elastic (Meyer and Reese, 1979). With the model assuming an elastic response as compared to an elasto-plastic response, this method is only suitable for small strains and unsuitable to calculate ultimate lateral resistance (Brødbæk et al 2009).

The three-dimensional finite element (F.E.) method is a powerful tool that is capable of modelling soil continuity, soil non-linearity, pile/soil interface behaviour, and 3-D boundary conditions. According to Bathe (1996), the finite element method is a numerical method to solve physical problems that involves idealisation of a physical problem to a mathematical model that is governed by differential equations resulting from the assumptions made. The model is then discretised by dividing it into a mesh of finite elements. To ensure the solution is valid, the solution “must satisfy equilibrium, compatibility, constitutive behaviour and boundary conditions” (Potts and Zdravkovic, 2001). Brown and Shie (1990) and Trochanis et al. (1991) were among the people who initially led the way to the usage of 3-D F.E. modelling to investigate the response of laterally loaded piles.

Following Brown and Shie (1990) and Trochanis et al. (1991), further 3-D F.E. studies have been carried out on laterally loaded piles by various researchers such as Pan et al. (2002) who studied the response of single piles to lateral soil movement, Karthigeyan et al. (2007) who studied the influence on vertical load on the lateral response of piles with varying slenderness ratios in both clayey and sandy soils and Kim and Jeong (2011) who analysed the soil resistance of large diameter piles in clay. 3-D F.E. research pertaining to the lateral behaviour of monopiles has also been carried out in recent years. These include Achmus et al. (2011), Hearn (2009), and Lesny and Wiemann (2006) who studied the lateral behaviour of monopiles in sand while Wu et al. (2009), Pradhan (2012), and Haiderali et al. (2013) studied the lateral behaviour of monopiles in clay.

Despite the extensive capabilities of 3-D F.E. modelling, the method has its issues. Firstly, the method requires large amounts of effort in computation and in modelling the problem. Secondly, the validity of the results is questionable as the results are “highly dependent on the applied constitutive soil models as well as the calibration of these models” (Brødbæk et al 2009); making it ideal to compare F.E. results to either field or centrifuge test results. Gaps between soil and pile are also hard to account for in the models. Considering these factors, the usage of this tool is primarily for research and requires validation with test results or physical models if usage for design is considered.

2.6 *p-y* Method

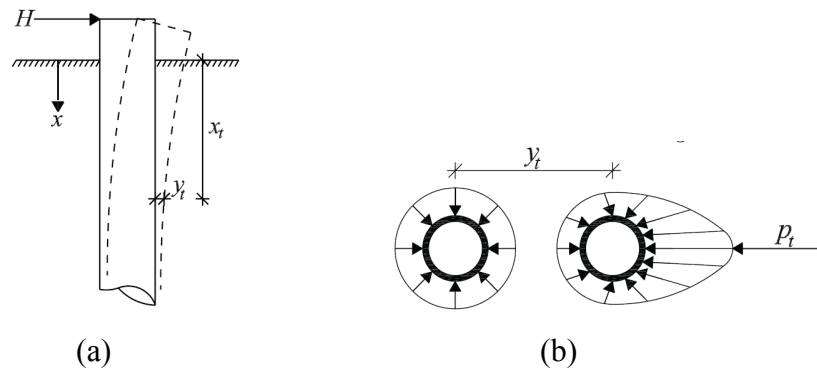


Figure 2.8 Distribution of Stresses against a Pile before and after Lateral Deflection (Brødbæk et al., 2009)

Of the five types of methods, the *p-y* method was adopted in the standard “Design of Offshore Wind Turbine Structures” (DNV, 2014) which represents the current state-of-the-art for design of monopiles in the offshore industry (LeBlanc, 2009). The *p-y* curves give the relation between the integral value p of the mobilised resistance from the surrounding soil when the pile deflects a distance y laterally, at a given point along the pile. The soil pressure at a given depth, x_t , before and after loading can be seen in Figure 2.8(b). The pile is modelled as a number of consecutive beam-column elements, supported by non-linear springs applied at each nodal point between the elements. The non-linear support springs are characterised by one *p-y* curve at each nodal point as displayed in Figure 2.9.

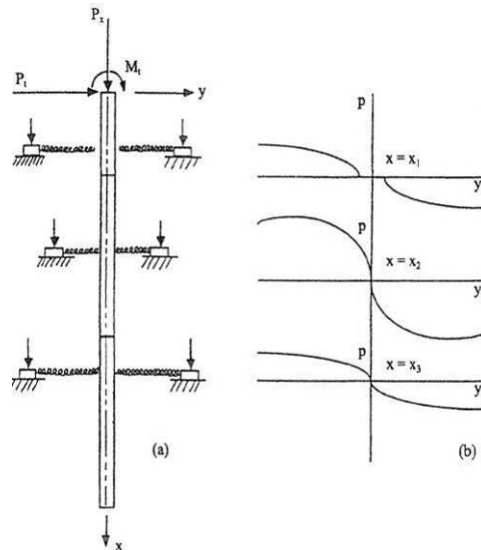


Figure 2.9 Model for a Pile under Lateral Loading with p - y Curves (Reese and Van Impe, 2001)

To solve for pile displacements and pile stresses in any point along the pile for any applied load at the pile head, a numerical procedure is required to solve the fourth-order differential equation for beam bending with the appropriate boundary conditions.

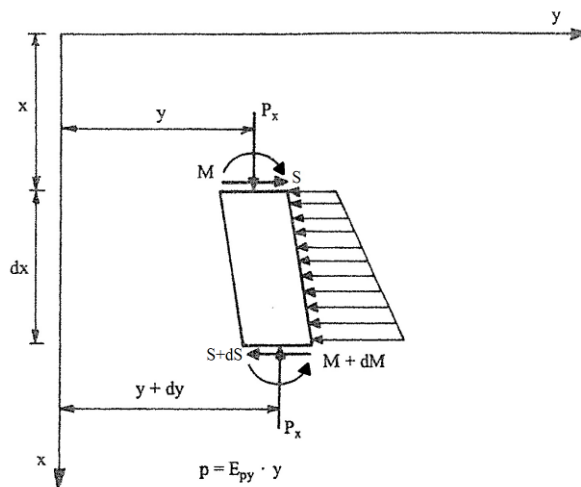


Figure 2.10 Element from Beam-Column (adapted from Reese and Van Impe, 2001)

To derive the differential equation, an infinitely small unloaded element, bounded by two horizontals a distance dx apart, is cut out of the pile as shown in Figure 2.10. The symbols in Figure 2.10 represent the following:

x	Position along the pile axis
y	Lateral displacement of the pile
M	Bending moment in the pile
S	Shearing force in the pile
P_x	Axial force in pile
p	Lateral soil reaction
E_{py}	Reaction modulus of pile under lateral loading (i.e. slope of p - y curve)

The equilibrium of moments leads to the equation

$$(M + dM) - M + P_x dy - Sdx = 0 \quad (2.1)$$

or

$$\frac{dM}{dx} + P_x \frac{dy}{dx} - S = 0 \quad (2.2)$$

Differentiating equation (2.2) with respect to x leads to the equation

$$\frac{d^2M}{dx^2} + P_x \frac{d^2y}{dx^2} - \frac{dS}{dx} = 0 \quad (2.3)$$

Considering that,

$$\frac{d^2M}{dx^2} = E_p I_p \frac{d^4y}{dx^4} \quad (2.4)$$

$$\frac{dS}{dx} = p \quad (2.5)$$

$$p = E_{py} y \quad (2.6)$$

Equations (2.4), (2.5), and (2.6) are substituted resulting in

$$E_p I_p \frac{d^4y}{dx^4} + P_x \frac{d^2y}{dx^2} - E_{py} y = 0 \quad (2.7)$$

where $E_p I_p$ represents the pile flexural rigidity. To analyse the pile under lateral loads, other beam formulas that are needed are:

$$E_p I_p \frac{d^3 y}{dx^3} + P_x \frac{dy}{dx} = S \quad (2.8)$$

$$-E_p I_p \frac{d^2 y}{dx^2} = M \quad (2.9)$$

and,

$$\frac{dy}{dx} = \text{Slope of Elastic Curve defined by pile axis} \quad (2.10)$$

By substituting, $d^2 y/dx^2$ with φ , equation (2.9) results in

$$-E_p I_p \varphi = M \quad (2.9a)$$

The sign conventions adopted are shown in Figure 2.11. Solving the differential equation would yield a set of curves similar to the ones displayed in Figure 2.12 except that in Figure 2.12, the curves give the response of a laterally loaded pile with no axial load applied. Though the axial load is small in comparison to the bending moment at the pile head and does not govern the design, axial load is to be included according to DNV (2014) standard as it may contribute to the bending moment and the mobilisation of lateral soil resistance owing to second-order effects.

The following assumptions were made in deriving the differential equation (Reese and Van Impe, 2001):

1. The pile is initially straight and has a uniform cross section;
2. The pile has a longitudinal plane of symmetry, in which loads and reactions lie;
3. The pile material is homogeneous and isotropic;
4. The elastic limit of the pile material is not exceeded;

5. The modulus of elasticity of the pile material is the same in tension and compression;
6. Transverse deflections of the pile are small;
7. The pile is not subjected to dynamic loading, and;
8. Deflections due to shearing stresses are small.

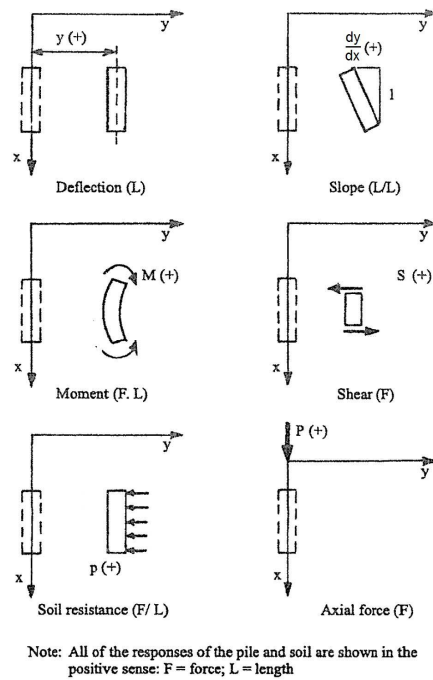


Figure 2.11 Adopted Sign Convention (adapted from Reese and Van Impe, 2001)

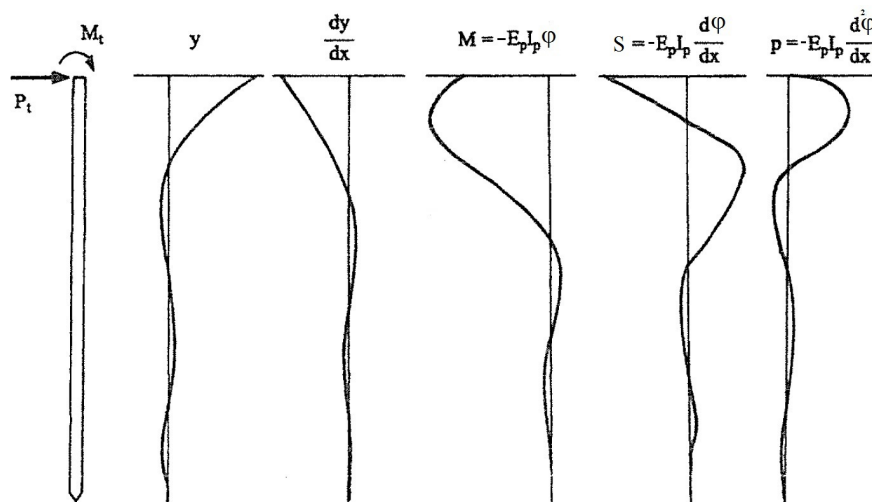


Figure 2.12 Complete Solution Results (adapted from Reese and Van Impe, 2001)

Many criteria have been made to construct the p - y curves for clay that include (1) soft clay criterion by Matlock (1970); (2) stiff clay criterion above the water table by Reese and Welch (1975); (3) stiff clay criterion below the water table by Reese et al. (1975); (4) Unified Clay criterion by Sullivan et al. (1980); (5) Integrated Clay criterion by Gazioglu and O'Neill (1984), and the most recent; (6) the use of Bezier curves to represent the p - y curves by Kodikara et al. (2010). The first five criteria were developed based on the results of full-scale lateral load tests for static and cyclic loading conditions. The p - y curves for these criteria are constructed as a function of two parameters. The static ultimate lateral resistance, p_u (which is a function of undrained shear strength, s_u and pile diameter, D) dictates the maximum soil reaction available while the reference deflection y_c (which involves a constant, pile diameter, D and ϵ_c , the strain which occurs at half the maximum deviatoric stress in laboratory undrained compression tests of undisturbed soil samples, which corresponds to s_u) dictates the stiffness of the p - y curves with respect to lateral displacement.

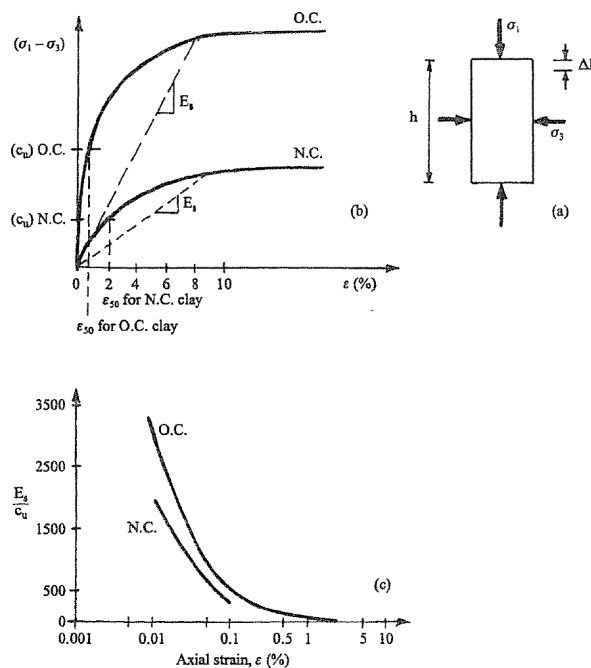


Figure 2.13 Undrained Stiffness to Undrained Shear Strengths for Clays with Low Plasticity (Reese and Van Impe, 2001)

ϵ_c is utilised as it is a parameter that effectively reflects the decay in undrained stiffness. In Figure 2.13, ϵ_{50} corresponds to ϵ_c and c_u correspond to s_u . As in Figure 2.13(b), the slope of the secant, E_s corresponds to the undrained stiffness. Figure 2.13(c) shows the decrease in E_s/c_u with increasing strain. Since the undrained shear

strength remains constant in a particular case, the curves in Figure 2.13(c) reflect the decay in E_s . The use of ε_{50} in p - y curves allows them to be normalised for clays whose stiffness degrades at different rates with strain.

Of the first five criteria, the soft clay criterion by Matlock (1970) and the stiff clay criterion below the water table by Reese et al. (1975) have been used extensively in the design of offshore platforms (Reese and Van Impe, 2001). Both criteria are adopted in the API (2011) RP2 Geotechnical and Foundation Design Considerations standard while the soft clay criterion is the only criterion adopted in the DNV (2014) “Design of Offshore Wind Turbine Structure” standard. The API standard categorises stiff clays to have $s_u > 96$ kPa while Appendix F of the DNV standard does not specifically mention that the soft clay criterion adopted is only applicable to soft clays. However, the DNV Classification Note 30.4 for Foundations (1992) does mention that the method in Appendix F is only applicable for soft clays having s_u values of up to 100 kPa. No method is mentioned in the DNV standard to develop p - y curves for stiff clays. This may be due to the possibility that the development of p - y curves for stiff clays can be subjective. According to the DNV (1992) classification notes and the API (2011) standard, the lateral resistance of stiff clays will deteriorate rapidly due to their brittle nature and that good judgement is required in developing the stress-strain and p - y curves. Therefore, the adoption of the soft clay criterion (Matlock, 1970) in the DNV (2014) standard may be for the purpose of producing conservative designs. Conservatism in ultimate resistance may, however, be unconservative when designing for natural frequencies of soft-stiff systems.

The construction of p - y curves via the Unified Clay criterion (Sullivan et al., 1980) and the Integrated Clay criterion (Gazioglu and O'Neill, 1984) is similar to both soft clay criterion and stiff clay criterion below the water table with the exception that both Unified Clay and Integrated Clay criteria suggests that the constant utilised in the calculation of reference deflection y_c is not a fixed number as suggested by Matlock (1970) and Reese et al. (1975), but a variable number that is dependent on the properties of the soil in question. Depending on the soil in question, the value utilised as the constant to calculate y_c can be lower than the values suggested by Matlock (1970) and Reese et al. (1975). Even though the suggestion is reasonable, both criteria failed to make their way into the DNV (2014) or API (2011) standards.

This could be due to how well established the soft clay and stiff clay below water table criteria is in the industry and possibly the greater conservatism that results from using a higher value constant to calculate y_c which in turn produces a softer p - y curve. Both the soft clay criterion and stiff clay criterion below the water table will be described in detail. The stiff clay criterion above water table will not be discussed as this criterion is not applicable for offshore conditions where the clay will always be below the water table. The Unified Clay criterion and Integrated Clay criterion will be described in detail for the purpose of comparison to the soft clay criterion. Even though use of Bezier curves to construct p - y curves is not well established in industry, the criterion will be described for completeness.

2.6.1 Soft Clay Criterion (Matlock, 1970)

This criterion was derived from field tests carried out by Matlock (1970) on 0.324 m diameter circular steel pipe piles embedded by 12.8 m (resulting in a slenderness ratio of 39.5) into soft clays having undrained shear strengths below 50 kPa. Figure 2.14 displays the equipment set-up for the restrained-head loading tests carried out by Matlock to simulate the effect of a jacket-type structure.

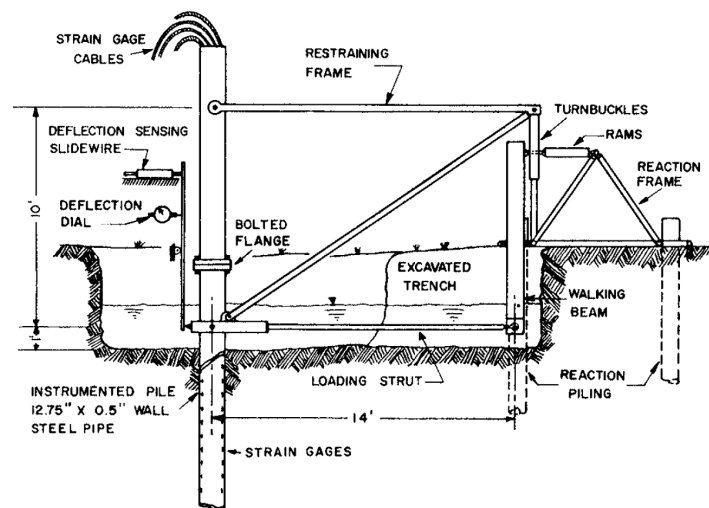


Figure 2.14 Arrangement for Field Tests using Restrained-Head Lateral Loading carried out by Matlock (1970)

Construction of p - y curves as outlined in Appendix F of the DNV standard (2014) requires the calculations of the static ultimate lateral resistance, p_u as follows:

$$p_u = \begin{cases} (3s_u + \gamma' X)D + Js_u X & \text{for } 0 < X \leq X_R \\ 9s_u D & \text{for } X > X_R \end{cases} \quad (2.11)$$

where,

X	Depth below soil surface
X_R	Transition depth, below which the value of $(3s_u + \gamma' X)D + Js_u X$ exceeds $9s_u D$
D	Pile diameter
s_u	Undrained shear strength of the soil
γ'	Effective unit weight of soil
J	Dimensionless empirical constant whose value is in the range 0.25 to 0.50. 0.50 is recommended for soft normally consolidated clay (DNV, 2014) while Matlock (1970) observed that a value of 0.25 fitted his data from Lake Austin that had heavily overconsolidated stiff, fissured clays subjected to desiccation.

Following calculation of static ultimate lateral resistance, the p - y curves for static and cyclic loading can be determined. Reference deflection, $y_c = 2.5\varepsilon_c D$ where ε_c is the strain at half the maximum deviatoric stress in laboratory undrained compression tests.

For static loading;

$$p = \begin{cases} \frac{p_u}{2} \left(\frac{y}{y_c} \right)^{1/3} & \text{for } y \leq 8y_c \\ p_u & \text{for } y \geq 8y_c \end{cases} \quad (2.12)$$

For cyclic loading and $X > X_R$;

$$p = \begin{cases} \frac{p_u}{2} \left(\frac{y}{y_c} \right)^{1/3} & \text{for } y \leq 3y_c \\ 0.72 p_u & \text{for } y > 3y_c \end{cases} \quad (2.13)$$

and for cyclic loading and $X \leq X_R$

$$p = \begin{cases} \frac{p_u}{2} \left(\frac{y}{y_c} \right)^{1/3} & \text{for } y \leq 3y_c \\ 0.72 p_u \left(1 - \left(1 - \frac{X}{X_R} \right) \frac{y - 3y_c}{12y_c} \right) & \text{for } y < 3y_c \leq 15y_c \\ 0.72 p_u \frac{X}{X_R} & \text{for } y > 15y_c \end{cases} \quad (2.14)$$

Utilisation of equations (2.12), (2.13), and (2.14) will yield p - y curves as shown in Figure 2.15(a) and 2.15(b). The p - y curve for reloading after cyclic loading can be generated as in Figure 2.15(c) by modifying Figure 2.15(b) to account for a possible gap between the soil and pile due to previous (more intensive) cyclic loading.

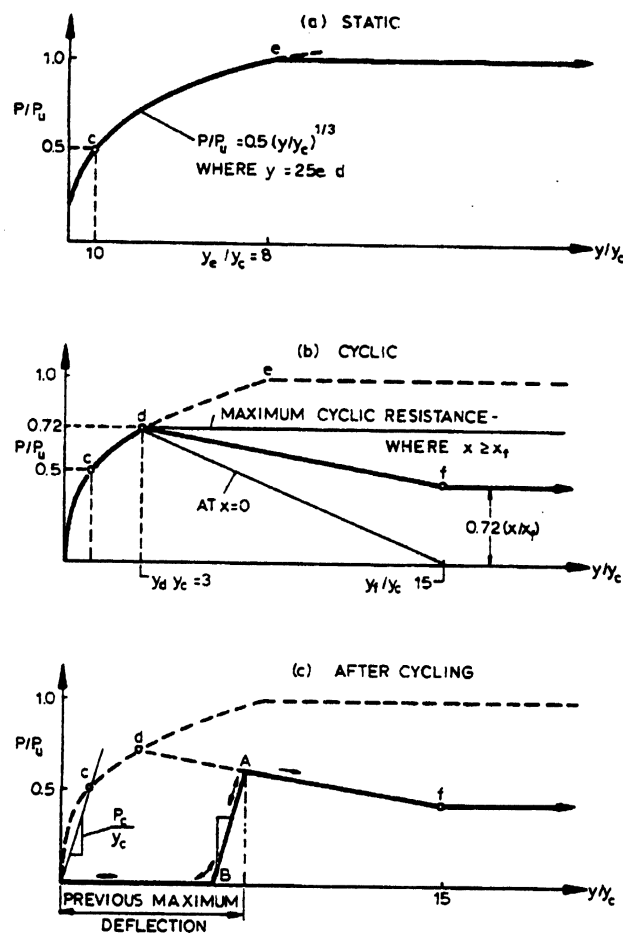


Figure 2.15 Characteristic Shapes of p - y Curves for Soft Clay (a) Static Loading (b) Cyclic Loading (c) After Cyclic Loading (DNV, 1992)

2.6.2 Stiff Clay Criterion below the Water Table (Reese et al., 1975)

This criterion was derived from field tests carried out by Reese et al. (1975) on 0.61 m diameter circular steel pipe piles with a final penetration depth of 14.94 m (resulting in a slenderness ratio of 35.5) into clays having undrained shear strengths ranging from 96 kPa at ground surface to 375 kPa at 4.75 m depth. Figure 2.16 displays the equipment set-up.

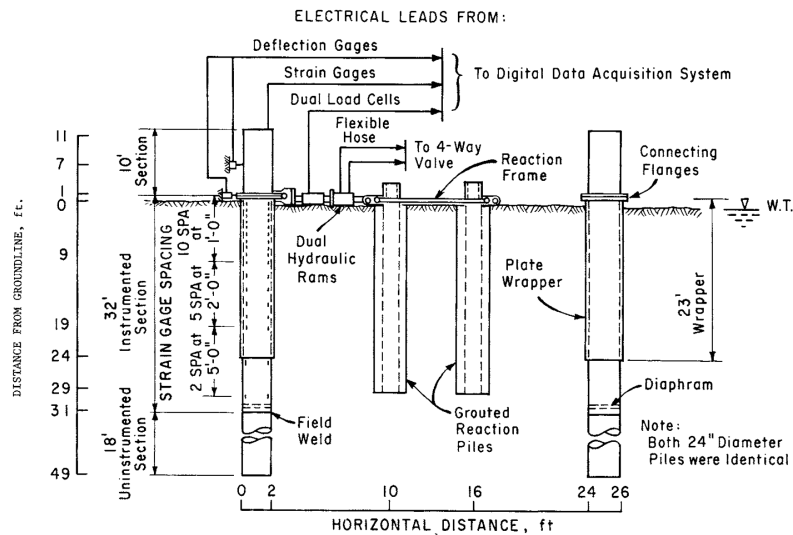


Figure 2.16 Field Test Setup for 0.61 m Diameter Test Piles by Reese et al. (1975)

To construct the p - y curves, static ultimate resistance is calculated and is taken as the lesser of the following equations:

$$p_u = \begin{cases} 2s_u D + \gamma' DX + 2.83s_u X \\ 11s_u D \end{cases} \quad (2.15)$$

For this criterion, the reference deflection, $y_c = \epsilon_c D$. To construct the static p - y curve as shown in Figure 2.17, multiple segments have to be established. The initial straight line portion of the p - y curve is defined as:

$$p = (k_s X)y \quad (2.16)$$

where k_s is the initial subgrade reaction modulus that is dependent on the undrained shear strength. This value can be determined from Table 2.1.

Subgrade reaction modulus k_s (MN/m ³)	Average s_u (kPa)		
	50-100	100-200	300-400
Static	135	270	540
Cyclic	55	110	540

Table 2.1 Recommended Values for k_s for Stiff Clays (Reese and Van Impe, 2001)

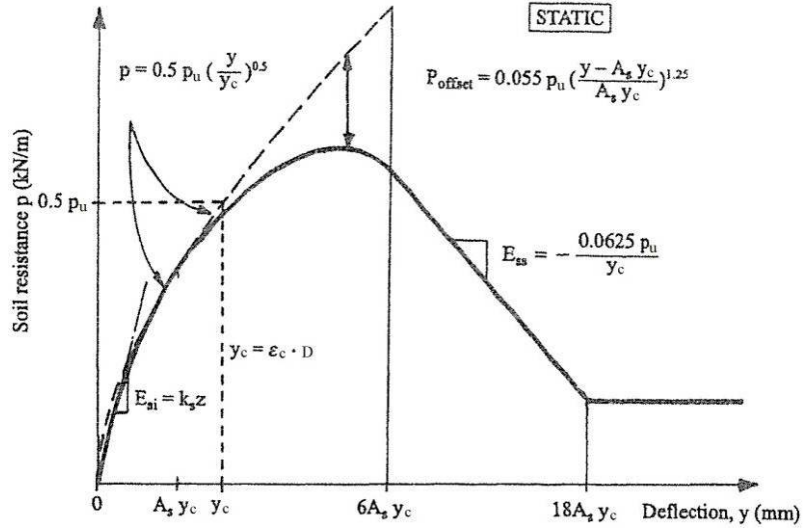


Figure 2.17 Static Load p - y Curve for Stiff Clay below Water Table (adapted from Reese et al., 1975)

The first parabolic segment is established by the following equation, beginning at the intersection with the initial linear segment and terminating at $y = A_s y_c$, with A_s being a constant whose value can be obtained from Figure 2.18.

$$p = 0.5 p_u \left(\frac{y}{y_c} \right)^{0.5} \quad (2.17)$$

The second parabolic segment is constructed as follows and begins from $y = A_s y_c$ and ends at $y = 6A_s y_c$.

$$p = 0.5 p_u \left(\frac{y}{y_c} \right)^{0.5} - 0.55 p_u \left(\frac{y - A_s y_c}{A_s y_c} \right)^{1.25} \quad (2.18)$$

The second linear segment that begins from $y = 6A_s y_c$ and ends at $y = 18A_s y_c$ is expressed as:

$$p = 0.5p_u(6A_s)^{0.5} - 0.411p_u - \frac{0.0625}{y_c} p_u (y - 6A_s y_c) \quad (2.19)$$

The final straight line portion going beyond $18A_s y_c$ is defined as:

$$p = 0.5p_u(6A_s)^{0.5} - 0.411p_u - 0.75p_u A_s \quad (2.20)$$

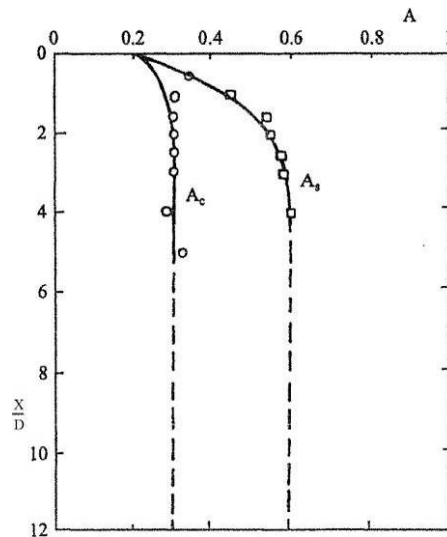


Figure 2.18 Values of Constants A_s and A_c Table (adapted from Reese et al., 1975)

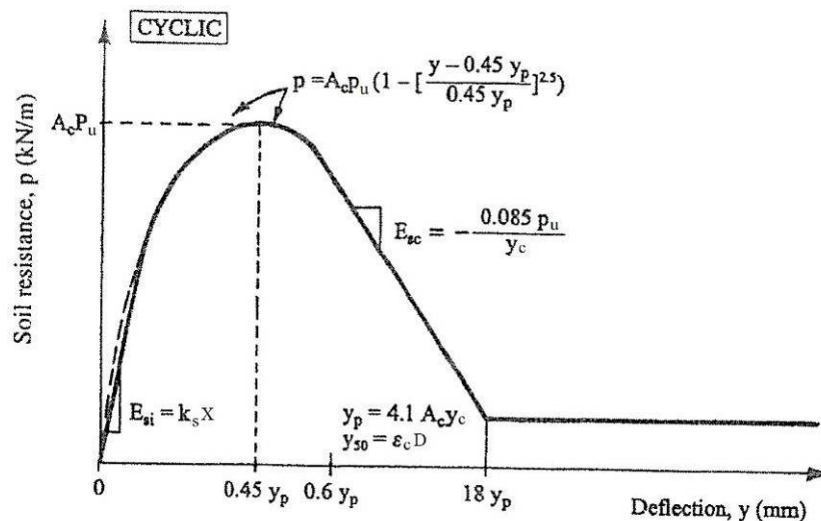


Figure 2.19 Cyclic Load p - y curve for Stiff Clay below Water Table (adapted from Reese et al., 1975)

The cyclic loading curve too has multiple segments as shown in Figure 2.19. Similar to the static p - y curve, the initial linear segment is obtained using equation (2.16). The first parabolic segment as defined in the equation below starts from the intersection

with the linear segment and stops at $y = 0.6 y_p$ where $y_p = 4.1 A_c y_c$ and A_c is determined from Figure 2.18.

$$p = A_c p_u \left[1 - \left(\frac{y - 0.45 y_p}{0.45 y_p} \right)^{2.5} \right] \quad (2.21)$$

The next straight line portion of the curve is defined from $y = 0.6 y_p$ to $y = 18 y_p$ and is constructed as:

$$p = 0.936 A_c p_c - \frac{0.085}{y_c} p_c (y - 0.6 y_p) \quad (2.22)$$

The final segment is established as follows and goes beyond $18 y_p$:

$$p = 0.936 A_c p_c - \frac{0.102}{y_c} p_c y_p \quad (2.23)$$

2.6.3 Unified Clay Criterion (Sullivan et al., 1980)

After reanalysing the field test results of Matlock (1970) and Reese et al. (1975) for both soft and stiff clays, Sullivan et al. (1980) proposed a unified approach to p - y curve construction for clays.

To construct the p - y curves, the ultimate resistance is calculated and is taken as the lesser of the following equations:

$$p_u = \begin{cases} \left(2 + \frac{\gamma'_{avg}}{(s_u)_{avg}} + \frac{0.833}{D} X \right) \times (s_u)_{avg} D \\ \left(3 + \frac{0.5}{D} X \right) s_u D \\ 9 s_u D \end{cases} \quad (2.24)$$

where,

$(S_u)_{avg}$ Average undrained shear strength above depth X
 γ'_{avg} Average effective unit weight from ground surface to depth at which p - y curves applies

To construct the static p - y curve as shown in Figure 2.20 multiple segments have to be established. Similar to the stiff clay criterion of Reese et al. (1975), the static p - y curve begins with a straight line.

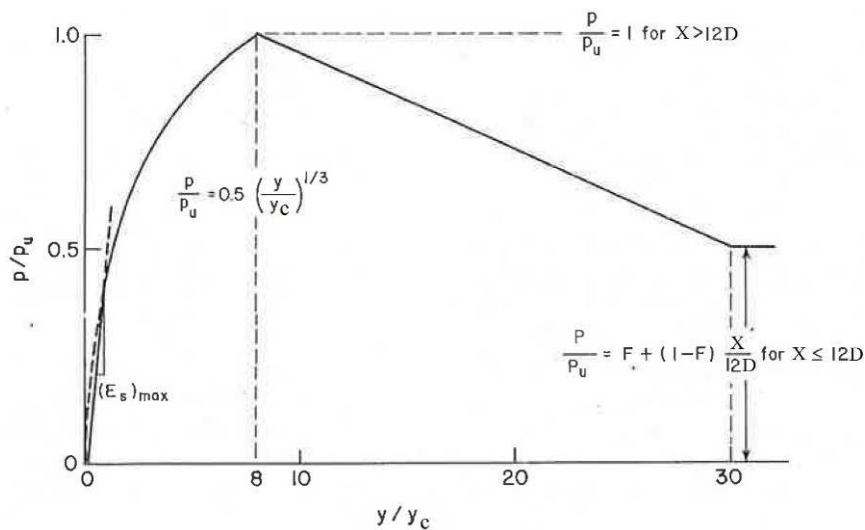


Figure 2.20 Static Load p - y Curve for Unified Clay Criterion (adapted from Sullivan et al., 1980)

The straight line is characterised as:

$$p = (E_s)_{max} y \quad (2.25)$$

where $(E_s)_{max}$ is the limiting maximum value of soil modulus on p - y curve for Unified Clay criterion. When no other method is available, $(E_s)_{max}$ can be estimated by:

$$(E_s)_{max} = k_s X \quad (2.26)$$

Representative values for k_s are given in Table 2.2. The curved section as shown in Figure 2.20 is defined in similar fashion to Matlock (1970) as in equation (2.12) of section 2.6.1. However, y_c is defined as $A \epsilon_c D$. A is the coefficient to define the shape of the p - y curve. In the final segment beyond $8y_c$, the soil resistance is calculated based on the depth in question. For $X \leq 12D$:

$$p = p_u \left[F + (1 - F) \frac{X}{12D} \right] \quad (2.27)$$

However, for $X > 12D$, $p = p_u$. F is the coefficient used to define deterioration of soil resistance at large deformations. The coefficients A and F were determined empirically by Sullivan et al. (1980) from the load test results of Sabine and Manor as shown in Table 2.3.

s_u (kPa)	k_s (MN/m ³)
12 – 25	8
25 – 50	27
50 – 100	80
100 – 200	270
200 – 400	800

Table 2.2 Recommended k_s Values for Clays for Different s_u (Sullivan et al., 1980)

Site	Sabine River	Manor
Clay Description	Inorganic, intact (s_u) _{avg} = 15 kPa $\varepsilon_c = 0.007$ $OCR \approx 1$ $S_r \approx 2$ LL = 92 PI = 68 LI = 1	Inorganic, very fissured (s_u) _{avg} = 115 kPa $\varepsilon_c = 0.005$ $OCR > 10$ $S_r \approx 1$ LL = 77 PI = 60 LI = 0.5
A	2.5	0.35
F	1.0	0.5

Table 2.3 Curve Parameters for Unified Clay Criterion (Sullivan et al., 1980)

To determine A and F , Sullivan et al. (1980) recommends that designers determine as many properties of the clay such as s_u , ε_c , liquid limit (LL), plasticity index (PI), liquidity index (LI), failure strain from stress-strain curve, OCR , degree of saturation, sensitivity (S_t), degree of fissuring, and ratio of residual to peak shear strength. Following that, designers can compare the properties of the soil in question to the properties of the Sabine and Manor clays in Table 2.3. However, if the properties are not similar, A and F have to be estimated using judgement.

The cyclic loading p - y curve is similar in shape to the static p - y curve as shown in Figure 2.21 and is constructed in similar fashion. The decrease in soil resistance due

to cyclic loading is consistent with Matlock (1970). Even though Sullivan et al. (1980) notes that the cyclic loading curve gives satisfactory agreement between the calculated and measured results of the full-scale experiments, Sullivan et al. (1980) states that the recommended shape of the cyclic p - y curve is completely empirical.

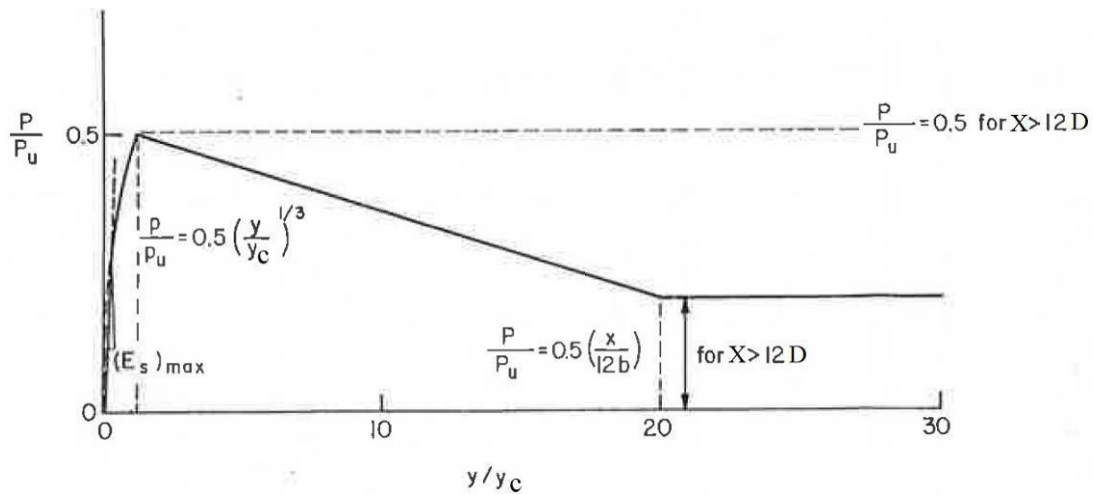


Figure 2.21 Cyclic Load p - y Curve for Unified Clay Criterion (adapted from Sullivan et al., 1980)

The shapes of the static and cyclic p - y curves in Figure 2.20 and Figure 2.21 are based on the assumption that there will be an intersection between the straight line and curved portion. However, if there is no intersection, Sullivan et al. (1980) states that the curve will be defined by equation (2.25) until intersection with the segment that defines the curves at greater pile deflections.

2.6.4 Integrated Clay Criterion (Gazioglu and O'Neill, 1984)

The Integrated Clay criterion developed by Gazioglu and O'Neill (1984) was developed to be applicable for all clays and to remove the subjective distinction of cohesive soils as soft clays or stiff clays. The criterion was developed based on the results of 21 full-scale, field lateral load tests on piles installed at 11 locations. Soil conditions varied from very soft to very stiff. To develop the criterion, Gazioglu and O'Neill (1984) made reasonable assumptions regarding the influence of factors such as pile diameter, pile length, and soil stiffness and by optimising several parameters to produce a procedure that provided the best agreement with the available data.

To construct the p - y curves, the ultimate soil resistance is calculated as

$$p_u = FN_p s_u D \quad (2.28)$$

where F is the soil degradability factor that can be determined based on failure strains measured from unconsolidated undrained (UU) triaxial compression tests. Values of F for both static, F_s and cyclic loading, F_c are shown in Table 2.4.

Factor	UU Triaxial Compression Failure Strain		
	<0.02	0.02-0.06	>0.06
F_s (static)	0.50	0.75	1.00
F_c (cyclic)	0.33	0.67	1.00

Table 2.4 Soil Degradability Factor, F (Gazioglu and O'Neill, 1984)

N_p is defined as follows:

$$N_p = \begin{cases} 3 + 6 (X/X_{cr}) & \text{for } X \leq X_{cr} \\ 9 & \text{for } X > X_{cr} \end{cases} \quad (2.29)$$

X_{cr} is the critical depth which is defined as $0.25L_c$. L_c is the critical pile length and is calculated as follows:

$$L_c = 3 \left(\frac{E_p I_p}{E_{sec} \sqrt{D}} \right)^{2.86} \quad (2.30)$$

Where $E_p I_p$ is the flexural stiffness of the pile and E_{sec} is the secant soil stiffness at half the deviator stress at failure in UU triaxial compression. E_{sec} values from the study are shown in Table 2.5.

s_u (kPa)	Soil Modulus, E_{sec} (kPa)
< 23.95	344.5
23.95 – 47.9	344.5 – 1,033.5
47.9 – 95.8	1,033.5 – 3,100.5
95.8 – 191.6	3,100.5 – 10,335
191.6 – 383.2	10,335 – 34,450
> 383.2	34,450

Table 2.5 Soil Modulus vs. Undrained Shear Strength for Integrated Clay Criterion (adapted from Gazioglu and O'Neill, 1984)

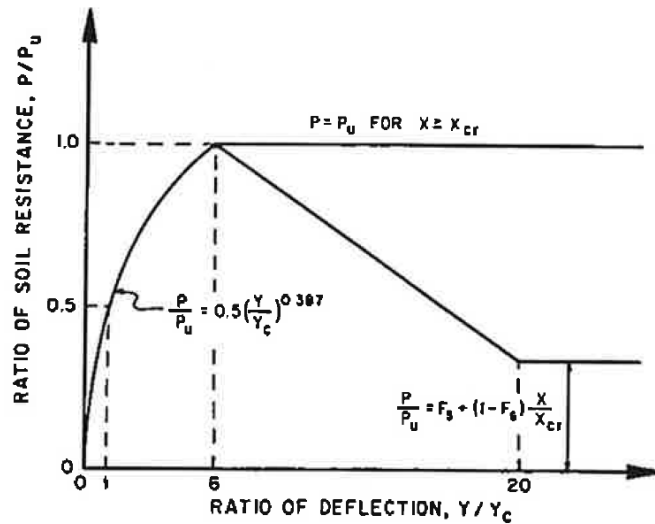
The reference deflection, y_c is calculated as

$$y_c = A' \varepsilon_c D^{0.5} \left(\frac{E_p I_p}{E_{sec}} \right)^{0.125} \quad (2.31)$$

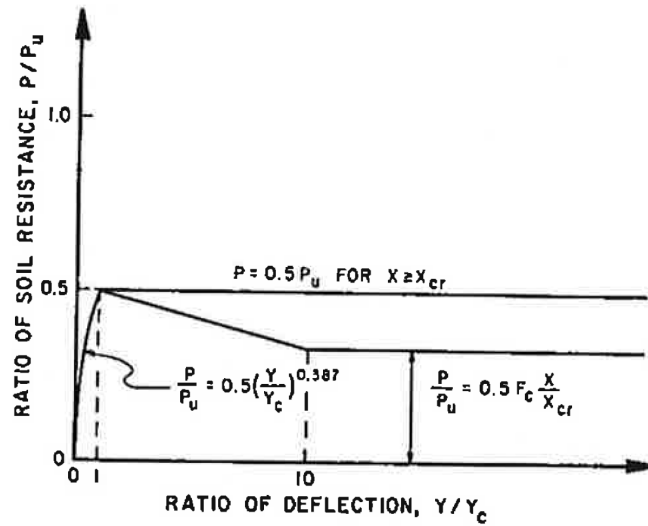
A' was determined through an optimisation technique based on modelling seven full-scale static and cyclic tests as shown in Table 2.6. As shown in Table 2.6, A' generally increases with increasing OCR and increases somewhat with increasing load. The two extremely large A' values at Houston and Manor were considered as anomalies. Gazioglu and O'Neill (1984) attributed this to the unstable moisture conditions at Manor and to the shear strength profile selected for analysis that modelled the soil near the surface as being too stiff for Houston. Based on the data available, Gazioglu and O'Neill (1984) decided that A' is 0.8 for all soils.

Site Location	Pile Head Condition	Lateral Load (kN)	Optimized A' Factor	Average A' Factor	Consolidation of Site Soil
Sabine, TX	Free	12.91	0.40	0.467	Approx. NC
		37.83	0.50		
		56.07	0.50		
Lake Austin, TX	Free	13.35	0.70	0.820	Slightly OC
		48.95	0.86		
		76.54	0.90		
Houston, TX (1.22m)	Free	315.95	0.50	0.727	OC
		574.05	0.60		
		756.50	1.08		
Houston, TX (0.27m)	Free	17.80	0.96	2.433	OC
		42.72	2.90		
		64.53	4.40		
Manor, TX (0.64m)	Free	48.95	1.50	2.833	Heavily OC
		178.00	3.00		
		293.70	4.00		
Sabine, TX	Restrained	21.36	0.40	0.667	Approx. NC
		55.63	0.60		
		76.10	1.00		
Harvey, LA	Restrained	5.34	0.30	0.373	Approx. NC
		16.91	0.31		
		24.48	0.51		

Table 2.6 Results of A' -Factor Optimisation Study (adapted from Gazioglu and O'Neill, 1984)



(a) Static Loading



(b) Cyclic Loading

Figure 2.22 p - y Curve for Integrated Clay Criterion (Gazioglu and O'Neill, 1984)

To construct the static loading p - y curve as shown in Figure 2.22(a), the initial portion for $y < 6y_c$ is characterised as:

$$p = \frac{p_u}{2} \left(\frac{y}{y_c} \right)^{0.387} \quad (2.32)$$

Beyond $6y_c$ and for $X < X_{cr}$, the p - y curve is constructed as follows:

$$p = p_u \left[F_s + (1 - F_s) \frac{X}{X_{cr}} \right] \quad (2.33)$$

Beyond $6y_c$ and for $X \geq X_{cr}$, $p = p_u$.

The cyclic p - y curve is constructed in similar fashion to the static p - y curve as shown in Figure 2.22 (b). The initial portion is constructed as shown in equation (2.32) until y_c . Beyond y_c , for $X < X_{cr}$, the soil resistance is modelled as :

$$p = 0.5F_c \frac{X}{X_{cr}} \quad (2.34)$$

Beyond y_c and for $X \geq X_{cr}$, $p = 0.5p_u$.

2.6.5 Use of Bezier Curves (Kodikara et al., 2010)

Figure 2.23 shows the typical representation of p - y curve of a single pile in soft clay. The first linear portion until displacement y_e is characterised by stiffness K_i (MPa), signifying the linear-elastic behaviour of soil. The second portion is the non-linear segment that leads up to the ultimate resistance p_u at displacement y_u . Beyond y_u , the resistance is considered to be constant for ideally plastic clay. To construct the p - y curve, the four parameters (y_u , y_e , K_i , and p_u) need to be evaluated. Kodikara et al. (2010) found that the family of curves known as Casteljau's algorithm introduced by the French engineer, Pierre Bezier, in the 1970s (Mortenson, 1985) that is currently used in automotive design to be worthy of consideration.

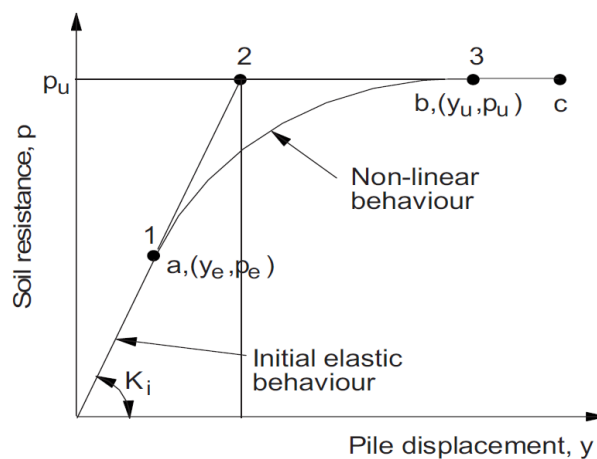


Figure 2.23 Typical Representations of p - y Curve (Bransby, 1996) and Bezier technique (Kodikara et al., 2010)

Therefore, for the prediction of the p - y curve as in Figure 2.23, one can consider $(y_1, p_1) = (y_e, p_e) = (y_e, K_i y_e)$, $(y_2, p_2) = (1 / K_i p_u, p_u)$ and $(y_3, p_3) = (y_u, p_u)$. Based on this basis, the p - y curve can be represented by the following equations. For the linear segment where $y \leq y_e$:

$$p = K_i y \quad (2.35)$$

Following the linear segment, the non-linear segment where $y_e \leq y \leq y_u$:

$$y = (1-u)^2 y_e + 2u(1-u) \frac{1}{K_i} p_u + u^2 y_u \quad \text{for } 0 \leq u \leq 1 \quad (2.36)$$

$$p = (1-u)^2 K_i y_e + 2u(1-u) p_u + u^2 p_u \quad \text{for } 0 \leq u \leq 1 \quad (2.37)$$

where u is a continuous dummy variable between 0 and 1. In the final segment where $y \geq y_u$, $p = p_u$.

To determine p_u , Kodikara et al. (2010) utilised the $p_u/s_u D$ curve derived from comprehensive FLAC modelling by Lee (2005) and Kodikara et al. (2006) that considered the pile as linear elastic and soil as Mohr-Coulomb materials under plane strain conditions. The FLAC curve is shown in Figure 2.24 and it compares well with the solutions of Randolph and Houlsby (1984) derived from classic plasticity theory.

Calculation of y_u , y_e , and K_i can be determined from the following equations:

$$y_u = \alpha D \left(\frac{s_u}{G} \right) \quad (2.38)$$

$$y_e = \beta D \left(\frac{s_u}{G} \right) \quad (2.39)$$

$$K_i = G \left[B \left(\frac{s_i}{s_u} \right) + C \right] \quad (2.40)$$

G is the soil shear modulus while s_i/s_u is the mobilised interface strength. Values of constants α , β , B and C for various interface and soil failure conditions are given in Table 2.7. In Table 2.7, σ_t , the soil tensile strength and σ_o , the initial compressive stress are utilised to determine if tensile failure takes place.

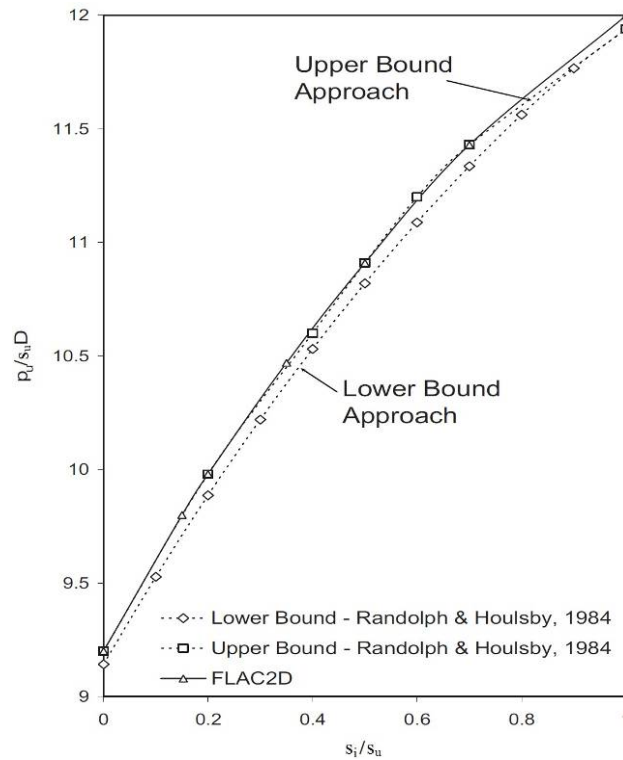


Figure 2.24 Variation in $p_u/c_u D$ with s_i/s_u (adapted from Kodikara et al., 2010)

Failure condition	α		β		B	C
	No interface adhesion ($s_i/s_u = 0$)	High-interface adhesion ($s_i/s_u = 1$)	No interface adhesion ($s_i/s_u = 0$)	High-interface adhesion ($s_i/s_u = 1$)		
No tension failure ($ \sigma_t + \sigma_o > 7s_u$)	6.615	7.142	1.065	1.093	0.4144	3.7881
Tension failure ($ \sigma_t + \sigma_o \leq 7s_u$)	52.960	54.600	1.169	1.290	0.8317	2.1190

Table 2.7 Values of Constants α , β , B and C for Tension and No-Tension Failure of Soils (adapted from Kodikara et al., 2010)

2.7 Issues with Current Methodology

The usage of p - y curves to design laterally loaded piles has proven to be effective due to the low failure rates of piles over several decades. However, LeBlanc et al. (2010b) highlighted that the design methodology is being used outside its verified range and does not take into account several design issues that will be discussed in the following sections.

2.7.1 Rigid Pile Behaviour vs. Flexible Pile Behaviour

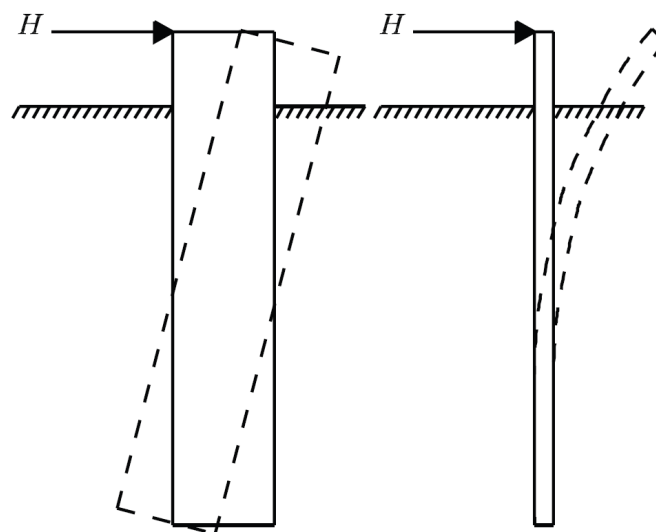


Figure 2.25 Rigid vs. Flexible Pile Behaviour (Brødbæk et al., 2009)

As in sections 2.6.1 and 2.6.2, the criteria used to construct p - y curves in clay were developed based on field tests on long, slender, and flexible piles that have slenderness ratios as high as 39.5. However, recently installed monopiles are designed to have slenderness ratios of around 5 (LeBlanc et al., 2010b), making monopiles short and rigid piles. As shown in Figure 2.25, there is a difference in behaviour between the two. A long flexible pile bends around a pivot point when laterally loaded. However, a short rigid pile rotates without flexing significantly and develops a significant “toe-kick” (lateral displacement at the end of the embedded pile shaft) that generates a shear force at the pile toe that increases total lateral resistance (Brødbæk et al., 2009). According to Reese and Van Impe (2001), even though tests have been made to quantify the pile toe shear force, no results from these tests have been published and no methods to quantify the shear force have been proposed.

According to Briaud et al. (1984), it is necessary to make a distinction between a pile that behaves in an almost rigid manner and one that is relatively flexible as the soil response is dependent on pile flexibility. Criteria to distinguish between rigid versus flexible pile behaviour have been proposed by various researchers, for example Dobry et al. (1982), Budhu and Davies (1987), and Poulos and Hull (1989). According to Poulos and Hull (1989), a pile behaves rigidly according to the following criterion:

$$L < 1.48 \left(\frac{E_p I_p}{E_s} \right)^{0.25} \quad (2.41)$$

E_s is the Young's modulus of elasticity of the soil. The criterion for flexible pile behaviour is

$$L > 4.44 \left(\frac{E_p I_p}{E_s} \right)^{0.25} \quad (2.42)$$

According to equations (2.41) and (2.42), a monopile with an outer diameter of 4 m, an embedded length of 20 m, and a wall thickness of 0.05 m behaves rigidly if $E_s < 7.6$ MPa. In contrast, the pile exhibits a flexible behaviour if $E_s > 617$ MPa. Since stiff clays and dense sands have $E_s < 100$ MPa (USACE, 1990), the monopile is expected to exhibit an intermediate behaviour that is a combination of both rigid and flexible behaviour. However, based on the equations above, Brødbæk et al. (2009) expects recently installed monopiles to behave more like a rigid pile than a flexible one.

As shown in Figure 2.26, Abdel-Rahman and Achmus (2005) carried out 3-D finite element modelling on a 7.5 m monopile embedded 30 m into sand with properties representative of the dense sand found in the North and Baltic seas off the German coast. The monopile was loaded with a horizontal force of 8 MN and a bending moment of 240 MN m at sea bed level. Based on their analysis, they determined that the monopile behaves as a rigid pile that rotates at depth. As shown in Figure 2.26, the monopile experiences lateral earth pressures of opposite signs at a rotation depth 22 m below the mudline, which is approximately 73% of the embedded depth.

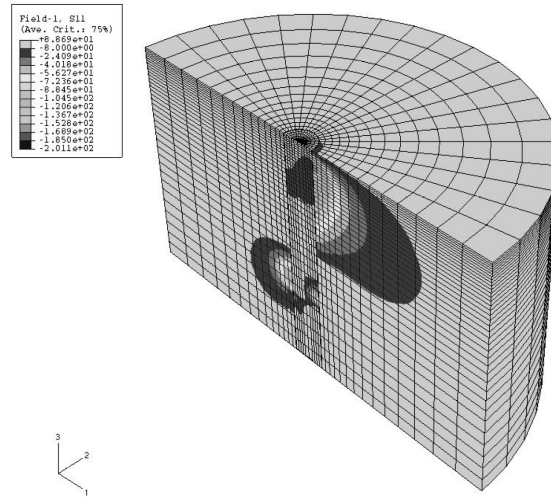


Figure 2.26 Mobilised Horizontal Stresses for a 7.5 m Monopile in 30 m Dense Sand (Abdel-Rahman and Achmus, 2005)

Monotonic centrifuge tests on monopiles in sand by Klinkvort and Hededal (2010) also show that the monopile behaves as a stiff and rigid pile that rotates at 80% of embedded depth. Considering the points above, not only is there the need to confirm the monopile's lateral behaviour, there is also the need to verify the suitability of the p - y curves for monopile design. In addition, since shear force is expected to act at the pile toe, there is a need to quantify its contribution to lateral resistance and determine the effects it has on the monopile's lateral behaviour.

2.7.2 Estimation of Initial Pile-Soil Stiffness

As highlighted in section 2.3, the natural frequency of the structure has to be designed to avoid the driving frequencies of turbine and the blades so that damage from resonance can be avoided. Therefore, it is crucial that the monopile be designed to have an appropriate stiffness that will prevent resonance. However, this can only be achieved provided the initial pile-soil stiffness, E^*_{py} (i.e. $E^*_{py} = dp/dy, y = 0$) is accurately estimated via the usage of the p - y design curves. Concerns have been raised regarding the appropriateness of the method to design monopiles by researchers such as Wieman et al. (2004), Abdel-Rahman and Achmus (2005), Lesny et al. (2007), and Augustesen et al. (2009) as their results suggests that the p - y method overestimates pile-soil stiffness for piles in sand. An example of this can be seen in Figure 2.27 from Abdel-Rahman and Achmus (2005) that shows the API (2011) p - y curves underestimating both lateral pile head displacement and rotation for horizontal forces exceeding 6 MN. Pradhan (2012) carried out F.E. analysis on monopiles in clay

and his results also suggests that the p - y method overestimates monopile-soil stiffness. This is unconservative for pile capacity and potentially problematic for natural frequency.

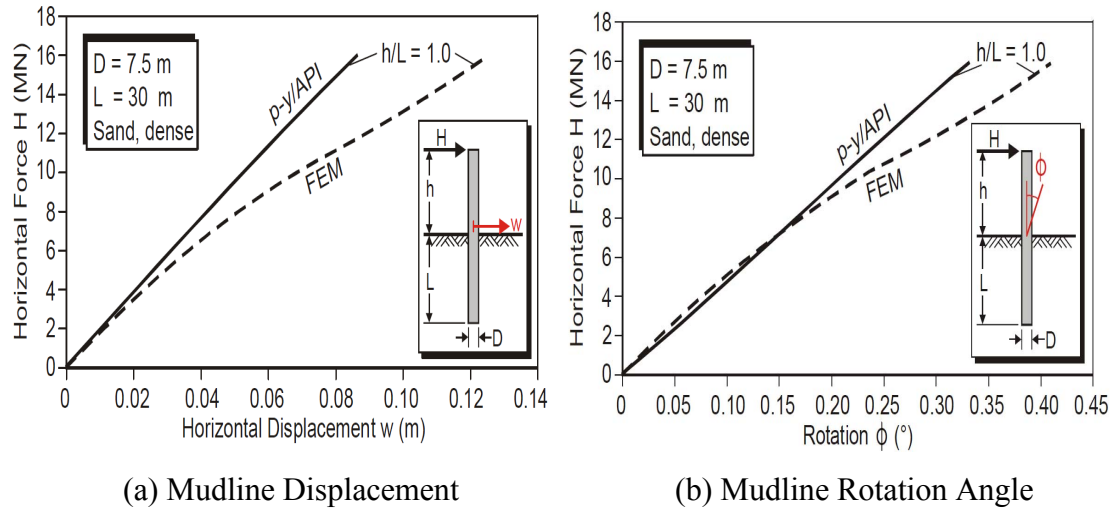


Figure 2.27 Comparison of Finite Element Results with p - y Results (Abdel-Rahman and Achmus, 2005)

Besides the accurate estimation of the initial soil stiffness, another area of concern has arisen. According to Lesny et al. (2007), the p - y method can be applied for pile diameters of 1 m – 2 m due to the experience gained over the many years. However, monopiles have much larger diameters ranging from 4.0 m to 7.5 m. Since there is the absence of experimental data or long-term pile behaviour experience that validates the applicability of the method on larger diameter monopiles, there is concern with regards to the effect pile diameter, D has on E_{py}^* . Research regarding the effects of D on the modulus of subgrade reaction, E_{py} (i.e. the secant modulus p/y) and E_{py}^* has been carried out over a number of years by numerous authors as highlighted in Table 2.8. Terzaghi (1955) analysed stress bulbs of piles in sand and clay and concluded that E_{py} is independent of pile diameter. Vesic (1961) came to the same conclusion based on his proposed relation between the modulus of subgrade reaction used in the Winkler approach and the soil (applicable to both sands and clays) and pile properties. Carter (1984) and Ling (1988) used a simple hyperbolic soil model to conclude that E_{py} is linearly proportional to D and found good agreement between their predictions and field test results on piles embedded in both sands and clays. Though their conclusions pertain to the modulus of subgrade reaction, E_{py} , their conclusions might also be applicable to the initial stiffness, E_{py}^* . Research on piles in sand by Ashford

and Juirnarongrit (2005) and Fan and Long (2005) regarding the diameter effect on E^*_{py} show that pile diameter has an insignificant influence on E^*_{py} . In summary, the research results are mixed, indicating the lack of a conclusive and consistent outcome.

Author	Method	Conclusion
Terzaghi (1955)	Analytical	Independent
Vesic (1961)	Analytical	Independent
Carter (1984)	Analytical expression against full-scale tests	Linearly dependent
Ling (1988)	Validation of method proposed by Carter (1984)	Linearly dependent
Ashford and Juirnarongrit (2005)	Numerical and large scale tests	Insignificant influence
Fan and Long (2005)	Numerical	Insignificant influence

Table 2.8 Chronological List of Research on Diameter Effect on Secant and Initial Stiffness of p - y curves (Brødbæk et al., 2009)

Due to the lack of a conclusive and consistent outcome, monopile focused research has been carried out to determine the influence diameter has on pile-soil stiffness by a variety of researchers. One example would be Achmus et al. (2011). Utilising a similar 3-D finite element model to Abdel-Rahman and Achmus (2005), Achmus et al. (2011) studied the lateral response of monopiles of varying diameters (0.61m, 1.5 m, 3.0 m, 4.0 m, 5.5 m and 7.5 m) embedded in sands of varying relative densities (loose, medium dense, dense, and very dense) and compared their results with the estimates from the p - y method. Figure 2.28 compares the numerically derived pile head displacements to the displacements from the p - y method.

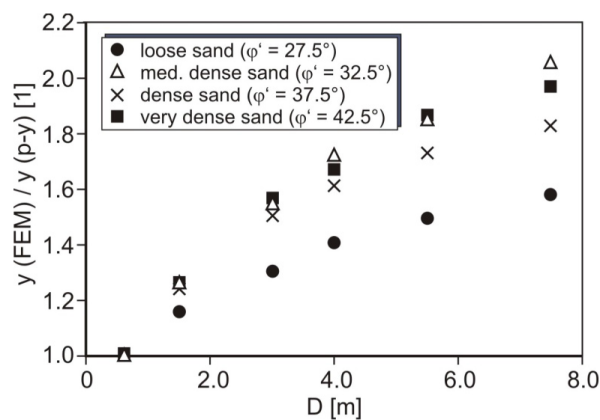


Figure 2.28 Ratio of Numerically Derived Pile Head Displacements to Displacements from p - y Method relative to Sand Relative Density and Pile Diameter (Achmus et al., 2011)

From Figure 2.28, it can be seen that with increasing diameter and starting from $D = 1.5$ m, the finite element displacements are larger than the displacements from the p - y method, with the effects being less pronounced for loose sands. For $D = 7.5$ m, depending on the soil conditions, the p - y method underestimates the F.E. displacement by 30% to 50%. Besides Achmus et al. (2011), other researchers who have investigated this matter include Lesny and Wiemann (2006) and Hearn (2009) who carried out finite element modelling on monopiles of varying diameters in sand and Leth (2013) who carried out centrifuge testing on stiff piles with diameters ranging from 1 m – 3 m and embedment lengths 6 to 10 times the diameter into dry sand. Similar to Achmus et al. (2011), their results suggests that for monopiles in sand, the p - y method overestimates the initial soil stiffness when applied to large diameter monopiles.

Though the results above pertain to monopiles in sand, there is the possibility that the E^*_{py} of monopiles in clay may also be inaccurately estimated. Research results pertaining to cohesive soils from Reese et al. (1975), Stevens and Audibert (1979), O'Neill and Dunnavant (1984) and Dunnavant and O'Neill (1985) suggests that E_{py} may be dependent on pile diameter, D . Reese et al. (1975) back-calculated curves for a 0.61 m diameter pile in order to predict the response of a 0.15 m pile. Though moment distributions were well estimated, the deflections were considerably underestimated to the measured values of the 0.15 m pile. Stevens and Audibert (1979) found that the Matlock (1970) and API (1978) criteria overestimated the pile deflections. In addition, the overestimation increased with increasing pile diameter, suggesting that E_{py} increases with D . O'Neill and Dunnavant (1984) and Dunnavant and O'Neill (1985) laterally loaded 0.27 m, 1.22 m, and 1.83 m piles in overconsolidated clay and found that there was a non-linear relation between deflection and D . Deflection at 50% of p_u decreased with increasing D , suggesting that E_{py} increases with D . Though the results pertain to E_{py} , their conclusions might be applicable E^*_{py} , highlighting the possibility that E^*_{py} of monopiles in clay may be inaccurately estimated by the recommended industry standard.

In addition, as highlighted at the end of section 2.6, the p - y criteria suggested by Sullivan et al. (1980) and Gazioglu and O'Neill (1984) raise the possibility that the constant utilised to calculate the reference deflection y_c is not a fixed number as

suggested by Matlock (1970) and Reese et al. (1975), but a variable number that is dependent on the properties of the soil in question. Depending on the soil in question, the value utilised as the constant to calculate y_c can be lower than the values suggested by Matlock (1970) and Reese et al. (1975). Assuming this is true, there is the possibility that monopiles designed via the soft clay and stiff clay below water table criteria may underestimate the initial pile-soil stiffness. One possible example that reflects this possibility is the Lely wind farm in IJsselmeer, Netherlands.

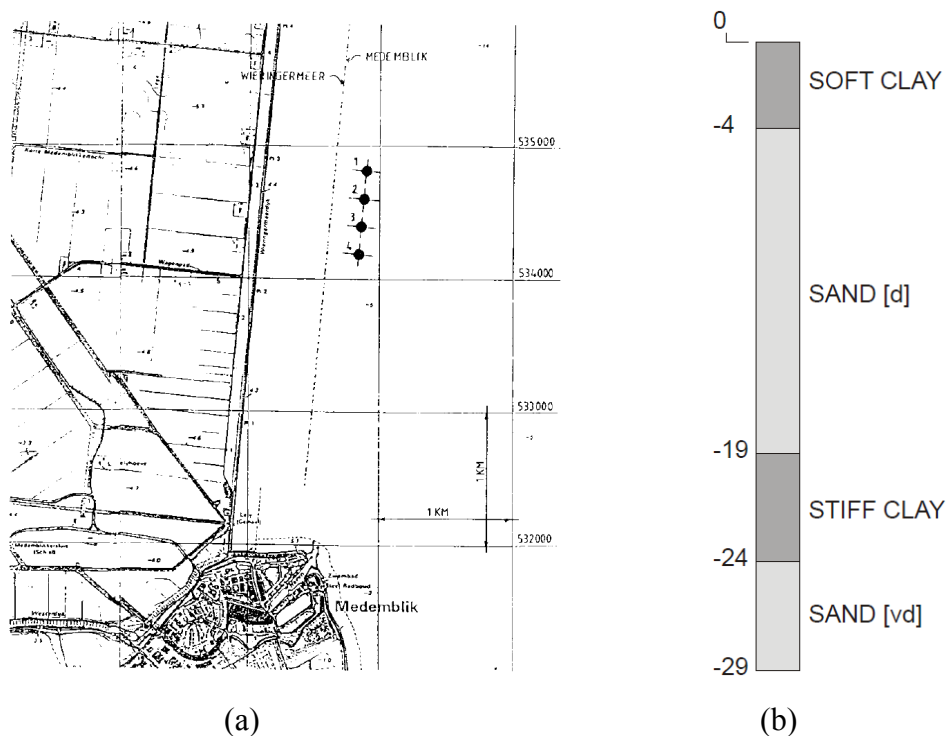


Figure 2.29 Lely Wind Farm (a) Layout of Wind Turbines (b) Typical Soil Profile (Delft University of Technology et al., 2003)

According to Kühn (2000), the Lely wind farm consists of four active-stall regulated 500 kW turbines supported by monopiles with $D = 3.2 \text{ m} - 3.7 \text{ m}$ and $L = 26 \text{ m} - 28 \text{ m}$. The location and the typical soil profile for the four wind turbines are shown in Figure 2.29. According to the Delft University of Technology et al. (2003), the average water depth at locations A1, A3 and A4 is between 5 m and 6 m while the average water depth at A2 is 10 m due to dredging. The soil generally consists of dense sand overlain with soft clay. The piles penetrate into the stiff clay layer, but do not reach the very dense sand. The layer of dense sand at A2 is thinner relative to the other locations, but it is unclear in the reference the precise stratigraphy at this location. Monopiles at location A1, A3, and A4 were designed to be “soft-stiff” while

A2 was designed to be “soft-soft” since the first natural frequency of the structure was predicted to be below the rotational frequency of the wind turbine rotor (Kühn, 2000).

Six months after installation, measurements of the eigenfrequencies of turbine A2 and A3 confirmed stiffer behaviour than predicted by design calculations as shown in Table 2.9. However, the difference between measured and predicted eigenfrequencies for turbine A2 was considerable and of such a magnitude to change the structure from the intended “soft-soft” to a “soft-stiff” structure (Kühn, 2000). According to Kühn (2001), a parametric study was carried out to investigate the cause of differences between predictions and measurements. The design calculations were also repeated with more realistic assumptions. However, the p - y curves were maintained since derivation from cone penetration tests and partly laboratory tests could be reproduced. Based on the investigation, three “speculative explanations” (Kühn, 2001) were offered. Firstly, site conditions could be different than assumed. Secondly, the design might not correspond to specifications and thirdly, the measurement at A2 might be wrong.

Turbine	1 st Bending Mode (Hz)			2 nd Bending Mode (Hz)		
	Predicted	Measured	Difference	Predicted	Measured	Difference
A2	0.399	0.634	-37%	1.6	3.7	-57%
A3	0.672	0.735	-9%	2.6	4.0	-35%

Table 2.9 Predicted and Measured Frequencies of Turbines in Lely Wind Farm (Delft University of Technology et al., 2003)

The soft clay criterion by Matlock (1970) was utilised to construct the p - y curves (Delft University of Technology et al., 2003). Given the possibility that the p - y curves from Matlock (1970) may underestimate the pile-soil stiffness (as highlighted by the comparison with Sullivan et al. (1980) and Gazioglu and O’Neill (1984)), it is possible that the large difference between measured and predicted frequencies at location A2 is due to underestimation of the pile-soil stiffness resulting from the usage of p - y curves derived from the soft clay criterion. Assuming the clay had similar properties to the heavily overconsolidated Manor clay tested by Sullivan et al. (1980), it is possible that the constant to calculate y_c could be as low as 0.35 instead of 2.5 as suggested by Matlock (1970).

An assessment of the maximum permanent monopile rotation requirement of 0.5° at mudline (Achmus et al., 2009) with respect to the p - y curves constructed based on the soft clay and stiff clay below water table criteria was carried out. This was done to determine where a typical design would fall with respect to the curves. If a 4 m diameter monopile embedded 20 m into soft clay rotated at 80% of its embedded depth (as observed in the centrifuge tests of Klinkvort and Hededal (2010) for monopiles in sand), the resulting displacement at mudline would be 0.14 m. The results of the assessment are summarised in Table 2.10 and Table 2.11. Values of ε_c for both normally consolidated (NC) and overconsolidated (OC) clays for different shear strengths were obtained from Peck et al. (1974) and Reese and Van Impe (2001). An A_s and A_c value of 0.2 was utilised based on the curves of Figure 2.18.

Consolidation State	s_u (kPa)	ε_c	y_c (m)	$3y_c$ (m)
<i>NC</i>	<48	0.02	0.2	0.6
<i>NC</i>	48 – 96	0.01	0.1	0.3
<i>OC</i>	50 – 100	0.007	0.07	0.21

Table 2.10 Reference Deflection for 4 m Monopile for Soft Clay Criterion

Consolidation State	s_u (kPa)	ε_c	Static Load (m)		Cyclic Load (m)	
			$6A_s y_c$	$18A_s y_c$	$0.6y_p$	$18y_p$
<i>NC</i>	96 – 192	0.005	0.024	0.072	0.0098	0.2952
<i>OC</i>	100 – 200	0.005	0.024	0.072	0.0098	0.2952
<i>OC</i>	300 – 400	0.004	0.0192	0.0576	0.0079	0.2362

Table 2.11 Reference Deflection for 4 m Monopile for Stiff Clay Criterion below Water Table

As can be seen from Table 2.10, the maximum displacement allowed at mudline is less than $3y_c$ based on the soft clay criterion. Since the requirement is well within the initial non-linear segment of the p - y curve as seen in Figure 2.15, it suggests that the linear segments of both static and cyclic loading curves are not important for monopile serviceability failure design in soft clays. The values also emphasize the importance of accurately estimating the pile-soil stiffness to prevent serviceability failure for monopiles in soft clays. In Table 2.11, the maximum displacement at mudline requirement greatly exceeds both $6A_s y_c$ and $0.6y_p$ of both static and cyclic p - y curves of the stiff clay below water table criterion, entering well into the linear segments where soil resistance degrades significantly as compared to Figure 2.17 and Figure 2.19. This suggests that the design for serviceability failure for monopiles in

stiff clay is similar to ultimate limit states design as conservatism is required to account for the reduction in soil resistance. The values in Table 2.11 also suggests that accurate estimation of the initial pile-soil stiffness may not be of great importance for monopiles in stiff clay as serviceability failure takes place beyond the initial non-linear segments of the p - y curves.

The points above highlight the need to determine if the p - y curves recommended by either API (2011) or DNV (2014) standards accurately estimate the initial pile-soil stiffness for large diameter monopiles. Since much research has been carried out in sand, there is a need to fill the gap in knowledge by carrying out research on monopiles in clay. Based on the assessment of the serviceability design requirements with respect to the p - y curves for clay, the values suggests that accurate estimation of the initial pile-soil stiffness is of greater importance for monopiles in soft clays than stiff clays. Therefore, research regarding the initial-pile soil stiffness for monopiles in soft clay is of greater importance as compared to monopiles in stiff clays.

2.7.3 Cyclic Loading Design

As highlighted in section 2.3, offshore wind turbines are expected to be subjected to at least 150 million cycles of load over their 25 year design lifespan due to wind and wave loads. Not only do designers have to consider extreme storm conditions but also serviceability conditions. This is because both intense and continuous cyclic loading may lead to accumulation of pile head deformation and rotation. Another area of concern is the changes in pile-soil stiffness due to long-term cyclic loading. Since the structure is a dynamic structure, changes in the pile-soil stiffness (degradation / stiffening) will alter the natural frequency of the system. Significant changes in natural frequency may lead to unplanned system resonances and excessive cyclic displacements that would result in failure of the structure.

Considering that “wind energy converters are relatively sensitive to deformations, in particular tilting” (Achmus et al., 2010) and that “long-term movements may significantly impact all parts of the wind turbine, including the support structure, machine components and blades” (LeBlanc, 2009), designers are faced with the arduous tasks of limiting the permanent rotation of the monopile and designing the monopile to maintain its stiffness over its long design lifespan of 25 years under

millions of cyclic loads. Their job is not made any easier by the strict displacement requirements. “In recent projects, a maximum permanent rotation of a monopile at mudline of 0.5° was required” (Achmus et al 2009). Despite the strict requirements, the tasks at hand are extremely difficult to achieve as very little is known on the effects of cyclic loading. This is especially true for clays and at the same time important as the “effects of cyclic loading are most significant for piles in cohesive soils” (DNV, 2014).

Even though much is demanded from designers, the p - y curves recommended by the DNV industry standard (2014) have various shortcomings when utilised for cyclic loading design. Firstly, the curves are designed primarily for the evaluation of ultimate lateral capacity as the p - y curves try to account for the cyclic effects by scaling down the ultimate lateral resistance (i.e. Figure 2.15(b)) to capture the steady state. As highlighted by Long and Vanneste (1994) who carried out cyclic lateral load tests on piles in sand, important factors that contribute to the resulting displacement such as cyclic load characteristics and number of load cycles are not accounted for.

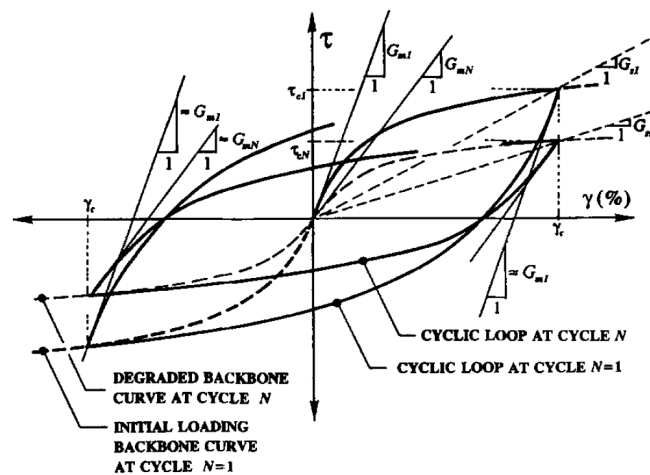


Figure 2.30 Clay Stress-Strain Curve from Cyclic Constant-Volume Equivalent Undrained Direct Simple-Shear Test (Matasović and Vucetic, 1995)

Secondly, the p - y curves for both soft and stiff clay were derived from piles subjected to 100 cycles of loading at most (Matlock, 1970, Reese et al., 1975), far less in comparison to the millions of load cycles a monopile experiences over its lifetime. Even though an equilibrium response was reported in less than 100 cycles, cyclic degradation and permanent deformation effects on the soil may be a lot more severe

past 100 cycles as “it is probable that application of hundreds or thousands of cycles would have caused additional deflection” (Reese and Van Impe, 2001). This is possible considering the nonlinear stress-strain behaviour of soil as shown in Figure 2.30 in which the stiffness of clay is observed to degrade with increasing strains as a result of cyclic loading. In Figure 2.30, γ_c is cyclic shear-strain amplitude, N is cycle number, τ_{cN} is cyclic shear-stress amplitude at cycle N , and G_{sN} is secant shear modulus at cycle N .

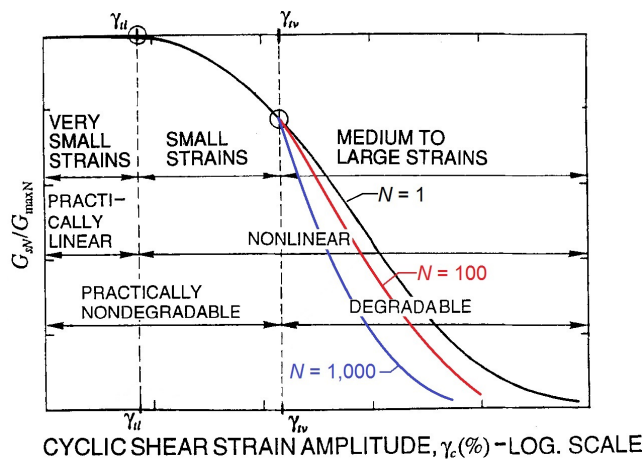


Figure 2.31 Secant Shear Modulus Reduction vs. Cyclic Shear Strain for Fully Saturated Soils (adapted from Vucetic, 1994)

As shown in Figure 2.31, adapted from Vucetic (1994), there are two cyclic threshold shear strains known as the linear cyclic threshold shear strain, γ_{ll} and the volumetric cyclic threshold shear strain, γ_{lv} . When $\gamma_c < \gamma_{ll}$, the soil behaves as a linearly elastic material. When $\gamma_{ll} < \gamma_c < \gamma_{lv}$, the soil becomes markedly nonlinear but remains largely elastic because permanent changes of its microstructure still do not occur or are negligible. However, when $\gamma_c > \gamma_{lv}$, significant permanent volumetric and microstructural changes take place and under repeated undrained cycles of load, excess pore water pressures build-up resulting in degradation of stiffness. With increasing γ_c , G_{sN} increasingly reduces relative to G_{maxN} , the maximum initial shear modulus at small strains. Cyclic dual-specimen direct simple shear (DSDSS) tests carried out by Cavallaro et al. (2003) on lightly overconsolidated clay and work by Darendeli and Stokoe (2001) who developed a framework to generate normalised modulus reduction curves, suggest that G_{sN} reduces with cyclic loading for the same γ_c , as shown by the modified curves in Figure 2.31

This leads to the third shortcoming, the fact that accumulated rotations and stiffness changes due to long-term cyclic loading are poorly accounted for by the p - y curves. To overcome this deficiency, engineers under the general understanding that the stiffness of clay degrades with cyclic loading (Thiers and Seed, 1968), utilise the following equation proposed by Idriss et al. (1978) to quantify stiffness degradation:

$$\delta = \frac{G_{sN}}{G_{s1}} = \frac{\gamma_c}{\tau_{c1}} = \frac{\tau_{cN}}{\tau_{c1}} = N^{-t_{dgrd}} \quad (2.43)$$

in which δ is the degradation index. δ can then be linked to the degradation parameter t_{dgrd} to take into account the rate of degradation with respect to the number of cycles. It is understood that the design of monopile relies to a large extent on stiffness degradation curves derived for earthquake loading such as the one shown in Figure 2.32 by Vucetic and Dobry (1988).

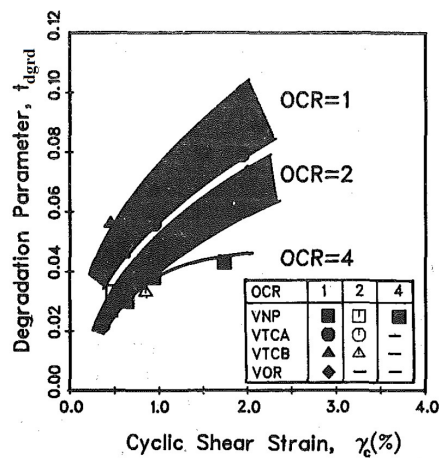


Figure 2.32 Variation of Degradation Parameter t_{dgrd} with γ_c and Overconsolidation Ratio (OCR) for Four Venezuelan Offshore Clays (adapted from Vucetic and Dobry, 1988)

Even though engineers can carry out various laboratory tests such as bender element (BE), resonant column and cyclic triaxial tests to evaluate the initial shear modulus and the degradation parameter t_{dgrd} to utilise in their design, the effectiveness and accuracy of equation (2.43) is heavily reliant on the t_{dgrd} values that are selected over the considered strain range as a small change of t_{dgrd} can have a large effect on modulus degradation. According to DNV guidelines (2002), rotating machines induce

of Dobry and Vucetic (1987) as shown in Figure 2.34 highlight the importance of considering the cyclic pore water response of clay.

Firstly, it shows that overconsolidated clays do not necessarily develop negative pore-water pressures at all times. Even though negative pore-water pressures may develop at the beginning, the pore-water-pressure generation trend may reverse as cycling continues and subsequently produce positive pore-water pressures that in turn reduce the strength and stiffness of the surrounding soil. Secondly, Figure 2.34 also indicates that because pore-water-pressure generation is dependent on OCR , the pore-water-pressure response of OC clays depends strongly on the loading history and the changes in clay microstructure during cyclic shear straining. Considering the limitations of the p - y curve, the lack of information regarding the generation of pore pressures due to cyclic loading and that no pore pressure measurements are monitored in the field (May, 2011), more research has to be carried out to determine the effects of excess pore water pressures generated by clay under cyclic loading onto the surrounding soil.

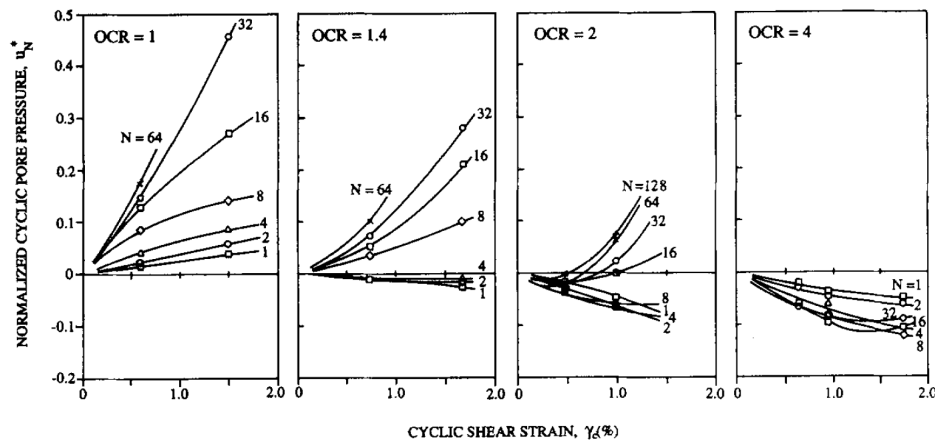


Figure 2.34 Pore-Water Pressure Variation during Cyclic Loading (Dobry and Vucetic, 1987)

According to Pender and Pranjoto (1996) and Tuladhar et al. (2008), a pile in cohesive soil subjected to cyclic lateral loading will cause the progressive formation of gaps in front and behind the pile shaft at the pile-soil interface. This leads to a potential shortcoming of utilising the recommended p - y curves for clays for monopile design; i.e. the p - y curves do not take into account the detrimental effects of gap formation resulting from cyclic loading. Based on the numerical studies carried out by

Pender and Pranjoto (1996), Prajonto and Pender (2003), and Allotey and El Naggari (2008) on gapping, their results suggest that gapping is the primary cause of cyclic degradation in the stiffness of piles embedded in clay. In addition, their results show that pile head lateral displacement, rotation, and maximum pile shaft moment are increased due to gap formation. Prajonto and Pender (2003) also observed that the gap depth increases with increasing load magnitude and number of cycles due to nonlinear soil behaviour. Despite the failure of the p - y curves to take into account the detrimental effects gap formation has on pile stiffness and pile head displacement and rotation, the p - y curves may take into account the effect gap formation has on reducing the pile lateral capacity. Tuladhar et al. (2008) studied the cyclic behaviour of laterally loaded 0.30 m diameter concrete piles embedded 24.8 m deep into cohesive soil and determined that gapping had a significant effect on the pile's lateral capacity. According to Tuladhar et al. (2008), the lateral load capacity of the specimen subjected to reverse cyclic loading degraded by 28% relative to monotonic loading. This is in-line with the factor of 0.72 recommended by the soft clay criterion of Matlock (1970) to calculate the reduced ultimate capacity from cyclic loading.

Due to the shortcomings of the p - y curve for cyclic design, the DNV standard (2014) states that caution should be exercised when the curves are utilised to carry out serviceability and fatigue analysis of the pile. Research has been carried out by various researchers to investigate the cyclic behaviour of monopiles and to develop suggestions to address the shortcomings of the p - y curve. Most research in this area has been carried out on monopiles in sand as shown in Table 2.12. Based on the summary in Table 2.12, the findings regarding the cyclic behaviour of laterally loaded monopiles are both varied and consistent over certain aspects. For example, research involving model and centrifuge testing such as Li et al. (2010), LeBlanc et al. (2010b) and Klinkvort and Hededal (2013) have produced results that show stiffness increase from cyclic loading instead of stiffness degradation as suggested by Achmus et al. (2009) who utilised cyclic triaxial test results and F.E. analysis to develop a degradation stiffness model. Accumulated rotations increased logarithmically in Li et al. (2010) while both LeBlanc et al. (2010b) and Klinkvort and Hededal (2013) characterised the increase of accumulated rotations utilising a power law.

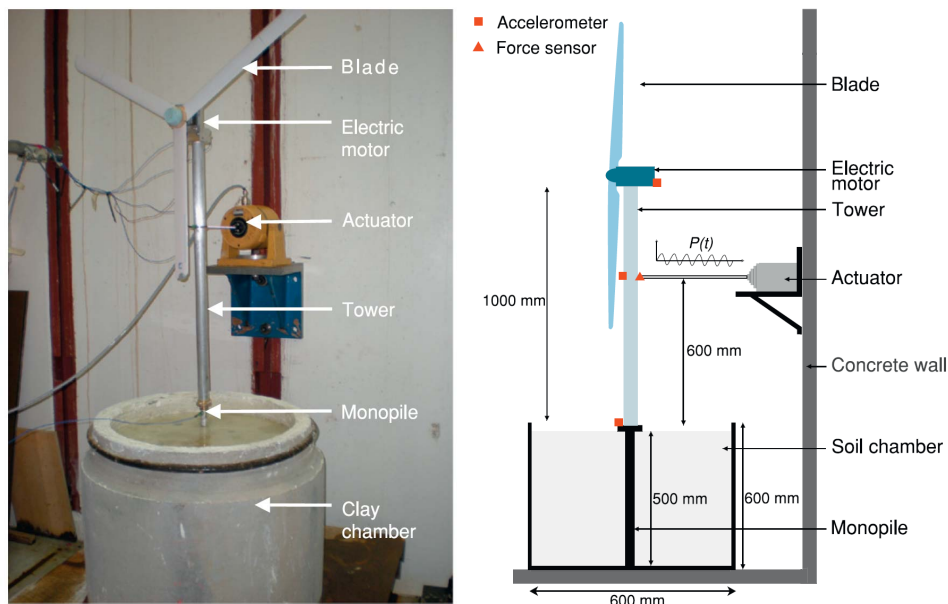
Author	Research Details and Important Findings
Lesny and Hinz (2007)	<ul style="list-style-type: none"> • Predict accumulated displacements using data from cyclic triaxial tests and F.E. modelling incorporating Miner’s law.
Achmus et al. (2009)	<ul style="list-style-type: none"> • Utilised cyclic triaxial test results and F.E. analysis to develop degradation stiffness model. • Degradation stiffness model used to produce design charts to evaluate accumulated deformation utilising loading and geometric parameters as inputs.
Cuéllar et al. (2009)	<ul style="list-style-type: none"> • Model scale cyclic tests on a monopile in saturated dense sand with 5×10^6 one-way cycles. • Accumulation of rotation behaviour change from increasing cyclic amplitudes to stabilising cyclic amplitudes after 100,000 cycles of load.
Li et al. (2010)	<ul style="list-style-type: none"> • Centrifuge testing on monopile in dense sand. • Pile lateral secant stiffness increases with cyclic loading as a result of local densification of sand. • Accumulation of displacements increased logarithmically.
LeBlanc et al. (2010a)	<ul style="list-style-type: none"> • Further developed accumulated rotation model to account for random two-way lateral loading that is based on Miner’s rule. • Model was validated by experiments with the same setup as LeBlanc et al. (2010b).
LeBlanc et al. (2010b)	<ul style="list-style-type: none"> • Model scale cyclic lateral load tests on a scaled monopile in loose sand. • Suggested equations that quantified both cyclic pile secant stiffness and cyclic accumulated rotations. <ul style="list-style-type: none"> ○ Pile secant stiffness increased logarithmically. ○ Accumulated rotations increased based on power law.
Klinkvort and Hededal (2013)	<ul style="list-style-type: none"> • Centrifuge testing on monopiles in dense sand that were monotonically and cyclically loaded. • Developed a model framework similar to LeBlanc et al. (2010b). <ul style="list-style-type: none"> ○ Secant stiffness increased logarithmically. ○ Accumulated rotations increased based on power law.
Rudolph et al. (2014)	<ul style="list-style-type: none"> • Centrifuge tests on monopiles in both loose and dense sand with direction varied and unidirectional cyclic loads. • Direction varied results showed significantly increased deformation accumulation relative to unidirectional case. • Suggested simple approach to estimate the additional displacement accumulation from direction varied cyclic loads relative to unidirectional loads.

Table 2.12 Research Summary on Monopile Cyclic Lateral Load Behaviour in Sand

Even though Klinkvort and Hededal (2013) suggested a model framework similar to LeBlanc et al. (2010b), Klinkvort and Hededal (2013) noted differences between the models. For example, instead of 1.6-way cyclic loading being the most detrimental,

Klinkvort and Hededal (2013) observed that one-way loading was most detrimental. LeBlanc et al. (2010b) observed accumulated rotation regardless of the cyclic load characteristic while Klinkvort and Hededal (2013) observed the pile move back against its initial position for pure two-way loading. Klinkvort and Hededal (2013) suggested that the differences were mainly attributed to the differences in stress conditions between model and centrifuge testing. Since the tests of LeBlanc et al. (2010b) were carried out in loose sand to model the maximum angle of friction correctly, the loose sand most likely started to compact when loaded. In addition, since model testing is unable to model the stresses, stiffness, and relative densities correctly, Klinkvort and Hededal (2013) suggests that the dilatant behaviour of sand could not be properly accounted for by LeBlanc et al. (2010b).

Research pertaining specifically to the cyclic loading behaviour of monopiles in clay has been extremely limited. So far, only Lombardi et al. (2013) has carried out research pertaining specifically to monopiles in clay by carrying out model cyclic tests on scaled model wind turbine in soft speswhite kaolin as shown in Figure 2.35.



(a) Physical Model (b) Model set-up and Instrumentation
 Figure 2.35 Lombardi et al. (2013) Model Cyclic Test Setup

To study the long-term behaviour, a series of tests were carried out in which the structure was subjected to between 32,000 and 172,000 cycles of horizontal loading with the utilisation of an electro-dynamic actuator. Based on the results, Lombardi et

al. (2013) concluded that cyclic loading of monopiles in clay is expected to cause softening depending on the soil strain level and ratio of system frequency to the forcing frequency. Lombardi et al. (2013) also developed guidance to monopile diameter selection based on bender element test results using the concept of volumetric threshold shear strain. Based on the guidance developed, the minimum monopile diameter that could potentially prevent progressive foundation stiffness degradation can be estimated. Despite the extensive testing carried out by Lombardi et al. (2013), the results are heavily questionable. Even though Lombardi et al. (2013) argue that their model scale test results can be scaled to prototype due to “conceptual understanding and knowledge gained from bender element tests on soils”, it is not physically possible for model testing to correctly model the prototype stresses and strains, resulting in incorrect modelling of the non-linear stress strain behaviour of soil. In addition, the excess pore pressure response from model tests in clay will not be correctly modelled as the response is strongly dependent on stress conditions, loading history, and changes in clay microstructure during cyclic shear straining.

Considering that the model test results of Lombardi et al. (2013) are heavily questionable, research related to rigid piles like Zhang et al. (2011) and Su et al. (2014) and research regarding the cyclic behaviour of piles in cohesive soil such as Heidari et al. (2014) were considered. Zhang et al. (2011) carried out centrifuge monotonic and two-way cyclic tests on a rigid pile in soft overconsolidated speswhite kaolin while Su et al. (2014) carried out model cyclic unidirectional and multidirectional laterally loaded tests on a rigid pile in soft compacted kaolin. Heidari et al. (2014) utilised the strain wedge method (SWM) to generate non-linear p - y curves which were then implemented as the backbone curve of developed beam on nonlinear Winkler foundation (BNWF) model to account for different response features of the pile-soil system, such as soil and pile nonlinearity, cyclic degradation of soil stiffness and strength, gapping, and radiation damping.

The monotonic and cyclic tests of Zhang et al. (2011) were carried out on a fixed-head 0.6 m diameter pile embedded 3 m into soft overconsolidated speswhite kaolin. The cyclic tests were displacement-controlled and across the tests, the minimum number of cycles applied was 20 cycles while the maximum was 100 cycles. The pile was loaded at 1 mm/s to ensure undrained conditions. Monotonic test results suggests

that the API (2000) criterion based on Matlock (1970) produces p - y curves that significantly underestimate the pile-soil stiffness of rigid piles. This is shown by the experimentally measured curve in Figure 2.36. Not only does the monotonic load-displacement curve display a significantly stiffer response relative to the API (2000) estimate, the lateral load capacity measured is 25% higher. Therefore, further research has to be carried out to verify if the Matlock (1970) criterion to constructing p - y curves produces inaccurate estimates of pile-soil stiffness.

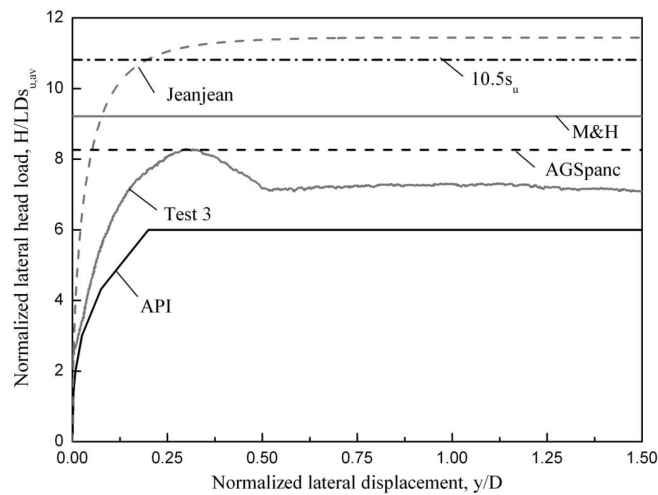


Figure 2.36 Comparison of Load Test and Calculated Ultimate Capacity (Zhang et al., 2011)

The monotonic test produced a gap whereas gaps were not observed in the cyclic tests, suggesting that gapping may not be an issue in cyclic loading. However, since only two-way cyclic tests were carried out, research involving cyclic loads of different characteristics as carried out by LeBlanc et al. (2010b) and Klinkvort and Hededal (2013) should be performed to verify if gapping will be an issue in cyclic loading. In the cyclic tests of Zhang et al. (2011), lateral stiffness was observed to degrade with cycles, with higher degradation rates for larger amplitude cycles. Tests involving increasing then decreasing amplitudes show that smaller amplitude cycles do not contribute to further remolding and stiffness degradation if the amplitude is reduced significantly. The findings of Zhang et al. (2011) are in line with the general understanding that cyclic loading causes stiffness degradation in clays (Thiers and Seed, 1968) and larger amplitude cyclic loads would induce greater strains that would cause greater reductions in stiffness relative to smaller amplitude cyclic loads.

Based on the results, Zhang et al. (2011) developed an approach to link cumulative lateral pile movement with cumulative remolding of cyclic T-bar test. The approach developed assumes that within a given lateral pile movement, y/D , the plastic component increases exponentially from zero for infinitesimal cycles to the total movement less some proportion (which was taken as 20%) of the pile diameter for large displacements. Therefore, in a given cycle, of amplitude y_{max}/D , the accumulated plastic strain (in addition to that from previous cycles) is

$$\left(\frac{y}{D}\right)_p = 4\left[\frac{y_{max}}{D} - f \tanh\left(\frac{y_{max}}{fD}\right)\right] \quad (2.44)$$

where y_{max} is the maximum displacement, a factor of 4 converts from the amplitude to the full cumulative two-way displacement, and f was taken as 0.2.

Zhang et al. (2011) assumed that one pass of the T-bar causes the same level of remolding as two diameters of fully plastic lateral movement of a pile. This is because two diameters is approximately the extent of the failure mechanism around a T-bar (Zhou and Randolph, 2009). With this assumption, any number of T-bar cycles (or partial cycles), ΔN_{T-bar} , can be converted to an equivalent plastic lateral pile movement, $(y/D)_p$ as

$$\left(\frac{y}{D}\right)_p = 4N_{T-bar} \quad (2.45)$$

To use these relationships, a link between the T-bar cycle number, N_{T-bar} and operative shear strength has to be determined from a cyclic T-bar test as shown by the example in Figure 2.37. Once this has been performed, equations (2.44) and (2.45) can be used to derive the shear strength applicable through a series of lateral pile cycles, which may be of varying amplitude. For a given lateral cycle of amplitude y_{max}/D , equation (2.44) indicates the plastic pile movement accumulated within that cycle, which can be converted to an equivalent change in accumulated T-bar cycles, ΔN_{T-bar} , using equation (2.45), allowing the corresponding operative strength to be identified.

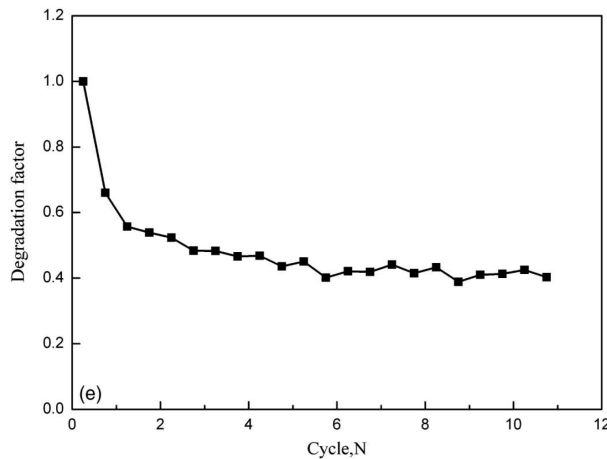
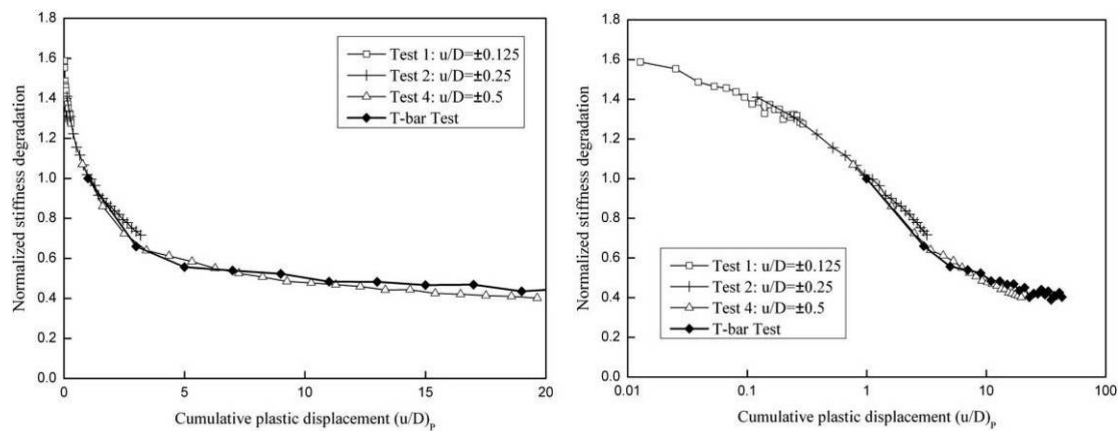


Figure 2.37 T-bar Resistance Degradation Factor (Zhang et al., 2011)

When these equations were used to combine the data from the cyclic T-bar test and pile tests (with pile stiffness expressed in a normalised form, dividing by the value at a plastic strain of $(y/D)_p = 1$), the estimates matched well as shown in Figure 2.38. However, this is partly attributable to the “highly tentative” and “rather arbitrary conversion factor” (Zhang et al., 2011) of equation (2.44).



(a) Linear Displacement Scale

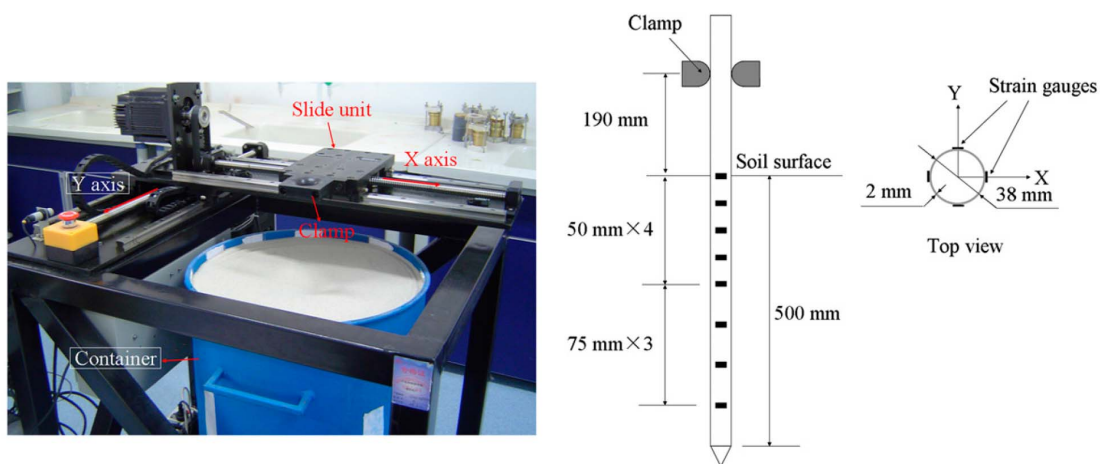
(b) Logarithmic Displacement Scale

Figure 2.38 Normalised Stiffness Degradation (Zhang et al., 2011)

The good agreement between the estimates and observations highlights the possibility of a link between the remolding behaviour during cyclic T-bar tests and cyclic lateral pile movement. However, the method may not be applicable for monopile design for various reasons. Firstly, the method may be limited to two-way cyclic loading as the estimates were matched to two-way cyclic loading results whereas monopiles will be subjected to cyclic loads of various characteristics. Secondly, the approach was tested against cyclic tests that involved at most 40 cycles whereas the monopile is expected

to experience millions of cycles over its lifetime. Utilisation of this method may result in inappropriate designs as it would be an extrapolation beyond its verified range. Thirdly, the good agreement between the estimates and observations was partly attributable to the “highly tentative” and “rather arbitrary conversion factor” (Zhang et al., 2011) of equation (2.44), indicating more research has to be carried out to justify the use of the conversion factor. Fourthly, fixed-head displacement-controlled cyclic tests are not representative of the conditions experienced by a monopile that moves freely based on the applied force. Therefore, the method may not be applicable for monopile design.

Zhang et al. (2011) carried out a test involving constant-amplitude cycles with intervening periods of reconsolidation of 1 year, 5.3 years, 6.5 years, and 7.5 years. The secant stiffness was observed to recover after each period of reconsolidation, suggesting that lateral stiffness may reach a steady state independent of cycle number, representing a balance between the damaging effects of cyclic loading and the healing effects of time and reconsolidation. Though there is basis behind the suggestion, it may be unconservative to assume a steady state independent of cycle number will be achieved for monopile design as it is unlikely the clay will be allowed to reconsolidate for such great periods of time due to the cyclic loads from both wind and wave forces.



(a) Biaxial Model Platform (b) Model Pile and Instrumentation
Figure 2.39 Experiment Setup of Su et al. (2014)

As shown in Figure 2.39, Su et al. (2014) carried out model cyclic unidirectional and multidirectional laterally loaded tests on a rigid 38 mm diameter aluminium tube with

a 2 mm thickness that was embedded 500 mm deep into soft compacted kaolin. This results in a slenderness ratio of 13.2. The pile head is clamped and is laterally loaded 190 mm above the soil surface with a computer-controlled biaxial motion platform. The maximum lateral off-centre displacement was 13 mm. All tests were displacement-controlled and at a constant rate of 0.1 mm/s. Two types of unidirectional displacement paths (regular and irregular) and three types of multidirectional displacement paths (cross, eight-shape, and irregular) were tested as can be seen by the pile head displacement plots of Figure 2.40.

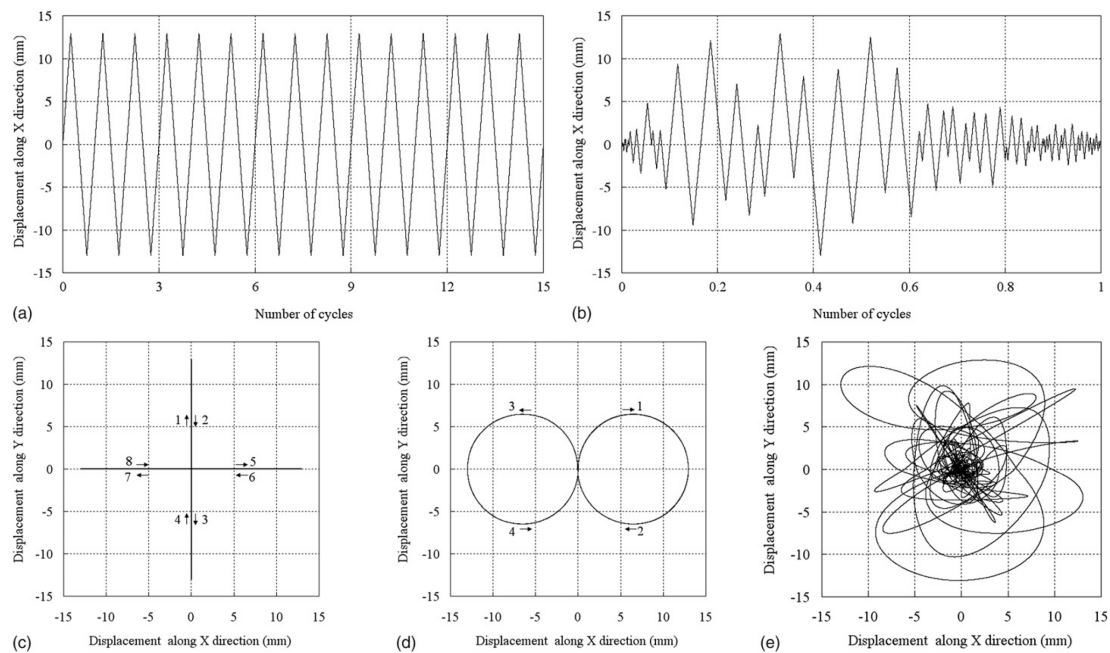
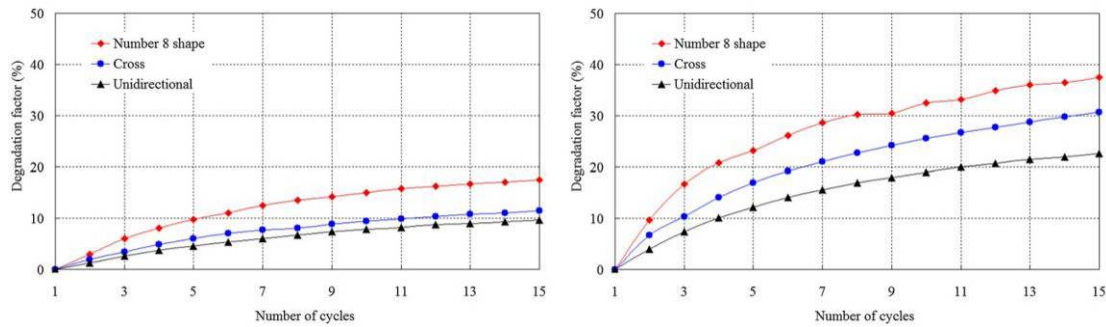


Figure 2.40 Pile Head Displacement (a) Time History of Unidirectional Cyclic Test (b) Time History of Unidirectional Irregular Test (c) Path for Cross Test (d) Path for Eight-Shape Test (e) Path for Multidirectional Irregular Test (Su et al., 2014)

In the unidirectional regular path tests, Su et al. (2014) observed that stiffness degradation was greater with increased displacement amplitude, similar to the observations of Zhang et al. (2011). In the multidirectional regular path tests, Su et al. (2014) noted that the multidirectional cyclic loads caused greater degradation to resistance as compared to unidirectional cyclic loads as shown in Figure 2.41. The degradation factor is defined as $(1 - F_N/F_1) \times 100\%$, where F_1 and F_N is the resistance in the first and N th cycle in the same test. In addition, the eight-shape path causes the greatest degradation to lateral resistance.



(a) 6 mm Displacement Amplitude

(b) 13 mm Displacement Amplitude

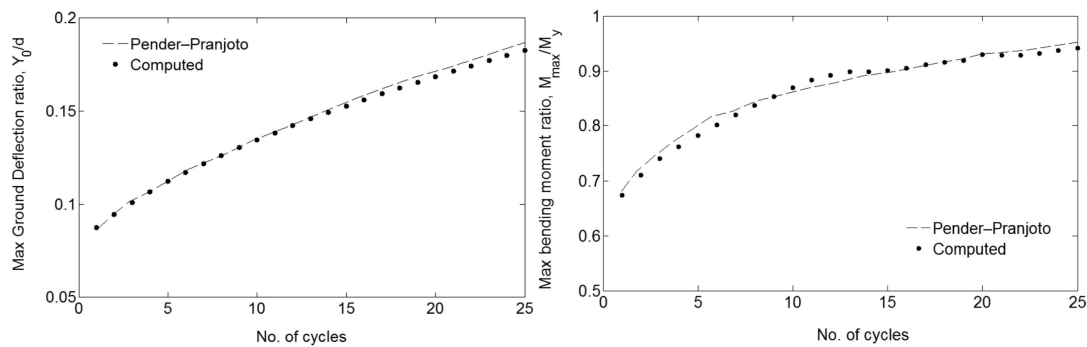
Figure 2.41 Displacement Path Influence on Resistance Degradation (Su et al., 2014)

As shown in Figure 2.41 for both 6 mm and 13 mm displacement amplitude, the degradation factor of the eight-shape path is 80% and 65% greater than the unidirectional path. Finally, it was observed in the unidirectional and multidirectional irregular path tests that the resistance of multidirectional loading is lower than unidirectional loading. Resistance of the multidirectional loading irregular path was 10% and 15% lower relative to the unidirectional irregular path, enforcing the suggestion that multidirectional loading causes greater resistance degradation to unidirectional loading. Based on the findings, Su et al. (2014) recommend that the effects of multidirectional cyclic loads be considered in design.

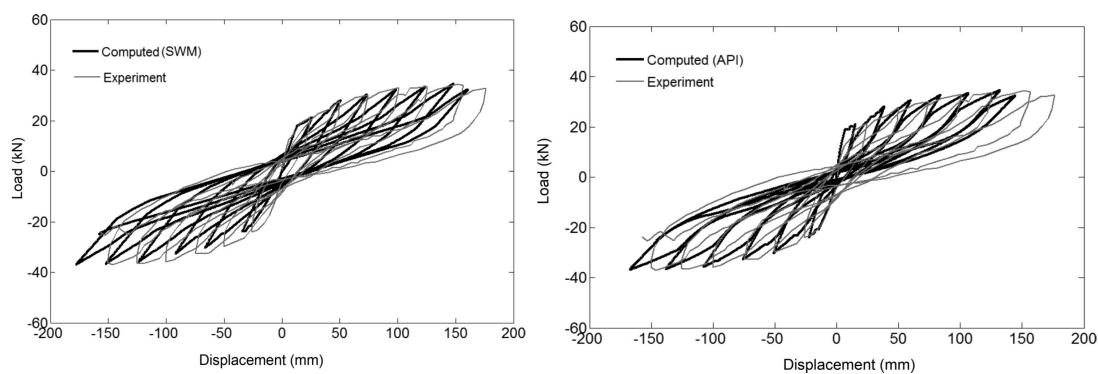
Even though the model tests of Su et al. (2014) fail to model the correct prototype stresses and strains, the findings are similar to the centrifuge tests on monopiles in both loose and dense sand of Rudolph et al. (2014) who observed that direction varied results showed significantly increased deformation accumulation relative to the unidirectional case. This suggests that the findings of Su et al. (2014) may be valid and the effects of multidirectional cyclic loads should be considered in design.

Heidari et al. (2014) utilised the strain wedge method (SWM) to generate non-linear p - y curves which were then implemented as the backbone curve of developed beam on nonlinear Winkler foundation (BNWF) model to account for different response features of the pile-soil system, such as soil and pile nonlinearity, cyclic degradation of soil stiffness and strength, gapping, and radiation damping. To test the validity of the model, the predictions of the model were compared to the two-way cyclic load tests carried out by Pender & Pranjoto (Pender and Pranjoto, 1996, Pranjoto and Pender, 2003) and Tuladhar et al. (2008). Pender-Pranjoto (Pender and Pranjoto, 1996,

Pranjoto and Pender, 2003) studied the response of a 12 m long reinforced concrete pile with diameter of 600 mm, embedded in uniform medium-stiff clay whereas Tuladhar et al. (2008) studied the response of 0.3 m diameter hollow precast prestressed concrete piles embedded 24.8 m deep into medium-stiff clay. The estimates from the model developed match well with the measurements of Pender & Pranjoto (Pender and Pranjoto, 1996, Pranjoto and Pender, 2003) as shown in Figure 2.42 that compares pile deflection at ground surface normalised to diameter, Y_o/d and the maximum bending moment ratio, defined as pile maximum bending moment (M_{max}) normalised by the pile yield moment (M_y). Increasing pile head displacements with the number of cycles is attributed to gap formation.



(a) Maximum Ground Deflection Ratio (b) Maximum Bending Moment Ratio
 Figure 2.42 Comparison between Estimates of Heidari et al. (2014) and Measurements of Pender-Pranjoto (Pender and Pranjoto, 1996, Pranjoto and Pender, 2003)



(a) SWM-based Model (b) API-based Model
 Figure 2.43 Load Displacement Comparison between Estimates of Heidari et al. (2014) and Measurements of Tuladhar et al. (2008) for Different Models

The estimates from the developed model also agree with the measurements of Tuladhar et al. (2008) as shown in Figure 2.43. A comparison between the estimates

from the SWM-based model and the API-based model suggests that the API-based model overestimates the pile-soil stiffness, reinforcing the concern that the p - y curves criterion suggested by Matlock (1970) may produce inaccurate estimates of the initial pile-soil stiffness.

The good agreement between the calculated and measured responses suggests that the model developed based on the SWM may be a reliable tool to predict the cyclic response of piles in cohesive soil. However, application of this model for monopile design may be inappropriate. Firstly, comparisons were carried out on long-flexible piles that were subjected to very few cycles of two-way cyclic loads whereas the monopile is expected to behave as a rigid pile and will be subjected to millions of cyclic loads of different characteristics. Secondly, even though the model is able to account for different response features including gapping, the consideration for gapping may instead produce inaccurate results for monopile design. As highlighted earlier, gaps were not observed in the centrifuge tests of Zhang et al. (2011) who carried out two-way cyclic loading on rigid piles in soft clay. Despite the limitations, the promising results indicate that the model developed based on the SWM can be further improved and could potentially be utilised for monopile design. However, this can only be achieved with data from either field or centrifuge tests.

From the review, there has been a lack of effort in evaluating the long-term effects of cyclic loading on monopiles in clay. In addition, there are barely any physical tests involving monopiles in overconsolidated clay that correctly model the non-linear stress strain behaviour of soil besides Zhang et al. (2011). Considering the lack of effort and the importance of modelling the correct stresses and strains, centrifuge testing appears to be the most practical approach to research the lateral behaviour of monopiles in overconsolidated clays. Since Zhang et al. (2011) carried out displacement-controlled two-way cyclic tests, centrifuge force-controlled cyclic testing on free-head monopiles in clay should be carried out to accurately model the loading conditions experienced in the field. Cyclic loads of various characteristics should be applied to the monopile as Klinkvort and Hededal (2013) reported different responses for cyclic loads of different characteristics. In addition, since Zhang et al. (2011) applied at most 100 cycles, the monopile should be subjected to cycles far greater than 100 to better determine the monopile's long-term cyclic behaviour.

Excess pore pressure measurements were not taken by Zhang et al. (2011). Since excess pore water pressure can affect the response of the monopile, excess pore pressure measurements should be taken to study the excess pore water pressure response throughout the monopile and to determine how it changes as a result of cyclic loading.

The results of Su et al. (2014) highlight the need for centrifuge testing involving multidirectional cyclic loads on monopiles in clay so that the effects on both stiffness and accumulated deformations can be quantified and considered in design. However, since the gap in knowledge is large and little is known about the unidirectional cyclic behaviour of monopiles in clay, centrifuge testing involving unidirectional cyclic loads on monopiles in clay should be carried out prior to multidirectional cyclic loads. This would enable comparisons to be made in the future between multidirectional and unidirectional test results. In addition, unidirectional centrifuge tests should be carried out first as time is required to develop better equipment for multidirectional centrifuge tests. The promising results of Heidari et al. (2014) indicate that the model developed based on the SWM could potentially be utilised for monopile design. Therefore, centrifuge testing on monopiles in clay should be carried out to provide the data necessary to further improve the model so that it may one day be applicable for monopile design.

2.8 Summary and Research Objectives

Monopiles are expected to be heavily utilised as the foundations for future offshore wind turbines. Since most of the planned offshore wind farms in the UK are in the north and central parts of UK, there is a high probability that the monopiles will be founded in overconsolidated clays. Monopiles have to be designed to resist large overturning moments from both wind and wave forces and to maintain its stiffness over its design lifetime to prevent resonance with the driving frequencies of the turbine. Monopiles are designed utilising the p - y method in which the soil is modelled as a series of non-linear springs that are characterised by the p - y curves. The criterion recommended by the DNV (2014) industry standard to construct p - y curves is the soft clay criterion by Matlock (1970). Even though the criterion is well established in the offshore oil and gas industry, issues regarding its suitability to design monopiles have

been raised. These issues include the suitability of the p - y curves derived from field tests on long flexible piles to design short rigid monopiles, the estimation of the initial pile-soil stiffness, and the shortcomings of the p - y curves for cyclic loading design.

A review of literature has indicated that research on monopiles in sand has been carried out by various researchers that involve 3-D F.E. modelling, model laboratory tests, and centrifuge testing. However, research on monopiles in overconsolidated clays is severely lacking. Considering the limitations of the p - y curves to design large diameter monopiles and to account for long-term cyclic loading effects, the lack of research in evaluating the cyclic load effects of monopiles in clay, and the importance of modelling the prototype stresses and strains in physical testing, this research project aims to model, both experimentally and analytically, the behaviour of monopile wind turbine foundations subjected to cyclic loading. The objectives are:

1. To correctly model the nonlinear stress-strain behaviour of soil by conducting centrifuge model tests on monopile.
2. To better understand the lateral behaviour of monopile foundations under monotonic loads.
3. To obtain centrifugal data on the performance of monopile foundations under axial and lateral loading, including a large number of cycles of lateral and moment loading.
4. To confirm the suitability of the Matlock (1970) p - y curves to design monopiles and develop recommendations for improvement.
5. To develop design suggestions and recommendations that addresses the shortcomings of the p - y curves for cyclic design.
6. To understand the long-term performance of monopiles when subjected to a large number of loading cycles of different characteristics.
7. To evaluate the validity and applicability of published research results by comparing with centrifugal data.
8. To optimise and improve current design of monopiles in UK by developing appropriate design guidelines.

CHAPTER 3

3. METHODOLOGY

3.1 Introduction

This chapter provides a description of how the research programme was designed and carried out to address the research objectives of section 2.8. Sections 3.2 and 3.3 cover the research approach, the basis behind the selection of centrifuge modelling to achieve the project objectives, and the principles behind centrifuge modelling. Section 3.4 describes the centrifuge facilities at the University of Cambridge while section 3.5 describes the experimental programme. Section 3.6 provides details regarding the instruments utilised in the experiments. The model preparation and experimental procedure is provided in section 3.7 while section 3.8 describes the triaxial testing equipment and procedure carried out as part of the experimental programme.

3.2 Research Approach

As mentioned in chapter 2, there is a lack of research in evaluating the effects of cyclic loads on monopiles in clay and a lack of physical validation of published research results. Full-scale physical validation is unfeasible due to the extreme cost and physical difficulties resulting from both the extreme sizes of the monopiles and the harsh environmental conditions offshore. As a result, small-scale model testing is the most feasible physical approach to experimentally and analytically study the cyclic behaviour of monopiles in clay.

To better replicate the soil-pile interaction and generation of pore pressure when the monopile is laterally loaded, it is crucial that the non-linear stress-strain behaviour of soil be correctly replicated by the model. Figure 3.1 adapted from Madabhushi (2014) illustrates the difference in soil behaviour at low and high confining stresses for both dense and loose sand. The stress-strain curve of dense sand reaches a peak stress, after which the dense sand will experience strain softening before reaching critical state at large strains. The stress-strain curve is smooth until it reaches critical state at large

strains. At low stresses and strains, the initial stiffness for both dense and loose sand is high. At large stresses and strains, the stiffness reduces. At very large stresses and strains close to critical state, the stiffness drops considerably to small values.

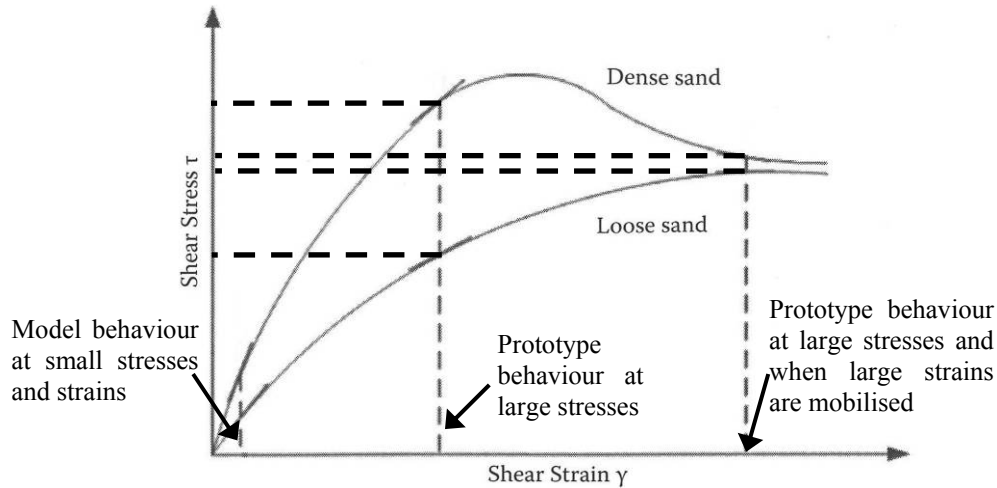


Figure 3.1 Soil Behaviour Difference between Model and Prototype (adapted from Madabhushi, 2014)

A scaled down laboratory model only exerts a small fraction of the stresses exerted by a prototype ‘ N_s ’ times bigger. As a result, the soil will respond with large stiffness and the observed deformation such as settlement will be small. However, the large prototype structure will exert larger stresses for the same soil, resulting in the soil responding with a lower stiffness and in turn producing much larger deformations. Therefore, any form of model testing that fails to model the stress-strain behaviour of the prototype will produce invalid results. To address this, centrifuge modelling was utilised to create prototype stresses and strains in the small-scale model.

3.3 Principles of Centrifuge Modelling

According to Madabhushi (2014), centrifuge modelling involves the testing of a $1/N_s$ scale model of a prototype in an enhanced gravity field of a geotechnical centrifuge. The gravity is increased by the same geometrical factor ‘ N_s ’ relative to earth’s gravity field of 1 g. This is illustrated in Figure 3.2. A block structure of mass M with dimensions $L \times B \times H$ on a horizontal soil bed exerts vertical stresses as follows:

$$\sigma_v = \frac{M g}{L \times B} \quad (3.1)$$

Similarly, the vertical strain induced in the soil for a characteristic length α as:

$$\varepsilon = \frac{\delta\alpha}{\alpha} \quad (3.2)$$

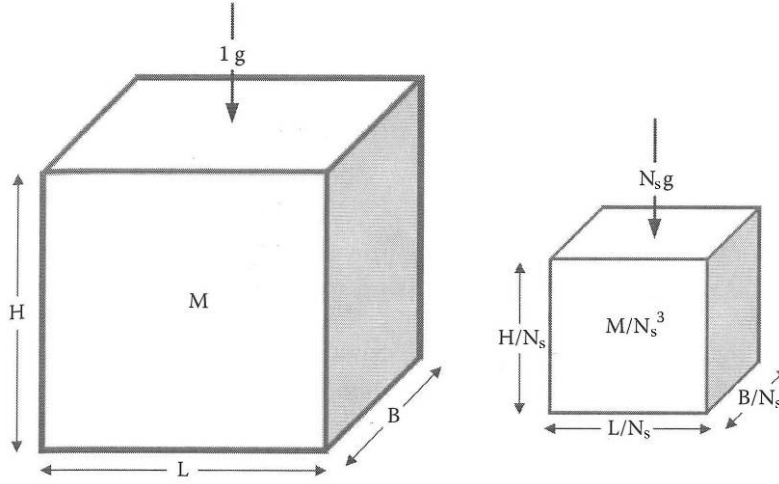


Figure 3.2 Principle of Centrifuge Modelling (adapted from Madabhushi, 2014)

In a scale model of the block, all dimensions are scaled down by a factor of N_s as shown in Figure 3.2. As all dimensions are scaled by a factor of N_s , the mass of the scaled down block will be M / N_s^3 . When the scale model of the block is placed in an increased gravity field of N_s x earth's gravity, the vertical stress underneath the scale model of the block changes as follows:

$$\sigma_v = \frac{\frac{M}{N_s^3} \times N_s g}{\frac{L}{N_s} \times \frac{B}{N_s}} = \frac{M g}{L \times B} \quad (3.3)$$

As a result, the vertical stress below the scale model of the block is the same as that below the larger block of equation (3.1). Similarly, the strains in the scale model in the increased gravity field are:

$$\varepsilon = \frac{\frac{\delta\alpha}{N_s}}{\frac{\alpha}{N_s}} = \frac{\delta\alpha}{\alpha} \quad (3.4)$$

Therefore, the prototype strain of Equation (3.2) is modelled accurately as changes in displacements and the original length are both scaled by N_s .

The two-way relationships between the parameters of the centrifuge prototype and the centrifuge model are defined by scaling laws. These laws were derived from the dimensional analysis by Schofield (1980) and Schofield (1981). The relevant laws for this research are given in Table 3.1.

Parameters	Model / Prototype
Mass	$1/N_s^3$
Length	$1/N_s$
Stress	1
Strain	1
Force	$1/N_s^2$
Bending moment	$1/N_s^3$
Soil reaction	$1/N_s$
Time (consolidation)	$1/N_s^2$
Time (dynamic)	$1/N_s$
Frequency	N_s

Table 3.1 Scaling Laws relevant to Centrifuge Modelling of Monopile

In centrifuge modelling, while the prototype is scaled down, the soil is not. This is because the soil is considered as a continuum and changing the soil medium would change its constitutive behaviour. Should the effect to be analysed approach the soil particle size, the continuum approach breaks down and destroys the validity of centrifuge modelling. In the centrifuge experiments carried out by Ovesen (1979), deviations were observed from common results when the foundation diameter to grain size ratio was less than about 15. Considering that clay has particle sizes less than $2 \mu\text{m}$, the foundation diameter to grain size ratio is well above 15. Therefore, the continuum approach holds true and renders particle size effects negligible.

3.4 Centrifuge Facilities at University of Cambridge

This section explains the centrifuge facilities of the University of Cambridge that were utilised to research the lateral behaviour of monopiles in overconsolidated clay.

3.4.1 Turner Beam Centrifuge at Schofield Centre

To produce the same stresses and strains experienced by the prototype, the gravity field of the scaled down model had to be increased by a factor of N_s . This was achieved by the usage of the Turner Beam Centrifuge as shown in Figure 3.3 that applied centrifugal acceleration to create an ' $N_s \times g$ ' environment. The design of the beam centrifuge and a full description of the facility can be found in Schofield (1980). The 10 m diameter centrifuge rotates around a central vertical axis with a working radius of 4.125 m. The payload capacity is 1 ton at an operational g level of 150 times of earth's gravity. Therefore, it is classified as a 150 g-ton machine. According to Madabhushi (2014), the centrifuge is "powered by a 260-kW, three-phase electric motor that is coupled to the beam centrifuge through a magnetic coupling and a bevelled gear box that drives a vertical shaft passing through the centre of the beam". Adjustment of the field strength on the magnetic coupling enables the speed to be controlled.



Figure 3.3 Turner Beam Centrifuge at Cambridge (Madabhushi, 2014)

3.4.2 2D-Actuator

To install the monopile foundation in-flight and subject it simultaneously to axial, cyclic lateral and moment loading, the computer-controlled two-axis servo actuator developed at the University of Cambridge was utilised. Further details regarding the design principles of the 2D-actuator can be found in Haigh et al. (2010). Table 3.2 displays the performance specification of the 2D-actuator.

Axis	X (horizontal)	Y (vertical)
Stroke (mm)	500	500
Max Speed (mm/s)	5	5
Min. Speed (mm/s)	0.005	0.005
Accuracy (mm)	±0.005	±0.005
Load Capacity (N)	±10,000	±10,000

Table 3.2 Performance Specification of 2D-Actuator (Haigh et al., 2010)

The actuator has external dimensions of 880 mm length, 530 mm width and 1100 mm height. It has been designed to withstand 100g of centrifugal acceleration and can apply a maximum vertical and horizontal load of 10 kN. In a 100g centrifuge test, these forces represent 100 MN. The actuator can be either force controlled or displacement controlled. It can apply cyclic loads in both vertical and horizontal directions, enabling the application of many cycles of fixed force amplitude (or fixed displacement amplitude) in the horizontal direction, while applying a constant vertical load. The cyclic loads can also be applied at varying rates as the actuator has a minimum speed of 0.005 mm/s and a maximum speed of 5 mm/s.

To achieve precise position control within a 100g gravity field, a stiff loading frame was manufactured with motion being achieved using ball screws turned by DC servomotors. Servomotors are controlled using NDrive HL servo amplifiers manufactured by Aerotech, which can be controlled with A3200 multi-axis motion control software. A/D converters integrated into the servo amplifiers enabled load-cell readings to be fed back into the system. This made it possible to implement a force-controlled cyclic load-control scheme to cyclically load the monopile.

3.4.3 Data Acquisition

Data acquisition on the Turner beam centrifuge was achieved by utilising the DasyLab (2004) software suite. The data acquisition card has 64 independent input channels, two analogue outputs and four digital outputs. All inputs and outputs are accessible using the DasyLab software suite.

3.5 Experimental Programme

Nine centrifuge tests were carried out to investigate the lateral behaviour of monopiles in clay and layered soils. A summary of these tests is provided in Table 3.3.

Phase	Test number	Test Nature	Pile diameter (m)	Vertical Load (MN)	Site Specification
I	OWF 01	Monotonic	3.83	6.5	B
	OWF 02			6.5	A
	OWF 03			4.0	C
II	OWF 04	Cyclic		4.0	C
	OWF 05			6.5	B
	OWF 06			6.1	A
	OWF 07			6.0	D
	OWF 08			6.1	E
III	OWF 09			7.62	12.0

Table 3.3 Experimental Programme in Prototype Scale

Displacement controlled monotonic tests were carried out in Phase I to provide the upper bound on ultimate lateral resistance and provided the correct backbone curve for lateral loading. In Phase II and III, load controlled cyclic tests were carried out on 3.83 m and 7.62 m diameter monopiles to investigate the monopile's cyclic behaviour. The tests were carried out using the 2D-actuator in an 850 mm diameter tub at 100g with the exception to OWF 04 that utilised a piezo-actuator that vibrated the pile at high frequencies. Data from OWF 04 was not considered as there were issues regarding the implementation of the piezo-actuator as a loading device. In addition, OWF 05 was not considered as issues due to the 2D-actuator undermined the integrity of the results. Therefore, OWF 04 and OWF 05 will not be discussed in the dissertation.

Site	Layer 1		Layer 2	
	Depth a (m)	Consolidation Pressure (kPa)	Depth b (m)	Consolidation Pressure (kPa)
A	13.5	500	13.5	500
B	13.5	300	13.5	300
C	13.5	180	13.5	180
D	5	180	22	500
E	10	180	17	500

Table 3.4 Site Specifications

Five different site conditions used in the test series are categorised in Table 3.4. Sites A to C consist of layers of clay pre-consolidated to their respective overburden pressures whereas sites D and E consist of a top soft layer underlain by a stiffer layer. To achieve the desired undrained shear strength and to simulate over-consolidated clay conditions found at depth in the North Sea (Bond et al., 1997), the clay was pre-

consolidated to behave as an over-consolidated clay in the centrifuge. As this project was a collaboration with industry, these tests were developed following an initial meeting with industrial collaborators on 15th August 2007 and subsequent email and telephone conference exchanges. Following this meeting, borehole logs and other site information from several offshore sites including Gunfleet, Ormonde, Westermost Rought, Walney, Barrow along the coast of UK and Ireland and some onshore sites such as London Array were investigated. The soil strata that were tested in the centrifuge as in Table 3.4 are simplified forms of real site conditions obtained from borehole logs and strength profiles.

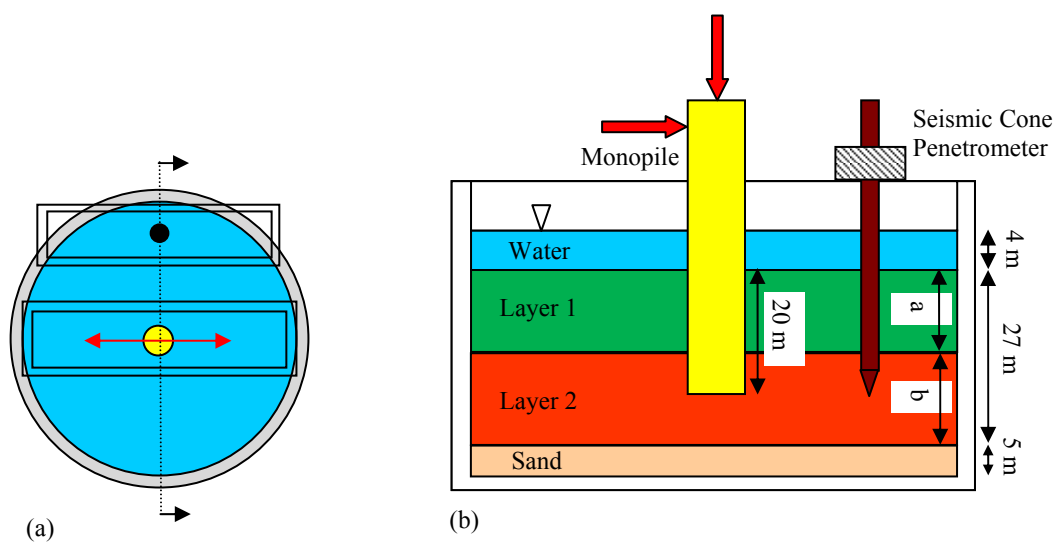


Figure 3.4 Schematic of Experiment Setup, Not to Scale (a) Plan View of the 850 mm Tub with Location of Monopile and CPT (b) Cross Section of Setup

The embedded prototype depth and total length of the monopile were 20 m and 52 m respectively in all tests. Lateral loading was at a prototype height of 30 m above the mudline. Both vertical load magnitude and height of lateral loading are similar to the values expected by Byrne and Houlsby (2003) for a 3.5 MW turbine. The vertical load magnitude of OWF 09 was doubled to 12.0 MN as it was assumed that the vertical load could potentially double for a monopile twice as large. Water at a height of approximately 40 mm was provided above the clay surface to simulate oceanic conditions in which the soil would be saturated throughout the experiment. As shown in Figure 3.4, the soil strength was measured using an in-flight miniature seismic cone penetrometer (henceforth referred to as SCPT), mounted on a separate gantry sufficiently far away from the monopile location so as not to influence the monopile behaviour. Prior to the development of the SCPT, a T-bar was utilised.

3.6 Experiment Instrumentation

Figures 3.5 to 3.6 show the instrumentation plan and experimental setup. The equipment and instruments utilised are as follows and will be described in the subsequent sections:

- Pore pressure transducers (henceforth referred to as PPTs)
- Lasers and microelectromechanical accelerometers (henceforth referred to as MEMS)
- Linearly Variable Differential Transformer (henceforth referred to as LVDT)
- T-bar
- Seismic Cone Penetrometer (referred to as SCPT)
- Strain-gauged monopile
- Vertical-Horizontal Load Cell (henceforth referred to as V-H Load Cell)
- Web Cameras

Experiment OWF 01 was repeated twice as the first run of OWF 01 did not involve use of a counterweight system. As a result, the pile sank into the soil as the total vertical load exceeded the pile's vertical capacity. In the first run of OWF 01, the T-bar was utilised but in the second run of OWF 01 that involved use of the counterweight, the SCPT was utilised to measure undrained shear strength, s_u .

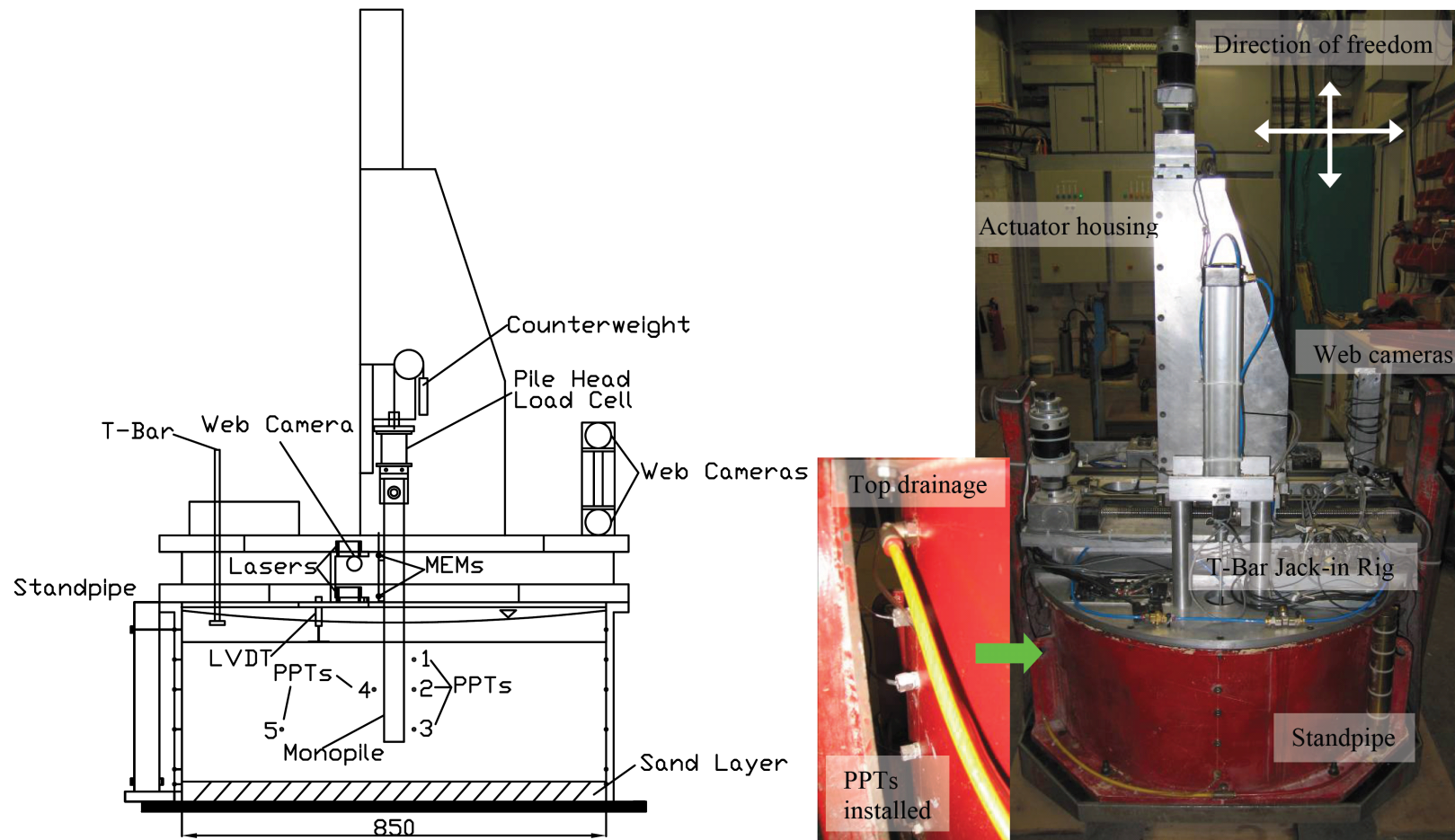


Figure 3.5 (a) Instrumentation Plan (b) Experimental Setup for Experiments OWF 01 (First Run with No Counterweight) to OWF 03

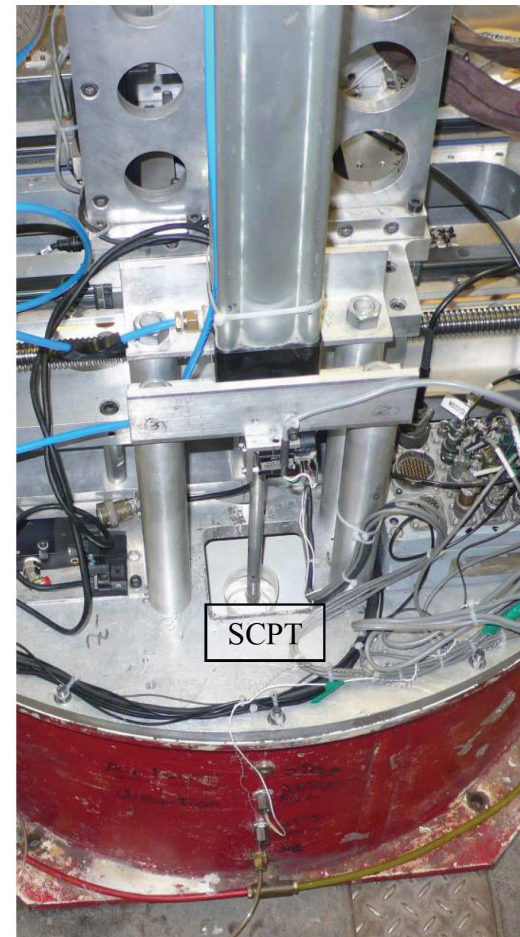
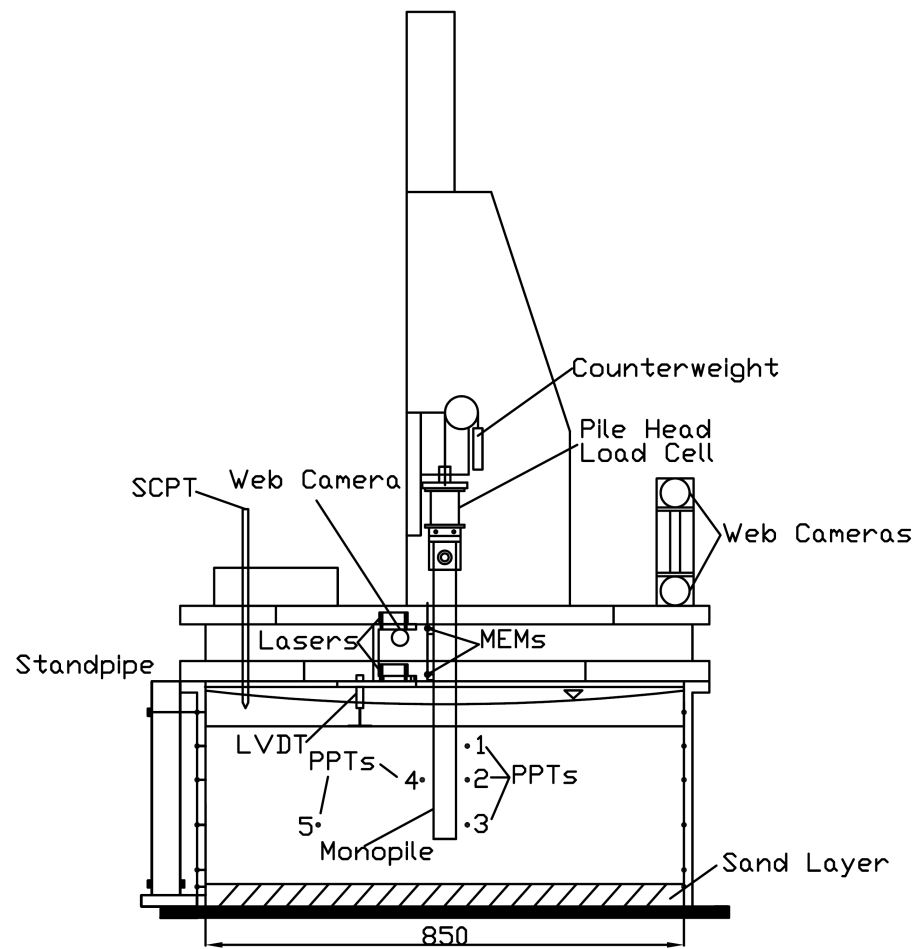


Figure 3.6 (a) Instrumentation Plan (b) SCPT Setup for Experiments OWF 01 (Second Run) and OWF 05 to 09

3.6.1 PPTs

As shown in Figures 3.5 to 3.6 (a), five PPTs were installed in the model to measure rapidly varying positive and negative pore pressures. Four PPTs were installed half-a-pile diameter away from the monopile to measure excess pore pressure generation during lateral loading of the monopile. The PPTs also serve to gauge the percentage of consolidation during the experiment by measuring the dissipation of excess pore pressure. The PPTs used in the experiment are 7-bar GE Druck miniature PDCR-81.

Ceramic stones were fitted in front of the diaphragm for protection from clay particles. Prior to installation, the PPTs were de-aired and submerged under highly pressurised de-aired water, (at pressure of 80% of the PPT capacity), multiple times in a pre-pressurisation apparatus to ensure complete saturation of the ceramic stones. This ensured quick response of the PPT to pore pressure changes and ensured accuracy of the pore pressure readings as pressure hysteresis is avoided (Take and Bolton, 2003).

3.6.2 Lasers and MEMS Accelerometers



Figure 3.7 Laser and MEMS behind Monopile

As shown in Figures 3.5 to Figure 3.6 (a) and Figure 3.7, Baumer close-range distance sensor lasers and Analog Devices MEMS were placed behind the monopile at separate elevations above the soil surface to measure both horizontal displacement and rotation of the monopile (by measuring g-field inclination) respectively. Utilising both laser sensors and MEMS and the assumption that the bending is negligible, the

rotation point of the monopile can be determined. Flat reflective plates were glued to the back of the monopile with Araldite to ensure that the laser light hits a flat surface, reducing error in the displacement readings.

Details of the lasers utilised in experiments are given in Table 3.5. The MEMs utilised in the experiments are the ADXL193 and ADXL78 MEMs with a capacity of 120g and 35g respectively. Both MEMs have a non-linearity of 0.2%. In the cyclic experiments, the ADXL78 MEM was predominantly used due to its greater sensitivity relative to the ADXL193. To improve its sensitivity to detect small accumulated rotations, the voltage of the ADXL78 MEM (with a 35g capacity) was offset to zero and amplified with a gain of 10.

Distance Sensor Code	Measuring Distance (mm)	Resolution (mm)	Linearity Error (mm)
OADM 1216430/S35A	16 – 26	0.002 – 0.005	± 0.006 to ± 0.015
OADM 2014440/S14C	30 – 50	< 0.01	± 0.03
OADM 2014460/S14C	30 – 130	0.05 – 0.07	± 0.15 to ± 0.22

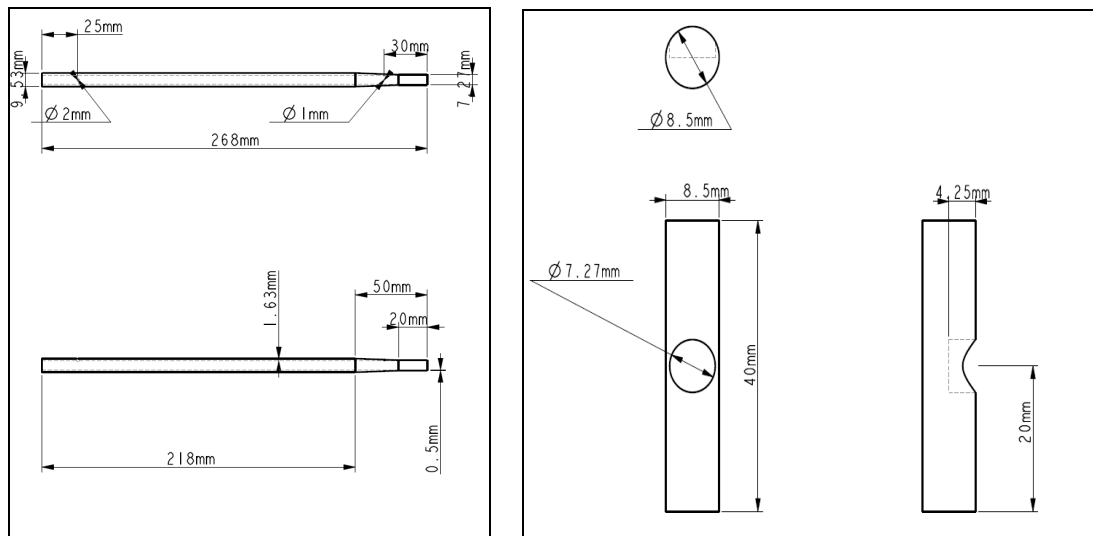
Table 3.5 Details of Distance Sensor Lasers Utilised

3.6.3 LVDT

The Solartron M922943A 241-18 DC 25 LVDT (with a maximum stroke length of 35 mm) was utilised to monitor the degree of consolidation of the clay during spin-up and to estimate the soil surface elevation at pushover. The LVDT was placed behind the laser platform as shown in Figures 3.5 to Figure 3.6 (a) and connected to a 4 mm diameter 1 mm thick plate to minimise pressure exerted on the soil during spin-up.

3.6.4 T-bar

The T-bar is a bar penetrometer that was used in experiments OWF 01 (first run) to OWF 03 to measure a continuous profile of s_u in the centrifuge as shown in Figure 3.8. When pushed into the soil, the penetration resistance is measured by a highly sensitive load cell situated immediately behind the bar. The penetration resistance is interpreted by making use of the plasticity solution for the limiting pressure acting on the cylinder moving laterally through cohesive soil (Randolph and Houlsby, 1984).



(a)

(b)



(c)

Figure 3.8 T-bar (a) Column Section (b) Cylindrical Section (c) Fully Assembled

The analysis assumes that the soil is able to flow around the cylinder from the front to the back without forming a gap, leading to a very localised plastic mechanism (Chung and Randolph, 2004). Based on the plasticity solution, s_u can be calculated utilising the following equation,

$$s_u = \frac{P}{N_b d} \quad (3.5)$$

where,

P	Force per unit length acting on the cylinder
d	Diameter of the cylinder
N_b	Bar factor with a value of 10.5 (Stewart and Randolph, 1991)

As shown in Figure 3.8(a), the strain-gauged section has a wall thickness of 0.5 mm to ensure the device was sensitive enough to detect strains resulting from a push-in into clay with an s_u of 25 kPa. In addition, the tube shaft was designed to resist buckling when tested in clays of 100 kPa strength. The cylindrical section was designed to have a length to diameter ratio (also known as the aspect ratio) of 4.75 as shown in Figure 3.8(b). Chung and Randolph (2004) studied the difference in measured resistance on T-bars with different aspect ratios and determined that the aspect ratio did not have an obvious effect on T-bar resistance, at least for aspect ratios from 4 to 10. Since Chung and Randolph (2004) concluded that T-bars with aspect ratios ranging from 4 to 8 would be suitable, the measured T-bar resistance should not be affected by aspect ratio effects.

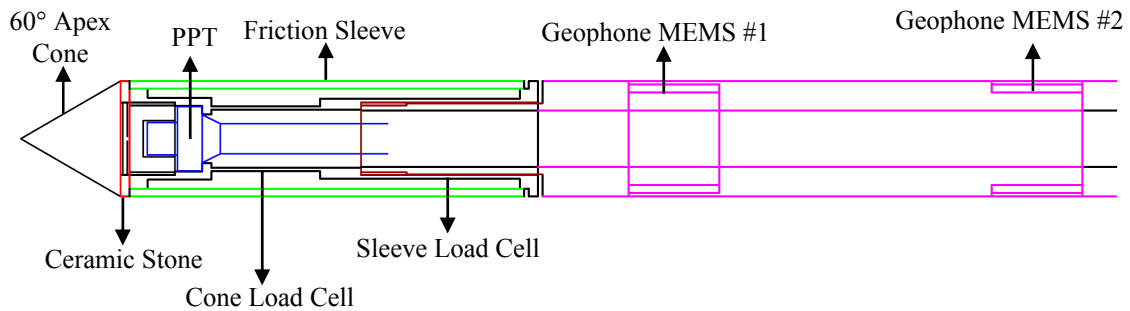
3.6.5 Seismic Cone Penetrometer

An SCPT was developed to measure undrained shear strength profile, s_u and small strain shear modulus, G_o of the soil simultaneously. However, the stiffness measuring feature of the SCPT was not utilised in the experiments. As shown in Figure 3.9(a), the SCPT was designed as a compression cone (Brouwer, 2007) to prevent strain resulting from cone compression and sleeve tension from influencing each other, resulting in greater accuracy of strain measurements. Strains on both cone and sleeve were measured by TML FCA-1-23 strain gauges that were arranged in a full Wheatstone bridge with consideration of temperature compensation. Two Analog Devices ADXL 001 MEMS were utilised as geophone MEMs in the SCPT. The full assembly of the SCPT is depicted in Figure 3.9(b).

The ceramic stone made out of Macor glass ceramic prevented clay particles from entering the PPT chamber. The PPT utilised is an Entran EPB C12-7B pressure transducer with a 7 bar capacity. The ceramic stone (i.e. the filter) and the PPT are placed behind the cone because (Lunne et al 1997)

- The filter is much less prone to damage and wear;

- Measurements are less influenced by element compressibility;
- Pore pressures measured can be used directly to correct cone resistance; and
- Measured pore pressures during a dissipation test are less influenced by procedure.



(a)



(b)

(c)

Figure 3.9 Seismic Cone Penetrometer (a) Design Details (b) Assembly (c) SCPT Head Submerged in Silicone Fluid

To ensure quick response of the PPT to pore pressure changes, the ceramic stone was saturated in Dow Corning 200 Silicone Fluid (viscosity of 50 centistokes) under vacuum conditions. Once the ceramic stone was saturated, silicone fluid was injected into the PPT chamber, followed with the installation of the ceramic stone. The SCPT head was submerged in a cup of silicone fluid before spin-up to maintain full saturation of the ceramic stone as in Figure 3.9(c).

The SCPT was pushed into the soil at an average velocity of 7.5 mm/s by setting an air pressure of 20 kPa while the valve on the jack-in-rig was locked to a small opening. This velocity is greater than velocity utilised in the cone penetrometer tests by Stewart

and Randolph (1991) of 3 mm/s into normally consolidated clay. The undrained shear strength, s_u was calculated by utilising a modification of the total cone resistance method (Lunne et al., 1997) that corrects cone resistance for pore pressure effects as follows:

$$s_u = \frac{q_t - \sigma_{vo}}{N_{kt}} \quad (3.6)$$

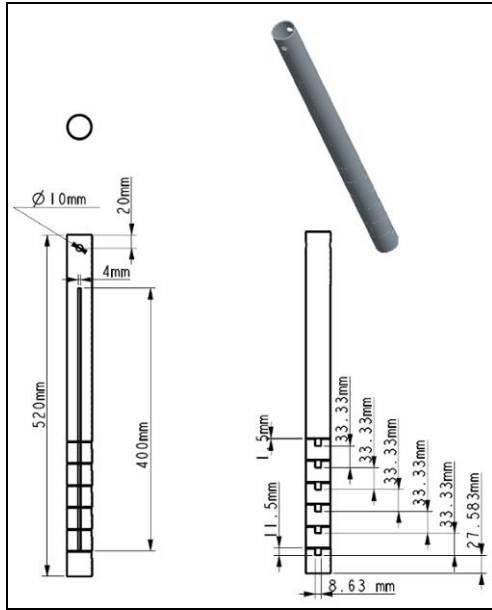
where,

- q_t Corrected total cone resistance; in which $q_t = q_c + u_2 (1 - a)$, where q_c is cone resistance, u_2 is pore pressure acting behind the cone, and a is cone area ratio
- σ_{vo} Total in-situ vertical stress
- N_{kt} Cone Factor; with a Plasticity Index of 31 (Clegg, 1981), a cone factor of 12 was calculated from the correlation by Aas et al. (1986).

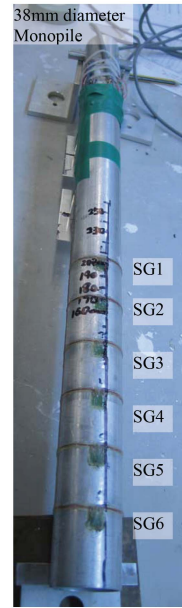
3.6.6 Strain-gauged Monopile, V-H Load Cell, and Pile Assembly

The monopile utilised in experiments OWF 01 to OWF 08 is a 38.3 mm diameter aluminium tube with a wall thickness of approximately 1.67 mm. In prototype scale, the bending stiffness, $E_p I_p$ is 222.4 GN m². As shown in Figure 3.10(a), a 10 mm hole is drilled 20 mm below the top of the tube. A steel pin is placed through the hole and acts as a hinged connection where horizontal load is applied to the monopile. The bending strain of the monopile is registered by twelve TML Tokyo Sokki Kenkyujo Co., Ltd. (henceforth referred to as TML) FLA-2-350-2H-23 strain gauges arranged in full bending moment bridges so as to be temperature compensated.

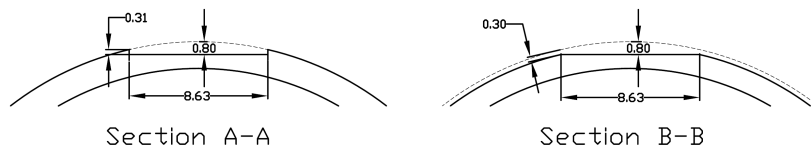
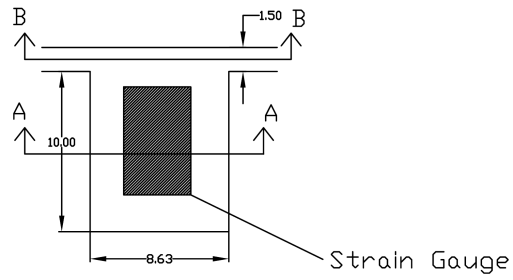
Recesses in Section A-A of Figure 3.10(c) were made on both sides of the monopile to protect the strain gauges from damage resulting from exposure to downward drag forces from the surrounding clay. Recesses as shown in Section D-D of Figure 3.10(d) were also made around the monopile to allow placement of the wires. Section C-C is the cross section of the vertical recess (as in Figure 3.10(a)) allowing placement of the wires to the top of the monopile. As shown in Figure 3.10(b), after installation of the strain gauges, ten thin layers of epoxy were applied onto the strain gauges and wires to provide protection against both water and downward drag forces.



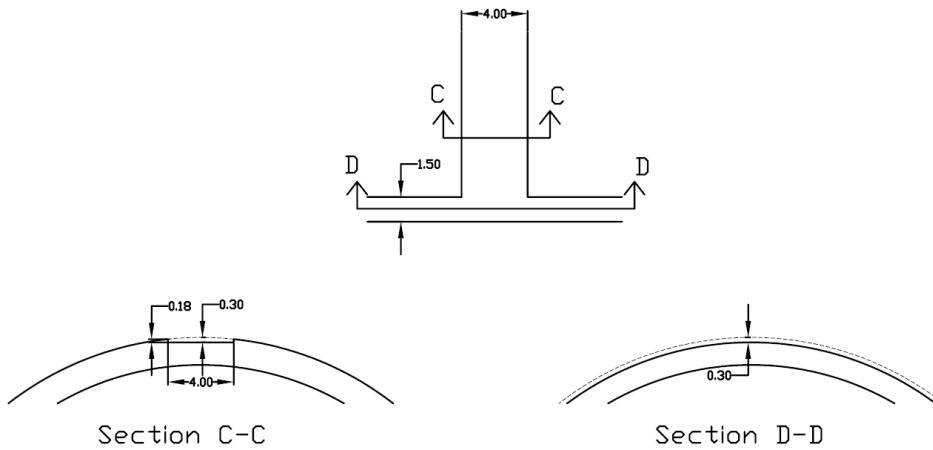
(a) Design Drawing



(b) Epoxy Coated



(c) Monopile Strain-gauge Recess Cross-Section (units in mm)



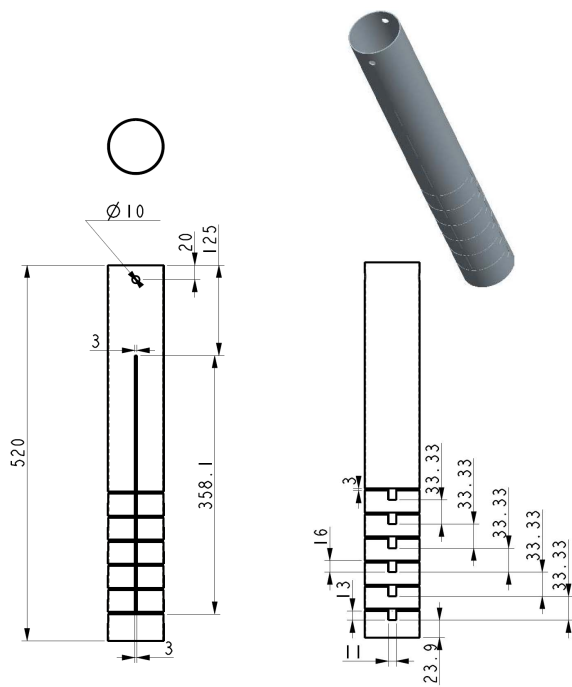
(d) Wire Recess Cross-Section (units in mm)

Figure 3.10 38.3 mm Diameter Monopile

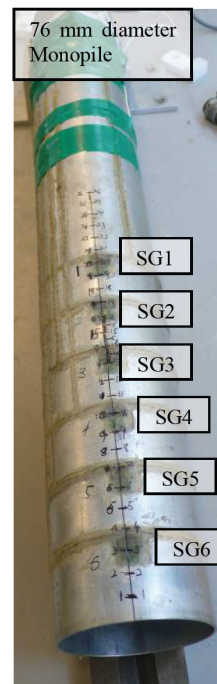
In OWF 09, a 76.2 mm diameter aluminium tube with a wall thickness of 1.67 mm was utilised as shown in Figure 3.11(a). In prototype scale, the bending stiffness, $E_p I_p$ is 1,901 GN m². Though 8.5 times stiffer in bending than the 38.3 mm diameter monopile, the same FLA-2-350-2H-23 strain gauges were utilised. This was because alternative strain gauges with greater sensitivity produced a high heat output that did not permit temperature compensation under full bridge connections. After experiment OWF 05, the strain gauges on the 38.3 mm diameter monopile were damaged due to water leakage. As a result, a new waterproofing method (that involved placing TML W-1 microcrystalline wax solid onto the strain gauges and wires followed with ten thin layers of epoxy) was tested in OWF 09.

Six recesses were cut along the aluminium tube to allow separate placement of the strain gauge wires. This was done to prevent damage to functional strain gauges when repair works were carried out on the damaged strain gauges. Dimensions of the recesses for the strain gauges and for the wires running up along the 76.2 mm tube are shown in Figures 3.11(c) and Figure 3.11(d) respectively.

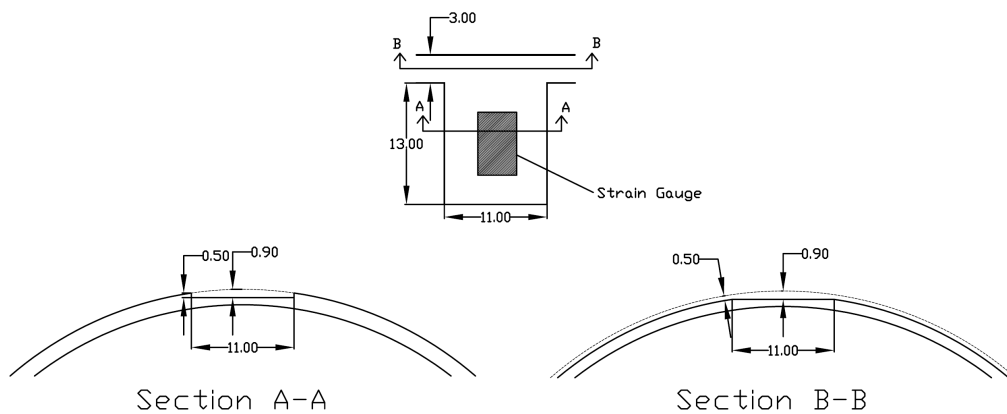
The pile head vertical and horizontal load condition in experiments OWF 01 to OWF 03 was captured by a cylindrical V-H load cell that was placed directly above the hinged connection as can be seen in Figure 3.12. In experiments OWF 05 to OWF 09, a smaller yet more sensitive H load cell was utilised as this enabled the 2D-actuator to carry out force controlled loading for small load magnitudes with greater accuracy. In Figure 3.12, a linear ball bearing and a vertical shaft are employed to achieve a vertical slider connection, so that the loading mechanism could accommodate the vertical settlement of the pile during the push-over. Shoulder bolts were employed to support the monopile from sinking during the early stages of consolidation as the soil would not have gained enough strength to support the vertical load from above. The counter-weight system that consists of an adjustable mass and a pulley system maintained the vertical load condition. It should be noted that the counterweight system was not utilised in OWF 09 as the vertical load of the assembly excluding the counterweight system was equal to the desired vertical load condition.



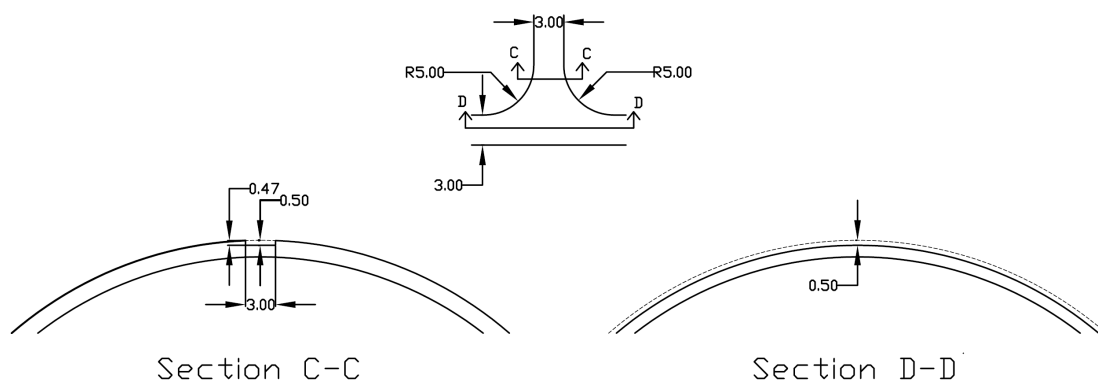
(a) Design Drawing



(b) Epoxy Coated



(c) Strain-gauge Recess Cross-Section (units in mm)



(d) Wire Recess Cross-Section (units in mm)

Figure 3.11 76.2 mm Diameter Monopile

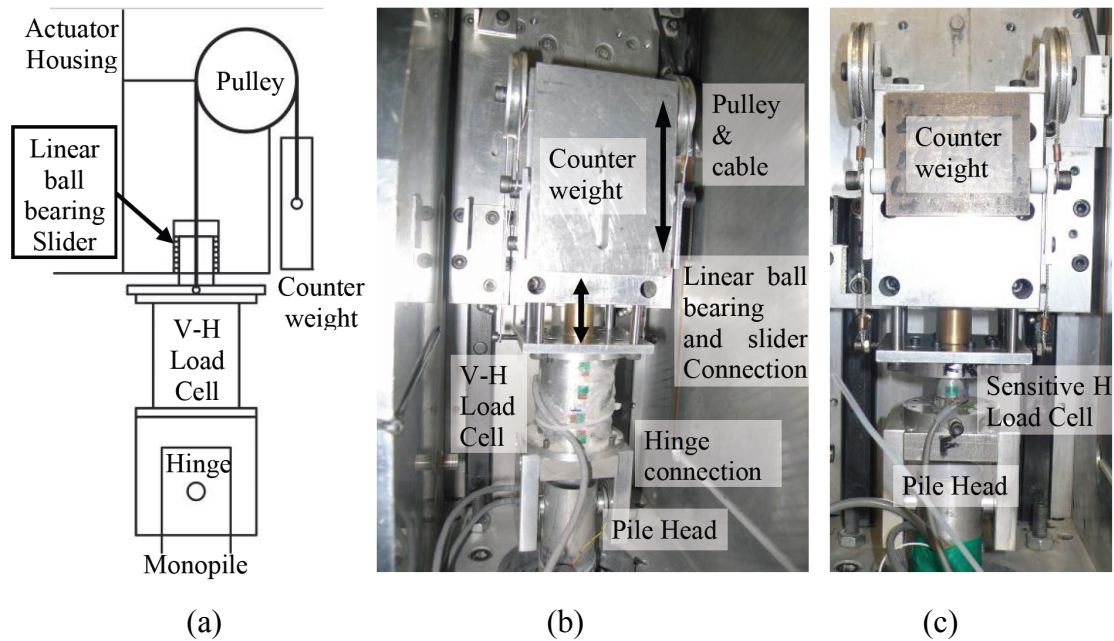


Figure 3.12 Top of Pile Assembly (a) General Assembly Schematic (b) OWF 02 and OWF 03 Assembly (c) OWF 05 to OWF 08 Assembly

3.6.7 Web Cameras

As shown in Figures 3.5 to Figure 3.6, three Logitech web cameras were utilised. Two were placed in front of the actuator at separate elevations to allow visual monitoring and recording of the slider connection above the monopile and of the monopile at the soil surface. The remaining web camera was placed behind the monopile (i.e. with the laser platform) to monitor and record soil deformation during lateral loading of the monopile. Photos were taken every 30 minutes and videos were recorded during the installation and lateral loading phases of the centrifuge test.

3.7 Model Preparation & Experimental Procedure

As described in section 3.5, nine experiments were carried out to investigate the lateral behaviour of monopiles under both monotonic and cyclic loadings in different overconsolidated clay profiles. The processes involved in carrying out each experiment can be categorised in the following order: soil preparation, installation of PPTs into the tub, model making and finally centrifuge testing. Each process will be discussed in the subsequent sections followed with the problems encountered in each experiment.

3.7.1 Soil Preparation

To provide for drainage beneath the clay, a 50 mm thick base layer of Fraction B or Hostun sand with a relative density of 70% was formed by mechanical vibration. Fraction B sand has a specific gravity, minimum void ratio, and maximum void ratio of 2.65, 0.52, and 0.79 respectively. It also has a diameter range from 0.6 mm to 1.1 mm (Cabalar et al 2010). On the other hand, Hostun sand has a specific gravity, minimum void ratio, maximum void ratio of 2.65, 0.555, and 1.041. Particle sizes range from 0.2 mm to 0.6 mm (Mitrani, 2006). The clay that was selected to be used is laboratory grade speswhite kaolin, as used in previous studies at Cambridge such as Williamson (2014) who studied the tunnelling effects of bored piles in clay, Lam (2010) who studied ground movements due to excavation in clay, and Take (2003) who studied the influence of seasonal moisture cycles on clay slopes. The properties of speswhite kaolin are shown in Table 3.6. Figure 3.13 summarises the sample preparation procedure.

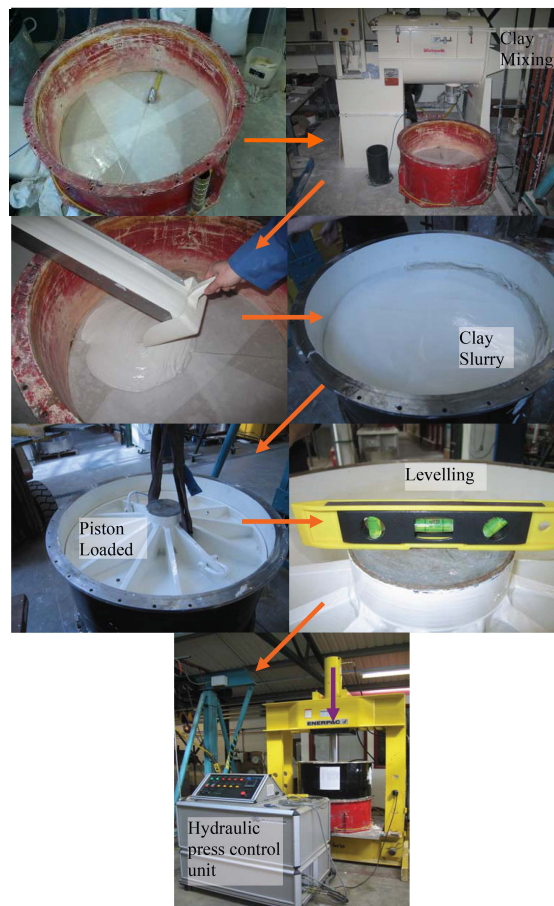


Figure 3.13 Sample Preparation Procedure

The clay was first mixed with de-aired water to about twice the liquid limit (120%) under vacuum for at least two hours. Prior to the placement of the clay slurry, the inner surface of the test container was coated with silicone grease to minimise friction against the clay. Clay slurry was then carefully placed on the drainage layer, covered by a thin layer of filter material. The final height of the slurry was 630 mm. The tub was then placed in a computer-controlled hydraulic press to be consolidated incrementally in order to achieve the desired undrained shear strength. Layered models were created by consolidating the stiff base layer before adding further slurry and consolidating at a lower stress to form the softer surficial deposit.

To achieve the objective of studying the soil-pile interaction at the desired undrained shear strength and to simulate the overconsolidated clay conditions found at depth in the North Sea (Bond et al., 1997), the clay is preconsolidated to an appropriate stress level to behave as overconsolidated clay in the centrifuge. Estimation of the preconsolidation stress is carried out utilising the Modified Cam-Clay model (Roscoe and Burland, 1968) based on critical state soil mechanics. Based on Table 3.6, the critical state parameters such as M_{CSL} , κ , λ , and Γ for speswhite kaolin clay can vary quite significantly. In the work described here, values reported in Table 3.7 that were determined from the consolidometer and triaxial measurements carried out as part of this research were used. Details of the triaxial testing are described in section 3.8. Specific gravity was obtained from the supplier, IMERYS (2008).

	Material Properties	Clegg (1981)	Airey (1984)	Elmes (1985)	Fannin (1986)	Al-Tabba (1987)	Phillips (1981)	Smith (1993)
PL	Moisture content at plastic limit (%)	38	38	-	-	-	31	-
LL	Moisture content at liquid limit (%)	69	69	-	-	-	64	-
G_s	Specific gravity	2.61	2.61	2.61	-	-	-	-
c_v	Coefficient of consolidation (mm^2/s)	-	-	0.5	-	-	-	-
M_{CSL}	Slope of csl in $q'-p$ plane	0.9	-	0.82 (comp)	0.88	0.90 (comp), 0.68 (ext)	-	0.80 (comp)
κ	Slope of unload-reload line	0.05	-	0.03	0.04	0.03-0.06	-	0.05
Γ	Intercept of csl at $p'=1$ kPa	3.44	-	2.87	3.51	3	-	3.34
λ	Slope of normal consolidation line	0.25	-	0.14	0.25	0.187	0.187	0.174

Table 3.6 Published Properties of Speswhite Kaolin Clay

Symbol	Material Properties	Value
G_s	Specific Gravity	2.60
PL	Moisture content at Plastic Limit (%)	30
LL	Moisture content at Liquid Limit (%)	63
M_{CSL}	Slope of critical state line in $q'-p$ plane	0.90
κ	Slope of unload-reload line	0.039
Γ	Intercept of critical state line at $p' = 1$ kPa	3.31
λ	Slope of normal consolidation line	0.22
N_{CL}	Intercept of isotropic consolidation line at $p'=1$ kPa (Modified Cam-clay)	3.49

Table 3.7 Measured Properties of Speswhite Kaolin Clay

The normalised soil parameter (NSP) concept, called “stress history and normalised soil engineering properties” (SHANSEP) can also be utilised to estimate the undrained shear strength profile of the soil (Ladd and Foott, 1974). According to SHANSEP, the undrained shear strength, s_u of overconsolidated clay can be determined as follows:

$$\left(\frac{s_u}{\sigma'_v} \right)_{OC} = \left(\frac{s_u}{\sigma'_v} \right)_{NC} OCR^m \quad (3.7)$$

where m is a soil parameter defining the relationship between normalised s_u values at different OCR levels.

According to Skempton’s correlation (1954, 1957) :

$$\left(\frac{s_u}{\sigma'_v} \right)_{NC} = 0.11 + 0.37PI \quad (3.8)$$

From Table 3.7, the plasticity index PI of the speswhite kaolin utilised is 0.33. This yields a $(s_u/\sigma'_v)_{NC}$ of 0.23. Based on critical state soil mechanics (Schofield and Wroth, 1968), Muir Wood (1990) showed that m should be calculated by

$$m = \frac{\lambda - \kappa}{\lambda} \quad (3.9)$$

Based on the values in Table 3.7, $m = 0.82$. This value compares well with the m values that result from the λ and κ values of Clegg (1981), Elmes (1985), and Fannin (1986) in Table 3.6. Utilising these values, the estimated s_u profile determined from

the SHANSEP method was determined to be similar to the s_u profile estimated from the Modified Cam-Clay method as in Table 3.8 (with estimates from the Modified Cam-Clay method being 11% larger than the SHANSEP estimates). Site D and E are not included in Table 3.8 as the upper and bottom layers were expected to be similar to sites C and A respectively at their applicable depths (as both upper and bottom layers were preconsolidated to the same pressures of sites C and A respectively).

Estimated Undrained Shear Strength Profile Comparison						
Site	Site A		Site B		Site C	
Depth (m)	SHANSEP	Modified Cam-Clay	SHANSEP	Modified Cam-Clay	SHANSEP	Modified Cam-Clay
5	70.49	78.57	46.03	51.24	30.19	33.58
10	80.60	89.67	51.71	58.5	34.55	38.33
15	87.18	96.86	56.97	63.24	37.39	41.45
20	92.46	102.66	60.43	67.00	39.67	43.93

Table 3.8 Comparison between Undrained Shear Strength Profile Estimates

3.7.2 PPT Installation into Tub

Upon reaching half of the required consolidation pressure, the tub is unloaded in 80 kPa increments to allow for installation of the PPTs into the tub. This was to ensure no weak spots existed behind the instruments. Long holes were drilled horizontally into the clay to the required length using a hand auger and guide through pre-drilled openings on the side wall. After drilling, the instruments were inserted into the hole. To ensure both holes and instruments were horizontal, a spirit level was utilised. Following insertion, unconsolidated clay slurry was injected to fill up the cavity behind the instruments. After installation, the sample was loaded back to its original pressure. Once equilibrium was achieved the consolidation pressure was increased to the final required pressure. Figure 3.14 displays the installation process.



Figure 3.14 Installation of PPTs

3.7.3 Model Making

A few days before the centrifuge test week, the sample was unloaded in 80 kPa increments. Upon completion of unloading, the tub was removed from the consolidometer and the piston was removed. Following removal, the clay surface was trimmed until the clay surface was 80 mm below the tub top. This provided sufficient clearance for the 40 mm high water to be poured above the clay surface as shown in Figure 3.4. Figure 3.15 displays preparation of the clay.



Figure 3.15 Preparation of the Clay

Prior to installation of the actuator onto the tub, the laser platform housing the lasers, a web camera, and the LVDT was installed beneath the actuator platform. Following installation of the actuator onto the tub, the monopile was rigidly connected to the actuator and pre-installed 160 mm into the centre position of the tub where the distance between the laser and the reflectors was at a minimum distance of 35 mm. The rigid connection was then replaced with the hinge connection. The remaining web cameras were then mounted onto the actuator to observe the performance of the system and the pile.

3.7.4 Centrifuge Testing Procedure

Balance calculations were carried out to determine the counter-weight of the package and the mass of the integrated package is weighed to ensure validity of balance calculations. Following that, the integrated package was transferred onto the centrifuge swing platform. This is fixed to the torsion-bar catches which permit the package to rotate into a fixed-end condition at a centrifuge acceleration of about 10g. Via the slip rings, water was slowly poured onto the clay surface to the required height for the centrifuge test to prevent an imbalance of mass on the centrifuge during

spin-up. Once all instruments and equipment were checked to be working, the test was carried out.

The centrifuge package was spun incrementally until a 100g centrifugal acceleration was achieved. Four hours later, after the soil has achieved 70% consolidation, the soil has gained sufficient strength to bear the vertical load of the monopile. The pile was then pushed an additional 40 mm vertically into the soil to achieve the required 200 mm embedded depth. At this stage, the vertical load applied on the pile head was maintained at specific level by the adjustable counter-weight and the pulley system. After an additional four hours, the excess pore pressures resulting from the pile installation have dissipated and the soil reaches 90% consolidation level as shown in Figure 3.16.

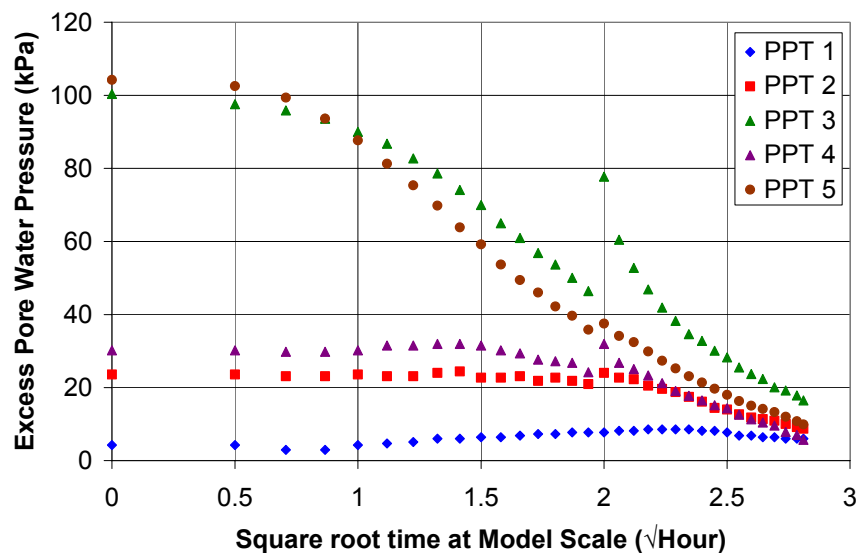


Figure 3.16 Dissipation of Excess Pore Water Pressure

Figure 3.17 shows the excess pore pressure isochrones under double drainage conditions. At this stage, the soil was characterised by utilising the T-bar or SCPT. Following soil characterisation, the monotonic or cyclic tests were carried out. Photos and manual readings were taken throughout the test to monitor changes in soil conditions throughout the test. Videos were taken during the pile installation and monotonic / cyclic phase of the test to observe changes at the soil surface.

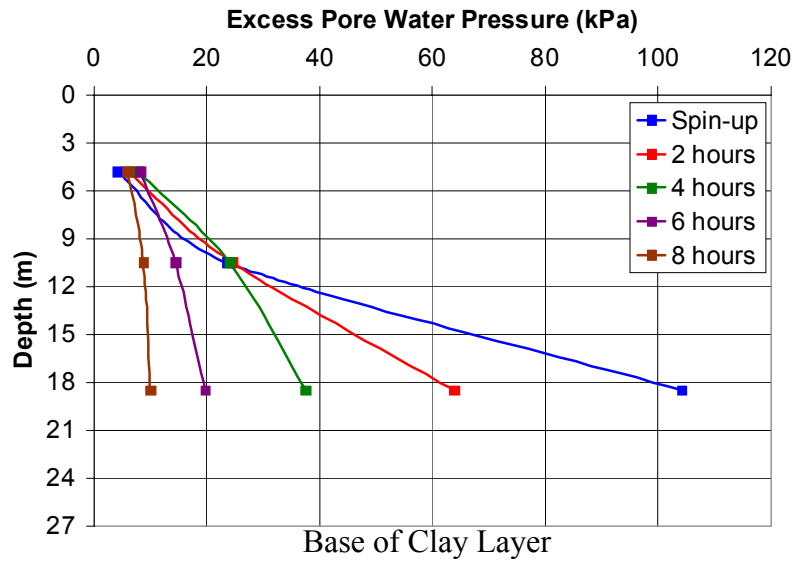


Figure 3.17 Excess Pore Pressure Isochrones during Reconsolidation

As highlighted earlier in Table 3.3, the experimental programme was divided into three phases. In Phase I, displacement controlled monotonic pushover tests were carried out on 3.83 m diameter monopiles whereas in Phase II, load controlled cyclic lateral loading tests were carried out on the same monopile. In Phase III, one load controlled cyclic lateral load experiment was carried out on a 7.62 m monopile. In the monotonic tests of Phase I, the pile head 300 mm above the soil surface was displaced 80 mm followed by an additional 40 mm of movement (in OWF 01, the pile head was only displaced 80 mm) at velocities of 4 mm/s to 5 mm/s. Details of the cyclic tests in Phases II and III are shown in Table 3.9. In Phase II and III, the 3.83 m and 7.62 m monopiles were subjected to 1-way and 1.25-way cyclic loadings, followed by a monotonic push utilising the 2D-actuator.

Stage	Experiment							
	OWF 06		OWF 07		OWF 08		OWF 09	
	Min, Max Load (N)	Cycles						
1	0, 3	1,000	0, 3	1,000	0, 3	1,000	0, 6	1,000
2	-3.2, 36		2, 32.5		0.2, 31.2		-1, 60	
3	-2.5, 79		-19.5, 56.5		3.6, 79		5, 150	
4	0, 100	100	-0.6, 100	500	10.6, 111	500	17.3, 223	500
5	NA		-30, 123	479	-30.6, 121		-65, 238	
6			14, 167.5	500	-12.5, 140		-86, 217	
7			Monotonic Push					

Table 3.9 Cyclic Experiment Loading Details in Model Scale

LeBlanc (2010b) observed that “the most onerous loading condition was found to be between one way and two way loading” with 1.6-way loading causing more than 4 times the accumulated rotation of 1-way loading. Even though cyclic loads of 1.6-way loading were planned, due to experimental error, 1.25-way loading was carried out instead.

To properly simulate the prototype cyclic loading conditions, the monopile has to be cyclically loaded with representative prototype frequencies and number of cycles. As shown in Table 3.1, to properly simulate the prototype loading frequencies, the model monopile has to be cyclically loaded at N_s times the prototype frequency in the centrifuge. Since the model is 100 times smaller than the prototype, the model monopile has to be loaded at 100 times the prototype frequency in the centrifuge. With respect to Figure 2.5, this would translate to approximately 25 Hz and 80 Hz in the centrifuge for $1P$ and $3P$ prototype frequencies. Since monopiles are expected to experience over 150 million cycles over its design lifetime of 25 years, the model monopile in the centrifuge should ideally be loaded to at least 1 million cycles. In addition, it is ideal to measure the natural frequency of the foundation system via impulse loading at appropriate intervals to determine how the natural frequency changes over cyclic loading. Efforts were made to achieve these conditions via utilisation of the piezo-actuator in OWF 04. However, due to the technical difficulties and limitations associated with the piezo-actuator, cyclic loading was carried out with the 2D-actuator subsequently.

Due to the technological limitations of the 2D-actuator, cyclic loading of the monopile in experiments OWF 05 to OWF 09 was not completely representative of the prototype loading conditions. To prevent the 2D-actuator from exceeding the specified load magnitude by failing to stop and reverse back to the datum load, the loading velocity was set at low velocities from 0.2 mm/s to 2.0 mm/s. As a result, quasi-static cyclic loads were applied onto the monopile, with low frequencies ranging from 0.14 Hz to 2.5 Hz. This translates to prototype frequencies that are many times below the prototype loading frequencies shown in Figure 2.5. With low loading frequencies and both time and physical constraints, it was not possible to load the pile to a million cycles. Therefore, the pile was cyclically loaded until no significant marginal displacement was observed; resulting in the number of cycles listed in Table

3.9. With the usage of the 2D-actuator, it was also not possible to measure the natural frequency of the foundation as an impulse load could not be applied to the system. Due to the limitations, the results from OWF 06 to OWF 09 may be limited to the long-term behaviour of monopiles under storm loadings.

3.7.5 Test Problems

As with any centrifuge testing programme, problems are expected to take place. Table 3.10 depicts the problems and issues that took place in each experiment.

Experiment	Problems and Issues
OWF 01 (first run)	<ul style="list-style-type: none"> • PPT at location 1 (as shown in Figure 3.5(a)) failed during test. • V-H load cell was non-functional as wires disconnected during test. • T-bar strain gauge delaminated during push-in. • Pile sank into soil as vertical load of assembly was greater than pile's vertical capacity.
OWF 02	<ul style="list-style-type: none"> • Top laser reflector plate failed due to poor adhesion by epoxy. • 2D actuator drive was replaced and encoder was cleaned due to dust accumulation.
OWF 03	<ul style="list-style-type: none"> • Plastic standpipe bent resulting in water level above soil-pile interface to be less than the planned 40 mm height.
OWF 06	<ul style="list-style-type: none"> • 2D actuator software acted up resulting in actuator moving beyond specified load with a total displacement of 15 mm. As a result, 1.5 way cyclic loading of -50,100 N and 1-way cyclic loading of 150 N was abandoned.
OWF 07	<ul style="list-style-type: none"> • Mistake was made in laser platform setup. As a result, pile was installed slightly away from the tub centre, in close proximity to PPTs at locations 1 to 3 instead of half a pile diameter away. • Valve connecting jack-in-rig with SCPT could not be released in centrifuge under 100g as it was placed in the wrong orientation. During spindown, switch was left open causing SCPT to be pushed in. As a result, s_u profile may not be accurate. • Pipe supplying water to tub kinked resulting in water level above soil-pile interface to be less than the planned 40 mm height. • 2D actuator control in lateral direction was switched to rotary due to position feedback error from encoder strip. • Due to a broken wire, monopile bending moment strain gauge readings at a prototype depth of 10.43 m were unavailable.
OWF 08	<ul style="list-style-type: none"> • Mistake was made in laser platform setup. As a result, pile was installed further away from tub centre, in close proximity to PPTs at locations 1 to 3 instead of half a pile diameter away.
OWF 09	<ul style="list-style-type: none"> • All monopile bending moment strain gauges failed due to water leakage.

Table 3.10 Experimental Troubles and Issues

3.8 Triaxial Testing

Triaxial undrained compression testing was carried out to investigate both material parameters and stress-strain behaviour of speswhite kaolin at different overconsolidation ratios (*OCR*). Measurements from the triaxial tests contributed to the values reported in Table 3.7 and the linking of *OCR* to mobilisation strain of Vardanega et al. (2012). The assembly is described as follows (Lam, 2010):

- 1) A Bishop and Wesley type cell is utilised and is designed to withstand 17 bars of internal fluid pressure. Both base pedestal and top cap are 50 mm in diameter. The base pedestal is connected to a bottom drainage line that is connected to a pore pressure transducer and then to a back pressure / volume controller. The top cap is connected to another drainage line to facilitate the flushing process.
- 2) A hydraulic piston located at the bottom of the cell helps push the sample upwards to compress the sample against a fixed load cell at the top of the cell.
- 3) Three GDS pumps are set up to control cell volume / pressure, back volume / pressure and volume / pressure for the piston at the bottom of the cell. The GDS controller pumps can control pressure to an accuracy of 1 kPa and volume within 1 mm³. The pumps can be manually operated or controlled by the computer program. The integrated computer interface allows communication between the pumps, allowing different settings of load conditions at various stages of the test.
- 4) De-aired water is used to fill the cell.
- 5) Axial load is measured by the submersible load cell mounted on top of the top cap. The load cell has a capacity of 4 kN with a precision of 0.2 N.
- 6) Two submersible linear variable differential transformers (LVDTs) are mounted vertically on the sample for evaluation of small strain stiffness over a gauge length of 40 mm. The capacity of the device allows measurement accuracy of 0.0001 mm and a measurement range of 10 mm.
- 7) An external LVDT measures the overall movement of the sample within a range of 50 mm.
- 8) Pore water pressure changes are measured with a pore pressure transducer at the bottom of the specimen. The transducer has a capacity of 34 bars.
- 9) Junction boxes connect all the instruments to gather signals from load cells, external LVDT, two local LVDTs and GDS controller pumps.

To obtain samples for testing, sharp edged thin walled copper tubes with an inner diameter of 50 mm are pushed vertically into a block of pre-consolidated clay from the centrifuge test. The samples are 100 mm high and 50 mm in diameter. The ends of the sample are trimmed to the required height with a thin wire saw. The ends are also trimmed with care to form a flat and perfectly smooth surface to ensure vertical contact between the base pedestal and top cap. The dimensions and weight of the sample are measured using a digital vernier and a digital balance respectively. The sample is then pushed out from the tube using a plunger and placed onto the pedestal with a wet porous stone. Another wet porous stone is placed above the sample followed with the placement of the radial drainage filter paper strip. Both the porous stones and filter paper help facilitate the consolidation process. Following that, the sample is encased by a rubber membrane that is held tightly to the porous stones by the use of O-rings. If strain measurements are required, two submersible LVDTs will be mounted onto the specimen by glue and pins.

Prior to testing, the air between the sample and the membrane has to be flushed out. To do so, a relatively low cell pressure of 10 kPa is kept in the cell. Then, a constant water flow is applied from the bottom pedestal to flush air out of the system through the top drainage system. The back pressure is closely monitored in the process to ensure that the back pressure does not exceed the cell pressure to avoid swelling and separation of the rubber membrane. The flow is stopped when the air bubbles are flushed out. The sample is then ready for testing. The triaxial test is divided into four stages as follows:

1) Saturation

During this stage, any remaining air in the system is dissolved into water under high pressure to ensure that the sample is fully saturated for testing, as partial saturation would affect the strength and stiffness of the sample. Throughout this stage, the cell pressure is 10 kPa greater than the back pressure to avoid separation of the membrane from the sample. The cell pressure is increased from an initial pressure of 10 kPa to 370 kPa, whereas the back pressure is increased from 2 kPa to 360 kPa. The whole process is carried out in 12 hours to allow the pore pressure within the specimen time to equilibrate.

2) B-value check

The B-value represents the degree of saturation of the sample. To check the B-value, the drainage taps connected to the sample are closed and the cell pressure is increased. Following the increase, the back pressure is measured. The B-value is the ratio of the change in pore pressure to the change in cell pressure. If the sample is fully saturated, the increase in back pressure should be almost equal to the increase in cell pressure, leading to a B-value of 1. Normally, a B-value of 0.97 or above can be achieved easily with the current setup.

3) Consolidation

In this stage, the back pressure tap is opened. The back pressure is set 200 kPa below the cell pressure and kept at a constant. The cell pressure is then increased to achieve the preconsolidation stress experienced by the soil model resulting in a normally consolidated sample. Each consolidation stage takes approximately 15 hours and by the end of this stage, the back and cell volume have reached a constant. To overconsolidate the sample, another consolidation stage is set up and the cell pressure is decreased to achieve the required overconsolidation ratio.

4) Compression

In this stage, the cell pressure is kept constant while the axial load is increased until the sample experiences failure. The specimen is compressed at a rate of 0.02 mm/min which is roughly 1.2% of strain deformation per hour, similar to that experienced by the soil when horizontal pushover takes place. During this stage, all drainage taps are closed to provide for undrained conditions, leading to deformation under constant volume. As a result, excess pore pressures are generated and these pressures are measured by the pore pressure transducer. Axial displacement is measured by the external LVDT and local submersible LVDTs attached to the sample. The axial load is measured using a submersible load cell and data is acquired at 3 second intervals. Following completion of the experiment, the sample is weighed and placed into the oven at 105 °C for 24 hours to determine the water content.

CHAPTER 4

4. MONOTONIC TESTS RESULTS

4.1 Introduction

This chapter presents the monotonic test results of OWF 01, OWF 02, and OWF 03 and corresponding analyses that are related to the lateral monotonic behaviour of monopile in clay. The main objectives of these tests are not only to determine and characterise the monotonic behaviour of monopiles, but also to suggest recommendations that could help improve the current design methodology. Findings from the monotonic tests will also contribute to the findings made in the cyclic tests. Experimental details of these tests can be found in section 3.5 that highlights the experimental programme and section 3.7.4 that discusses the experimental procedure.

4.2 Soil Strength Profile for Uniform Preconsolidated Soils

The undrained shear strength, s_u of the soil was measured via various means that included the T-bar and the seismic cone penetrometer, SCPT as described in section 3.7.4. Estimation of s_u was carried out based on the on the excess pore pressure distribution at 90% reconsolidation (as shown in Figure 3.17), the resulting *OCR* profile (as shown in Figure 4.1) and using the parameters in Table 3.7.

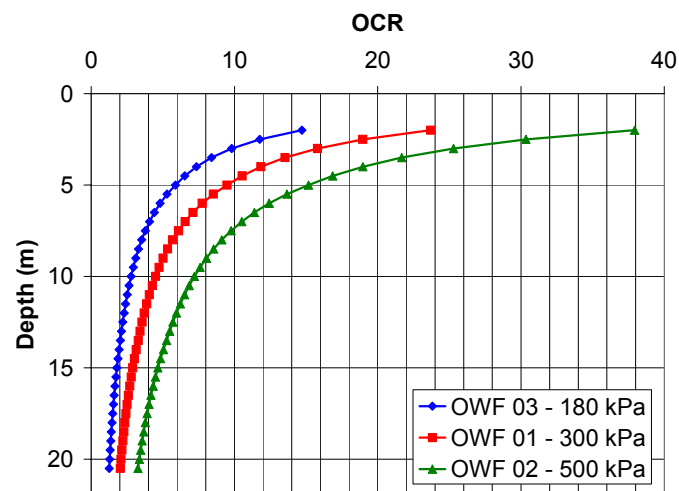


Figure 4.1 *OCR* Profile at 90% Reconsolidation

Based on the data from the triaxial tests of section 3.8, Vardanega et al. (2012) reports that $m = 0.68$ for speswhite kaolin. However, the measurements were compared to the estimates from SHANSEP utilising $m = 0.82$ and the Modified Cam-Clay method as shown in Figure 4.2. Explanation regarding the usage of $m = 0.82$ is provided in section 4.2.2. As shown in Figure 4.1, the clay is heavily over-consolidated at the surface and the OCR reduces with increasing depth.

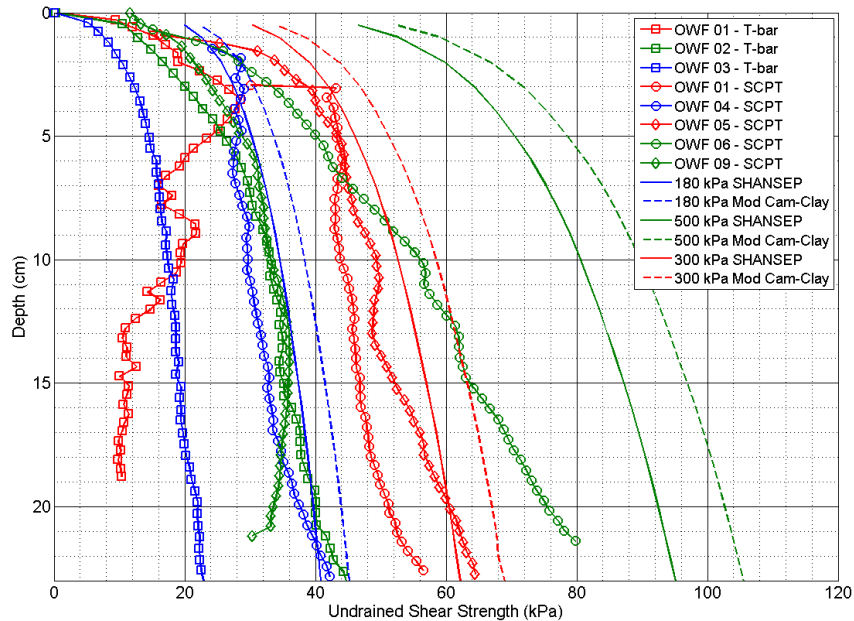


Figure 4.2 s_u Comparison for Uniform Pre-consolidated Soils

4.2.1 T-bar Measurements

As shown in Figure 4.2, T-bar measurements from OWF 01, OWF 02, and OWF 03 were far lower than estimates from both SHANSEP and Modified Cam-Clay. In OWF 01, due to the decreasing readings with increasing depth, it is postulated that the strain gauges delaminated from the T-bar shaft; resulting in it not registering a further increase in strain and hence strength.

In OWF 02, the T-bar measurements were over 50% lower than the estimates whereas in OWF 03, the measured profile was approximately 50% lower than the SHANSEP estimates. As a result, an investigation was carried out to determine the factors that may have contributed to the low measurements. According to White et al. (2010) as shown in Figure 4.3(b), the soil flow around the T-bar is categorised into “shallow” and “deep” mechanisms in which the soil will either heave forming a gap behind the

T-bar or flow around the T-bar. To measure s_u accurately, the “deep” mechanism has to take place.

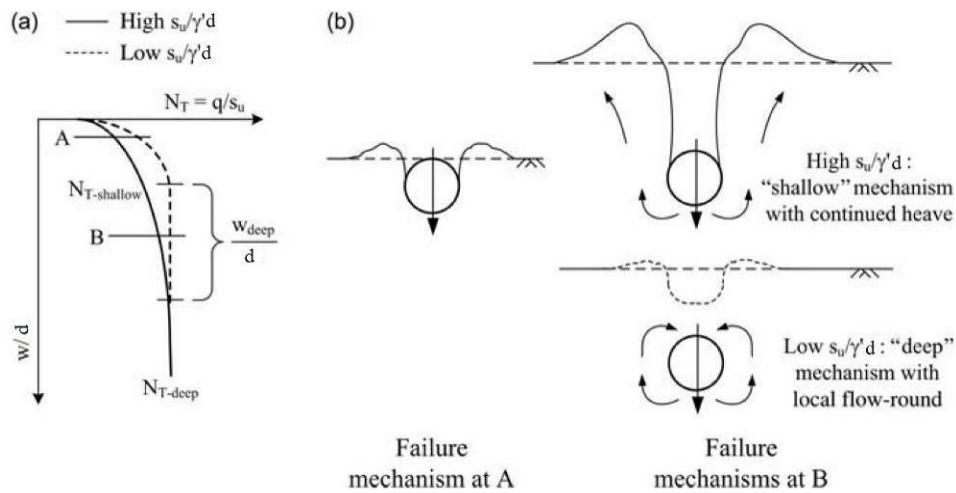


Figure 4.3 Idealised Behaviour associated with Shallow and Deep T-bar Penetration
 (a) Variation in Bearing Factor Depth (b) Shallow and Deep Failure Mechanisms
 (adapted from White et al., 2010)

The bearing factor, N_T , determines whether a shallow or deep failure mechanism takes place. It is defined as:

$$N_T = \frac{q_{t-bar}}{s_u} \quad (4.1)$$

where q_{t-bar} is the undrained penetration resistance of the T-bar. N_T values at which the “deep” mechanism takes place is categorised as N_{T-deep} whereas N_T values that are lower in magnitude than N_{T-deep} (where “shallow” mechanism takes place) is categorised as $N_{T-shallow}$. Based on the plasticity limit analysis by both Randolph and Houlsby (1984) and Martin and Randolph (2006), the “deep” mechanism takes place at N_{T-deep} values ranging from 9.14 for a fully smooth interface to 11.94 for a fully rough interface. Since T-bars in both centrifuge and field are neither fully smooth nor fully rough, an N_{T-deep} value of 10.5 is usually adopted (Stewart and Randolph, 1991).

According to White et al. (2010), the depth at which the transition from shallow to deep failure mechanism takes place (i.e. when $N_t \approx N_{t-deep}$) is affected by the dimensionless group $s_u/\gamma'd$, where γ' is the effective unit weight of the soil and d is diameter of the T-bar. As shown in Figure 4.3(a) that plots normalised T-bar depth

below soil surface, w to T-bar diameter d , vs. N_t , the low $s_u/\gamma'd$ curve reaches the deep failure mechanism at a shallower depth relative to the high $s_u/\gamma'd$. Based on the series of large deformation finite element (LDFE) analyses of the T-bar penetration process carried out by White et al. (2010), the depth at which deep failure takes place, w_{deep} , can be estimated by the following equation:

$$\frac{w_{deep}}{d} = 2.58\left(\frac{s_u}{\gamma'd}\right)^{0.46} + 0.24\left(\frac{s_u}{\gamma'd}\right)^{-0.63} \quad (4.2)$$

Considering the estimated SHANSEP profile that suggests an average s_u of approximately 35 kPa and 80 kPa for the 180 kPa and 500 kPa pre-consolidated soils respectively as in Figure 4.2, the γ' of 7.79 kN/m³ and d of 0.85 m in prototype scale, w_{deep} would be 4.79 m and 6.94 m for the 180 kPa and 500 kPa pre-consolidated soils respectively. Even though the calculation suggests that the T-bar should accurately measure s_u at depths greater than w_{deep} , the T-bar measurements relative to the SCPT measurements and the estimates suggests otherwise.

It is also possible that the “shallow” flow mechanism took place at depths deeper than the estimates of equation (4.2), resulting in lower readings that were not representative of the actual s_u of the model. In excavations, z_{cr} , the height of unsupported excavation of a water-filled trench is $2s_u/\gamma'$. With an average s_u of approximately 35 kPa for the 180 kPa pre-consolidated soils, z_{cr} is 9 m. For test OWF 03, the “shallow” flow mechanism may have contributed to the reduced s_u measurements in the top 9 m. However, this fails to explain why the T-bar failed to measure s_u accurately for the bottom 11 m. Considering that the T-bar was designed according to Stewart and Randolph (1991) and Chung and Randolph (2004), it was concluded that the T-bar was not functioning properly in test OWF 03.

z_{cr} is 20.54 m for the 500 kPa pre-consolidated soil with an average s_u of 80 kPa. In test OWF 02, the “shallow” flow mechanism took place throughout the push-in, causing a gap to form above the T-bar, resulting in low readings that were not representative of the actual s_u . Figure 4.4 displays the soil surface at the T-bar after spin-down for both experiments OWF 03 and OWF 02. No gap is apparent for OWF 03 but a gap is apparent for OWF 02.



(a) OWF 03

(b) OWF 02

Figure 4.4 Soil Surface at T-bar after Spin-down

Based on the measurements and on the investigation, it was concluded that the T-bar was not suitable for the measurement of the strength of stiff soils with high undrained shear strengths and that the T-bar was not functioning properly in test OWF 03. As the T-bar results were not representative of the true strength profile, an SCPT was hence used for later experiments and the strength measured by it, with identical sample preparation were assumed to have also existed in tests OWF 01 – 03.

4.2.2 SCPT Measurements

Based on the regression fitted through the triaxial test data by Vardanega et al. (2012) as shown in Figure 4.5, the m value of speswhite kaolin for the SHANSEP estimation of s_u is 0.68.

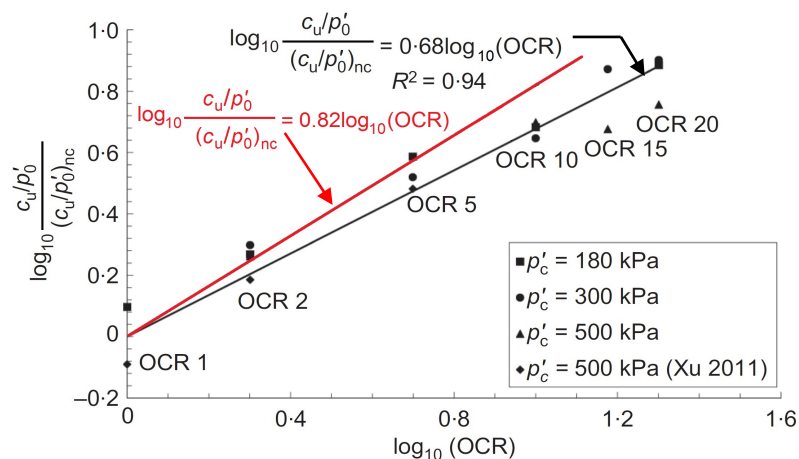


Figure 4.5 Fitting of Triaxial Test Data (adapted from Vardanega et al., 2012)

As shown in Figure 4.6, utilisation of $m = 0.68$ would result in softer s_u profiles relative to the estimates from $m = 0.82$. For the 500 kPa preconsolidated soil, the

$m = 0.68$ estimates are on average 40% lower compared to the $m = 0.82$ estimates. Despite the high coefficient of determination of the fitted regression in Figure 4.5 and despite how well the $m = 0.68$ estimates appear to match the SCPT measurements of OWF 06 and the lower half of the SCPT measurements of OWF 04 and OWF 05, the SHANSEP s_u estimates resulting from $m = 0.82$ were selected for use in analysis for various reasons.

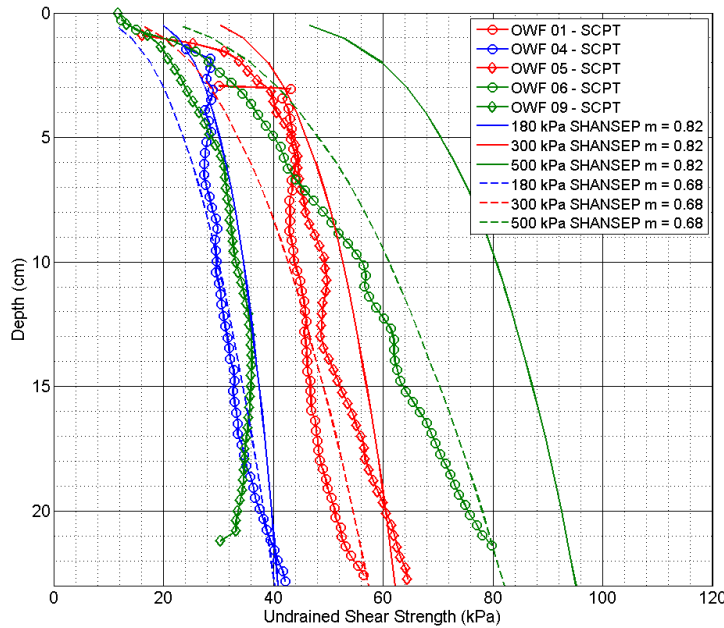


Figure 4.6 SHANSEP s_u Comparison for Different m Values

The m values that result from the reported λ and κ values of Clegg (1981), Elmes (1985), and Fannin (1986) in Table 3.6 of 0.80, 0.79, and 0.84 respectively, compare well with $m = 0.82$ determined here. A regression with $m = 0.82$ is shown in Figure 4.5 to fit the upper boundary of the triaxial data quite well from $1 \leq OCR \leq 5$. The best fit slope obtained from Figure 4.5 is very sensitive to the strength obtained at $OCR = 1$, as the regression is forced through the origin. It can be seen that in the data of Vardanega et al (2012), the two data points at $\sim OCR = 1$ show significant divergence. Ignoring the data point with higher strength at $OCR = 1$ results in an m value of 0.76. The degree of confidence in the precise m value from the limited triaxial data of 18 samples is thus not particularly high. A final reason for the assumption that $m = 0.82$ is given by the monotonic pushover testing detailed in section 4.4.2. If strengths associated with $m = 0.68$ are assumed, lateral resistances greater than the theoretical

upper-bound solution are required to explain the data. An assumption of $m = 0.82$ thus seems more justified.

As shown in Figure 4.6, readings from OWF 06 and 09 were much lower than the $m = 0.82$ SHANSEP estimates. Investigations after experiment OWF 06 indicated that the waterproof silicone layer above the sleeve load cell was delaminating. Since the silicone layer was connected to the silicone layer above the cone load cell, it is possible that the cone load cell readings were affected by the pull resulting from the contact between the silicone layer and the sleeve casing during the push-in.

Investigation after experiment OWF 09 did not reveal any physical problems associated with the SCPT and consolidation records indicated that the soil was properly overconsolidated to 500 kPa. However, review of experimental data indicated that the SCPT was pushed in at a lower velocity of 2.8 mm/s despite utilising the same valve and air pressure settings. Kim et al. (2008) normalises the penetration rate as follows:

$$V = \frac{vD_{cone}}{c_v} \quad (4.3)$$

where,

V	Dimensionless penetration rate
v	Penetration rate
D_{cone}	Cone diameter of 12.70 mm
c_v	Coefficient of consolidation

According to Kim et al. (2008), the transition from undrained to partially drained takes place at V values approximately equal to 10. Based on settlement records, the c_v on the normal consolidation line is approximately 0.58 mm²/s. Based on the ratio between λ and κ of speswhite kaolin (values as given by Table 3.7), the c_v on the unload-reload line is approximately 3.27 mm²/s. According to equation (4.3), a minimum penetration rate of 2.6 mm/s is required to induce an undrained response in overconsolidated speswhite kaolin. Since the penetration rate is only slightly higher

than the minimum, it is possible that the SCPT did not penetrate fast enough to induce a completely undrained response.

4.3 Analysis of Bending Moments

4.3.1 Calculation of Soil Reaction

As discussed in section 3.6.6, twelve strain gauges arranged in full bending moment bridges were installed at six heights along the monopile to measure the bending strains. The heights selected ensured that the strain gauges would be beneath the soil surface upon installation of the monopile 20 m into the soil. As a result, it was possible to measure the bending moments of the monopile within the soil strata during the monotonic pushover. Since no flexure occurred at the toe, the toe bending moment was assumed to be zero. As a result, seven discrete data points were available for bending moment analysis. An example of this is shown in Figure 4.7.

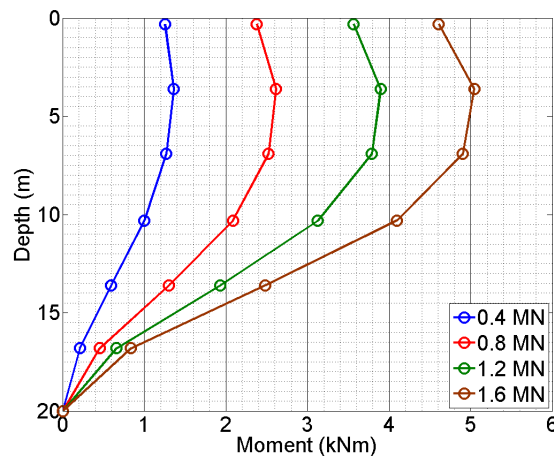


Figure 4.7 OWF 03 Measured Bending Moment

As shown by the beam bending equations in section 2.6 and the complete solution results of Figure 2.12, the lateral behaviour of the monopile can be evaluated through double-differentiation and double-integration of the bending moment curves. Double-differentiation of the bending moment curve results in soil reaction curves that depict the lateral earth pressures acting on the pile whereas double-integration of the bending moment curves divided by the pile bending stiffness ($E_p I_p$) accompanied with the use of two displacement boundary conditions would result in pile displacement curves that depict the pile-soil stiffness relative to displacement. However, this is only possible provided there is sufficient data to construct an accurate and representative

bending moment curve. Since there were only seven discrete data points available to construct the bending moment curve across the 20 m embedded depth, an appropriate interpolating function that generated artificial points between the seven data points had to be selected.

Interpolation of the bending moment data was carried out in MATLAB (Mathworks, 1984). Multiple fitting functions were available in MATLAB including the cubic spline interpolant, the shape-preserving cubic interpolant (piecewise cubic Hermite interpolation), and polynomial fittings ranging from linear fits to 10th degree polynomials. As shown in Figure 4.8(a), the bending moment curves resulting from the cubic spline, the shape-preserving interpolant, and the 5th-order polynomial fit are similar to each other and match the general shape of the measured bending moment curve. However, the double-differentiated soil reaction curves as shown in Figure 4.8(b) are different from each other, especially the soil reaction curve resulting from the shape-preserving interpolant that appears to be greatly distorted. This is due to the differing nature of the fitting functions. Since it is not physically possible for the soil reaction curve to have sharp linear discontinuities that vary significantly in magnitude throughout the monopile, the shape-preserving interpolant was deemed to be unsuitable for analysis.

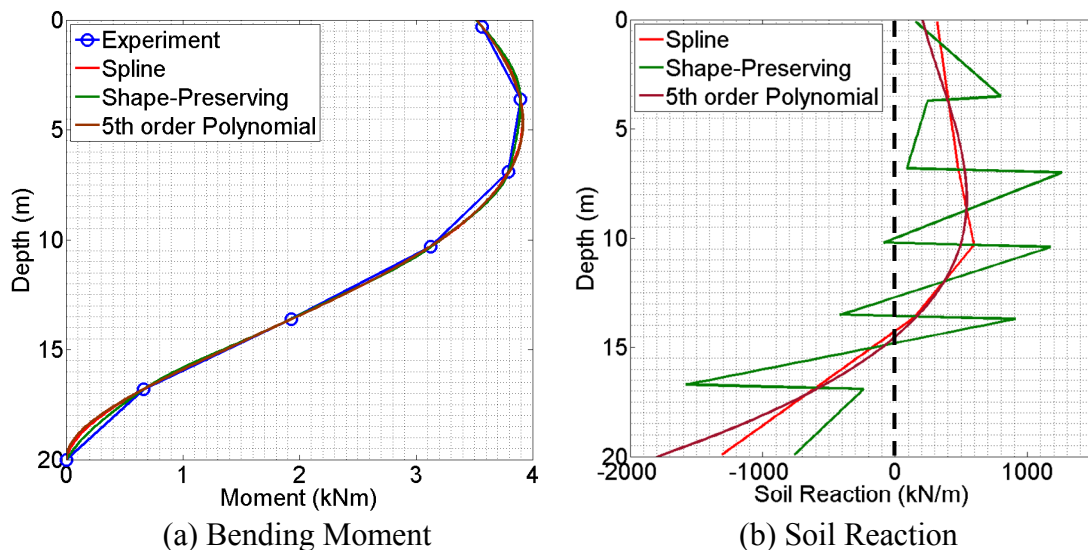


Figure 4.8 Comparison of Results from MATLAB Fitting Functions

Double-differentiation of the high order polynomial fitting produced a smooth soil reaction curve whereas double-differentiation of the spline fitted bending moment

curve produced a soil reaction curve with sharp linear corners that was similar in shape to the polynomial fit. As mentioned in Lau et al. (2014) and as shown in the example of Figure 4.8(b), despite being similar in shape to each other, the polynomial fittings produced elevated soil reaction values at the pile toe and mudline. As a result, the cubic spline was determined to be the most appropriate fitting function to be utilised for further analysis.

4.3.2 Estimation of Rotation Depth

Review of the soil reaction curves showed a single zero soil reaction point throughout the monotonic pushover, indicating that the monopile rotated at depth. An example of this can be seen in Figure 4.8(b) which shows the monopile experiencing soil reactions of opposite signs above and below the zero soil reaction point. Utilising the point of zero soil reaction from the derived soil reaction curves, the rotation depth, d_{rot} throughout the three monotonic experiments was estimated, as shown in Figure 4.9. As shown in Figure 4.9, the rotation point is initially at a depth of 8 m. The rotation point then quickly drops to depth of 14.5 m, and proceeds to stabilise at 14 m (i.e. 70% of the embedded depth).

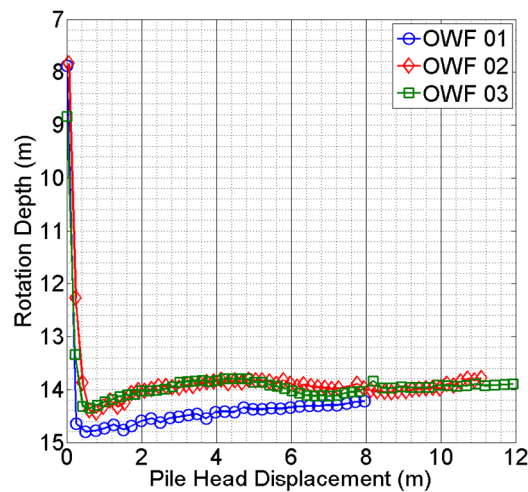


Figure 4.9 Rotation Depth from Point of Zero Soil Reaction

Lateral pushover centrifuge tests carried out by Klinkvort and Hededal (2010) on variously sized monopiles in Fountainbleu sand and model static tests by Zhu et al. (2014) in sandy silt at different relative densities suggests that d_{rot} is at 80% of the embedded depth. Utilisation of these findings would result in a d_{rot} of 16 m below the

mudline rather than 14 m. The findings of Klinkvort and Hededal (2010) may be limited to monopiles in sand as the variation of strength in sand with depth is different from that of overconsolidated clay whereas the findings of Zhu et al. (2014) may not be representative as their model tests do not properly model the correct stress states. Finite element analysis by Haiderali et al. (2014) that simulated the monotonic tests indicate that the rotation point is at 75% of the embedded depth while finite element analysis by Abdel-Rahman and Achmus (2005) on a 7.5 m monopile in dense sand show that the rotation depth is approximately 73% of the embedded depth. These results are comparable to the experimental results of Figure 4.9.

4.3.3 Calculation of Pile Displacement

As mentioned earlier, pile displacement throughout the pushover can be calculated via double integration of the bending moment curves divided by pile bending stiffness ($E_p I_p$) accompanied with the use of two displacement boundary conditions. This can be expressed as follows:

$$y = y_{int} + bx + c \quad (4.4)$$

where y is lateral pile displacement, y_{int} is the pile displacement from double integration, and x is the depth along the pile. Both b and c are unknowns that have to be resolved through the use of two displacement boundary conditions.

To ensure displacements were accurately estimated within the soil layer, it was necessary to select a displacement boundary condition that was within the soil strata. As mentioned in section 4.3.2, the single zero soil reaction point was utilised to estimate d_{rot} . Besides indicating d_{rot} , reference to Figure 2.12 shows that the zero soil reaction point is also the depth at which pile displacement is zero. Since the monopile rotated at depth throughout the monotonic pushover, d_{rot} at which zero pile displacement took place was utilised as a boundary condition.

The second boundary condition that was selected was the laser displacement readings above the mudline. Readings were taken from the laser located 10 cm above the mudline as the laser was the closest in distance to the soil surface. This was done to improve the accuracy of the pile displacement estimated within the soil strata. Since

the second boundary condition was above the mudline, the bending moment above the mudline had to be estimated in absence of measurements above the soil surface. The bending moment above the mudline was estimated by assuming cantilever behaviour above the mudline.

As shown in Figure 4.10, the bending moment was assumed to decrease linearly from the interpolated bending moment at the soil surface until zero bending moment at the point of load application 30 m above the mudline. This approach is valid as there is zero flexure at the point of load application. In addition, the top bending strain gauges are located approximately 0.3 m in prototype scale below the mudline, ensuring that the moment at the mudline was accurately estimated from the spline fitting.

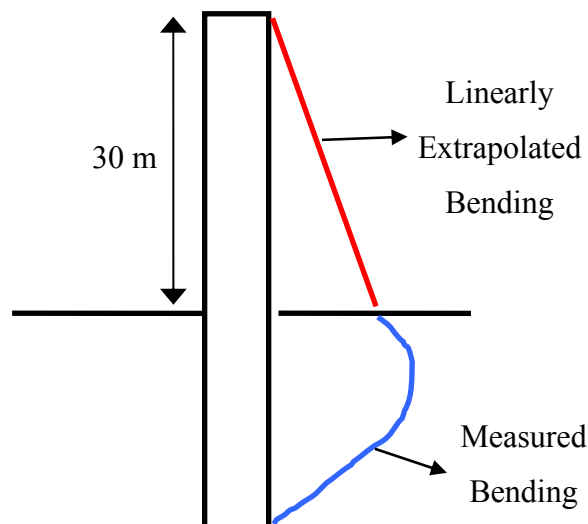


Figure 4.10 Linear Extrapolation of Bending Moment above Soil Surface

After resolving b and c through the utilisation of the boundary conditions, estimation of the pile displacement above and below the mudline was possible. An example of the calculated pile displacement curves is shown in Figure 4.11 for test OWF 03. At low magnitude lateral loads of 0.4 MN and 0.8 MN, the monopile rotates at the rotation point yet at the same time flexes. This is in line with the expectation made in section 2.7.1 where the monopile was expected to exhibit both rigid and flexible pile behaviour. However, with increasing load magnitude, the flexure of the monopile reduces relative to the magnitude of rotation. Upon reaching 1.6 MN lateral load, the monopile behaves much closer to a short, rigid pile without significant flexure. Since

the monopile rotates without flexing significantly, an undesirable toe-kick will be developed (DNV and Risø National Laboratory, 2002).

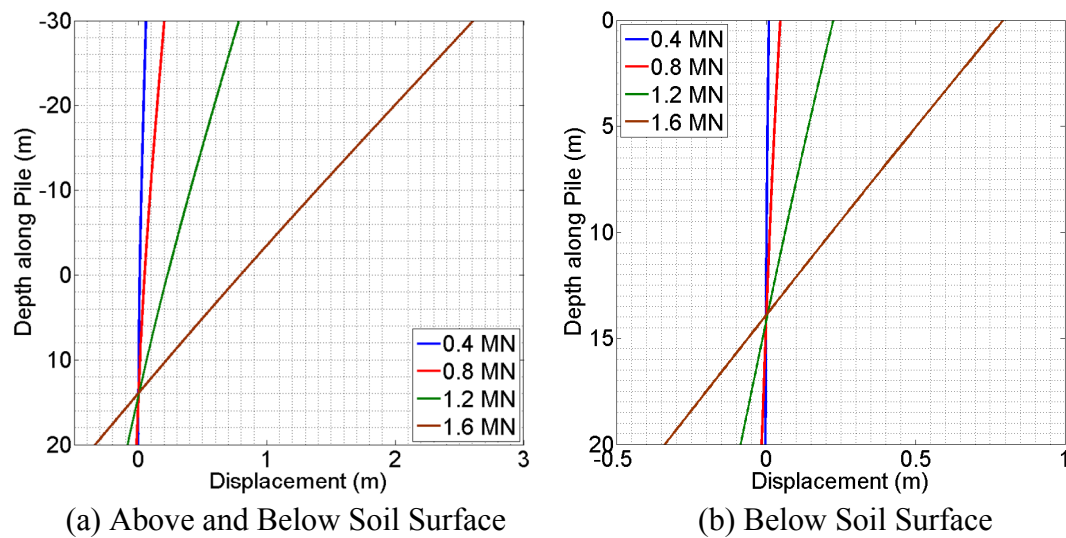


Figure 4.11 OWF 03 Pile Displacement Curves

4.4 p - y Curves

With both soil reactions and pile displacements calculated from the double-differentiation and double integration of the bending moment curves, construction of the experimental p - y curves at depths along the monopile was carried out. Section 4.4.1 discusses the comparison between the experimental and DNV design p - y curves while section 4.4.2 discusses the comparison between the experimental and DNV estimated load-displacement behaviour. Section 4.4.3 discusses the characterisation of the experimental p - y curves. Section 4.4.4 discusses how the experimental p - y curves compare with other criteria suggested by other researchers. Finally, recommendations for p - y curve construction for static loading are made in section 4.4.5.

4.4.1 Comparison between Experimental and DNV Design p - y Curves

Utilising the calculated soil reactions and pile displacements from the bending moment curves, the experimental p - y curves along the monopile depth were constructed. The experimental curves were then compared to the DNV design p - y curves. The DNV p - y curves were constructed utilising equations (2.11) and (2.12) for static loading of section 2.6.1.

The reference deflection, ε_c was determined from Vardanega et al. (2012) using the following equation that was derived from the triaxial tests as described in section 3.8.

$$\log_{10}(\gamma_{M=2}) = 0.68 \log_{10}(OCR) - 2.395 \quad (4.5)$$

where

$\gamma_{M=2} = 1.5\varepsilon_c$ Shear strain at half strength
 OCR over-consolidation ratio

The OCR utilised to estimate ε_c was determined from the 90% pore pressure dissipation OCR profile of Figure 4.1 to estimate s_u . As the triaxial tests reported in Vardanega et al. (2012) were not carried out beyond an OCR of 20, the OCR at shallow depths where $OCR \geq 20$ was capped to 20.

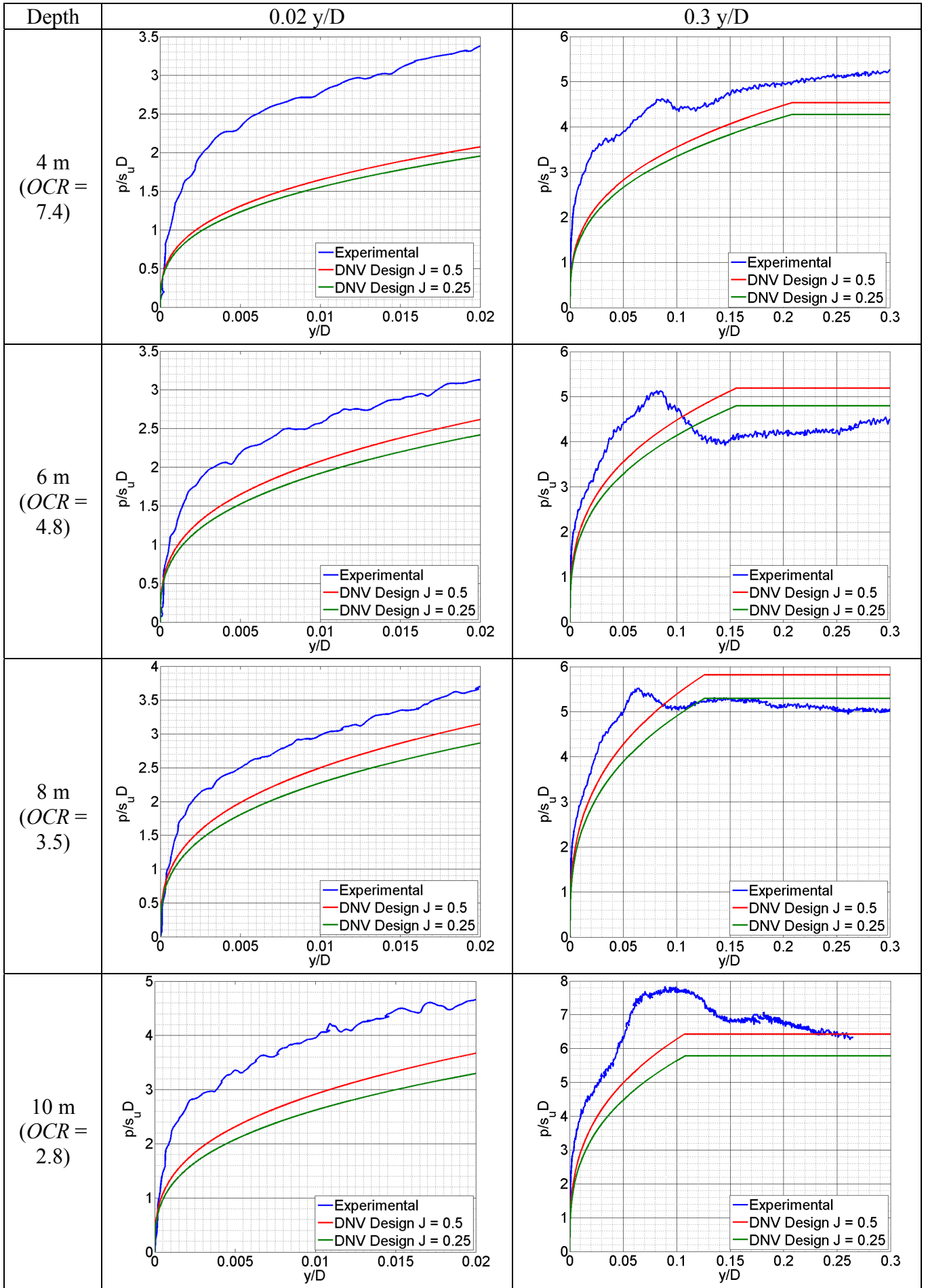
Comparison between the experimental and DNV design p - y curves was carried out by normalising the soil reaction by $s_u D$ and by normalising displacement by D . This can be seen in Figures 4.12 to 4.14 for the three monotonic tests. The figures have been revised from Lau et al. (2014) as the s_u has been revised from the SCPT readings to the $m = 0.82$ SHANSEP estimates (with the biggest change to observations applicable to OWF 02). According to Matlock (1970) and the DNV (2014), the value of J utilised to calculate the $3s_u$ component of ultimate soil reaction, p_u in equation (2.11) varies from 0.25 to 0.50. 0.50 is recommended for soft normally consolidated clay (DNV, 2014) whereas Matlock (1970) observed that a value of 0.25 fitted his data from Lake Austin for heavily overconsolidated stiff, fissured clays subjected to desiccation. Considering that the soil was heavily overconsolidated, comparisons were also made with the DNV design curves calculated with J of 0.25.

As seen in Figures 4.12 to 4.14, the experimental curves from 4 m to 16 m display a stiffer response than the suggestions made by the DNV, quickly mobilising soil reactions ranging from $2p/s_u D$ to $4p/s_u D$. The p - y curves above 4 m are not shown as the curves were not well defined due to errors introduced by fitting. This was also the case for the curves at 14 m depth as it was close to the rotation point where displacements were small. The pile toe displays a very stiff response and mobilises

soil reactions far greater than the maximum $9s_uD$ at displacements greater than $0.02 y/D$ (except for OWF 02 which mobilises $9s_uD$). This is most likely due to the shear force acting on the base of the pile that results from the “toe-kick” at the pile toe, contributing additional resistance in excess of that estimated by the DNV. The OWF 01 pile toe curve seems extremely stiff in comparison to OWF 02 and OWF 03. This is possibly due to errors introduced by the spline fitting. A review of the pile toe curves indicate that the ultimate reaction is achieved at large displacements of approximately $0.2 y/D$. This suggests that the shear force is fully mobilised only at large displacements.

As the pushover continues, the $p-y$ curves eventually soften and come closer to the design curves. However, with respect to Figure 4.1 and Figures 4.12 to 4.14, the experimental $p-y$ curves at depths where $OCR \geq 4$ show greater softening and approach the $J = 0.25$ design curves. This suggests that the ultimate soil reaction criteria by Matlock (1970) captures the reduced resistance in heavily overconsolidated soil fairly well. The stiffness of the experimental $p-y$ curves at the 12 m and 16 m depths reduces with the maximum mobilised soil reaction reaching 59% to 67% of the maximum suggested by the DNV. This is most likely due to the close proximity of these depths to the rotation point.

As shown in Figures 4.13 and 4.14 for experiment OWF 01 and 02, the transition depth X_R (below which the value of $(3s_u + \gamma'X)D + Js_uX$ exceeds $9s_uD$) for the DNV $p-y$ curves was calculated to be below the base of the pile. Figure 4.12 shows that X_R was located at the base of the pile in experiment OWF 03 for $J = 0.5$. These results are consistently much deeper compared to Randolph and Houlsby (1984) who suggests that X_R is located at a depth of about 3 pile diameters.



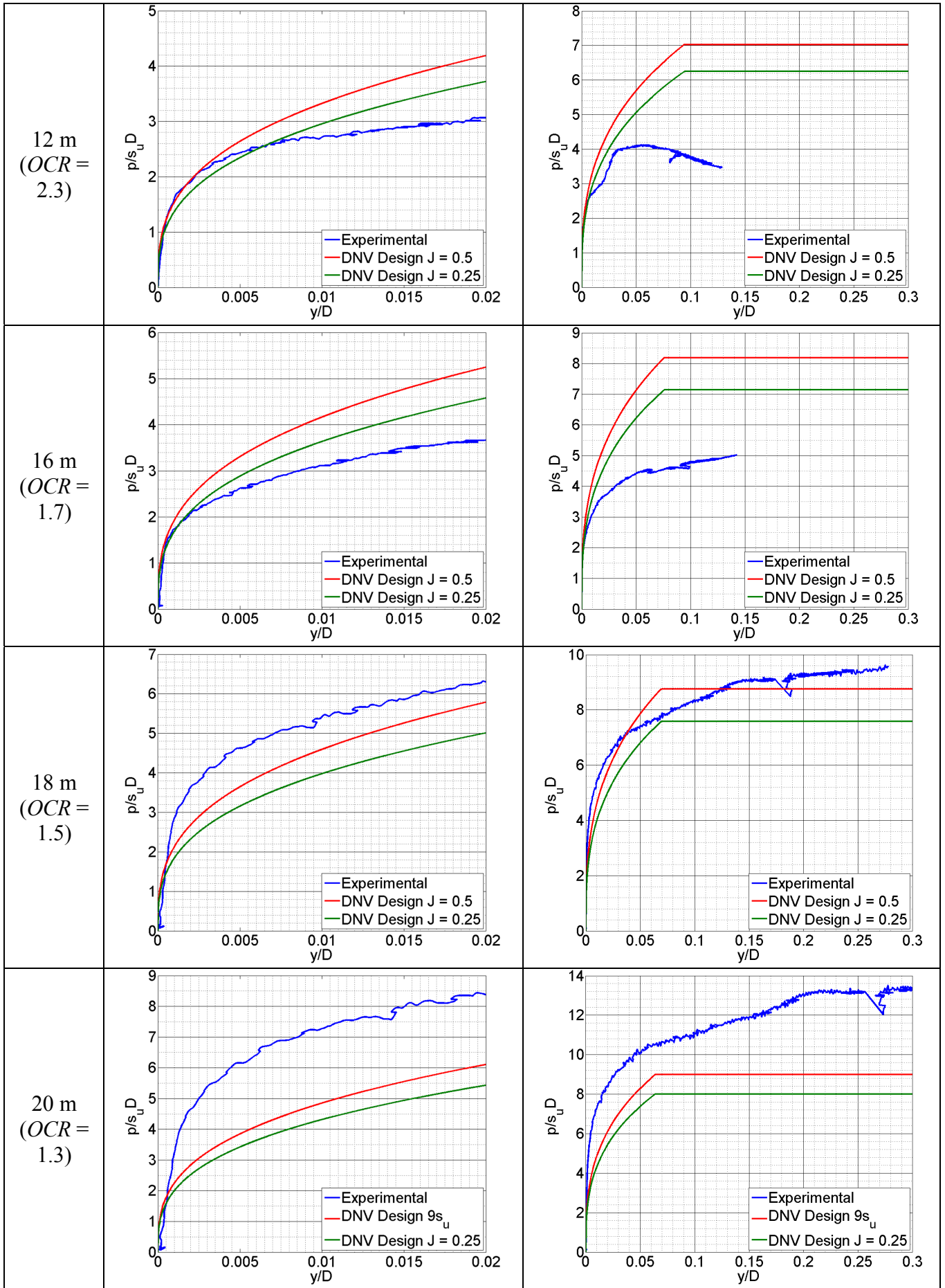
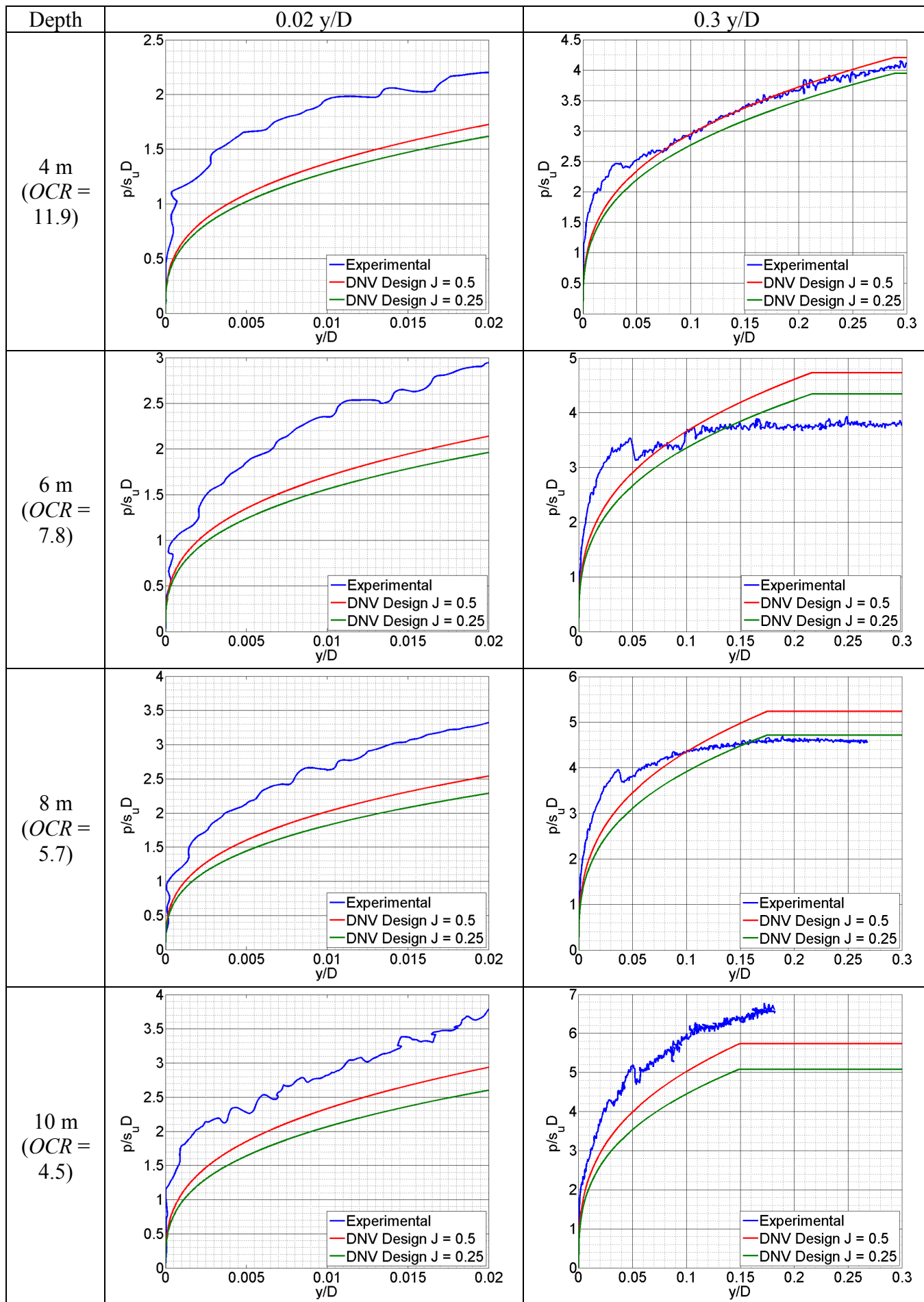


Figure 4.12 Experimental vs. DNV Design p - y Curves of OWF 03 – 180 kPa Preconsolidated



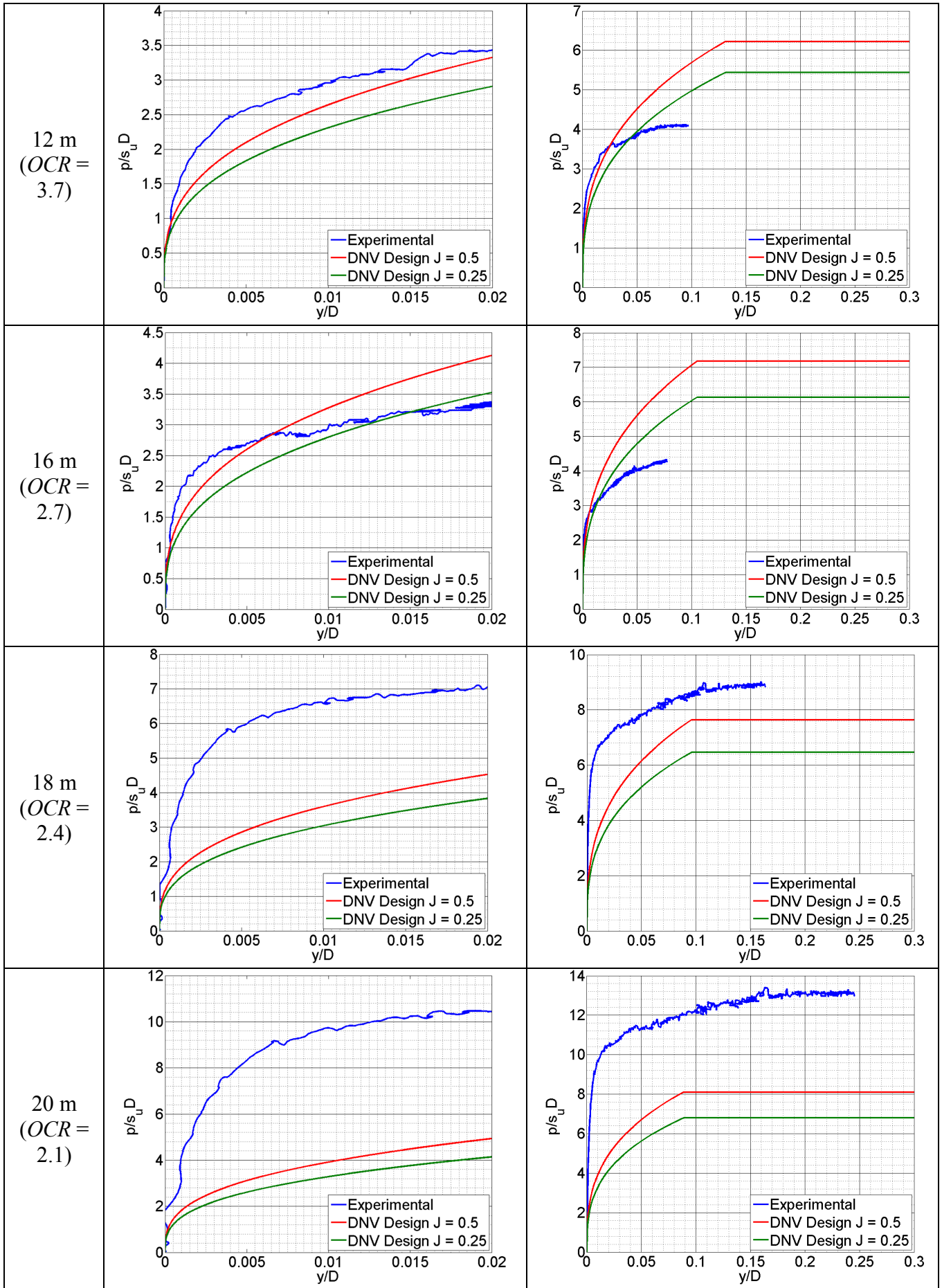
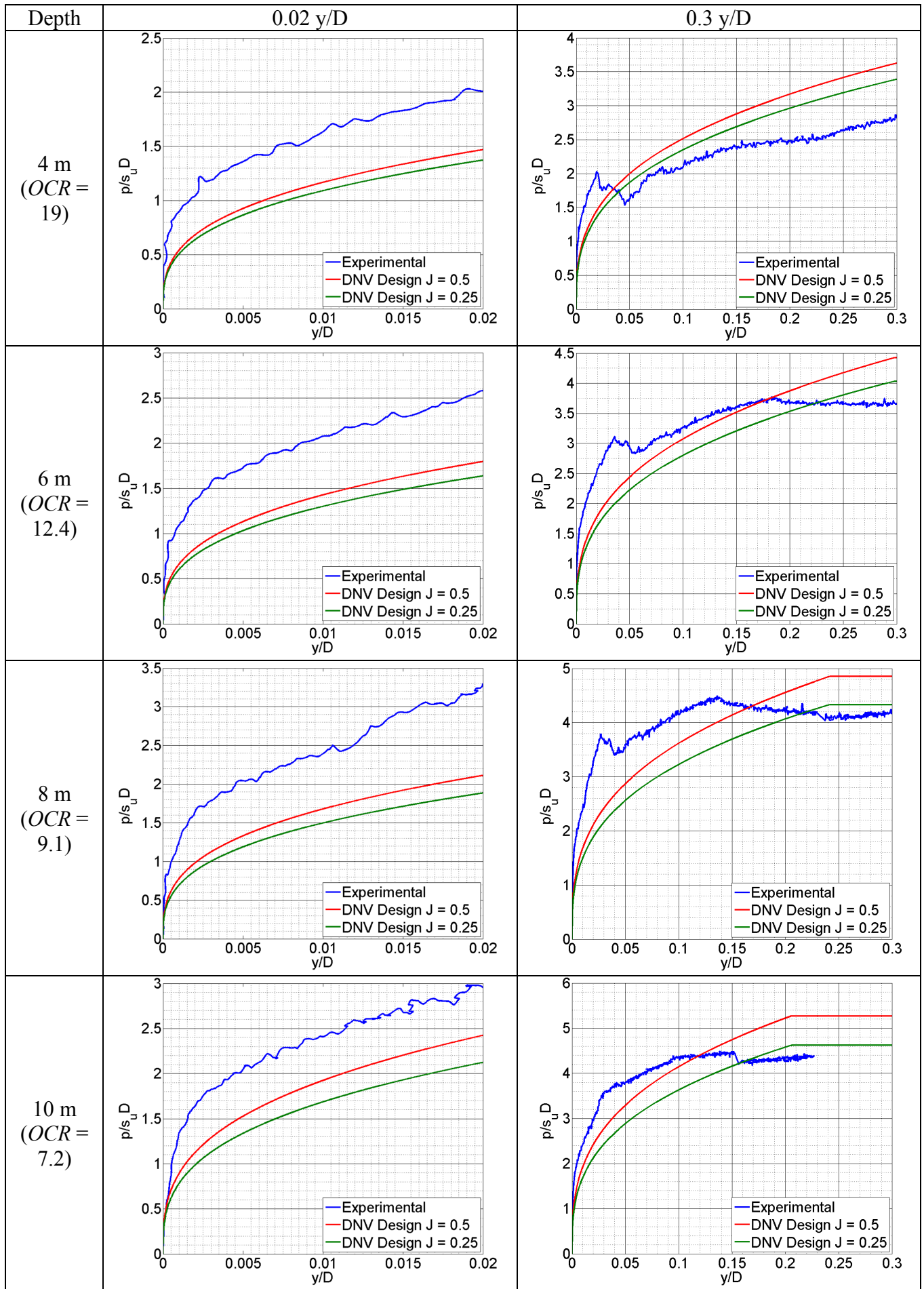


Figure 4.13 Experimental vs. DNV Design p - y Curves of OWF 01 – 300 kPa Preconsolidated



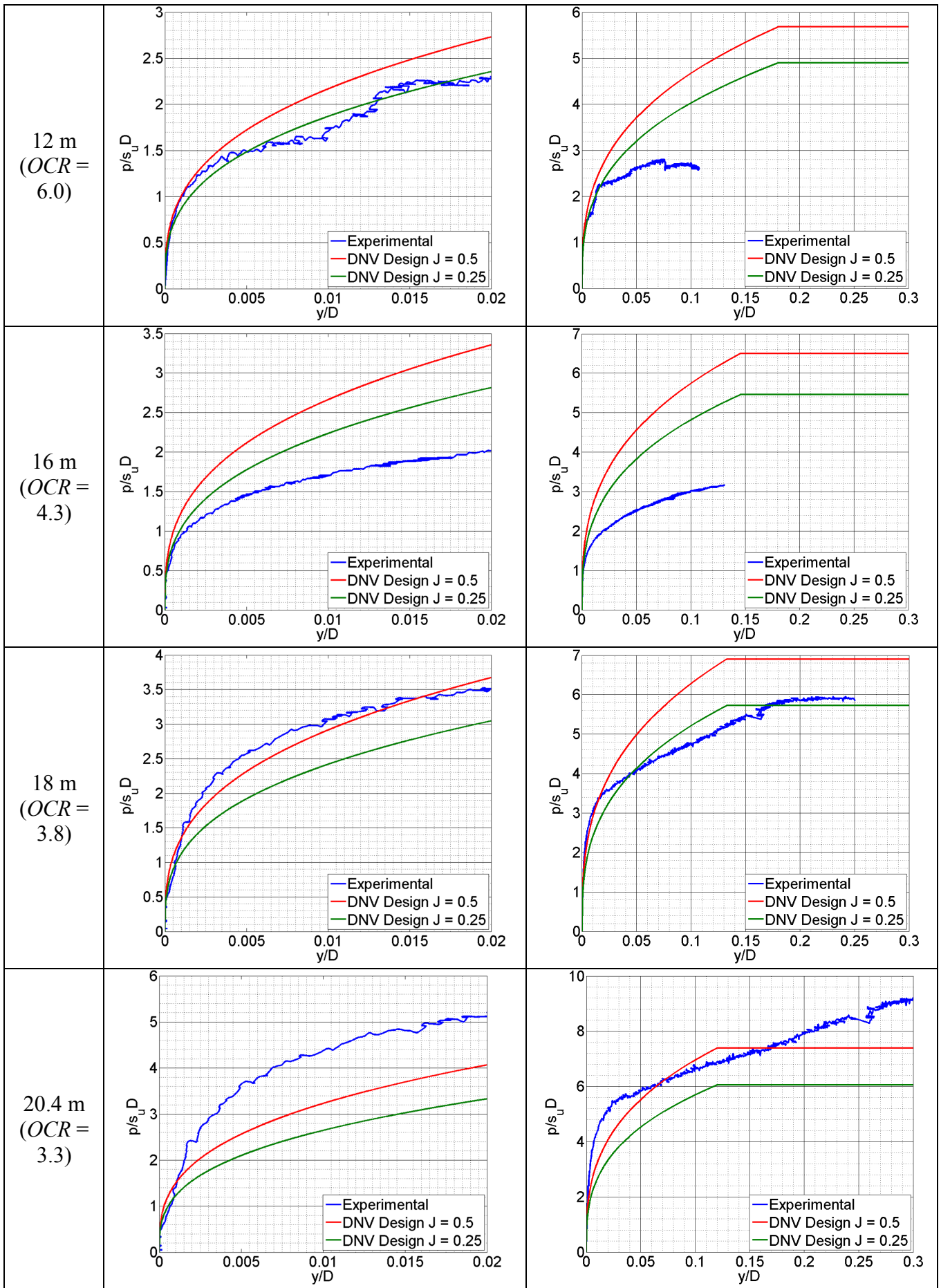


Figure 4.14 Experimental vs. DNV Design p - y Curves of OWF 02 – 500 kPa Preconsolidated

4.4.2 Experiment vs. DNV Design Load-Displacement Comparison

To evaluate the monopile's response under lateral loading using the DNV design p - y curves, the lateral pile response computer program LPILE (Reese and Van Impe, 2001) was utilised. The monopile was modelled to follow the experimental setup with the section properties listed in Figure 4.15. The soil was divided into 10 equally spaced layers and the DNV design p - y curves were manually inputted into the program. The ultimate soil reaction at depths with $OCR \geq 4$ was calculated by utilising a J value of 0.25 in equation (2.11) while a J value of 0.5 was utilised at depths where $OCR < 4$.

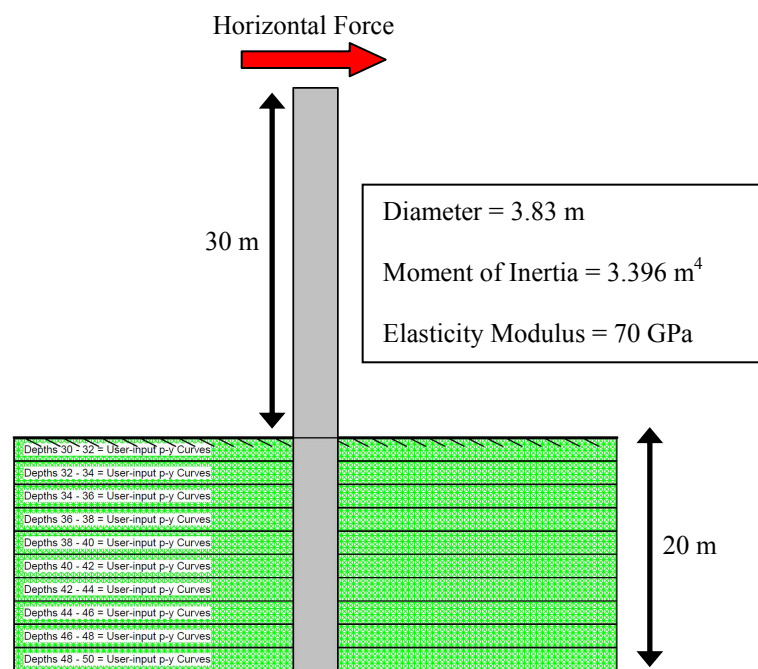


Figure 4.15 LPILE Analysis Setup

As shown in Figure 4.16, the soil surface bending moment (M_{soil}) should include the moment resulting from the horizontal force acting at the top ($F_x h$) of the pile and the moments resulting from the vertical forces (both self weight, W_{pile} + counterweight force, W_{c-w}) as the displacement at the monopile top increases throughout the pushover. A plot of load cell force vs. moment at soil surface as shown in Figure 4.17 indicates that there was little contribution from the vertical forces above the soil to the moment at the soil surface, moments from self weight and counterweight forces having cancelled each other out.

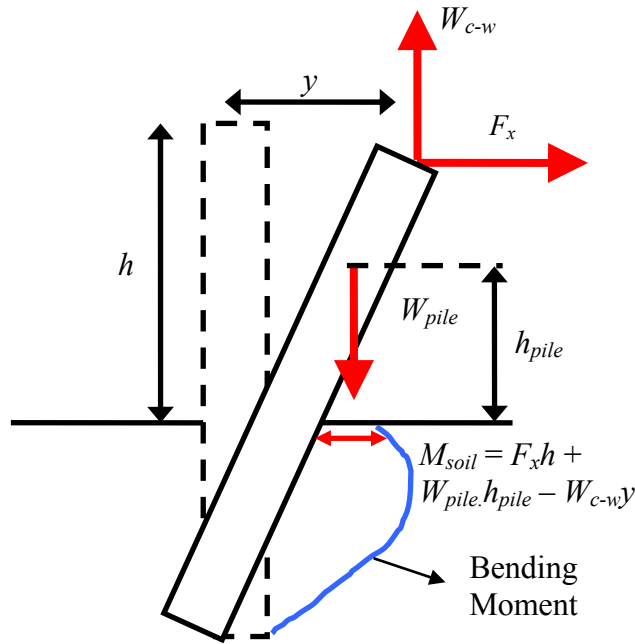


Figure 4.16 Free Body Diagram of Centrifuge Test

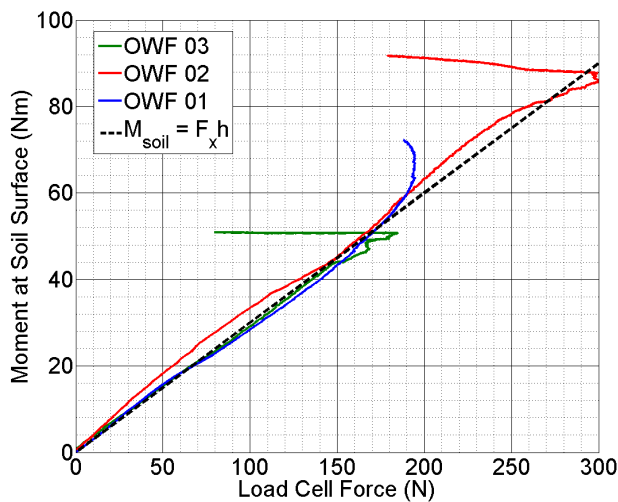


Figure 4.17 Load Cell Force vs. Moment at Soil Surface

As a result, all LPILE analysis of the monopile was carried out with a zero vertical load condition with the exception of test OWF 09 involving the 7.62 m monopile without a counterweight system attached. This should not undermine the integrity of the analysis as the finite element analysis carried out by Haiderali et al. (2013) indicates that axial load does not significantly influence the monopile's ultimate lateral capacity or lateral displacements unless the axial load was close to the axial capacities of the monopile.

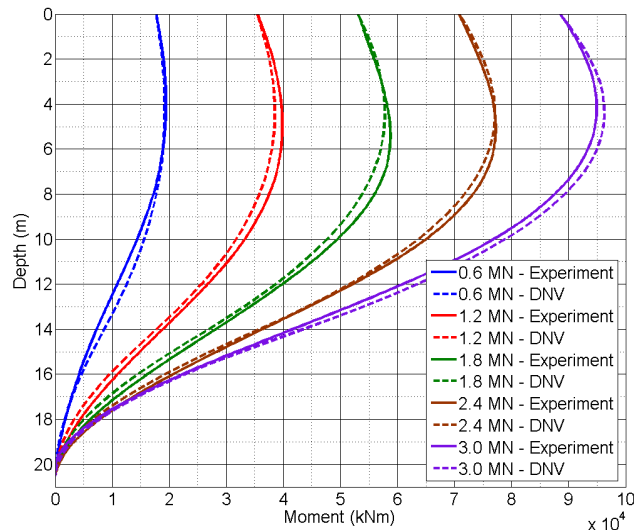
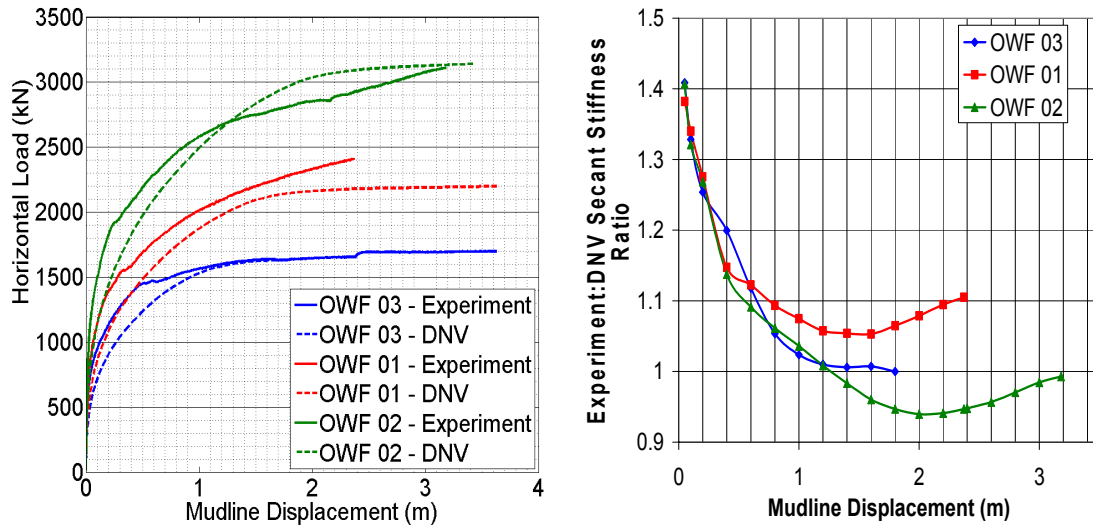


Figure 4.18 OWF 02 Bending Moment Comparison between Experiment and DNV Design in Prototype Scale

Figure 4.18 depicts the bending moment comparison between experimental observations in OWF 02 and LPILE calculated moment curves utilising the DNV design criteria. It can be seen that the LPILE bending moment curves are very similar to those observed in the experiment, with little difference in values. This was also observed in experiments OWF 01 and OWF 03. Besides producing similar bending moment curves, LPILE predicts that the monopile behaves as a semi-flexible pile that both flexes and rotates at 70% of the pile depth, similar to the experimental observations in Figure 4.9 and Figure 4.11.

Despite the similarities in the bending moment curves, the load-displacement output resulting from the DNV design methodology displayed a much softer response, as can be seen in Figure 4.19(a). The similarity in bending moment distribution implies that LPILE is calculating the correct lateral resistance profile from the DNV p - y curves. The underestimate in global initial stiffness suggests that while the stiffness distribution along the pile is broadly correct, the stiffness of all p - y curves should be increased. Figure 4.19 (b) shows that the experimental curves display secant stiffness 30% to 40% greater than the DNV design output. However, as the pushover continues, the experimental secant stiffness reduces and converges with the DNV design output. This observation is consistent with the observations seen in the experimental p - y curves of Figure 4.12 to 4.14 that display a greater initial stiffness but eventually soften to the DNV calculated ultimate soil reaction values.



(a) Horizontal Load vs. Mudline Displacement (b) Secant Stiffness
 Figure 4.19 Load-Displacement and Stiffness Comparison between Experiment and DNV Design

Assuming a monopile-wind turbine system is designed as a “soft-stiff” structure according to the DNV design methodology in soil similar to overconsolidated speswhite kaolin, the actual lateral stiffness of the system would be 40% stiffer than that designed for. As a result, the natural frequency will be greater than estimated. Based on these results, the DNV design curves may be inappropriate for cyclic loading design as the initial soil soil-foundation stiffness is significantly underestimated. Considering that the initial soil-foundation stiffness may be significantly underestimated, there is a strong need to characterise the p - y curves and investigate the influence that the pile toe shear force, F_{shear} has on the monopile’s lateral behaviour.

4.4.3 Characterising Monopile p - y Curves

Characterisation of the experimental p - y curves was first done by fitting a linear equation to p - y curves on a log-log axis as shown in Figure 4.20, resulting in a power-law relationship. Based on the average obtained from the linear fittings across the three experiments, the p - y curves generally have a power of 0.29, only slightly lower than Matlock’s (1970) value of 1/3.

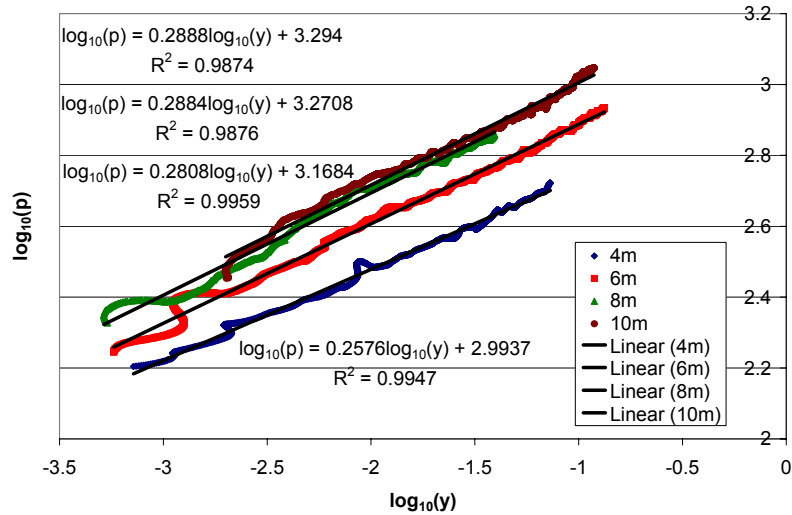


Figure 4.20 Logarithmic Plot of p - y Curves for OWF 02

A review of Figures 4.12 to 4.14 indicates that the ultimate soil reaction is well estimated by Matlock's (1970) equation (equation (2.11) in section 2.6.1) utilising a J value of 0.5 for normally consolidated clays and a value of 0.25 for heavily overconsolidated clays. Considering that Matlock's equation estimates the ultimate soil reaction very well, the next step was to determine the displacement (relative to Matlock's definition of y_c) at which the ultimate soil reaction was mobilised. Out of all the p - y curves above the rotation point across the three experiments as shown in Figures 4.12 to 4.14, the OWF 03 p - y curves at 4 m, 6 m, and 8 m depths provide the clearest indication that the ultimate soil reaction is mobilised at approximately $4y_c$. Considering this, equation (2.12) was modified as shown in equation (4.6).

$$p = \begin{cases} \frac{P_u}{4^{0.29}} \left(\frac{y}{y_c} \right)^{0.29} & \text{for } y \leq 4y_c \\ P_u & \text{for } y \geq 4y_c \end{cases} \quad (4.6)$$

Utilising Equation (4.6), modified DNV curves were plotted against the experimental p - y curves as shown in Figures 4.21 to Figure 4.23. Soil reaction was normalised to $s_u D$ while displacements were normalised to y_c (where $y_c = 2.5 \varepsilon_c D$). Comparisons were not done with the 12 m and 16 m p - y curves as the curves were distorted due to their close proximity to the rotation point.

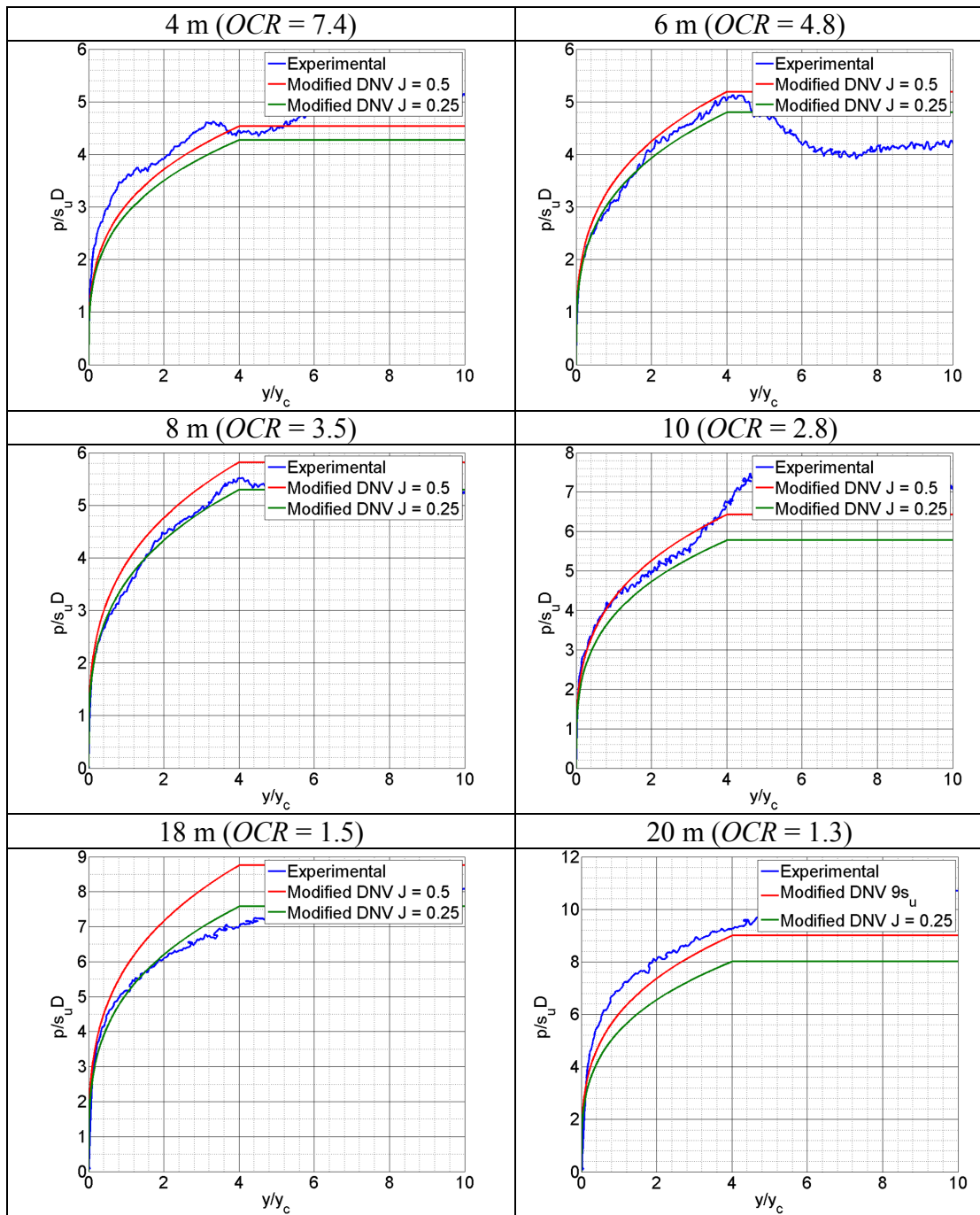


Figure 4.21 Experimental vs. Modified DNV Design p - y Curves of OWF 03 – 180 kPa Preconsolidated

As shown by Figures 4.21 to 4.23, the initial stiffness of the experimental p - y curves from 4 m to 10 m depths are well captured by the modified DNV curves. From the graphs, a J value of 0.25 should be utilised at depths where $OCR \geq 4$ while a J value of 0.5 should be utilised at depths where $OCR < 4$ as curves produced based on this criteria would help achieve a good balance between capturing stiffness and estimating the ultimate soil reaction available. For example, even though the $J = 0.25$ curve of

the 8 m curve of Figure 4.22 is slightly softer than both experimental and $J = 0.5$ p - y curve, the ultimate soil reaction is better estimated. This can also be seen in the other p - y curves of Figure 4.22 and Figure 4.23.

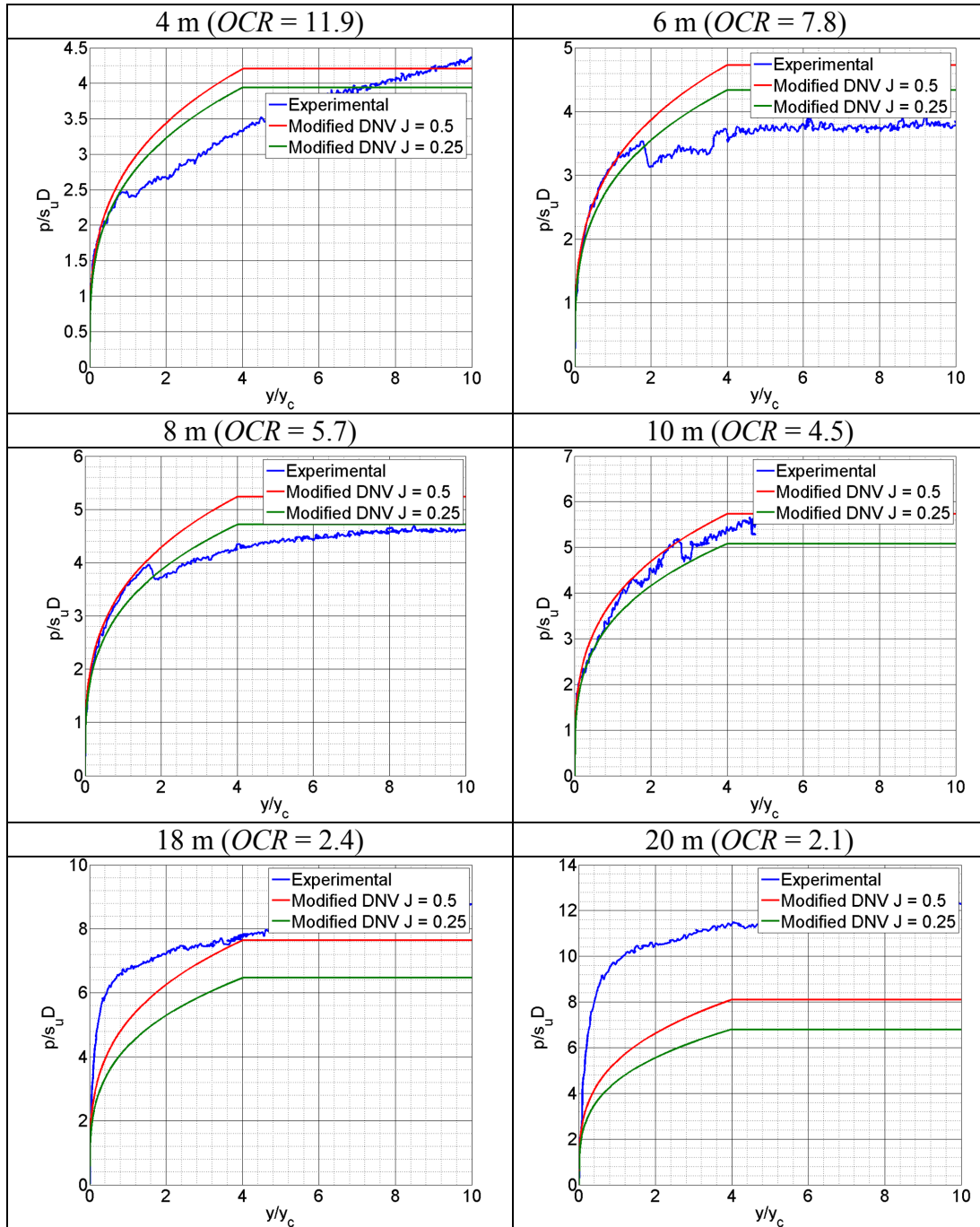


Figure 4.22 Experimental vs. Modified DNV Design p - y Curves of OWF 01 – 300 kPa Preconsolidated

With the exception of OWF 01, the Modified DNV curves near the pile toe also seem to capture the general shape and the initial stiffness of the experimental p - y curves very well until a displacement of approximately y_c . Though there is a divergence due

to the influence of the shear force acting at the pile toe, the curves suggest that the shear force is not fully mobilised immediately from the beginning of the pushover but builds up as the pushover proceeds.

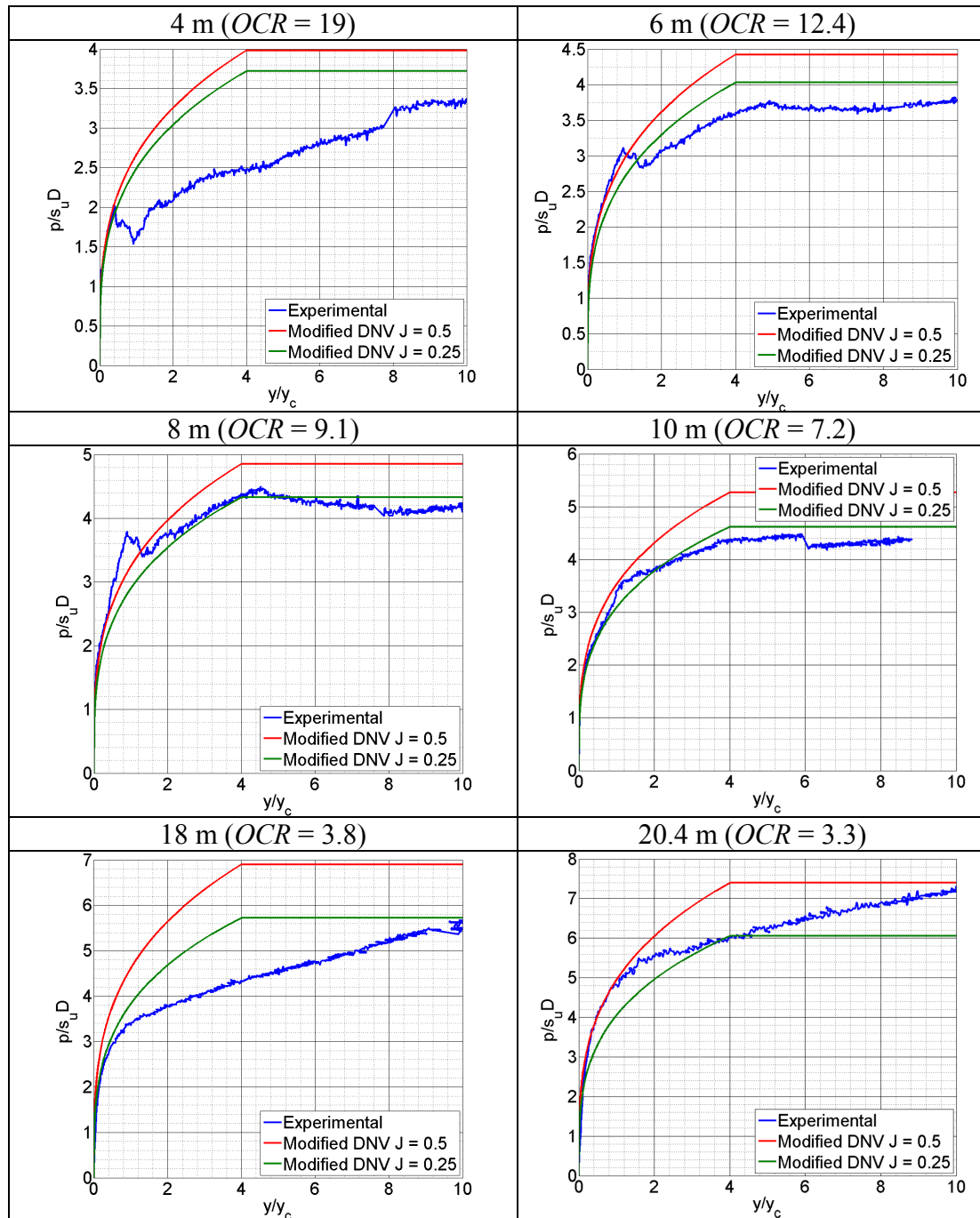


Figure 4.23 Experimental vs. Modified DNV Design p - y Curves of OWF 02 – 500 kPa Preconsolidated

Figure 4.24(a) displays a comparison of the horizontal load vs. mudline displacement curves between the experimental observations and the LPILE output based on the modified DNV criterion. An exponential power of 1/3 was also utilised for

comparison. Based on Figure 4.24(a), the ultimate load capacities are fairly well captured by the modified DNV criterion curves with exponential powers of 0.29 and 1/3, indicating that the change in power has a minor effect on results. Though the curves resulting from the Modified criterion are slightly stiffer relative to the experimental curves, the general shape of the experimental load-displacement curve is still well captured up to a mudline displacement of 0.3 m, significantly greater than might be allowed in design.

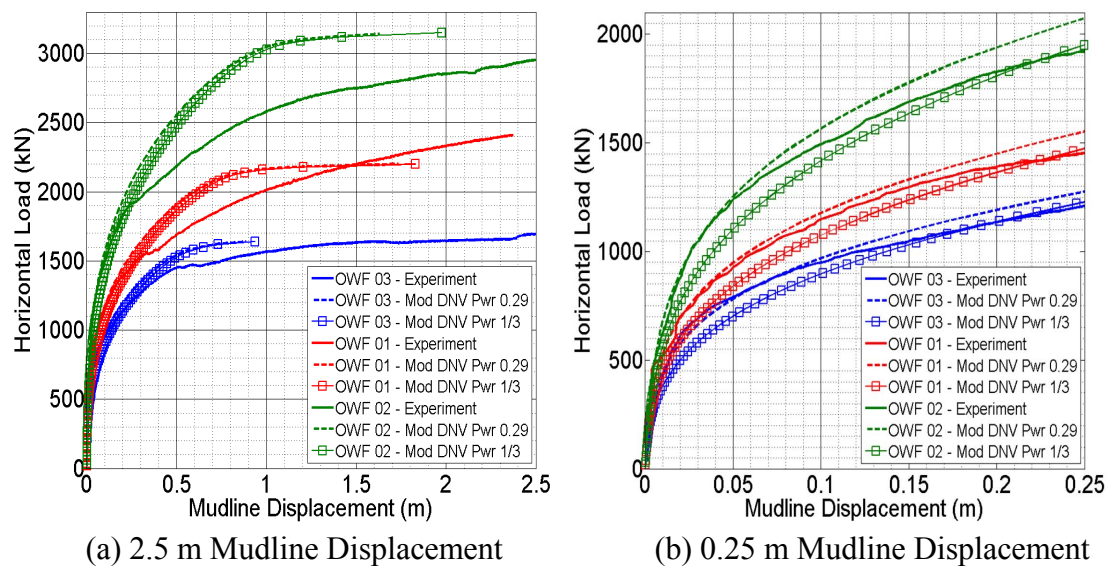


Figure 4.24 Horizontal Load vs. Mudline Displacement Comparison between Experiment and Modified DNV Design

Figure 4.24(b) displays the same curves for mudline displacements less than 0.25 m. According to Achmus et al. (2009), a maximum permanent rotation of a monopile at mudline of 0.5° has been specified in recent projects. If the depth of rotation is 14 m, this corresponds to a mudline displacement of 0.12 m. Based on Figure 4.24(b), the stiffness of the experimental curves are slightly better captured with an exponential power of 0.29 as the output resulting from an exponential power of 1/3 are softer. Even though the general shape is captured, the results suggest that the usage of an exponential power of 0.29 for the p - y curves better captures the monopile-soil stiffness.

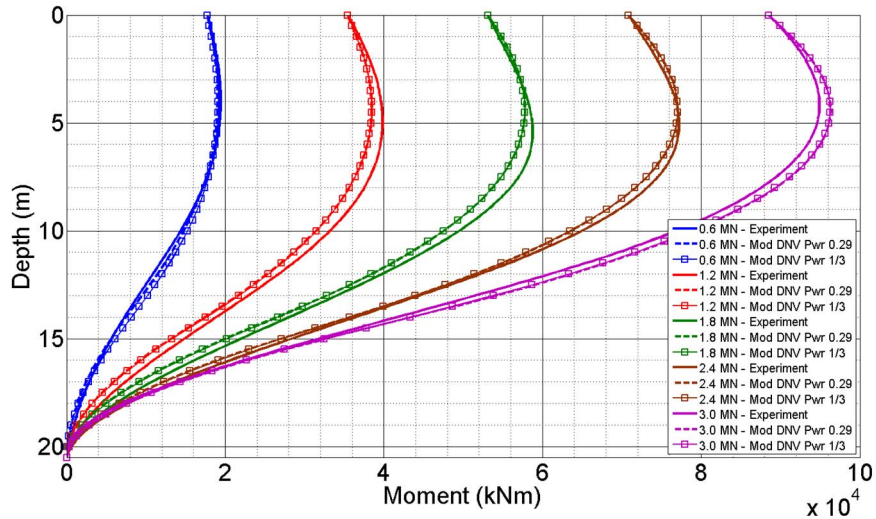


Figure 4.25 OWF 02 Bending Moment Comparison between Experiment and Modified DNV Design in Prototype Scale

The general shape of the bending moment curves are still well estimated by the modified DNV criterion as shown in Figure 4.25 for experiment OWF 02. There is very little difference between the bending moment curves resulting from the usage of an exponential power of 0.29 and 1/3 to construct the p - y curves. The curves resulting from the modified DNV criterion have slightly lower values as shown in Figure 4.25, with differences observable starting from a depth of 4 m. It is possible that the differences in bending moment are due to effects of pile toe shear force, F_{shear} that have yet to be accounted for. The effects of F_{shear} and its characterisation will be discussed in the subsequent sections.

4.4.4 Comparison to Other Criteria for Constructing p - y Curves for Clay

As discussed in the previous section, not only do the experimental p - y curves mobilise p_u at $4y_c$ instead of $8y_c$, the curves also increase at an exponential power of 0.29 instead of 1/3. Considering the differences, reference was made to the Unified Clay criterion (Sullivan et al., 1980) and Integrated Clay criterion (Gazioglu and O'Neill, 1984) that were mentioned in sections 2.6.3 and 2.6.4 respectively.

As highlighted by the alternative criteria suggested by Sullivan et al. (1980) and Gazioglu and O'Neill (1984), the constant utilised in the calculation of the reference deflection y_c is not a fixed number of 2.5 as suggested by Matlock (1970), but a variable number that is dependent on the properties of the soil in question. Depending

on the soil in question, the value utilised as the constant to calculate y_c can be lower than 2.5. Based on equation (4.6), if y_c is $2.5\varepsilon_c D$, $0.67p_u$ is mobilised at a displacement of y_c . However, this is not in line with the definition of y_c since $0.5p_u$ is not mobilised at y_c . To determine the displacement at which $0.5p_u$ is mobilised, equation (4.6) can be resolved as follows:

$$\left(\frac{y}{y_c}\right)^{0.29} = 0.5 \times 4^{0.29} \quad (4.7)$$

Based on the above equation, $0.5p_u$ is mobilised at y of $0.3665y_c$. This in turn redefines the constant to calculate the reference deflection from 2.5 to a lower value of 0.916 for the tested speswhite kaolin. Relative to the constants recommended by Sullivan et al. (1980) of 2.5 for normally consolidated clays similar to the Sabine River site and of 0.35 for heavily overconsolidated clays similar to the Manor site, the constant is in between the recommended constants. Even though the speswhite kaolin was heavily overconsolidated as the Manor site, it is possible that the differences in soil properties between the two soils such as plasticity index, liquidity index, and sensitivity contributed to the differences in constants. Since the constant to calculate can vary based on soil properties, Sullivan et al. (1980) suggests that the constant be estimated using judgement should the soil properties differ from the Sabine River and Manor clays.

An evaluation of y_c was carried out based on the definition of y_c (equation (2.31) of section 2.6.4) provided by Gazioglu and O'Neill (1984). The secant soil stiffness at half the deviator stress at failure in UU triaxial compression, E_s was estimated based on the values provided in Table 2.5 that linked s_u with E_s . Based on equation (2.31), it was determined that the constant A' was 0.4 for the tested speswhite kaolin. This value is similar in magnitude to the values that Gazioglu and O'Neill (1984) observed at their sites at Sabine, Texas and Harvey, Los Angeles that were approximately normally consolidated clays. However, the speswhite kaolin in the experiment was a heavily overconsolidated clay. This indicates that A' may be a function of other factors besides overconsolidation ratio, as highlighted by Sullivan et al. (1980) who recommended that various soil properties be considered in the estimation of the constant to calculate y_c .

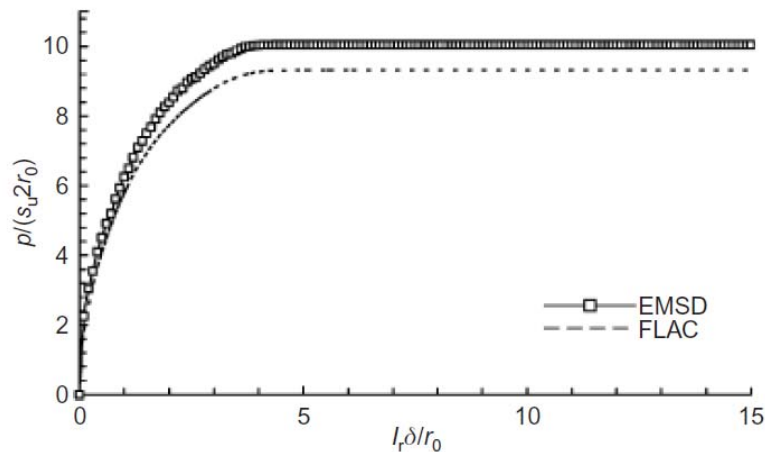


Figure 4.26 Smooth Pile Comparison between EMSD and Finite Difference Method for Truncated Power Law (Klar and Osman, 2008)

Results from other researchers suggest that the constant to calculate y_c is constant and is not dependent on soil properties. Skempton (1951) defined y_c as $2\varepsilon_c D$ based on his work to estimate settlement of a circular footing in saturated clays with no water content change under applied stress whereas Klar and Osman (2008)'s analysis on the new extended mobilisable strength design (EMSD) work as shown in Figure 4.26 would result in a y_c that is approximately $1.5\varepsilon_c D$. Relative to the experimental results and considering the work of Sullivan et al. (1980) and Gazioglu and O'Neill (1984), the results suggest that the constant to calculate y_c is dependent on the properties of the soil in question.

Since the results suggest that the constant to calculate y_c is dependent on the properties of the soil in question, it is suggested that y_c be reformulated as $2.5\alpha\varepsilon_c D$, where α is a constant that is dependent on the soil in question. Based on Sullivan et al. (1980), $0.14 \leq \alpha \leq 1$. Based on the experimental results, α is 0.367 for overconsolidated speswhite kaolin. Since no change was required to α to characterise the experimental p - y curves, α appears to be unaffected by overconsolidation ratio. However, α may be dependent on other soil characteristics that are unknown since no data is available. Assuming α for a clay in question is as low as 0.14 as suggested by Sullivan et al. (1980) for the Manor site, monopile design with the assumption that α is 1 would produce a system with stiffness 76% greater than estimated. As a result, the actual natural frequency of the system would be greater than estimated. Therefore, it is crucial that an appropriate α be utilised in design to better estimate the stiffness of

the system. Since no data is available on regarding the factors that may influence α , further research involving centrifuge or field tests should be carried out.

4.4.5 Recommendations for p - y Curve Construction for Static Loading

Based on the findings, the following methodology is recommended for constructing static loading p - y curves for design:

1. Calculate the ultimate lateral resistance, p_u utilising equation (2.11) of section 2.6.1. J of 0.5 should be used for lightly or normally consolidated soils with $OCR < 4$ and a J of 0.25 for heavily overconsolidated soils with $OCR \geq 4$.
2. Calculate the reference deflection, y_c at which 50% of the ultimate soil reaction is mobilised. y_c is $2.5\alpha\varepsilon_c D$, where α is a constant that is dependent on the soil in question. Based on Sullivan et al. (1980), $0.14 \leq \alpha \leq 1$
3. Calculate the static loading p - y curves utilising as below:

$$p = \begin{cases} \frac{p_u}{2} \left(\frac{y}{y_c} \right)^{0.29} & \text{for } y \leq 10.92y_c \\ p_u & \text{for } y \geq 10.92y_c \end{cases} \quad (4.8)$$

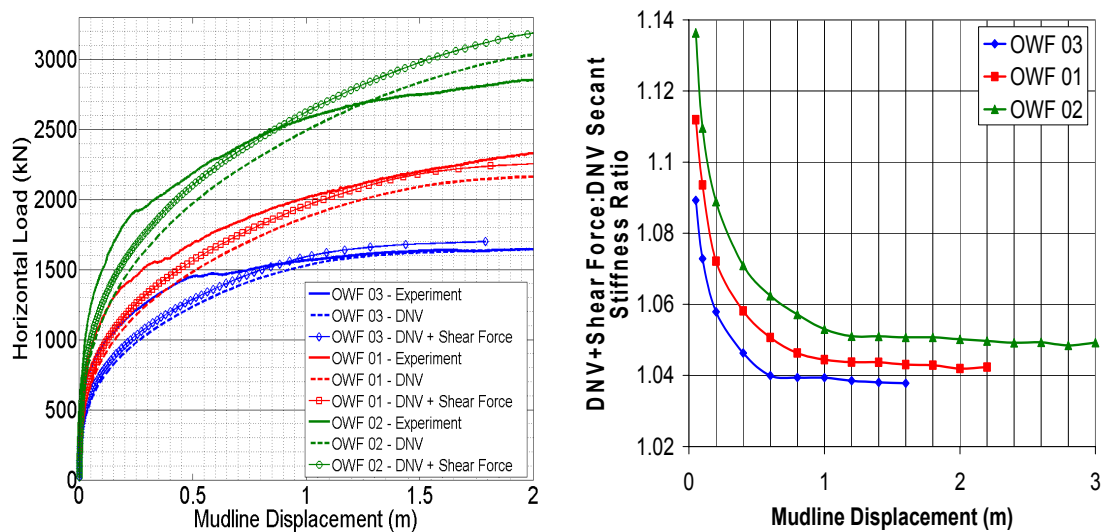
4.5 Pile Toe Shear Force

Since the monopile behaves as a short and rigid pile, it rotates at depth and produces a toe-kick that generates a shear force at the pile toe. The shear force at the pile toe will contribute to the pile's lateral resistance (Lau et al., 2014, Abdel-Rahman and Achmus, 2005, Brødbæk et al., 2009). However, at this point of time, it is unknown how much additional resistance is provided by the shear force as there are no publications on how to characterise the shear force as a function of deflection.

4.5.1 The Effect of Pile Toe Shear Force on Pile Lateral Behaviour

To study the influence of shear force on the monopile's lateral behaviour, a shear resistance of $A_{\text{comb}}S_u$ (where A_{comb} is the combined cross-sectional area of monopile and enclosed soil plug) was used together with the DNV design p - y curves in LPILE.

This corresponded to base shear force values of 457 kN, 696.2 kN, and 1070.5 kN for experiments OWF 03, OWF 01, and OWF 02 respectively. The shear force was defined as being fully mobilised throughout the pushover. As shown by Figure 4.27(a), the presence of a shear force at the pile toe does increase the lateral resistance of the monopile and based on Figure 4.27(b), the monopile initially experiences 9% to 14% greater stiffness. However, the increase in stiffness quickly drops to around 4.5% at a mudline displacement of 0.5 m.



(a) Horizontal Load vs. Mudline Displacement (b) Secant Stiffness Comparison

Figure 4.27 Load-Displacement and Stiffness Comparison between Experiment, DNV Design and DNV Design with Pile Toe Shear Force

Though there is a significant “toe-kick” to generate a shear force at the pile toe, the results of Figure 4.27 suggest that the shear force does not contribute significantly to the ultimate lateral resistance of the monopile. Soil reaction curves resulting from the “DNV” and “DNV + Shear Force” in OWF 01 soil strength conditions as shown in Figure 4.28(a) were reviewed to determine the cause behind the limited contribution. As shown in Figure 4.28(a), base capacity contributes little to ultimate lateral resistance as only 25% of the pile length (that is below the rotation point) mobilises less lateral resistance. Base capacity also pulls the rotation depth slightly deeper towards the pile toe. Bending moment curves resulting from the “DNV” and “DNV + Shear Force” in OWF 01 soil strength conditions are shown in Figure 4.28(b). Based on Figure 4.28(b), the shear force causes a slight increase in bending moment starting from a depth of 5 m. The greatest difference in bending moment occurs at depths of approximately 16 m to 18 m, close to the pile toe.

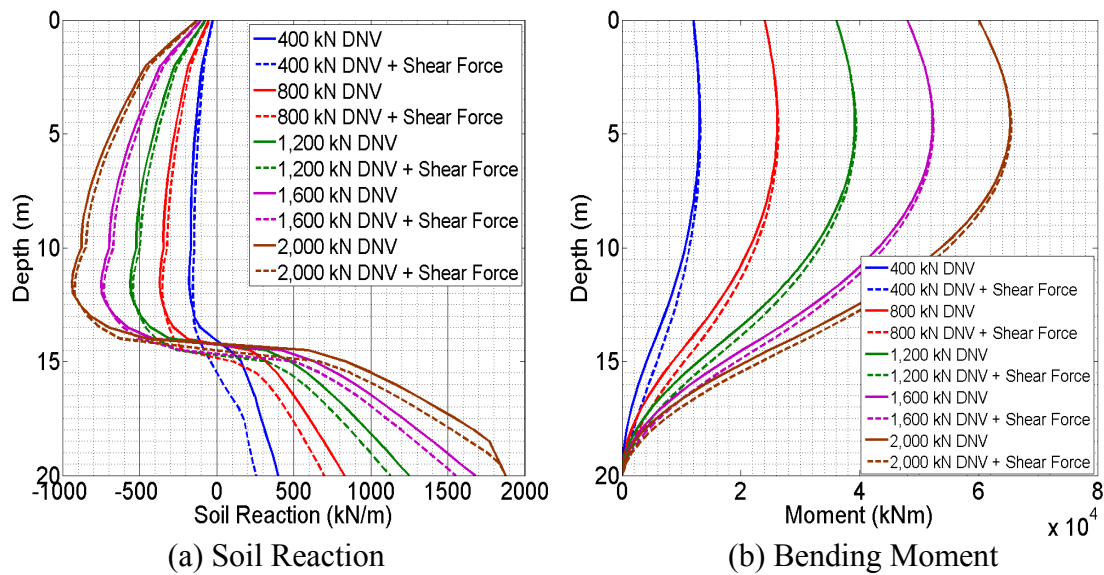


Figure 4.28 OWF 01 Soil Comparison between DNV and DNV + Shear Force

Based on Figures 4.27 and 4.28, shear force does not contribute significantly to the ultimate lateral resistance of the monopile and its effects on both stiffness and bending moments are minimal. Since monopile design to resist bending moments is dictated by the largest moment closer to the soil surface, slight increases in bending moments towards the pile toe by the shear force would be of little concern. Though concern has been raised by Brødbæk et al. (2009) regarding the role of pile toe shear force in monopile design, the figures suggest that the effects of pile toe shear force are minimal and may not need to be included in design. However, the effects of shear force may have to be considered for much stubbier structures that have much larger widths and lower slenderness ratios.

4.5.2 Characterising the Pile Toe Shear Force

Even though the pile toe shear force, F_{shear} does not significantly improve the monopile's lateral resistance, it does enhance the mobilisation of capacity at low displacements as seen in Figure 4.28(a) as well as affecting bending moments to some extent. It is hence of some interest to characterise this force.

Since soil is not a linearly elastic perfectly plastic material, it can be assumed that the shear force increases exponentially with displacement, similar to the p - y curves. To determine which exponent provided the best fit, F_{shear} curves that increased exponentially by powers of 0.1, 0.2, and 0.3 were used in LPILE. The displacements

at which shear force was fully mobilised were also varied to determine the effect displacement had. Following that, the bending moment vs. pile toe displacement curves at depths of 17 m and 18 m were then compared with the experimentally observed curves. An example of this is shown in Figure 4.29 for test OWF 03. To be consistent with experimental findings, y_c is defined as $0.916\varepsilon_c D$.

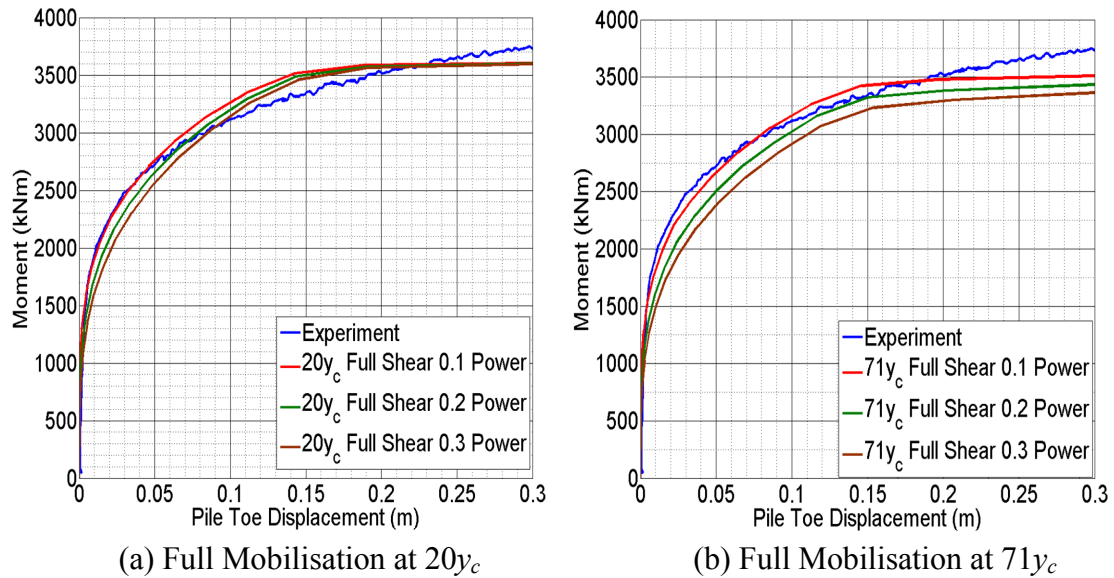


Figure 4.29 OWF 03 Bending Moment Curves at 18 m Depth showing Different Exponential Powers and Displacements for Shear Force Mobilisation

As shown in Figure 4.29, an exponential power of 0.1 seems to fit the experimental curve. In addition, the curves also show that the displacement at which F_{shear} is fully mobilised does very little to influence the stiffness of the curves. Though an exponential power of 0.1 fits the bending moment curve of OWF 03, an exponential power of 0.3 and 0.2 provides a better fit for experiment OWF 01 and 02 respectively, as seen in Figures 4.30 to 4.31. Based on the results, the power the shear force increases exponentially by ranges from 0.1 to 0.3. However, an exponential power of 0.2 appears to be an appropriate fit that would match across the three experiments even though it may overestimate the bending moments as seen in Figure 4.30.

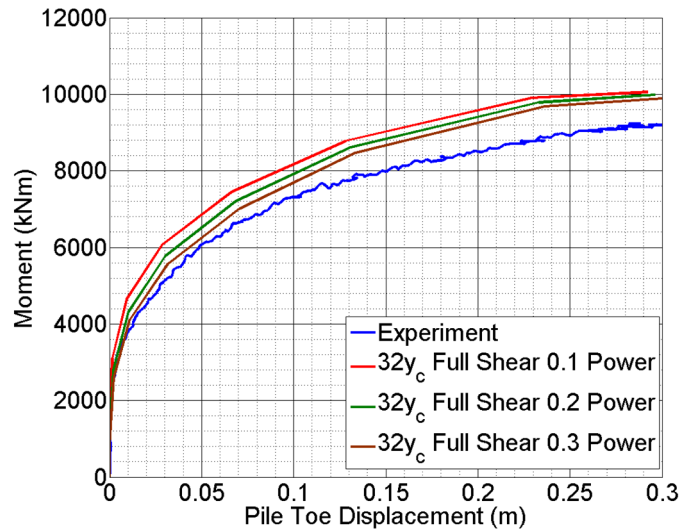


Figure 4.30 OWF 01 Bending Moment Curves at 17 m Depth Comparison for Shear Force with Different Exponential Powers at $32y_c$ Full Mobilisation

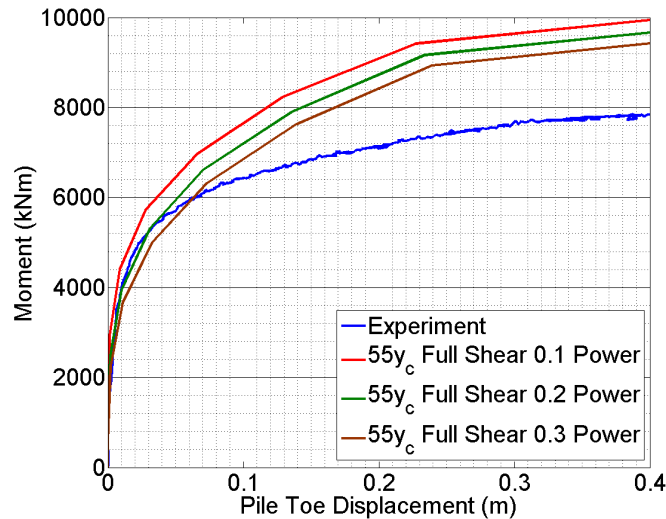


Figure 4.31 OWF 02 Bending Moment Curves at 18 m Depth Comparison for Shear Force with Different Exponential Powers at $55y_c$ Full Mobilisation

A review of the p - y curves at the pile toe of Figures 4.12 to 4.14 was carried out to determine the displacement at which F_{shear} was fully mobilised, $y_{shear\ full}$. Figure 4.32 shows the experimental pile toe curves plotted on the same figure and expanded to a larger scale. As a reminder, the pile toe displacement was normalised to Matlock's (1970) definition of y_c of $2.5\epsilon_c D$. As shown in Figure 4.32, it can be observed that the soil reaction eventually flattens off and plateaus as the pushover comes closer to reaching its end. The plateau is achieved at pile toe displacements of approximately $25y_c$, $15y_c$, and $20y_c$ for experiments OWF 03, OWF 01, and OWF 02 respectively. By taking an average, the results suggest that F_{shear} is fully mobilised at an average displacement of $20y_c$.

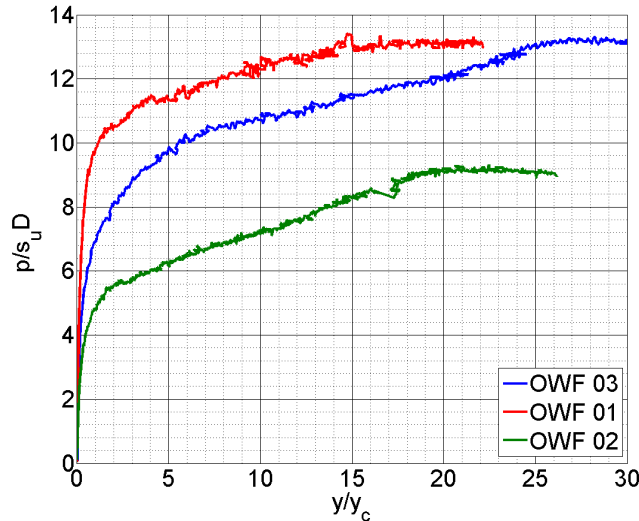


Figure 4.32 Experimental Pile Toe Normalised p - y Curves

If y_c is defined as $0.916\varepsilon_c D$ based on experimental findings for speswhite kaolin, this would translate to an average displacement of $55y_c$ (as utilised in Figure 4.31). However, as shown in Figure 4.29, $y_{shear\ full}$ has little influence on the resulting bending moments. Therefore, the need to accurately define the reference deflection at which $0.5F_{shear}$ is mobilised is low. In addition, it is not possible to accurately define the reference deflection at which $0.5F_{shear}$ is mobilised since the exponential power the shear force increases exponentially by ranges from 0.1 to 0.3. Considering this, the shear reference deflection, $y_{shear\ ref}$ can be set equal to y_c even though the proportion of F_{shear} mobilised would vary based on the exponential power and the $y_{shear\ full}$ selected to construct the F_{shear} curve.

4.5.3 Recommendations for Constructing Pile Toe Shear Force Curve

Based on the findings, the following methodology is recommended for constructing the pile toe shear force curve.

1. Set the shear reference deflection, $y_{shear\ ref}$ to equal y_c of section 4.4.5.
2. Calculate $y_{shear\ full}$, the displacement at which F_{shear} is fully mobilised as follows:

$$y_{shear\ full} = \chi \cdot y_{shear\ ref} \quad (4.9)$$

where χ is a constant that varies based on α utilised to calculate y_c . χ is defined as:

$$\chi = \frac{20}{\alpha} \quad (4.10)$$

Since $0.14 \leq \alpha \leq 1$, therefore $20 \leq \chi \leq 143$.

3. Calculate the pile toe shear force curve as below:

$$F_{shear} = \begin{cases} \frac{A_{comb} S_u}{\chi^\beta} \left(\frac{y}{y_{shear\ ref}} \right)^\beta & \text{for } y \leq \chi \cdot y_{shear\ ref} \\ A_{comb} S_u & \text{for } y \geq \chi \cdot y_{shear\ ref} \end{cases} \quad (4.11)$$

where $0.1 \leq \beta \leq 0.3$.

4.6 Summary

The basis behind the selection of the undrained shear strength profile utilised in analysis and the methodology to derive the experimental p - y curves was explained to provide the foundation underlying the LPILE analysis. Based on the displacement curves, the monopile behaves as both a flexible pile that flexes and a short rigid pile that rotates at depth, producing an undesirable toe-kick that in turn generates a shear force at the pile toe. Experiment results indicated that the DNV (2014) design methodology greatly underestimated the lateral stiffness of the foundation, resulting in underestimation of the system's natural frequency. As a result, there was a strong need to characterise the p - y curves.

To characterise the experimental p - y curves, the DNV design methodology based on Matlock's (1970) recommendations for soft clays was modified and this in turn enabled better estimation of the monopile's lateral stiffness. LPILE results corresponded very well with the experimental curves within the maximum permanent rotation at mudline of 0.5° as specified by Achmus et al. (2009) and estimated the ultimate lateral load very well. However, the modified DNV methodology overestimates lateral stiffness beyond a permanent rotation at mudline of 1.0° . This

indicates that the modified DNV methodology may be suitable for monopile wind-turbine designs but may be unconservative for applications where ultimate lateral stiffness is of greater importance such as in the design of anchor piles.

Reference to literature indicates that the reference deflection, y_c at which 50% of the ultimate soil reaction is mobilised can vary widely and is dependent on the soil. Therefore, further research should be carried out to confirm how the constant varies relative to the soil properties. From experiment results, the constant that defines y_c appears to be unaffected by overconsolidation ratio.

Based on the LPILE study, the increase in lateral stiffness by the pile toe shear force, F_{shear} is marginal as the lateral resistance improving effects are limited to depths below the rotation point that account for 25% of the monopile's length. Therefore, the effects of F_{shear} are minimal and may not need to be considered in monopile design. Despite the marginal effects of F_{shear} , effort was made to characterise F_{shear} as F_{shear} was observed to enhance the mobilisation of capacity at low displacements and affect bending moments to some extent. As a result, recommendations and equations to characterise F_{shear} were developed based on experimental results. The recommendation may be suitable for the design of much stubbier structures that have much larger widths and lower slenderness ratios as F_{shear} may have a greater impact on the lateral behaviour.

CHAPTER 5

5. CYLIC TESTS RESULTS

5.1 Introduction

This chapter presents the cyclic test results of OWF 06 to OWF 09 and the corresponding analyses that are related to the cyclic behaviour of the monopile in clay. The main objectives of these tests are to better understand the different aspects of monopile cyclic behaviour and to also suggest recommendations that the industry can utilise when considering the cyclic aspect of monopile design. Experimental details of these tests can be found in section 3.5 that provides information on the vertical load condition, monopile diameter, and soil consolidation profile and section 3.7.4 regarding the centrifuge testing procedure and the cyclic loads applied.

5.2 Soil Strength Profile for Cyclic Experiments

In experiments OWF 04 to OWF 09, the seismic cone penetrometer, SCPT was utilised to measure the undrained shear strength, s_u . The measurements were then compared to the $m = 0.82$ SHANSEP estimates as in Figure 5.1.

For experiments with uniformly pre-consolidated soils, Figure 5.1 shows that the measurements in OWF 04 and OWF 05 compare well with the SHANSEP estimates. However, the readings of OWF 06 and OWF 09 were lower than the SHANSEP estimates for a 500 kPa pre-consolidated speswhite kaolin soil. Even though the readings are lower than the SHANSEP estimate, for the reasons discussed in section 4.2.2 (i.e. delaminating silicone layer above strain gauges in OWF 06 and low penetration velocity that failed to induce a completely undrained response in OWF 09), it is highly unlikely that the readings for OWF 06 and OWF 09 are representative of the in-situ s_u profiles. Due to the discrepancies in OWF 06 and OWF 09 and considering the good correlation with the SHANSEP estimates for experiment OWF 04 and OWF 05, the SHANSEP estimates were selected for usage in analysis.

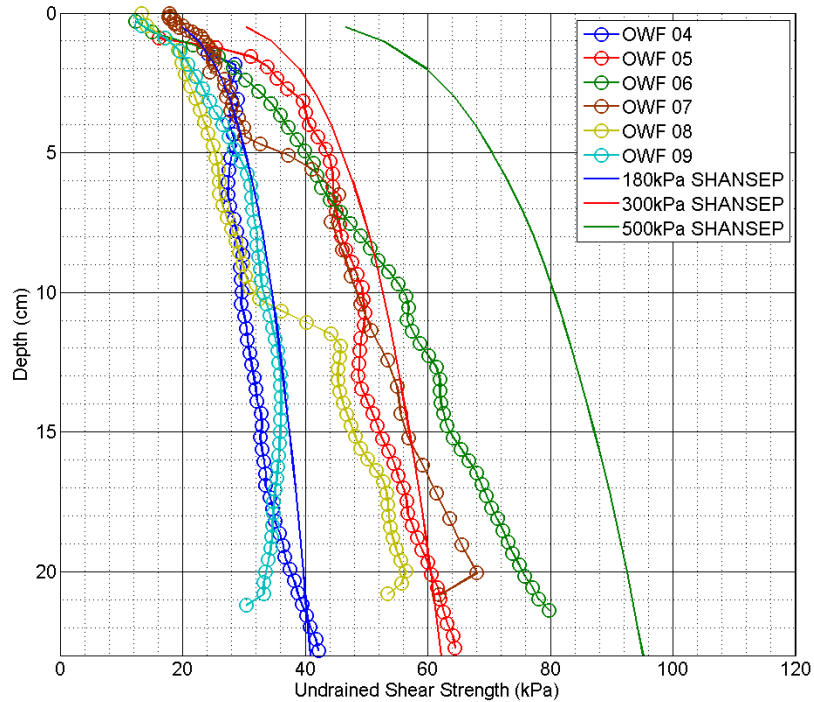


Figure 5.1 Undrained Shear Strength Comparison for Cyclic Experiments

As shown in Tables 3.3 to 3.4, only experiments OWF 07 & OWF 08 have two layers of soil pre-consolidated to pressures of different magnitudes (i.e. 500 kPa on the lower layer and 180 kPa on the upper layer). The difference in s_u can be seen in Figure 5.1 that shows a jump in the readings as the SCPT travels from the soft upper layer into the stiffer lower layer. Even though the lower layer was pre-consolidated to a pressure of 500 kPa, the SCPT readings consistently show that the s_u of the lower layer is closer to the SHANSEP estimates for a 300 kPa speswhite kaolin. The reduction in s_u can be attributed to the process involved in preparing the layered models.

As described in section 3.7.1, the layered models were created by consolidating the stiff base layer before adding further slurry and consolidating at a lower stress to form the softer surficial deposit. As a result, access to water at atmospheric pressure was provided to the stiff base layer when the clay slurry was poured on top of the clay. Since the stiff base layer had been pre-consolidated to 500 kPa, the base layer was in strong suction at that stage. This caused the stiff base layer to experience severe swelling and experience almost total lost of effective stress for a period of at least four weeks. This in turn could have led to loss of some part of the stiff base layer's stress history, reducing the effective maximum consolidation pressure to a value below

500 kPa, and therefore reducing the strength expressed in the centrifuge tests through the reduction of OCR . As a result, the SCPT measured s_u within the stiff base layer were lower than the SHANSEP estimates due to 500 kPa surcharge. Section 5.3.2 will provide further evidence that further validates the SCPT strength measurements of OWF 07 and OWF 08.

5.3 Analysis Conditions

5.3.1 Filter Frequency Parameters

To analyse the experimental data, voltage readings from all instruments were filtered with a uniform low-pass filter using the mathematical computing software known as MATLAB (Mathworks, 1984). This ensured that phase-shifts did not occur between different instruments, ensuring uniformity. A filter frequency of 12 Hz and an order of 5 were utilised. Not only was this frequency above the dominant frequency of all measuring instruments, this frequency was also the lowest frequency that ensured that the readings across all instruments were not altered substantially.

5.3.2 Vertical and Horizontal Load Conditions

To categorise the cyclic load applied in the experiments, a similar definition to LeBlanc et al. (2010b) was utilised. Instead of utilising bending moments, horizontal load applied onto the top of the monopile was utilised as in the parameters below:

$$\zeta_b = \frac{F_{\max}}{F_{\text{capacity}}} \quad \zeta_c = \frac{F_{\min}}{F_{\max}} \quad (5.1)$$

F_{capacity} refers to the monotonic load capacity and F_{\min} and F_{\max} are the minimum and maximum forces in a load cycle. A graphical representation of the cyclic load parameters is given in Figure 5.2. As ζ_b is a measure of the size of the cyclic load with respect to the monotonic load capacity, it follows that $0 < \zeta_b < 1$. The ratio ζ_c that ranges from $-1 \leq \zeta_c \leq 1$ quantifies the cyclic load characteristic and takes the value 1 for a static test, 0 for one-way loading, and -1 for two-way loading.

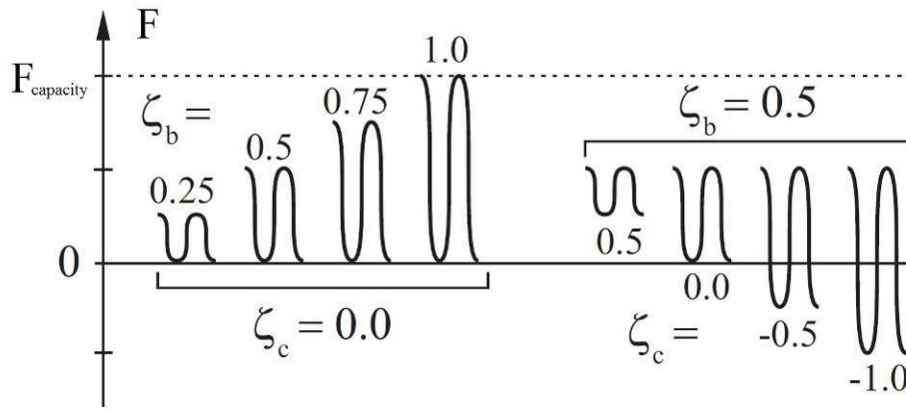


Figure 5.2 Cyclic Loading Characteristic Defined in Terms of ζ_b and ζ_c (adapted from LeBlanc et al., 2010b)

To establish $F_{capacity}$ and the vertical load conditions of experiments OWF 07 and OWF 08, it was necessary to compare the experimentally measured $F_{capacity}$ with the LPILE calculated values as shown in Table 5.1. As in the table, two soil conditions were considered that included s_u measured from the SCPT and the SHANSEP estimated s_u for the 500 kPa pre-consolidated stiff base layer. For each soil condition, three vertical load conditions were considered. p - y curves were constructed based on the recommended methodology of section 4.4.5 while pile toe shear force was calculated utilising the methodology of section 4.5.3 with an exponential β of 0.2.

Cases	$F_{capacity}$ for Experiment in Model Scale(N)	
	OWF 07	OWF 08
Experiment Measurement	207.7	196.1
LPILE Calculated		
SCPT Strength Soil		
Zero Vertical Load	203	194
6MN Vertical Load	157	176
3MN Vertical Load	176	168.1
SHANSEP Estimated Strength Soil		
Zero Vertical Load	244	215
6MN Vertical Load	185	163
3MN Vertical Load	207	181

Table 5.1 Monotonic Load Capacity of Experiments OWF 07 & OWF 08

As shown in Table 5.1, the LPILE calculated $F_{capacity}$ values under zero vertical load with SCPT measured s_u soil match the experimental $F_{capacity}$. Considering how well the values match, not only do these values strongly suggest the presence of a zero vertical load condition for experiments that involved usage of the counter-weight (as mentioned in section 4.4.2), these values also confirm the validity of the SCPT

measured s_u of OWF 07 and OWF 08 of Figure 5.1, indicating that severe swelling contributed to the reduction in s_u of the stiff base layer.

Since the monotonic pushover was not carried out completely in experiment OWF 06, $F_{capacity}$ was estimated utilising LPILE under zero vertical load to be 310 N. This value is most likely representative as the value matches the monotonic load reported for OWF 02 in Figure 4.19(a). In addition, both soil and experimental setup conditions of OWF 06 were the same as OWF 02. As mentioned in section 3.6.6, the counterweight system was not utilised in experiment OWF 09 as the weight of the assembly excluding the counterweight system achieved the desired 12 MN vertical load. Distribution of the vertical loads can be seen in Figure 5.3(a) in the subsequent section. The measured $F_{capacity}$ of 545 N was observed to be lower than the LPILE estimate of 600 N with zero vertical load. Considering the absence of the counterweight system, the vertical load from self-weight acted on the pile in OWF 09. This contributed to a reduction in $F_{capacity}$.

For the purpose of consistency and considering how well the LPILE $F_{capacity}$ matches the experimental observed $F_{capacity}$, the LPILE $F_{capacity}$ of experiments OWF 06 to OWF 08 were utilised to calculate ξ_b . Based on the load magnitudes in Table 3.9, ξ_b and ξ_c values of experiments OWF 06 to OWF 09 were calculated, producing the values in Table 5.2. Since most of the ξ_c values across the experimental stages were very close to zero, these stages were categorised as 1-way cyclic loading.

Stage	Experiment							
	OWF 06		OWF 07		OWF 08		OWF 09	
	ξ_b	ξ_c	ξ_b	ξ_c	ξ_b	ξ_c	ξ_b	ξ_c
1	0.010	0	0.015	0	0.015	0	0.011	0
2	0.12	-0.09	0.16	0.06	0.16	0.01	0.11	-0.02
3	0.25	-0.03	0.28	-0.35	0.41	0.05	0.28	0.03
4	0.32	0	0.49	-0.01	0.57	0.10	0.41	0.08
5	NA		0.61	-0.24	0.62	-0.25	0.44	-0.27
6			0.83	0.08	0.72	-0.09	0.40	-0.39
7			1.00	0	1.00	0	1.00	0

Table 5.2 Cyclic Load Characteristics of Experiment OWF 06 to OWF 09

As in section 3.7.4, due to experimental error, 1.25-way cyclic loading was carried out in experiments OWF 07 to OWF 09 instead of the intended 1.6-way loading that was meant to verify the findings of LeBlanc et al. (2010b) on 1.6-way loading. Besides 1.25-way loading, 1.4-way loading was also carried out in experiments OWF 07 and OWF 09. It should be noted that due to the excessively small voltage readings in stage 1, analysis of the data in stage 1 was not possible and was not carried out.

5.4 Verification of OWF 09 Vertical Load Condition and Applicability of Suggested p - y Curves

To verify the vertical load condition and applicability of the suggestions of chapter 4 on the 7.62 m diameter pile, the vertical load condition of Figure 5.3(a) was considered in LPILE.

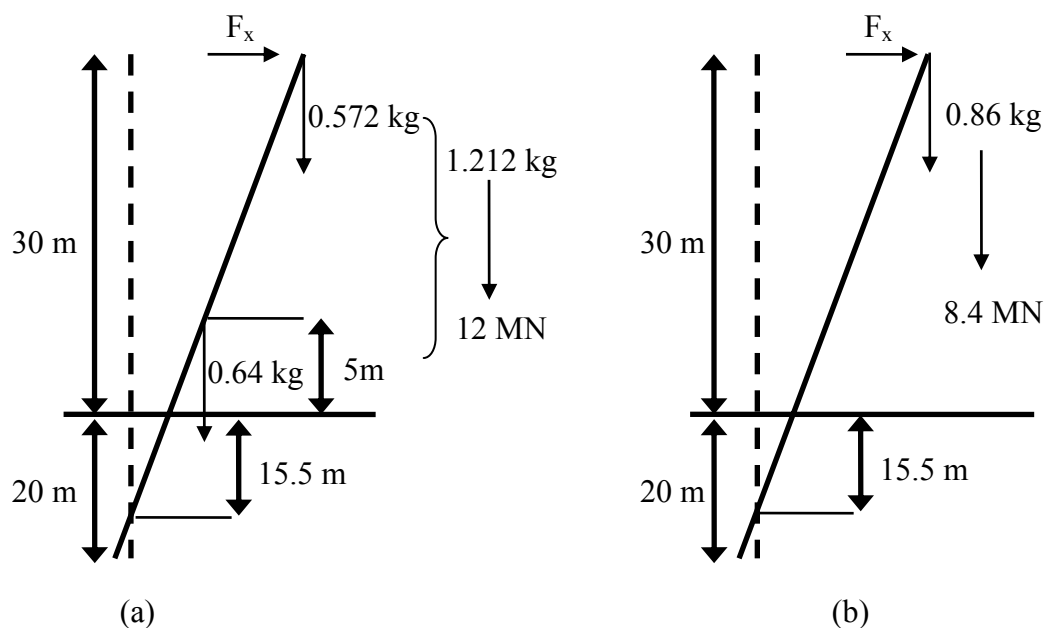


Figure 5.3 OWF 09 Vertical Load Condition for (a) Experimental Assembly (b) LPILE Modified Matching Bending Moment Condition

Since LPILE does not enable application of load at other points along the pile, the vertical load above the pile was modified as in Figure 5.3(b) to match the bending moment condition of 5.3(a) by taking moments about the point of rotation, d_{rot} . Since soil reaction curves could not be calculated due to the failure of the bending moment strain gauges as reported in section 3.7.5, the peak load d_{rot} was calculated trigonometrically using both laser displacement readings 10 m above the mudline and

MEMs rotation readings (with the assumption that the pile is completely rigid with zero flexing) as shown in Figure 5.4. As shown in Figure 5.4, the peak load d_{rot} was calculated to be 15.5 m.

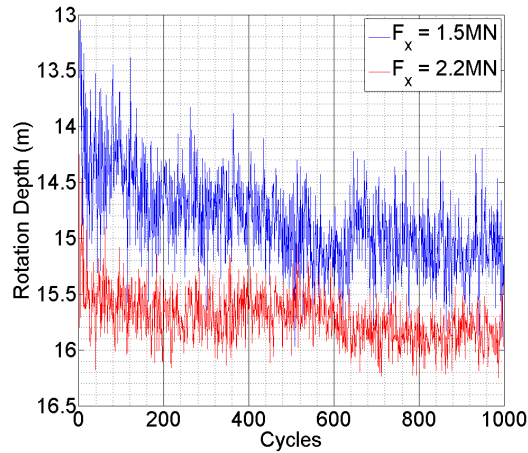


Figure 5.4 OWF 09 Peak Load Rotation Depth

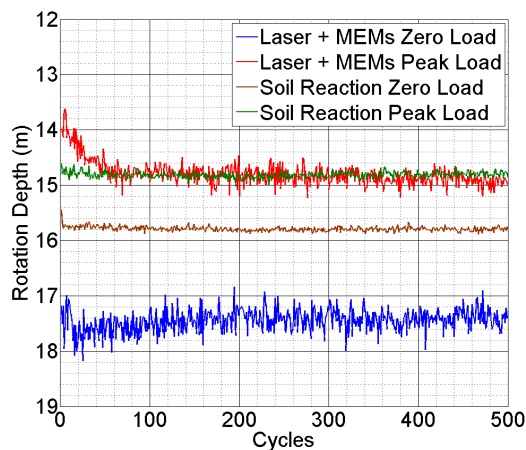


Figure 5.5 OWF 08 Stage 4 Rotation Depth Difference between Soil Reaction Estimate and Laser & MEMs Estimate

To determine the reliability of d_{rot} calculated at peak load utilising both laser and MEMs readings, a comparison was carried out between the d_{rot} calculated from the “soil reaction data” and from the “laser and MEMs readings”. d_{rot} at zero load was also considered. An example of this can be seen in Figure 5.5 for OWF 08 Stage 4. Similar to the observation in Figure 5.5, d_{rot} at zero load was observed to be deeper than d_{rot} at peak load across experiments OWF 06 to OWF 09. In addition, the zero load d_{rot} estimated from soil reaction was consistently observed to be much shallower than the d_{rot} estimated from laser & MEMs readings. However, the peak load d_{rot}

calculated from both soil reaction and laser & MEMs readings were similar to each other. Therefore, even though d_{rot} may be inaccurately estimated at zero load using the laser and MEMs readings, the similarity of d_{rot} at peak load calculated from both soil reaction and laser & MEMs readings suggests that the peak load d_{rot} is accurately estimated by the laser & MEMs readings.

The 15.5 m rotation depth of OWF 09 is deeper than the observed 14 m rotation depths of the monotonic experiments as described in section 4.3.2. After carrying out a parametric analysis that considered pile slenderness ratio, undrained shear strength s_u , p - y curve stiffness, and pile toe shear force F_{shear} , it was determined that d_{rot} was pulled deeper only when F_{shear} was modelled utilising equation (4.11) to increase at an exponent power β of 0.1 instead of 0.2 that was suggested in section 4.5.2 to be an appropriate fit to the results of the monotonic experiments. This can be seen in Figure 5.6 that displays the d_{rot} of the 3.83 m and 7.62 m monopiles (with zero vertical load) with F_{shear} of 0.2 and 0.1 exponents. As shown in Figure 5.6, F_{shear} with an exponent of 0.1 is observed to have a greater effect on pulling the d_{rot} of the 7.62 m monopile deeper as compared to the 3.83 m monopile. This difference in effect is not only due to the exponential power but also due to the magnitude of F_{shear} that greatly increases with diameter (i.e. increase of D by 2 increases F_{shear} by 4, but only increases lateral resistance along the pile shaft by 2).

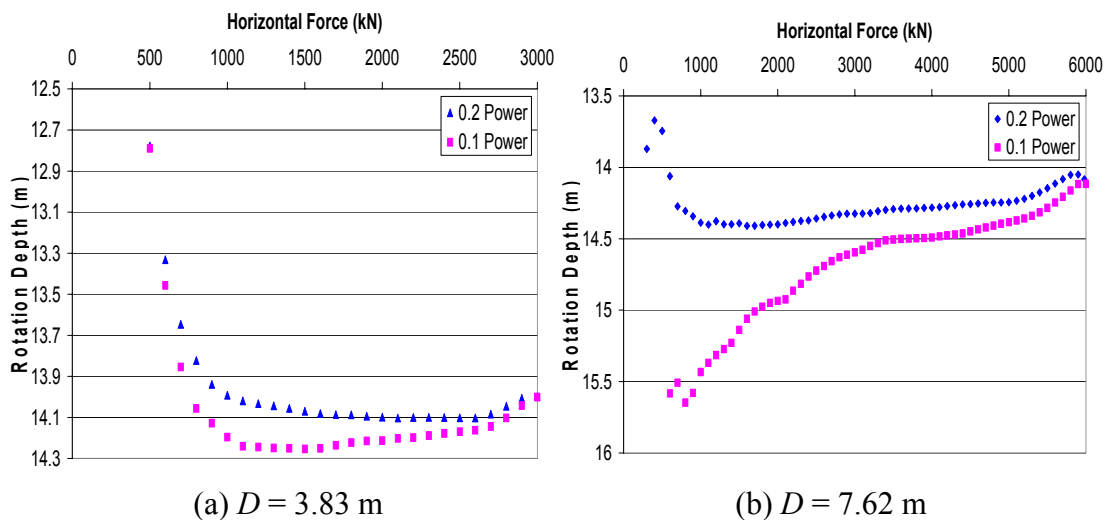


Figure 5.6 Rotation Depth Comparison between 3.83 m and 7.62 m Monopile in 500 kPa Preconsolidated Speswhite Kaolin for F_{shear} of Different Exponents

This difference in d_{rot} was also observed in Haiderali's (2012) numerical modelling of 35 m long monopiles in clays of different strengths. As shown in Table 5.3, for soil of the same s_u , the 7.5 m diameter monopile has a deeper rotation depth compared to the 5 m diameter monopile. In addition, as s_u increases, the difference in the d_{rot} between the 5 m and 7.5 m monopile increases. Though Haiderali (2012) does not discuss the effects of base shear, the results of Table 5.3 suggest that a factor related to D contributes to the difference in rotation depth.

s_u (kPa)	Rotation depth (m)	
	$D = 5$ m	$D = 7.5$ m
50	22.8	23.5
75	20.9	23.3
100	18.9	22.5

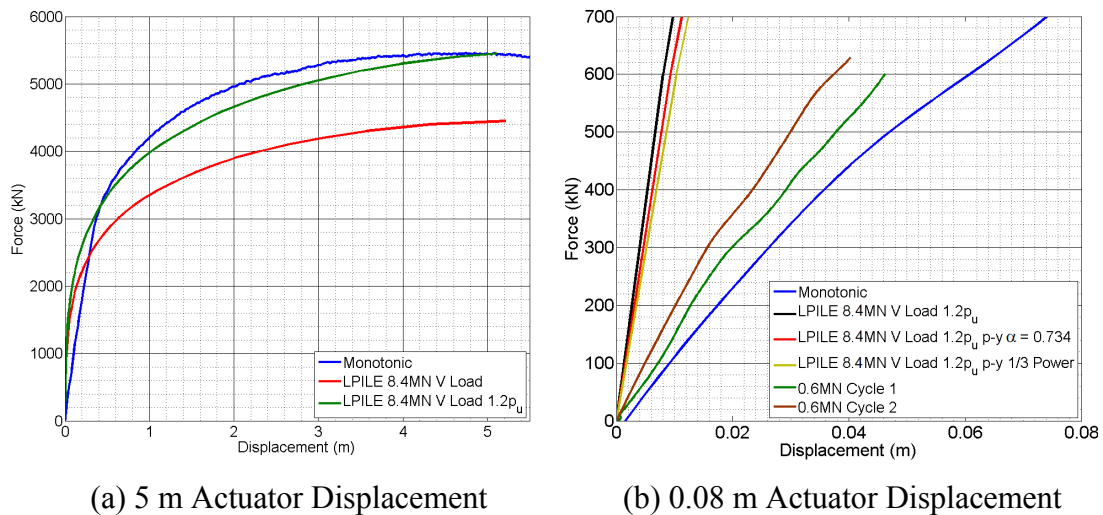
Table 5.3 Rotation Depth of 35 m Long Monopile (Haiderali, 2012)

Considering the good match between the observed d_{rot} of OWF 09 and the LPILE parametric analysis and the results from Haiderali's (2012) numerical modelling, the results strongly suggest that F_{shear} increases with a 0.1 exponential power. As a result, F_{shear} was modelled with a 0.1 exponential power in LPILE.

To verify the vertical load condition and p - y curve suggestions of Chapter 4, the actuator displacement observed during the monotonic stage of OWF 09 was compared to the estimates from LPILE as in Figure 5.7. With the inclusion of the 8.4 MN vertical load at the monopile top, $F_{capacity}$ from LPILE drops from 6,000 kN (reported in section 5.3.2) to 4,450 kN as shown in Figure 5.7(a). In order to match the $F_{capacity}$ from the experiment, the ultimate soil reaction, p_u had to be increased by 20%. Though the comparison suggests the possibility that the recommendation in section 4.4.5 underestimates p_u by 20%, the LPILE curve displays a softer overall response compared to the experiment, indicating that the system has stiffened as a result of the previous cyclic loading stages.

A comparison was also made between the first and second cycles of actuator displacements of stage 2 as shown in Figure 5.7(b) to determine how well the stiffness of the system was modelled by the suggestions in chapter 4. Based on Figure 5.7(b), the initial stiffness of the system is greatly overestimated as compared to the results.

Attempts made to match the load-displacement curves of stage 2 involved softening the p - y curve by doubling α from 0.367 to 0.734 and by increasing the exponential from 0.29 to $1/3$. However, these attempts failed to soften the load-displacement curve to match the cyclic curves of stage 2.



(a) 5 m Actuator Displacement (b) 0.08 m Actuator Displacement
 Figure 5.7 OWF 09 Horizontal Load vs. Actuator Displacement Comparison between Experiment and LPILE Estimates

Attempts were not made to increase the exponential beyond $1/3$ as an increase in exponential caused a significant reduction in $F_{capacity}$. Considering that $\alpha \leq 1$ and the limit on increasing the exponential, the comparison suggests two possibilities. Firstly, the suggested methodology in section 4.4.5 to construct the p - y curves may be inappropriate to estimate the small strain stiffness of monopiles of greater diameters or lower slenderness ratios. However, the overall response is well modelled as shown in Figure 5.7(a). Therefore, further research has to be carried out to improve the methodology and address this limitation. Secondly, an unknown factor that has not been considered is contributing to the observed reduced stiffness. Considering this, it is recommended that experiment OWF 09 be repeated in the future with functioning bending moment strain gauges that will give an accurate picture of the vertical load condition and the lateral behaviour of the monopile within the soil strata.

5.5 Cyclic Stiffness Regimes

5.5.1 Investigating Cyclic Stiffness

With the data available from the tests, there are two ways to quantify the change in cyclic stiffness; firstly, changes in monopile secant stiffness, k and secondly, changes in p - y curve stiffness. Monopile secant stiffness k was quantified as:

$$k = \frac{F_{\max} - F_{\min}}{\theta_{\max} - \theta_{\min}} \quad \text{for } \xi_c \approx 0$$

or

$$k = \frac{F_{\max} - F_{\text{zero}}}{\theta_{\max} - \theta_{\text{zero}}} \quad \text{for } \xi_c < 0 \quad (5.2)$$

F_{zero} is load magnitude at time of zero lateral load, and θ_{\max} , θ_{\min} , and θ_{zero} are pile rotation at maximum, minimum, and zero lateral load of each cycle. F_{zero} and θ_{zero} are utilised to calculate k for $\xi_c < 0$ in order to make comparison possible with k for $\xi_c \approx 0$. A visual of the quantification of k is shown in Figure 5.8.

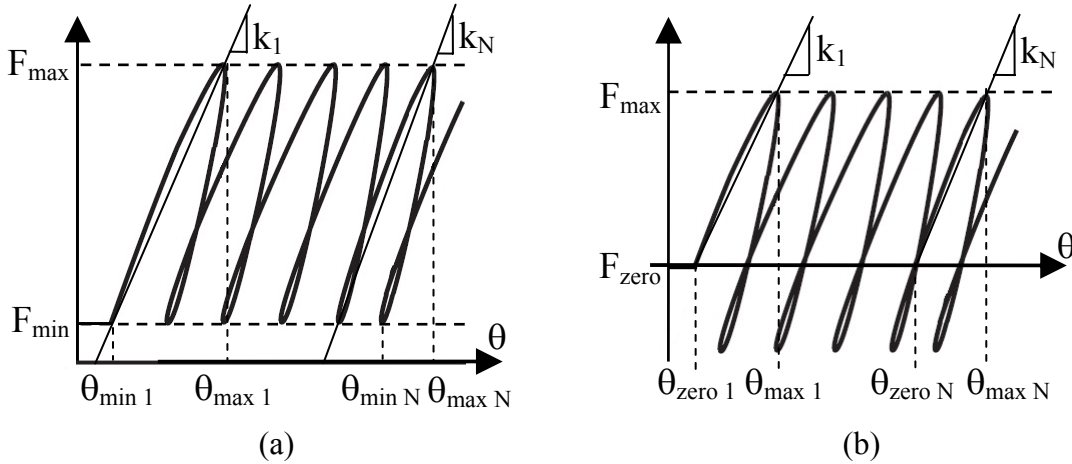


Figure 5.8 Method to Determine Stiffness for (a) $\xi_c \approx 0$ (b) $\xi_c < 0$

To study the changes in p - y curve stiffness, the p - y curves were derived using the methodology as mentioned in sections 4.3.1 and 4.3.3. The beginning and end points of the curves were determined using the points of reference as in Figure 5.8. To evaluate the change in p - y curve stiffness across the cycles, the curves were fitted with a linear function and the linear slopes were extracted and compared to each other. Since the result of a linear fit to a non-linear p - y curve is dependent on the extent of

the data, it was determined that the fit be taken from the beginning and end points using the points of reference as in Figure 5.8. This not only ensured uniformity across the linear fits at different depths, it also ensured that no subjectivity was applied in the selection of the data points at different depths.

Besides analysing the changes in cyclic stiffness, other aspects that could have contributed to changes in cyclic stiffness were investigated. These include bending moments at the time of zero load application (referred to as M_{zero}), changes in soil reaction, and excess pore pressures across the monopile. M_{zero} was reviewed as Kirkwood and Haigh (2014) reported that locked in stresses played a role in influencing the cyclic behaviour of monopiles in sand. In their centrifuge tests, they observed an increasing locked in M_{zero} for cyclic loads with ξ_c ranging from -0.01 to 0.54. In addition, the M_{zero} was observed to increase logarithmically with increasing cycles. Based on the observations, Kirkwood and Haigh (2014) suggested that the locked in moments were caused by the locked in soil stresses. With increasing lock in stresses, foundation stiffness in turn increases. To assess whether the findings of Kirkwood and Haigh (2014) are also applicable in clays, M_{zero} was analysed.

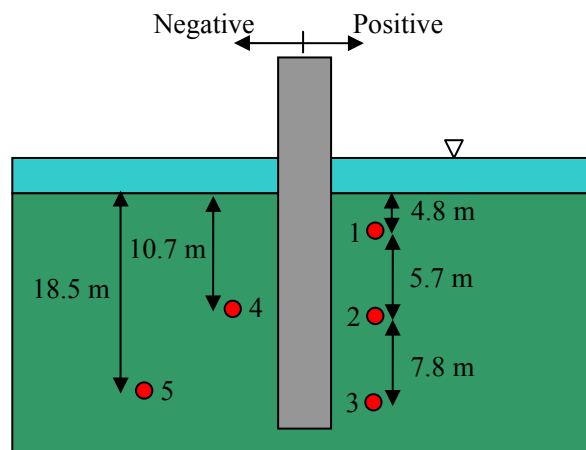


Figure 5.9 Layout of PPTs

The excess pore pressure behaviour across the monopile was reviewed to study the link between the excess pore pressure behaviour and the cyclic stiffness behaviour. As mentioned in section 3.6.1, five PPTs were installed throughout the experimental model to measure the changes in pore pressure as shown in Figure 5.9. PPTs 1 to 4 are located half a diameter away from the monopile to measure the cyclic excess pore

pressure response while PPT 5 was installed 20.5 m away from the monopile to gauge the percentage of consolidation during the experiment. Since the initial pore pressure in each cyclic load stage was observed to be very close hydrostatic, the excess pore pressure was measured by utilising the initial gauge pressure of the first stage of each respective experiment.

The initial excess pore pressure, Δu measured when the monopile was loaded corresponds to what one would expect based on loading under plane-strain conditions. When the monopile was loaded in the positive load direction as shown in Figure 5.9, PPTs 1 and 2 measured positive excess pore pressures while those at locations 3 and 4 measured negative excess pore pressures. The reverse took place when the pile was loaded in the negative direction. This is due to the changes in stress conditions. In plane-strain conditions:

$$\Delta s' = \frac{\Delta \sigma'_v + \Delta \sigma'_h}{2} \quad (5.3)$$

$$\Delta t = \frac{\Delta \sigma'_v - \Delta \sigma'_h}{2} \quad (5.4)$$

where, $\Delta s'$ is the change in effective mean stress, Δt is the change in deviator stress, $\Delta \sigma'_v$ is the change in effective vertical stress, and $\Delta \sigma'_h$ is the change in effective horizontal stress. When the monopile is loaded in the positive direction, the soil above the rotation point at PPTs 1 and 2 and the soil below the rotation point on the opposite side, will experience lateral compression; no change in axial stress but an increase in effective horizontal stress. As a result,

$$\Delta s' = \frac{\Delta \sigma'_h}{2} \quad (5.5)$$

$$\Delta t = \frac{-\Delta \sigma'_h}{2} \quad (5.6)$$

At the same time, the soil above the rotation point at PPT 4 and below the rotation point at PPT 3 will experience a decrease in confining stresses as the pile moves away. As a result,

$$\Delta s' = \frac{-\Delta \sigma'_h}{2} \quad (5.7)$$

$$\Delta t = \frac{\Delta \sigma'_h}{2} \quad (5.8)$$

By plotting the total and effective stress paths on the $s' - t$ space as in Figure 5.10, the difference between total and effective stress paths shows that positive excess pore pressures are generated when the soil is laterally compressed and negative excess pore pressures arise when the soil experiences a decrease in confining stresses.

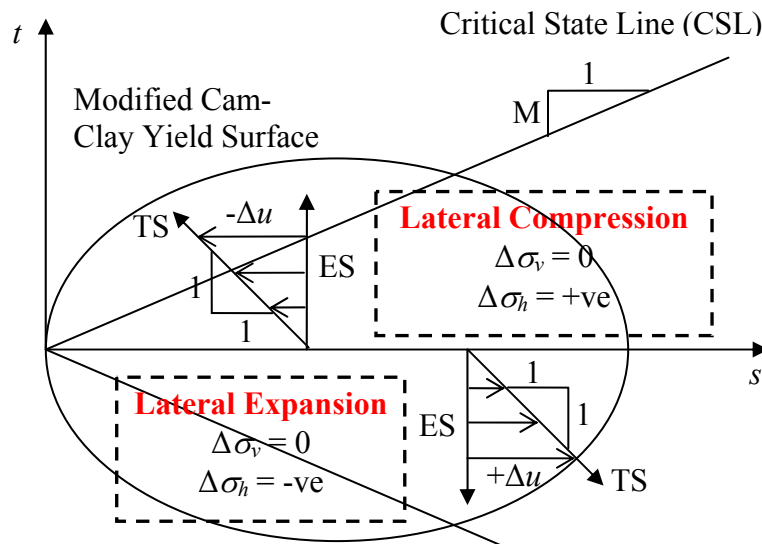


Figure 5.10 Plotting of ES (Effective Stress) and TS (Total Stress) on $s' - t$ Space for Biaxial Lateral Compression and Lateral Expansion

Though the above explains the principles behind the generation of positive and negative excess pore pressures, a review of the excess pore pressure behaviour indicates that Critical State Soil Mechanics theory is not comprehensive enough to explain the differences in cyclic stiffness behaviour observed between the cyclic loads of different characteristics. However, changes in stress conditions and the OCR at depth in question that influence the excess pore pressure will in turn dictate the cyclic stiffness behaviour of the monopile. Since measurements were made half a diameter away, the measurements are unlikely to capture the actual magnitude of excess pore pressures developed. Despite the limitations, the measurements were analysed to determine how excess pore pressures contributed to the cyclic stiffness behaviour.

Two cyclic stiffness regimes were observed; the stiffening regime and the softening regime. The stiffening regime was observed in experimental stages involving $\xi_c \approx 0$ and $\xi_c \approx -0.35$ whereas the softening regime was observed in stages involving cyclic loads of $\xi_c \approx -0.25$. The regimes are discussed in the following sections.

5.5.2 Stiffening Regime

5.5.2.1 $\xi_c \approx 0$

The monopile was observed to experience stiffening (with both marginal rotation and marginal actuator displacement decreasing) when the monopile was subjected to cyclic loads of $\xi_c \approx 0$. Similar to Kirkwood and Haigh (2014), M_{zero} was observed to build up with increasing cycles, suggesting that locked in stresses increase with increasing cycles. An example of this can be seen in Figure 5.11. Across some of the cyclic load stages of $\xi_c \approx 0$, two distinct log slopes were observed, one within the first 100 cycles and another beyond 100 cycles. The stiffening rates in the first 100 cycles were observed to be lower than the stiffening rates beyond 100 cycles.

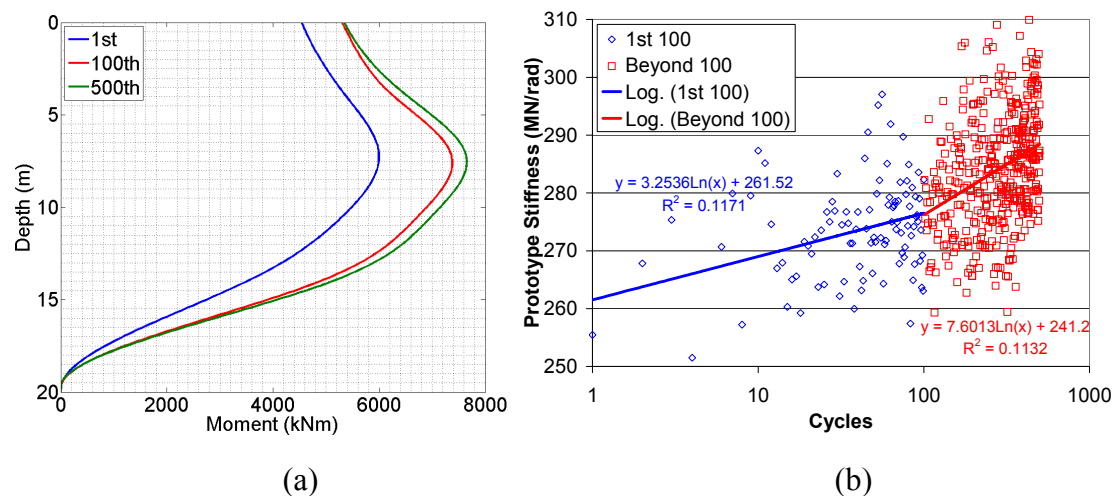
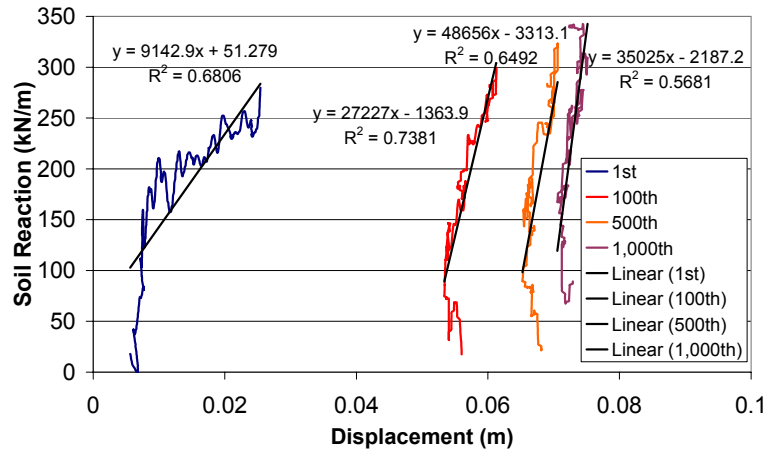
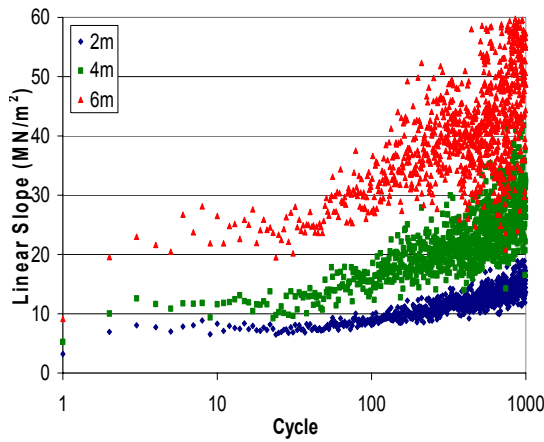


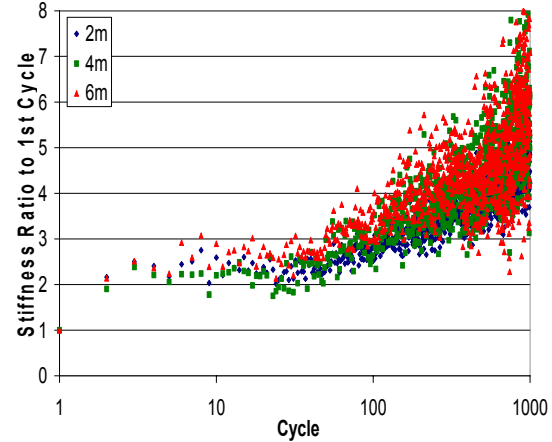
Figure 5.11 OWF 08 Stage 4 $\xi_b = 0.57$, $\xi_c = 0.10$ (a) Prototype Scale Bending Moment at Zero Load (b) Prototype Rotational Stiffness



(a) Linear Fitting



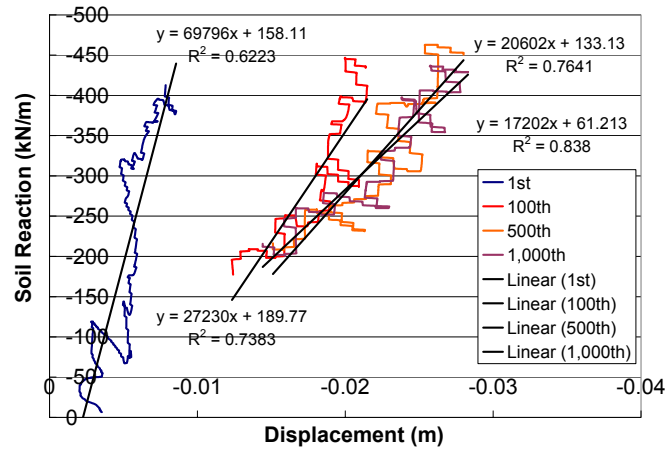
(b) Linear Slope Change



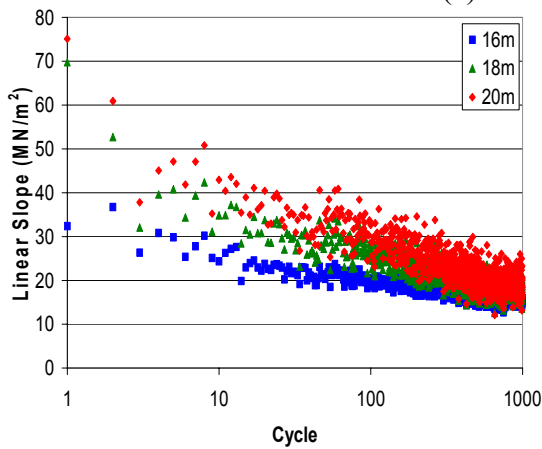
(c) Linear Slope Ratio

Figure 5.12 OWF 08 Stage 3 $\xi_b = 0.41$, $\xi_c = 0.05$ p - y Curve above Rotation Point
Stiffness Quantification

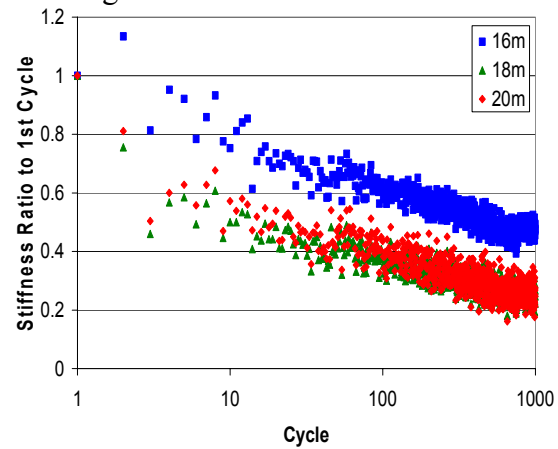
During the stiffening regime, the p - y curves above the rotation depth were observed to stiffen. This can be seen by the example in Figure 5.12. Relative to the first cycle, the p - y curves above the rotation point were observed to stiffen at the same rate and ratio. Though stiffening takes place above the rotation point, the p - y curves below the rotation point were observed to experience softening. This can be seen in the example of Figure 5.13. Similar to the p - y curves above the rotation point, the p - y curves below the rotation point soften at similar rates and ratio. With the p - y curves stiffening across 70% of the pile length, the net effect is stiffening. This corresponds to the observed increase in secant stiffness with increasing cycles. Relative to Figure 5.11(b), the p - y curves similarly stiffen at a lower log slope in the first 100 cycles and stiffen at a higher log slope beyond 100 cycles.



(a) Linear Fitting



(b) Linear Slope Change



(c) Linear Slope Ratio

Figure 5.13 OWF 08 Stage 3 $\xi_b = 0.41$, $\xi_c = 0.05$ p - y Curve below Rotation Point
Stiffness Quantification

The general pore pressure behaviour for $\xi_c \approx 0$ is similar to the example shown in Figure 5.14. When the monopile is loaded in the positive direction, positive excess pore pressures are initially generated at locations 1 and 2 while negative pore pressures are initially generated at locations 3 and 4. This is in line with the Critical State Soil Mechanics theory in the previous section. However, the excess pore pressure behaviour at locations 1 and 2 as compared to locations 3 and 4 are distinct from each other. At locations 1 and 2, the positive excess pressures are greater in magnitude relative to the negative excess pressures. However, with increasing cycles, positive excess pore pressures decrease while negative excess pore pressures increase. Beyond 100 cycles, the logarithmic rate of the behaviour increases. Relative to Figure 5.12, the excess pore pressure behaviour corresponds to the stiffening behaviour of the p - y curves above the rotation point.

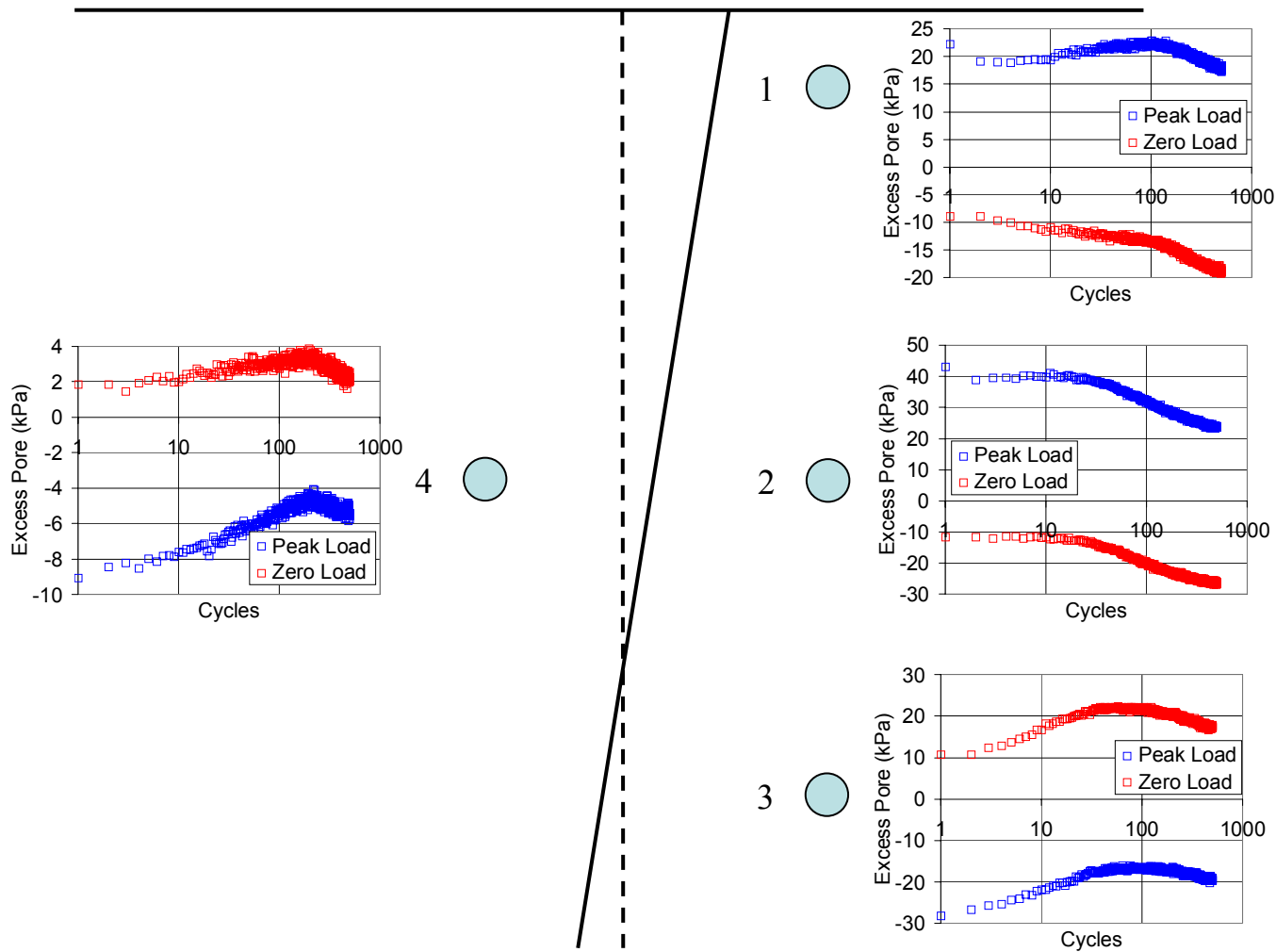


Figure 5.14 OWF 08 Stage 4 $\xi_b = 0.57$, $\xi_c = 0.10$ Excess Pore Pressure Behaviour

At locations 3 and 4, negative excess pore pressures are initially greater in magnitude than the positive excess pore pressures. Within the first 100 cycles, negative excess pore pressures decrease and positive excess pore pressures increase. However, beyond 100 cycles, the excess pore pressure behaviour changes significantly with the negative excess pore pressures increasing and positive excess pore pressure decreasing with increasing cycles.

The negative excess pore pressure trend on the passive side at locations 1 and 2 is similar to the observations made by Dobry and Vucetic (1987) (shown in Figure 2.34) who observed VNP clay with an $OCR = 4$ developing negative excess pore pressures under undrained cyclic loading. This observation was markedly different compared to the lightly overconsolidated VNP clay with $OCR < 4$ that produced greater positive excess pore pressures following the first few cycles that generated small suctions. The difference in excess pore pressure behaviour between the lightly overconsolidated and heavily overconsolidated soils is most likely due to the difference in shear behaviour. High OC clays have a tendency to dilate. As a result, under undrained conditions with zero volume change, negative excess pore pressure is produced. Considering that the experimental observations are similar to Dobry and Vucetic (1987), it is likely that the negative excess pore pressure trend is linked to the heavily overconsolidated state of the soil above the rotation point where $OCR \geq 4$. With dilation and hence reducing pore pressure, the soil above the rotation point on the passive side experiences stiffening, as seen by the stiffening of the p - y curves above the rotation point.

Since pore pressure measurements were not taken below rotation point on the passive side, a hypothesis can only be made regarding the excess pore pressure behaviour. According to the p - y curves of Figure 5.13, the soil below the rotation point on the passive side experiences softening throughout cyclic loading. This softening is most likely due to the excess pore pressures. As in Figure 2.34, Dobry and Vucetic (1987) observed that lightly overconsolidated VNP clay with $OCR < 4$ developed increasingly greater positive excess pore pressures with increasing cycles following the first few cycles that generated low negative excess pore pressures. Since the soil below the rotation point is lightly overconsolidated with $OCR < 4$, it is likely that positive excess pore pressures developed and increased with increasing cycles. As a result, the soil below the rotation point progressively softens with cyclic loading.

Though this is most likely to be the case, it is necessary to carry out experiments with a PPT placed on the passive side below the rotation point to confirm that the lightly overconsolidated state of the soil below the rotation point on the passive side is contributing to the positive excess pore pressure behaviour.

The excess pore pressure behaviour also contributes to the distinct log slopes of the first 100 cycles and beyond 100 cycles. This can be seen by comparing the excess pore pressure behaviour of Figure 5.14 with the secant stiffness curve of Figure 5.11(b). In the first 100 cycles, the log slope is lower due to the low generation rate of negative excess pore pressures at locations 1 and 2 and the softening effects of the increasing positive excess pore pressures at locations 3 and 4. However, beyond 100 cycles, greater negative excess pore pressures are developed across the monopile, contributing to the greater stiffening rate.

In OWF 09 involving the 7.62 m diameter monopile, a slight difference was observed in the excess pore pressure behaviour at location 3 for stages 2 and 3 as shown in Figure 5.15.

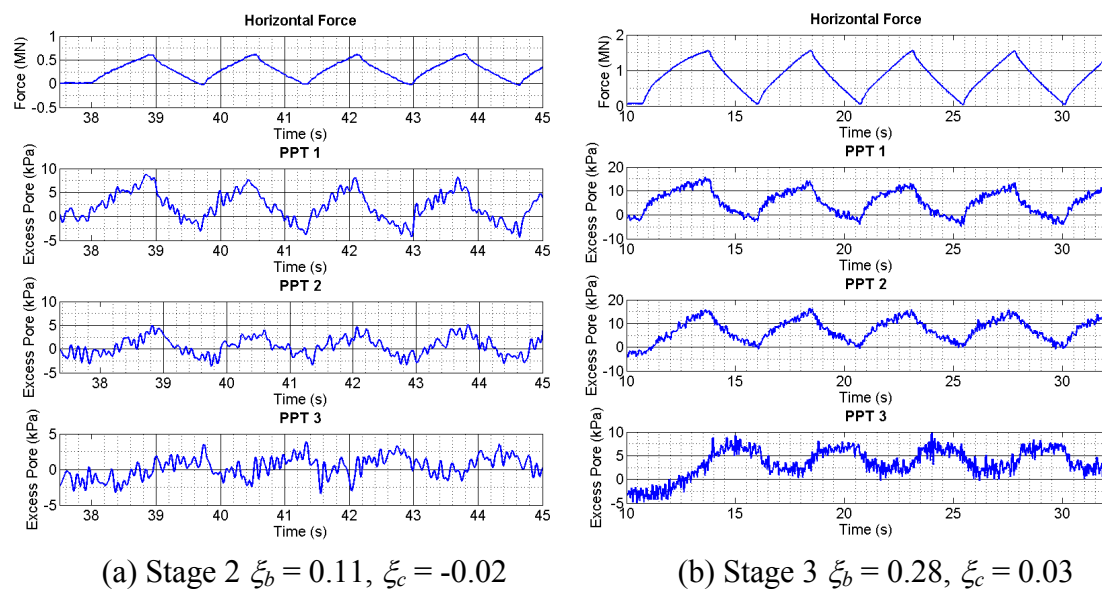


Figure 5.15 OWF 09 Location 1 to 3 Excess Pore Comparison with Horizontal Force

Initially when the monopile is loaded, the monopile is expected to rotate at depth. This causes the soil below the rotation point to experience a decrease in horizontal stresses, which in turn should initially produce negative excess pore water pressures.

However, in stages 2 and 3, an initial positive excess pore water pressure is developed in the first cycle as shown in Figure 5.15. Despite the initial positive excess pore water pressure, negative excess pore pressure is generated in the following cycles when the monopile is loaded to peak load. Based on Figure 5.15, it is suggested that the monopile in stages 2 and 3 experienced a transition of behaviour from flexing at depth (which caused compression of the soil at location 3) to rotating at depth (causing reduction in horizontal stresses). Following the first cycle, the monopile rotates at depth with cyclic load.

As shown in Figure 5.16, the excess pore pressure at location 3 remains positive at both peak load and zero load for most of the cyclic loading stage. This is most likely due to the rotation depth difference at peak load and zero load. As highlighted in Figure 5.5, the rotation depth at zero load is deeper relative to the rotation depth at peak load. In addition, both Figure 5.4 and Figure 5.6 strongly suggests that F_{shear} increases at an exponential power β of 0.1 which pulls the rotation depth deeper towards the pile toe. Considering that the 7.62 m monopile has a deeper rotation depth than the 3.83 m monopile at peak load, it is very likely that the same applies at the point of zero load application.

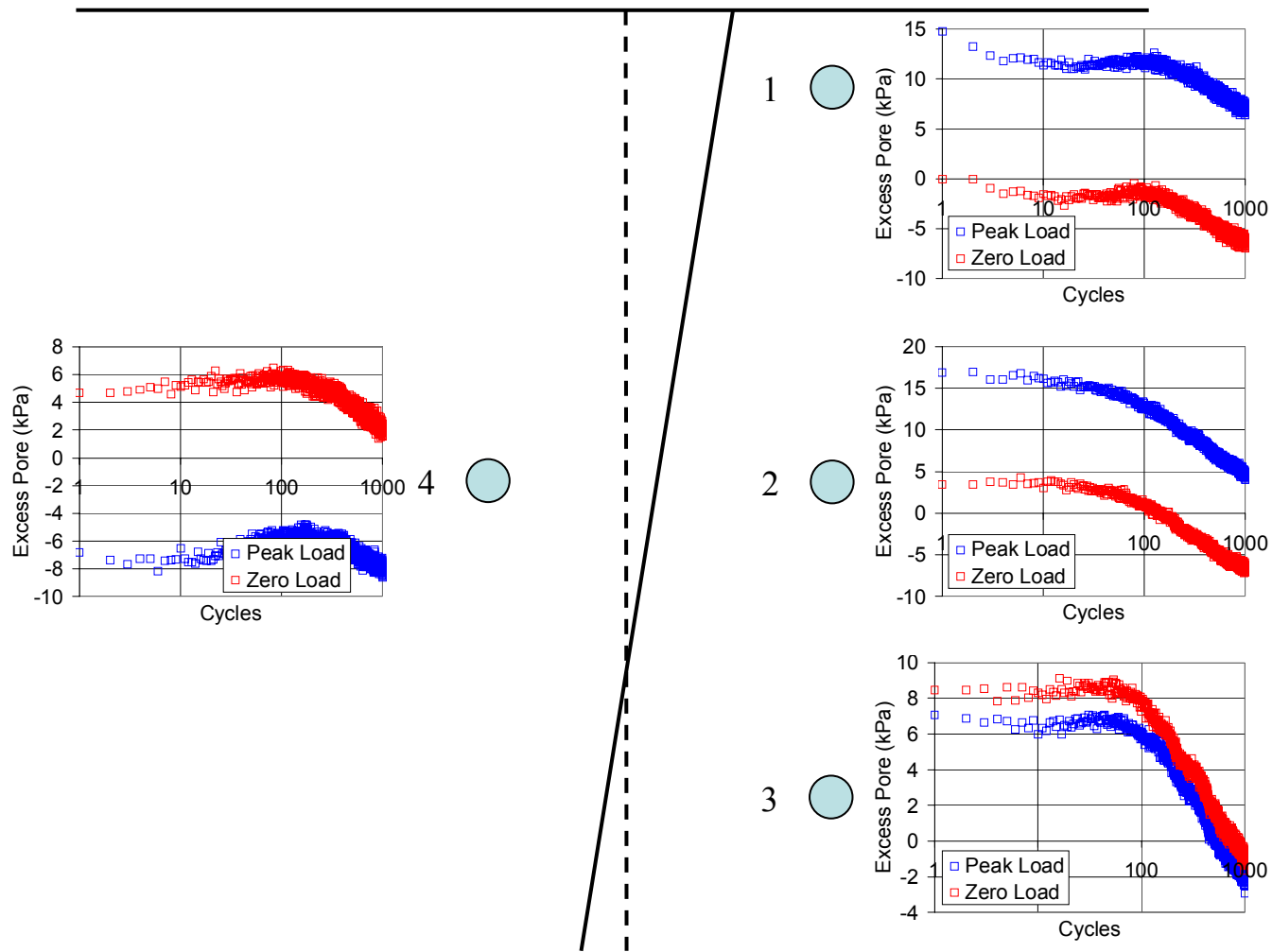


Figure 5.16 OWF 09 Stage 3 $\xi_b = 0.28$, $\xi_c = 0.03$ Excess Pore Pressure Behaviour

With a much deeper rotation point at zero load, the soil at location 3 will experience a decrease in horizontal stress of lower magnitudes relative to the 3.83 m monopile while the rotation depth travels upwards when the monopile is loaded. This in turn causes lower magnitude negative excess pore pressures to be developed relative to the 3.83 m monopile. Though the rotation depth travels deeper when unloaded, the positive excess pore pressure generated is greater in magnitude relative to the negative excess pore pressures. As a result, the excess pore pressures at location 3 remains positive well throughout the cyclic loading stage.

Despite the difference in excess pore pressure behaviour at location 3, the 7.62 m monopile exhibited stiffening behaviour similar to the behaviour observed for the 3.83 m monopile experiments of Figure 5.11(b). Therefore, this suggests that the slight difference in excess pore pressure behaviour at location 3 had little influence on the resulting cyclic stiffness behaviour. Similar to Figure 5.14, beyond 100 cycles, greater negative excess pore pressures are developed relative to the rate within the first 100 cycles, contributing to the higher stiffening rate.

In summary, the bending moment curves, the secant stiffness curves, the p - y curves and the excess pore pressure curves are consistent with each other. Based on the curves, it is likely that changes in locked in stress conditions (which affect the soil stress conditions) and the OCR of the soil dictate the excess pore pressure behaviour of the soil which in turn dictates the cyclic stiffness behaviour of the monopile. For cyclic loads of $\xi_c \approx 0$ in overconsolidated clay, the resultant behaviour is stiffening with increasing cycles.

5.5.2.2 $\xi_c \approx -0.35$

The monopile was also observed to experience stiffening (with both marginal rotation and marginal actuator displacement decreasing) in stages 3 and stage 6 of OWF 07 and OWF 09 respectively where cyclic loads in the reverse direction of $\xi_c \approx -0.35$ and -0.39 were applied. Though loading was applied in the reverse direction, M_{zero} and k were observed to continuously increase logarithmically with increasing cycles instead of decreasing. Figure 5.17 shows M_{zero} and k of OWF 07 stage 3 while Figure 5.18 shows k of OWF 09 stage 6.

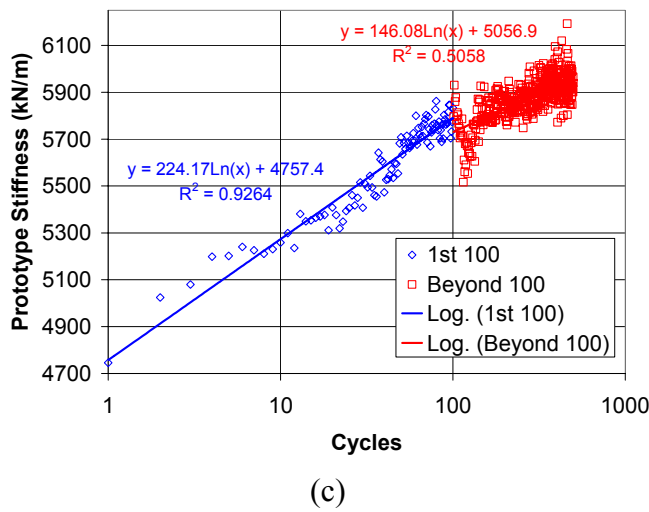
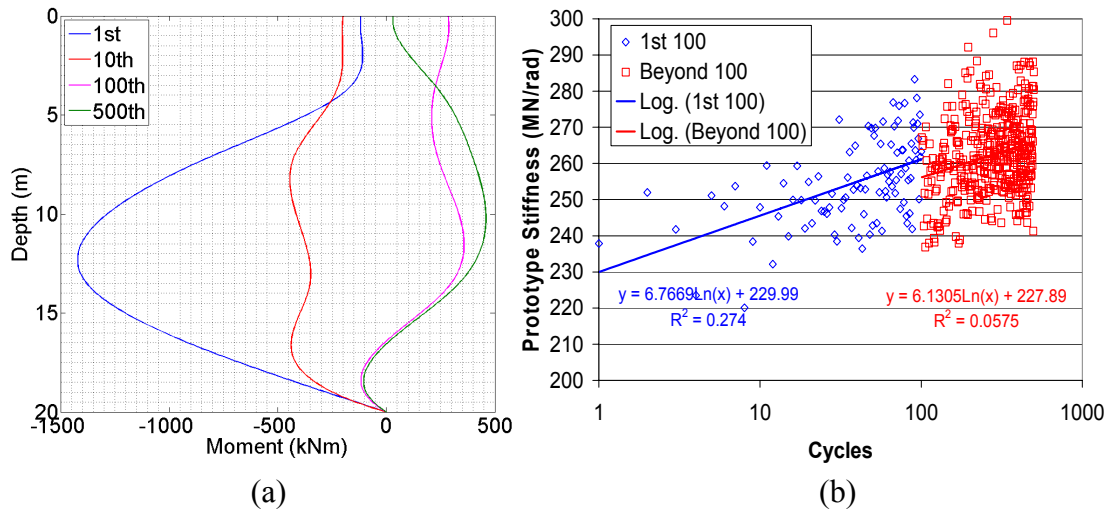


Figure 5.17 OWF 07 Stage 3 $\xi_b = 0.28$, $\xi_c = -0.35$ (a) Bending Moment at Zero Load (b) Rotational Stiffness (c) Stiffness relative to Marginal Actuator Displacement

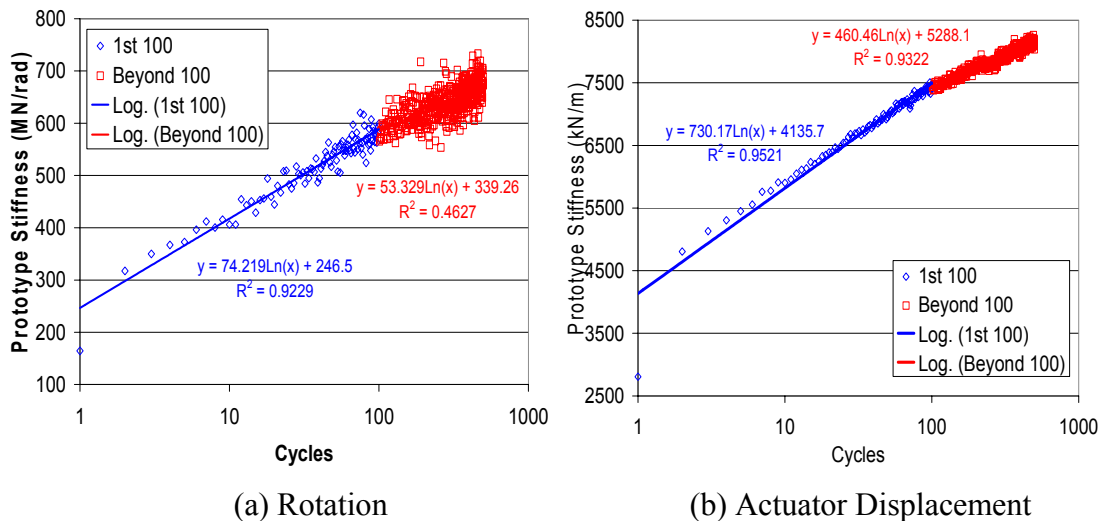


Figure 5.18 OWF 09 Stage 6 $\xi_b = 0.40$, $\xi_c = -0.39$ Secant Stiffness

Similar to $\xi_c \approx 0$, two distinct log slopes were observed, one within the first 100 cycles and another beyond 100 cycles. However, the log slope in the first 100 cycles was observed to be higher than the log slope beyond 100 cycles. Due to the high noise to signal ratio of the MEMs, the trend was not clear in Figure 5.17(b). However, the trend was more distinct when k was evaluated with respect to marginal actuator displacement. The same trend was observed in OWF 09 stage 6 when k was evaluated with respect to marginal rotation and actuator displacement as can be seen in Figure 5.18, reinforcing that the log slope beyond 100 cycles is lower relative to the first 100 cycles. On average, the log slope beyond 100 cycles is 67% of the log slope in the first 100 cycles.

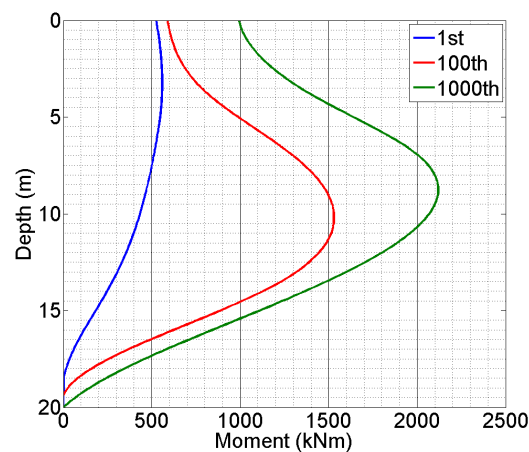


Figure 5.19 OWF 07 Stage 2 $\xi_b = 0.16$, $\xi_c = 0.06$ Bending Moment at Zero Load

Figure 5.19 shows the bending moment at zero load of OWF 07 stage 2. Comparison between Figure 5.19 and Figure 5.17(a) suggests that the locked in stresses from stage 2 were completely destroyed by the first cycle of $\xi_c \approx -0.35$. However, with increasing cycles, M_{zero} increases, indicating that stresses are being locked in.

Figure 5.20 and Figure 5.21 show the change in p - y curve stiffness above and below the rotation point of OWF 07 stage 3. Similar to the behaviour of Figure 5.12, the p - y curves above the rotation point increase in stiffness at similar rates and ratios. Similar to the secant stiffness curves of Figure 5.17 and Figure 5.18, the log slope beyond 100 cycles is less than the log slope in the first 100 cycles. Figure 5.21 suggests that the stiffness of the p - y curves below the rotation point is relatively stable throughout the stage. Since bending moment data is limited to OWF 07 stage 3, it is recommended

that more experiments be carried out to verify the change in p - y curve stiffness below the rotation point.

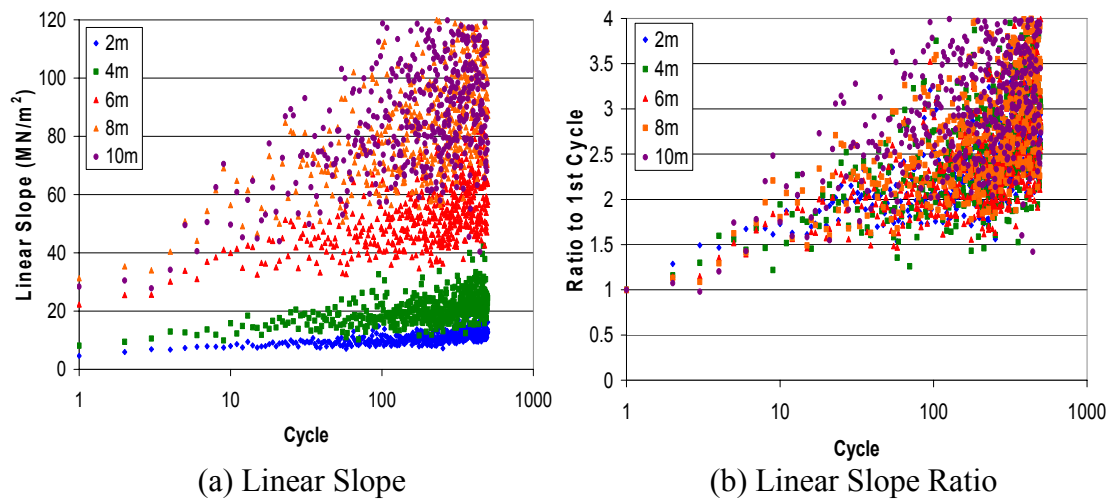


Figure 5.20 OWF 07 Stage 3 $\xi_b = 0.28$, $\xi_c = -0.35$ p - y Curve above Rotation Point Stiffness

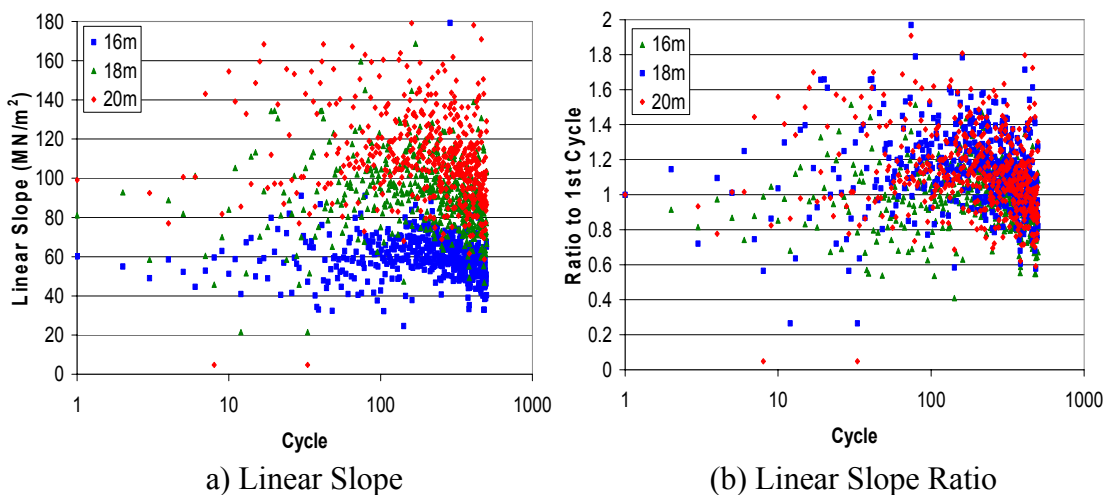


Figure 5.21 OWF 07 Stage 3 $\xi_b = 0.28$, $\xi_c = -0.35$ p - y Curve below Rotation Point Stiffness

Figure 5.22 and Figure 5.23 show the excess pore pressures of OWF 07 stage 3 and OWF 09 stage 6 respectively. Relative to Figure 5.14 for $\xi_c \approx 0$, the excess pore pressure behaviour displayed in Figure 5.22 is fairly similar at locations 1 to 3. The behaviour at location 4 is quite different relative to Figure 5.14 as both positive excess pore pressures reduce and negative excess pore pressures increase throughout the cyclic loading stage. However, at location 2, the log rate of negative excess pore pressure generation drops beyond 100 cycles, contributing to the reduced stiffening rate seen in Figure 5.17(b) and (c).

The excess pore pressure behaviour of OWF 09 stage 6 of Figure 5.23 is similar to that of OWF 07 stage 3 in Figure 5.22. However, the reduced log rate of negative excess pore pressure beyond 100 cycles is a lot more distinct at locations 1 and 4 relative to the measurements in Figure 5.22. Based on the behaviour in Figure 5.18, the reduced log slope beyond 100 cycles is most likely due to the reduced log rate of negative excess pore pressures at locations 1 and 4.

Considering the differences in bending moments at zero load, cyclic stiffness behaviour, p - y curve cyclic stiffness, and excess pore pressure behaviour between cyclic loads of $\xi_c \approx 0$ and $\xi_c \approx -0.35$, the results for $\xi_c \approx -0.35$ cyclic loading suggests that cyclic loads of different characteristics can influence the cyclic stiffness behaviour of the monopile. This is because cyclic loads of different characteristics will influence the locked in stress conditions differently, causing changes in soil stress conditions that in turn influence the excess pore pressure behaviour. This in turn would affect the resulting cyclic stiffness behaviour. Though no excess pore pressure measurements were made opposite of location 3, the p - y curve stiffness measured in Figure 5.21 suggests that both positive and negative excess pore pressures were relatively constant. However, since only one data set is available, it is not possible to draw a strong conclusion on the effects of $\xi_c \approx -0.35$ cyclic loads on both p - y curve stiffness and excess pore pressure behaviour for depths below the rotation point. Therefore, more experiments involving $\xi_c \approx -0.35$ with measurements below the rotation point on both sides of the monopile should be carried out to verify this.

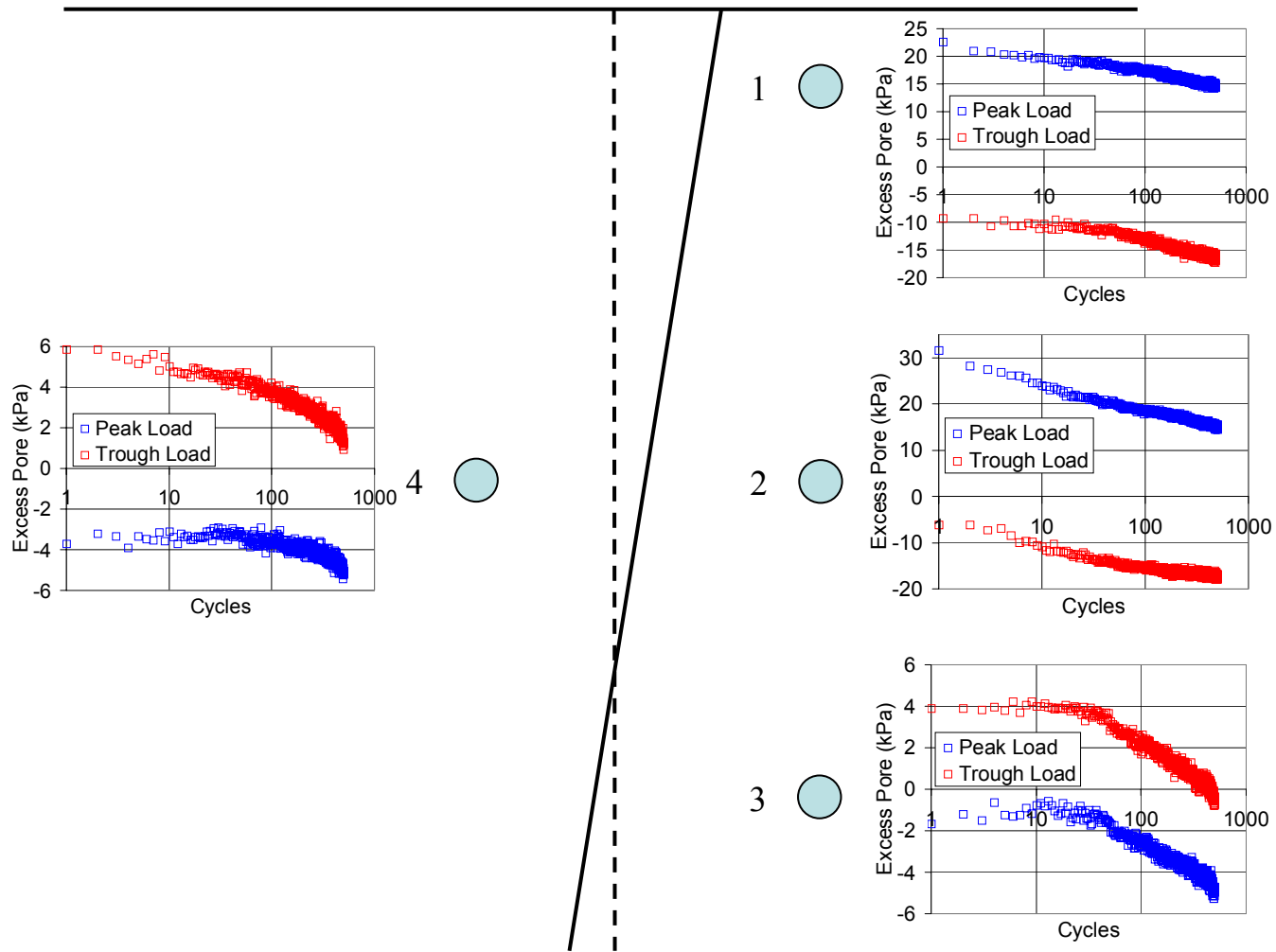


Figure 5.22 OWF 07 Stage 3 $\xi_b = 0.28$, $\xi_c = -0.35$ Excess Pore Pressure Behaviour

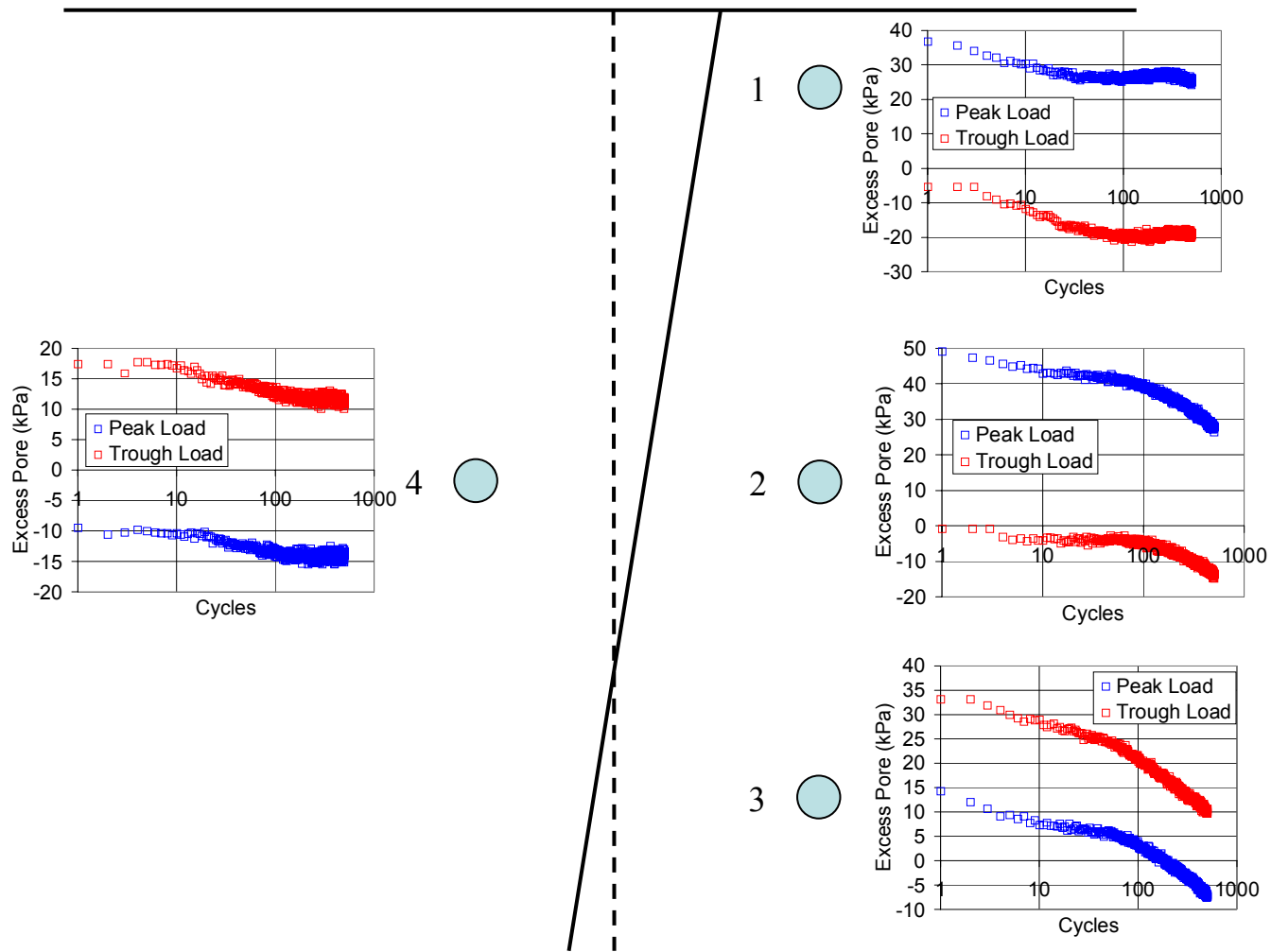


Figure 5.23 OWF 09 Stage 6 $\xi_b = 0.40$, $\xi_c = -0.39$ Excess Pore Pressure Behaviour

5.5.3 Softening Regime

5.5.3.1 $\xi_c \approx -0.25$

Softening took place in stage 5 of experiments OWF 07 to OWF 09 involving cyclic loads of $\xi_c \approx -0.25$ (1.25-way loading). As shown in Figure 5.24, M_{zero} was observed to decrease in the first 100 cycles, suggesting that locked in stresses are being progressively destroyed by the load in the reverse direction. This is quite different from the behaviour observed in the previous section for $\xi_c \approx -0.35$ where locked in stresses appear to be completely destroyed in the first cycle. Beyond 100 cycles, M_{zero} starts to increase slowly. The change in k also corresponds to the changes in accumulated bending moments in which k drops rapidly in the first 100 cycles. In OWF 09, k was observed to significantly drop to 50% of the initial stiffness. According to Kirkwood and Haigh (2014), the reduction in k is most likely due to the reduction or destruction of locked in stresses when load is applied to the pile head in the reverse direction. Beyond 100 cycles, k increases slowly.

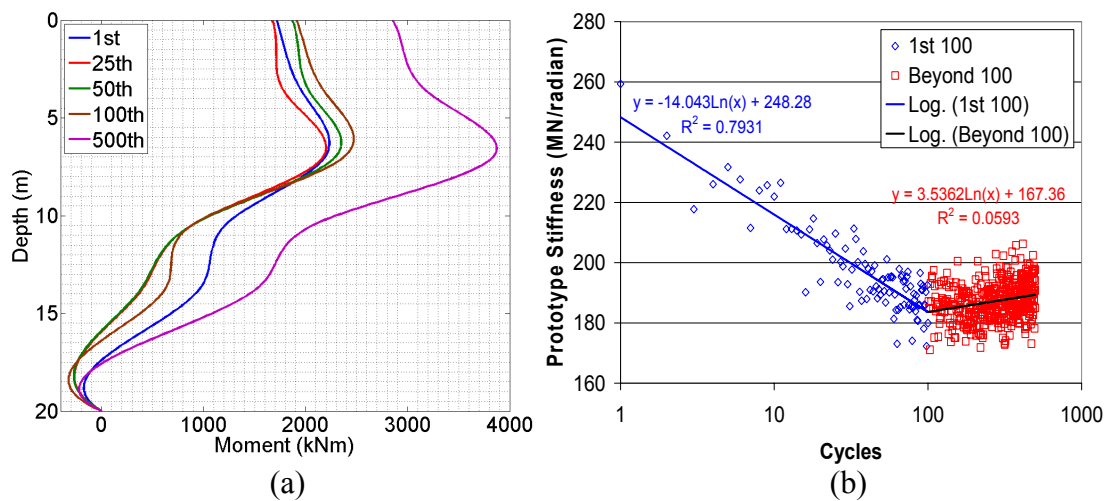


Figure 5.24 OWF 08 Stage 5 $\xi_b = 0.62$, $\xi_c = -0.25$ (a) Prototype Scale Bending Moment at Zero Load (b) Prototype Rotational Stiffness

The change in p - y curve stiffness above and below the rotation point is shown in Figure 5.25 and 5.26 respectively. The p - y curves above the rotation point reduce in stiffness similar to the reduction in secant stiffness seen in Figure 5.24(b). Beyond 100 cycles, the p - y curves slowly increase in stiffness. The p - y curves below the rotation point behaves similarly to the p - y curves of Figure 5.21 for OWF 07 stage 3 involving $\xi_c \approx -0.35$ cyclic loads and do not experience a significant change in stiffness throughout the cyclic loading stage.

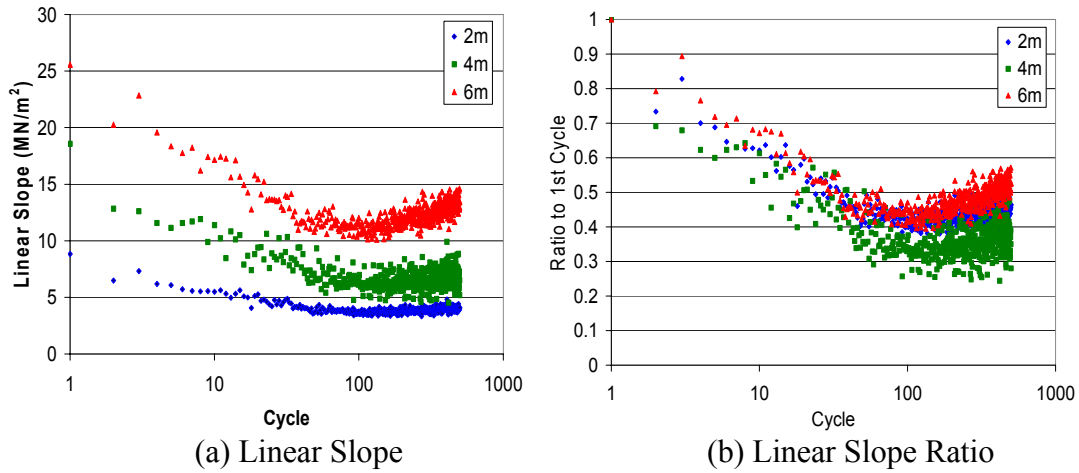


Figure 5.25 OWF 08 Stage 5 $\xi_b = 0.62$, $\xi_c = -0.25$ p - y Curve above Rotation Point Stiffness

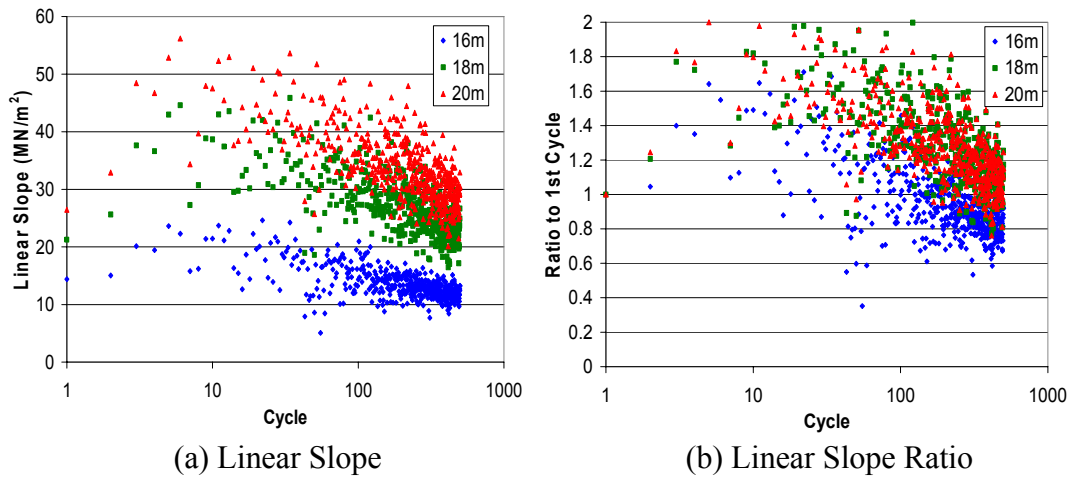


Figure 5.26 OWF 08 Stage 5 $\xi_b = 0.62$, $\xi_c = -0.25$ p - y Curve below Rotation Point Stiffness

An example of the excess pore pressure behaviour observed for stages involving cyclic loads of $\xi_c \approx -0.25$ is shown in Figure 5.27 for OWF 08 stage 5. Relative to Figure 5.14 for $\xi_c \approx 0$ and Figure 5.22 for $\xi_c \approx -0.35$, the excess pore pressure behaviour is significantly different. At location 1, the positive excess pore pressure at peak load maintains relatively constant whereas the negative excess pore pressures at the trough load reduce in magnitude in the first 100 cycles. Beyond 100 cycles, the negative excess pore pressures at the trough load slowly increase in magnitude. At location 2, positive excess pore pressures increase and negative excess pore pressures reduce in the first 100 cycles. Beyond 100 cycles, positive excess pore pressures slowly reduce and negative excess pore pressures slowly increase. A similar pattern is seen at location 3. At location 4, the positive and negative excess pore pressures remain relatively constant and equal in magnitude throughout the loading stage.

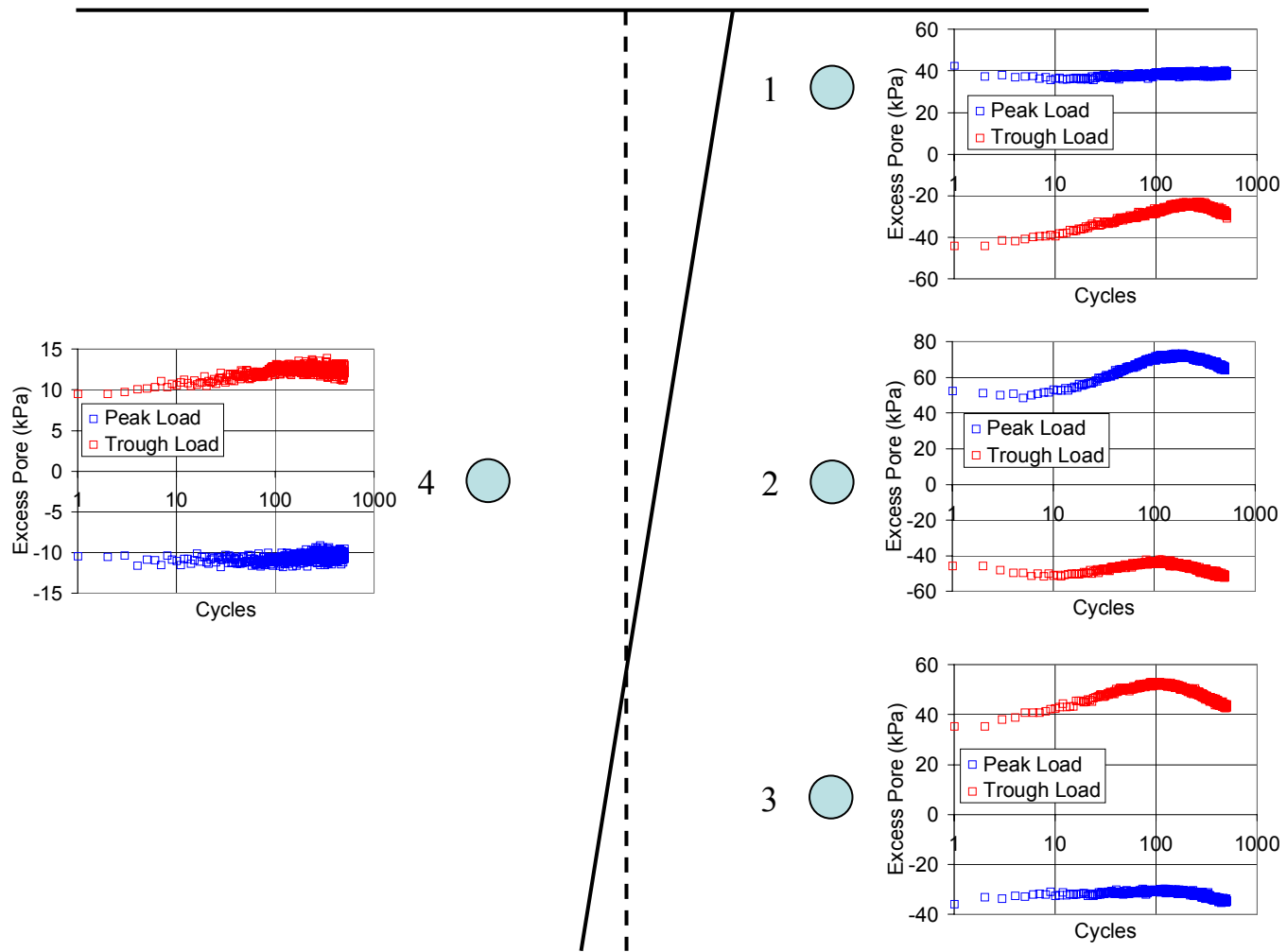


Figure 5.27 OWF 08 Stage 5 $\xi_b = 0.62$, $\xi_c = -0.25$ Excess Pore Pressure Behaviour

Based on the excess pore pressure behaviour, the greater positive excess pore pressures generated at locations 1 and 2 in the first 100 cycles during the progressive destruction of locked in stress contributed to the reduction in secant stiffness shown in Figure 5.24(b). After the destruction of the locked in stresses by the 100th cycle, stresses start to lock into the system with increasing cycles, causing negative excess pore pressures at locations 1 and 2 to slowly build up, resulting in the slow stiffening of the system. Similar to what was reported in the previous section for $\xi_c \approx -0.35$, the p - y curves experienced little change in stiffness. Since no measurements were made below the rotation point on the opposite side of location 3, it can only be suggested that the changes in stress conditions caused both positive and negative excess pore pressures to remain fairly constant. To verify this, experiments involving $\xi_c \approx -0.25$ with measurements below the rotation point on both sides of the monopile can be carried out.

Considering the significant difference in behaviour relative to $\xi_c \approx 0$ and $\xi_c \approx -0.35$, the results reinforce that cyclic loads of different characteristics can influence the cyclic stiffness behaviour of the monopile quite significantly as it can significantly influence the locked in stress conditions. This in turn changes the soil stress conditions which resultantly affect the excess pore pressure behaviour. Changes in excess pore pressure behaviour dictate the resulting cyclic stiffness behaviour. In the experiments carried out, the change was significant enough to cause significant softening in only 100 cycles instead of stiffening as observed in the stages involving $\xi_c \approx 0$ and $\xi_c \approx -0.35$ cyclic loads.

Despite the differences in cyclic stiffness behaviours observed for the different ξ_c tested, the results do not conclusively show that the resulting cyclic stiffness behaviour is solely dependent on ξ_c . Instead, there are other factors that contribute to the resulting cyclic stiffness behaviour. These factors will be discussed in the following section.

5.5.4 Factors and Conditions to Stiffening & Softening Regimes

To investigate the factors governing whether the monopile stiffens or softens, a comparison of the soil reaction curves at trough load was carried out between stage 4 for $\xi_c = 0$, stage 5 for $\xi_c = -0.24$, and stage 3 for $\xi_c = -0.35$ of experiment OWF 07 as shown in Figure 5.28.

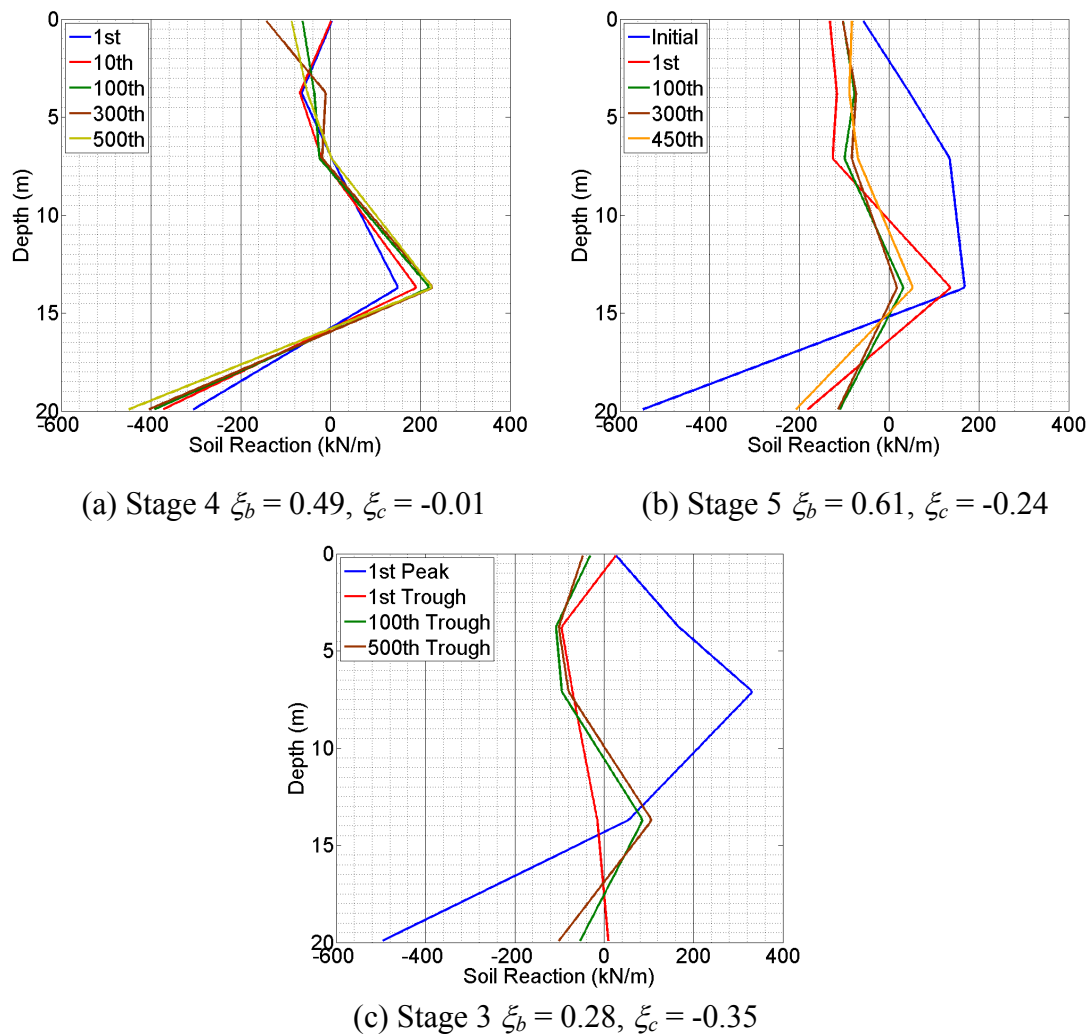


Figure 5.28 OWF 07 Soil Reaction at Trough for Different Stages

Similar to the behaviour of moment building up as in Figure 5.11(a) of section 5.5.2.1, Figure 5.28(a) for $\xi_c \approx 0$ shows similar behaviour with the soil reaction, p at trough/zero load building up throughout the monopile with increasing cycles, indicating the accumulation of locked in stresses. In Figure 5.28(b), cyclic loads of $\xi_c = -0.24$ causes a progressive reduction in p throughout the monopile in the first 100 cycles, indicating that locked in stresses are being progressively destroyed. Based on the graph, the progressive destruction of locked in stress is initiated by the reversal of

soil reaction above the rotation point due to loading in the reverse direction. However, beyond 100 cycles, p starts to increase and build up towards the forward loading side, indicating that stresses are gradually being locked in after being substantially destroyed in the first 100 cycles.

In Figure 5.28(c), the first cyclic load of $\xi_c = -0.35$ can be seen not only to cause soil reaction reversal above the rotation point but also a minor soil reaction reversal below the rotation point. However, as cycling progresses, resistance throughout the monopile depth progressively builds up. This suggests that soil reaction reversal throughout the whole monopile caused either substantial or complete destruction of locked in stresses in the system. With zero or little locked in stresses, the monopile system can only proceed to lock in stress with cyclic loading, causing an increase in the system's stiffness.

To confirm this, the soil reaction curves of OWF 08 stage 7 were reviewed as shown in Figure 5.29. In stage 7, after a monotonic push was carried out in the forward direction, a monotonic push was carried out in the reverse direction. Based on Figure 5.29, a slight soil reversal takes place below the rotation point and the lateral resistance at the pile toe is brought to zero when the reverse loading is 38.7% of the load magnitude in the forward direction. Beyond this magnitude, soil reaction reversal at the pile toe takes place. Based on the results, it can be suggested that a reverse load with a magnitude of at least 40% of the load magnitude in the forward direction will cause soil reaction reversal below the rotation point.

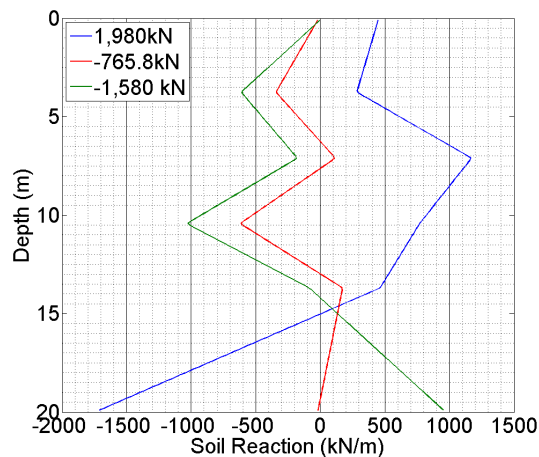
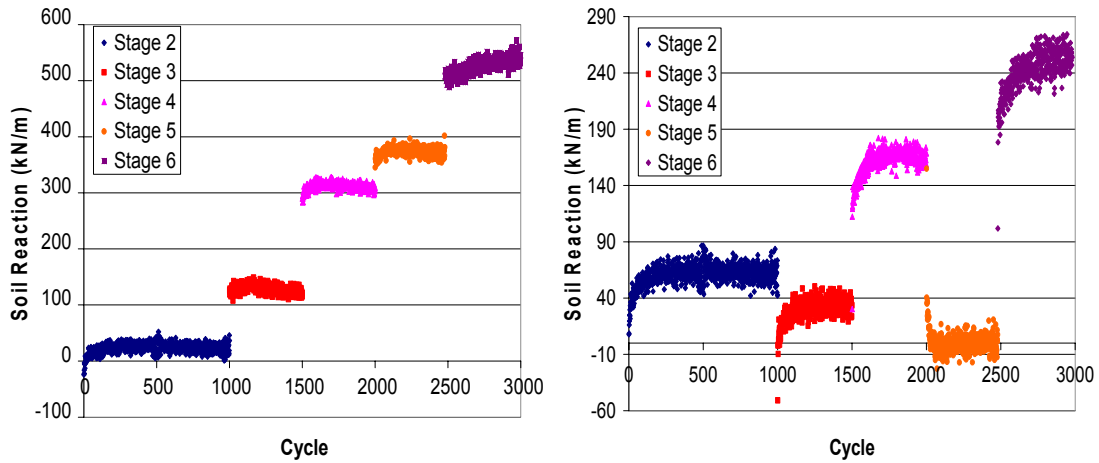


Figure 5.29 OWF 08 Stage 7 Monotonic Soil Reaction



(a) Peak Load (b) Zero Load
 Figure 5.30 OWF 07 Soil Reaction Change at 12m Depth

The role that locked in stress plays in the monopile's cyclic behaviour can be seen in Figure 5.30, showing an example of how the soil reaction changes as a result of the effect of locked in stresses. As can be seen from Figure 5.30(a), the peak soil reaction increases as the experiment proceeds from one stage to the next. In addition, the peak soil reaction remains relatively constant. This is to be expected as the peak load increases from one stage to the next. At time of zero load, the soil reaction in stage 2 increases with a rate that decreases with increasing cycles, corresponding to the behaviour that one would expect for cyclic loads of $\xi_c \approx 0$. In stage 3 where $\xi_c = -0.35$, the locked in stresses from stage 2 are completely destroyed, as shown by the plunge in soil reaction at zero load at the beginning of stage 3. With zero locked in stresses, the system proceeds to accumulate stresses, stiffening the system. In stage 5 where $\xi_c = -0.24$, the destruction of locked in stress does not occur immediately and progresses during the first 100 cycles. Beyond 100 cycles, the soil reaction at zero load slowly builds up. In stage 6, stresses get locked in at a greater rate with $\xi_c \approx 0$.

Based on the results shown from Figures 5.28 to 5.30, accumulated locked in stresses from previous cyclic loads and the cyclic loads of different ξ_c that follow can cause significant changes to the locked in stress conditions which in turn influences the cyclic stiffness behaviour of the monopile. However, the results are not conclusive enough to show that ξ_c is the sole factor that dictates the monopile's cyclic stiffness behaviour. Considering that locked in stresses play a role, it is highly likely that the maximum load magnitude relative to capacity, ξ_b plays a role in dictating the cyclic

stiffness behaviour. As shown in Table 5.2, ξ_b either increased with the progression of stages or was similar in magnitude to the ξ_b of the previous stage (henceforth referred to as $\xi_{b\text{ prv}}$). Therefore, the stiffening and softening regimes observed for $\xi_c \approx -0.35$ and $\xi_c \approx -0.25$ are limited to conditions where $\xi_b \geq \xi_{b\text{ prv}}$. Based on the results and the locked in stress conditions of the experiments, a flow chart was developed as shown in Figure 5.31 to summarise the possible range of cyclic load conditions that would lead to the stiffening and softening regimes.

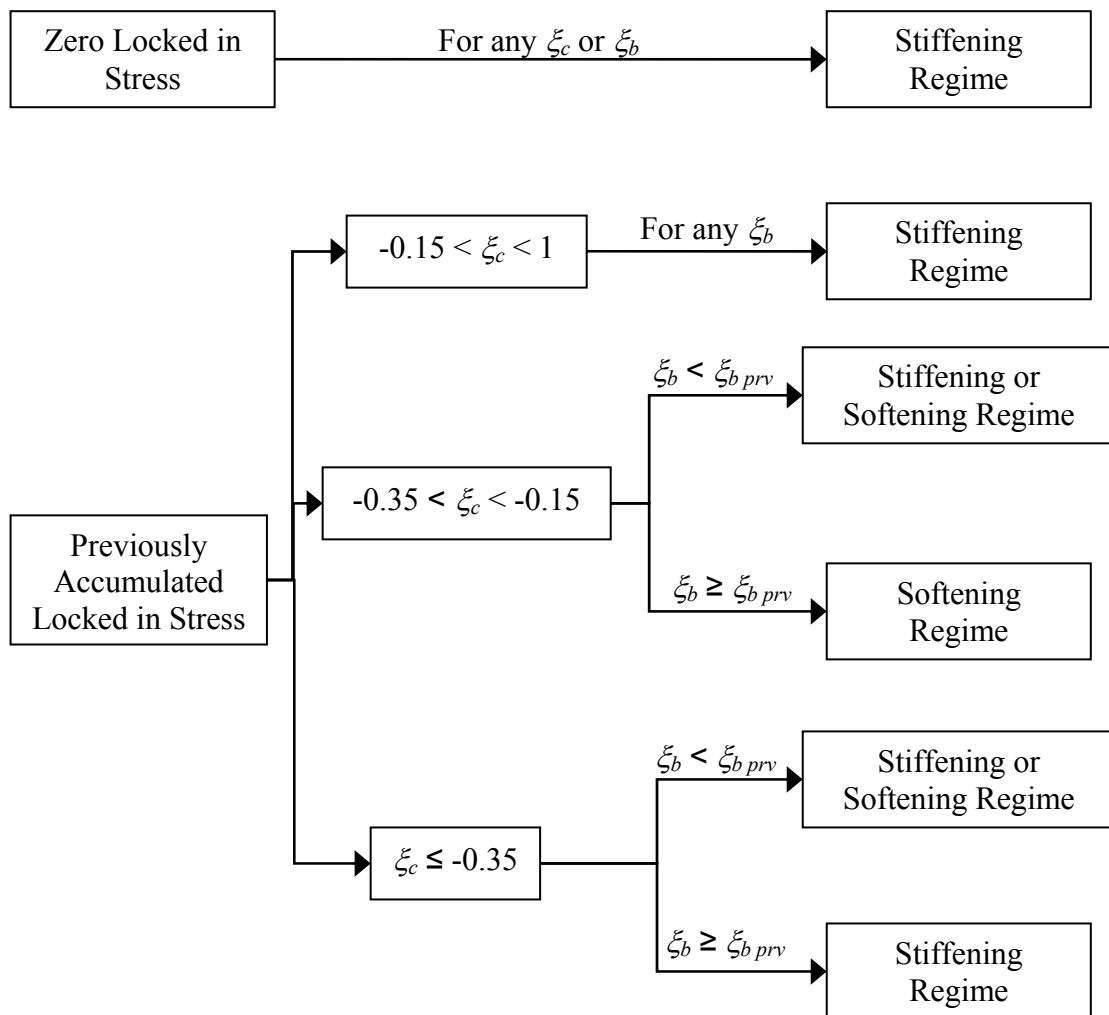


Figure 5.31 Cyclic Load Conditions Dictating Stiffening and Softening Regime

Since stiffening was observed in both $\xi_c \approx -0.35$ and $\xi_c \approx -0.25$ after locked in stresses were destroyed, the results strongly suggest that stiffening would take place under zero locked in stress conditions regardless of ξ_c or ξ_b . However, the cyclic stiffness behaviour of the monopile under previously accumulated locked in stress conditions is

dependent on ξ_c and ξ_b relative to $\xi_{b\text{ prv}}$. Since stiffening was observed for $\xi_c \approx 0$ regardless of ξ_b , since no load reversal takes place for $\xi_c > 0$ and since it is unlikely that significant load reversal will take place above the rotation point for $\xi_c > -0.15$, it was postulated that stiffening would take place under $-0.15 < \xi_c < 1$ regardless of ξ_b .

If $\xi_b \geq \xi_{b\text{ prv}}$ cyclic loads are applied under previously locked in stress conditions, cyclic loads of $-0.35 < \xi_c < -0.15$ would most likely cause significant load reversal above the rotation point that would cause progressive destruction of the locked in stresses, leading to softening. However, if $\xi_b < \xi_{b\text{ prv}}$, softening or stiffening may take place. In addition, the resulting behaviour is most likely to be dependent on the ratio of ξ_b relative to $\xi_{b\text{ prv}}$. For cyclic loads of $\xi_b \geq \xi_{b\text{ prv}}$, $\xi_c \leq -0.35$ cyclic loads will most likely cause soil reaction reversal above and below the rotation point, causing the complete destruction of locked in stresses. As a result, the system will proceed to accumulate locked in stresses with cyclic loading, causing stiffening. However, if $\xi_b < \xi_{b\text{ prv}}$, softening or stiffening may take place and similarly, the resulting behaviour will most likely be dependent on the ratio of ξ_b relative to $\xi_{b\text{ prv}}$.

Since Figure 5.31 was developed based on the limited results, there are uncertainties over the exact ξ_c value that would cause the transition from stiffening to softening or from softening to stiffening with $\xi_b \geq \xi_{b\text{ prv}}$ magnitude loads under previously accumulated stress conditions. These uncertainties are shown in Figure 5.32.

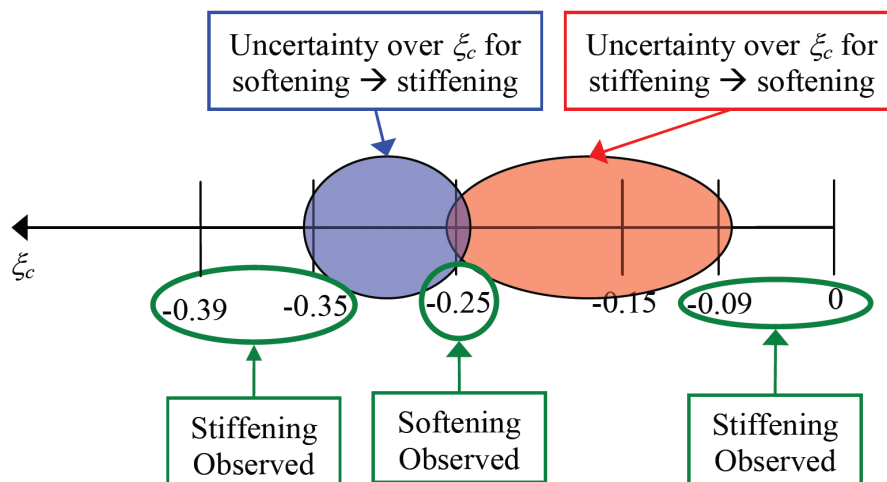


Figure 5.32 Summarised Observations and ξ_c Uncertainty Range Dictating Cyclic Stiffness Regime for $\xi_b \geq \xi_{b\text{ prv}}$

Based on Figure 5.32, further research should be carried out to determine the exact ξ_c value that would cause the transition from stiffening to softening or from softening to stiffening with $\xi_b \geq \xi_{b\text{ prv}}$ magnitude loads. In addition, further research should be carried out to determine the resulting cyclic stiffness behaviour from reverse cyclic loading with $\xi_b < \xi_{b\text{ prv}}$ magnitudes under previously accumulated locked in stress conditions and determine how the resulting behaviour is dependent on the magnitude of ξ_b relative to $\xi_{b\text{ prv}}$.

5.6 Estimating Cyclic Stiffness

5.6.1 Secant Stiffness over p - y Curve Stiffness

As mentioned in section 5.5.1, there are two ways to quantify the change in cyclic stiffness; firstly, changes in monopile secant stiffness, k and secondly, changes in p - y curve stiffness. Though it is ideal to quantify the change in cyclic stiffness via the p - y curves, there may be limitations that make it unsuitable. To determine if quantification of the p - y curves was sufficient to model the cyclic stiffness change, an exercise was carried out with LPILE for a 3.83 m monopile in 500 kPa preconsolidated speswhite kaolin (similar to the conditions of experiment OWF 06) with zero vertical load.

Case	p - y Curves Stiffness Ratio Change for Depths	
	0 m to 14 m	16 m to 20 m
1	1.5	0.6
2	2.0	0.6
3	2.5	0.6
4	0.5	1.0

Table 5.4 LPILE p - y Curve Stiffness Change Study Cases

Four cases were considered as detailed in Table 5.4. Cases 1, 2, and 3 simulate the stiffness change observed in $\xi_c \approx 0$ of OWF 07 stage 4, OWF 07 stage 2 and OWF 08 stage 6 respectively whereas case 4 simulates the stiffness change for $\xi_c \approx -0.25$ of OWF 07 stage 5. The stiffness ratios from the experimental stages mentioned can be seen in Table 5.5. To evaluate the appropriateness of quantifying the p - y curve stiffness change, the rotation depths of cases 1 to 4 were compared to the non-modified case. The rotation depth difference to the non-modified case is summarised in Table 5.6.

Depth (m)	Final Stiffness Ratio Relative to First Cycle at Stage			
	OWF 07 Stage 2 ($\xi_c = 0.06$)	OWF 07 Stage 4 ($\xi_c = -0.01$)	OWF 07 Stage 5 ($\xi_c = -0.24$)	OWF 08 Stage 6 ($\xi_c = -0.09$)
2	2.00	1.5	0.46	2.00
4	2.35	1.66	0.46	2.30
6	1.59	1.73	0.40	2.50
8	NA	1.73	0.36	NA
10	NA	1.60	0.36	NA
12	0.23	NA	0.35	NA
14	0.57	NA	0.47	NA
16	NA	NA	NA	0.84
18	NA	0.60	1.00	0.63
20	NA	0.50	1.00	0.64

Table 5.5 *p-y* Curve Final Stiffness Ratio Relative to First Cycle

ξ_b	Rotation Depth (m)	Rotation Depth of Case (m)			
	Non-modified	1	2	3	4
0.14	12.28	11.51	11.13	NA	13.78
0.17	12.92	12.10	11.65	11.34	14.33
0.20	13.57	12.72	12.29	11.95	14.69
0.25	14.02	13.23	12.86	12.56	14.85
0.33	14.22	13.49	13.19	12.99	14.93
0.50	14.26	13.52	13.34	13.11	14.87

Table 5.6 LPILE Rotation Depth Comparison between Study Cases

It can be seen that cases 1 to 3 display a shallower rotation depth compared to the non-modified case while case 4 has a deeper rotation depth. This is to be expected as an increase of stiffness above the rotation point will pull the rotation depth towards the mudline. In case 4, since the *p-y* curves below the rotation point are relatively stiffer than the *p-y* curves above the rotation point, the rotation point is pulled deeper towards the pile toe. The effect of *p-y* curve stiffness change on rotation depth can be quite significant, as shown by the values for both cases 3 and 4.

LPILE estimates indicate that rotation depth should change in correspondence to the change in stiffness of the *p-y* curves along the monopile. However, the rotation depth at peak load extracted from the soil reaction curves do not agree. As reported in Table 5.7, besides OWF 08 Stage 5 that experiences a deeper rotation depth as a result of the weakening of the *p-y* curves above the rotation point and OWF 07 stage 2 that experiences a deeper rotation depth instead of a shallower rotation depth as predicted by LPILE, the rotation depth of the other experimental stages do not experience

changes in rotation depth of the magnitudes reported in Table 5.6 and is very stable within the same cyclic loading stage.

Experiment	Rotation Depth (m) at Cycle		
	1st	100th	Final
OWF 06			
Stage 2 ($\xi_b = 0.12, \xi_c = -0.09$)	12.65	13.00	13.10
Stage 3 ($\xi_b = 0.25, \xi_c = -0.03$)	13.10	13.50	13.60
OWF 07			
Stage 2 ($\xi_b = 0.16, \xi_c = 0.06$)	11.55	12.50	12.70
Stage 3 ($\xi_b = 0.28, \xi_c = -0.35$)	14.32	14.45	14.30
Stage 4 ($\xi_b = 0.49, \xi_c = 0.01$)	14.77	14.9	14.83
Stage 5 ($\xi_b = 0.61, \xi_c = -0.24$)	14.74	14.78	14.75
Stage 6 ($\xi_b = 0.83, \xi_c = 0.08$)	14.81	14.73	14.74
OWF 08			
Stage 2 ($\xi_b = 0.16, \xi_c = 0.01$)	13.20	13.70	13.70
Stage 3 ($\xi_b = 0.41, \xi_c = 0.05$)	14.80	14.74	14.65
Stage 4 ($\xi_b = 0.57, \xi_c = 0.10$)	14.74	14.84	14.80
Stage 5 ($\xi_b = 0.62, \xi_c = -0.25$)	14.67	15.10	15.22
Stage 6 ($\xi_b = 0.72, \xi_c = -0.09$)	15.15	15.08	15.04

Table 5.7 Rotation Depth at Peak Load from Experiment Soil Reaction Curves

Based on the results of the exercise, it was determined that the quantification of p - y curve stiffness from cyclic loading via LPILE was unsuitable. This is most likely due to the limitations of LPILE as it is not able to capture the changes in locked in stresses and how the soil reaction changes with respect to the changes in locked in stresses. Considering that quantification of the p - y curve stiffness change is insufficient to capture the cyclic rotational depth behaviour and considering the unavailability of p - y curve stiffness data for the 7.62 m monopile of OWF 09, a method to estimate cyclic stiffness was developed based on monopile secant stiffness, k .

5.6.2 Estimating Cyclic Stiffness of Stiffening Regime

According to the model cyclic tests of LeBlanc et al. (2010b) in sand, the variation of secant stiffness for a monopile in sand due to cyclic loading can be estimated as below:

$$\tilde{k}_N = \tilde{k}_o + A_k \ln(N) \quad (5.9)$$

where \tilde{k}_N is the dimensionless pile stiffness at the N th cycle, \tilde{k}_o is the dimensionless first cycle pile stiffness, and A_k is a dimensionless constant. To determine \tilde{k}_o ,

$$\tilde{k}_o = K_b(\xi_b)K_c(\xi_c) \quad (5.10)$$

where K_b and K_c are dimensionless functions dependent on cyclic load characteristic and sand relative density. Review of LeBlanc et al. (2010b) suggests that the work was carried out under zero locked in stress conditions and does not take into consideration the effect of locked in stress. Though not specifically mentioned in LeBlanc et al. (2010b) whether the experiments were carried out separately from each other (instead of successive stages), the recommendations and results suggest that the experiments were carried out under zero locked in stress conditions. Although the experiments of LeBlanc et al. (2010b) use sand rather than clay as described here, the experiments of Kirkwood and Haigh (2014) also show substantial effects of locked-in stresses in sand.

To determine \tilde{k}_o , K_b and K_c have to be determined based on Figure 5.33. Based on the figure, it can be implied that K_c was determined relative to \tilde{k}_o of $\xi_c = 0$. However, in order to ensure that K_c can be accurately determined without it being affected by other factors, the cyclic experiments have to be done separately from each other.

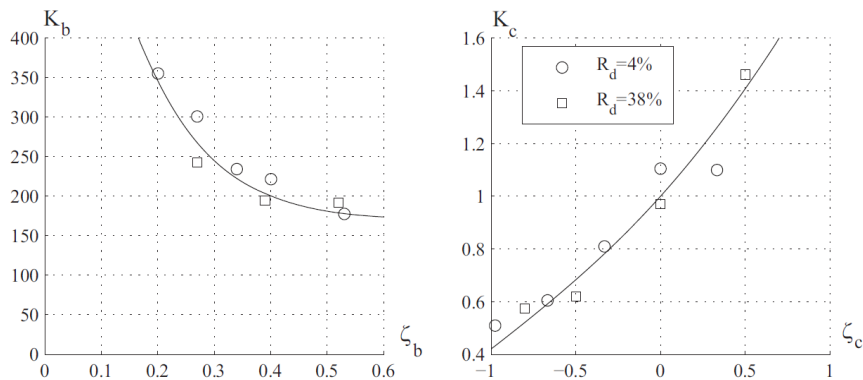


Figure 5.33 Values of K_b and K_c as a Function of Relative Density, R_d , and the Characteristics of the Cyclic Load in terms of ξ_b and ξ_c (LeBlanc et al., 2010b)

This can also be seen in Figure 5.34 that shows that K_c was calculated relative to the stiffness of $\xi_c = 0$, which is only possible when the experiments are done separately under zero locked in stress conditions. Based on the information available, LeBlanc et al.'s (2010b) recommendation is most likely valid under zero locked in stress conditions, which may not be true in practice owing to the varying nature of pile loading.

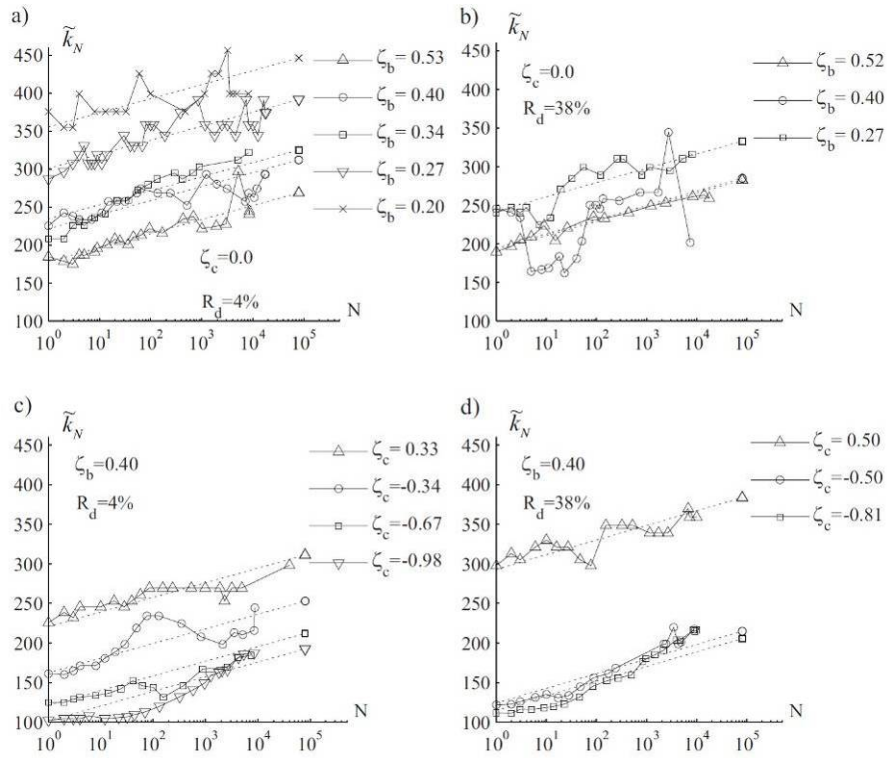


Figure 5.34 Measured Non-Dimensional Stiffness Results of LeBlanc et al. (2010b)

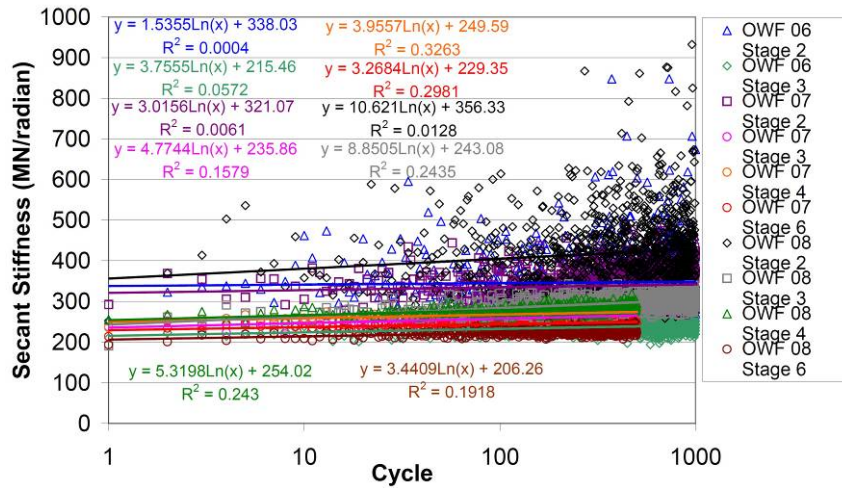
Despite the differences in locked in stress conditions, since secant stiffness was observed to increase logarithmically with number of cycles as shown in Figures 5.11(b) and 5.17(b), it was determined that cyclic stiffness be quantified similarly to equation (5.9). However, since the tests were carried out in succession with changing locked in stress conditions and the tests were not as extensive as LeBlanc et al. (2010b), it is not possible to estimate the first cycle stiffness as in equation (5.10).

According to equation (5.9), \tilde{k}_N increases at constant dimensionless rate of A_k of 8.02 that is “independent of both relative density and load characteristic” (LeBlanc et al., 2010b). According to LeBlanc et al. (2010b), non-dimensional stiffness, \tilde{k} is:

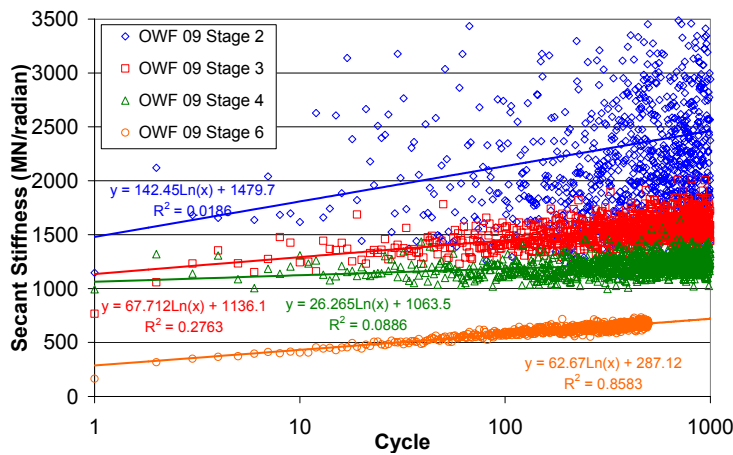
$$\tilde{k} = \frac{k}{L^5 D \sqrt{p_a \gamma'}} \quad (5.11)$$

where L is pile embedded length, D is pile diameter, p_a is atmospheric pressure, and γ' is effective unit weight. Based on the equation, k is linearly dependent on both L and D . If one were to keep L constant but double D , \tilde{k} would double, which is within expectations. Based on equations (5.9) and (5.11), this would also in turn double the

rate of stiffness increase. However, based on the logarithmic fits of Figure 5.35, the rate of stiffness increase in experiment OWF 09 for $D = 7.62$ m is 7 to 38 times greater than the rate of stiffness increase observed in experiment OWF 06 stage 3 where D is 3.83 m. Therefore the rate of stiffness increase for monopiles in clay is not as straightforward as what is suggested by LeBlanc et al. (2010b) and it is most likely that the suggestion by LeBlanc et al. (2010b) is limited to monopiles in sands.



(a) OWF 06 to OWF 08 ($D = 3.83$ m)



(b) OWF 09 ($D = 7.62$ m)

Figure 5.35 Secant Stiffness Logarithmic Fits of Cyclic Experiments

To determine if stiffness rate increase, A_k was dependent on strain, stage 2 and stage 3 marginal actuator displacements for experiments OWF 06 and OWF 09 were compared to each other as these stages had similar ξ_b and ξ_c values. In addition, the soil in both experiments was pre-consolidated to 500 kPa. Marginal strain, $\Delta\varepsilon_{pile}$ was

calculated by dividing the actuator displacement, Δy_{act} , by pile diameter, D using equation (5.12) and compared to each other as in Figure 5.36.

$$\Delta \varepsilon_{pile} = \frac{\Delta y_{act}}{D} \quad (5.12)$$

Figure 5.36 confirms that for the same ξ_b and for the same ξ_c , the initial k of the 7.62 m monopile is twice that of the 3.83 m monopile as suggested by equation (5.11). However, with increasing cycles, k of the 7.62 m monopile increases at a greater rate than the 3.83 m monopile, achieving a stiffness that is 3 to 3.5 times greater than the 3.83 m monopile after 1,000 cycles. Considering the change of $\Delta \varepsilon_{pile}$ of OWF 09 relative to $\Delta \varepsilon_{pile}$ OWF 06 throughout cyclic loading, it is highly likely that A_k is a function of $\Delta \varepsilon_{pile}$.

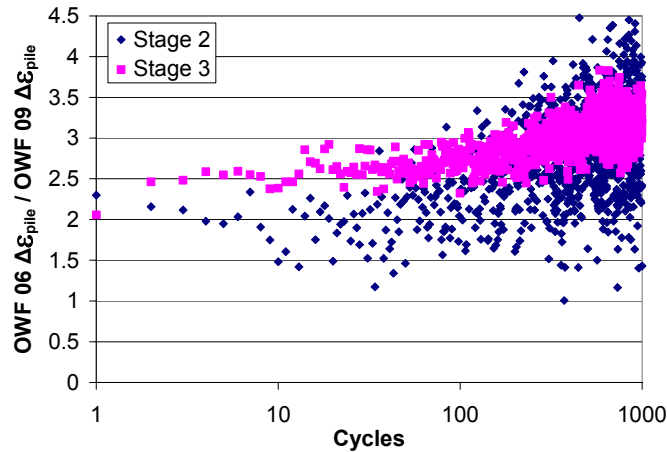


Figure 5.36 Marginal Strain Comparison between OWF 06 and OWF 09

To quantify the rate of increase of stiffness relative to strain, stiffness was firstly quantified as follows:

$$k_N = k_o \left(1 + \frac{A_k}{k_o} \ln(N) \right) \quad (5.13)$$

where k_N is monopile secant stiffness at the N th cycle and k_o is the fitted monopile secant stiffness at 1st cycle. Stiffness was calculated by utilising both marginal rotation as in equation (5.2) and marginal actuator displacement, Δy_{act} to determine which of the two was a better method of quantifying cyclic stiffness change. After

quantifying stiffness, A_k/k_o was then plotted against marginal rotation, $\Delta\theta$ and $\Delta\varepsilon_{pile}$ of the third cycle as in Figure 5.37. It should be noted that due to 2D-actuator trouble, 4.56 MN (i.e. $\xi_b = 0.837$) was applied prior to cyclic loading in OWF 09 stage 6. As a result, the system was significantly softened and compromised the stiffness data, producing an exceedingly high A_k/k_o far outside of the value range of Figure 5.37. Therefore, data from OWF 09 stage 6 was not considered. A similar incident with the 2D-actuator took place in OWF 07 stage 3 where four cycles of 0.82 MN (i.e. $\xi_b = 0.404$) of $\xi_c = 0$ were applied prior to the cyclic loads. Fortunately, as a result of the slightly larger load magnitude relative to the cyclic loads of $\xi_b = 0.28$ that followed, the system was not softened significantly and produced A_k/k_o values that are close to the other data points.

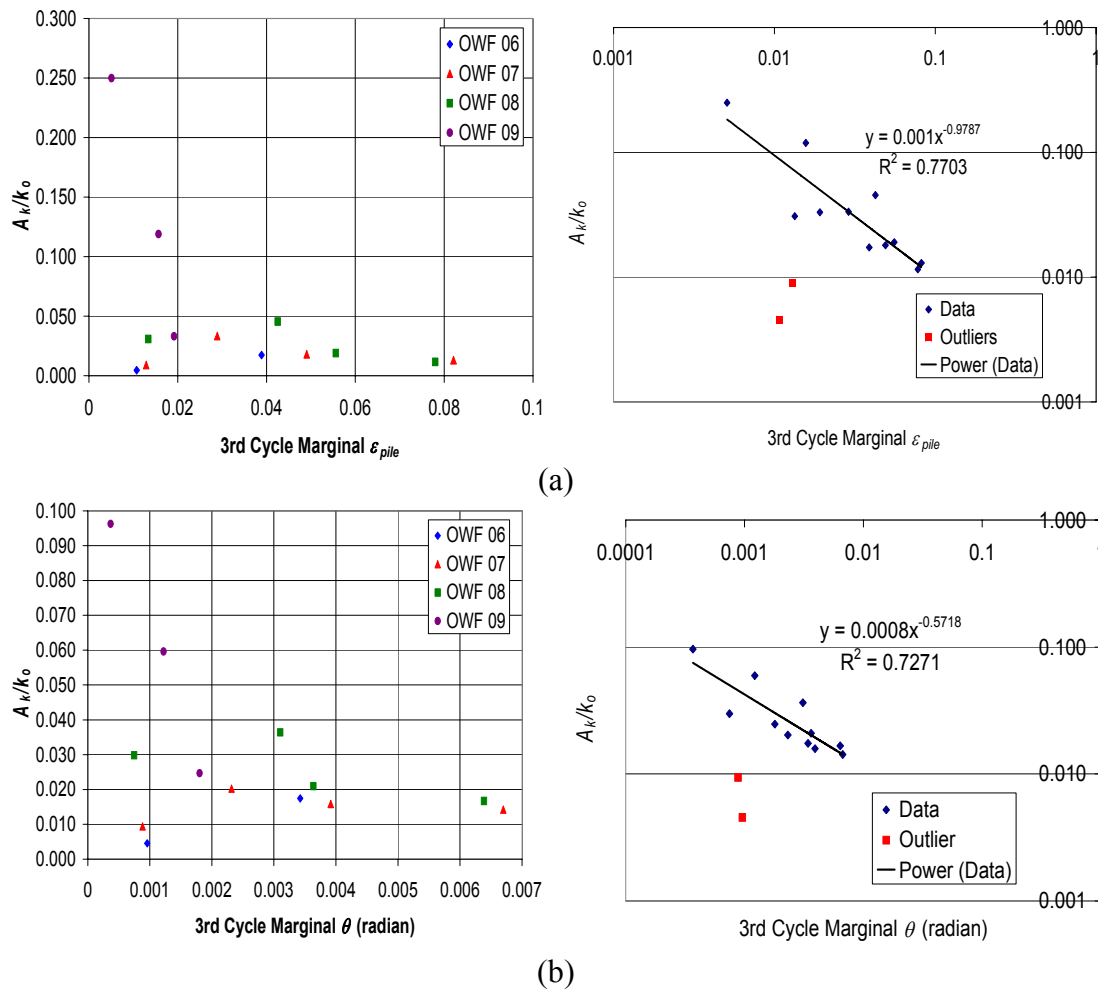


Figure 5.37 Power Function Fitting to (a) A_k/k_o vs. $\Delta\varepsilon_{pile}$ (b) A_k/k_o vs. $\Delta\theta$

It is quite clear that the A_k/k_o points of experiment OWF 09 are much higher relative to the points from experiment OWF 06 to OWF 08. In addition, vertical load was free to act in OWF 09. Therefore, it can be argued that the experimental points of OWF 09 should be analysed separately from OWF 06 to OWF 08. However, if one were to consider the monopile-soil system as a simple spring system as in Figure 5.38, it is expected that the vertical load would reduce the rate of stiffness increase instead of increasing it as shown in Figure 5.37. Since this is not the case, it was decided that the data be analysed together. When put together, the data points strongly suggest that the rate of stiffening, A_k with respect to the initial stiffness, k_o is a function of the initial $\Delta\varepsilon_{pile}$ or the $\Delta\theta$. In addition, it suggests that A_k/k_o decreases with increasing $\Delta\varepsilon_{pile}$ and $\Delta\theta$. In normal space, the data points suggest the shape of a power function.

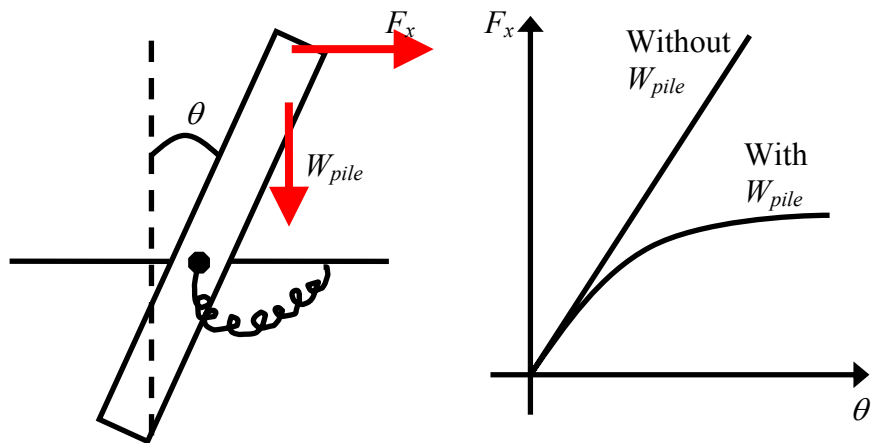


Figure 5.38 Behaviour Comparison between Pile With and Without Vertical Load

Before a function was fitted, the outliers were determined by calculating significance of correlation more commonly known as the *p-value*. According to Montgomery et al. (2004), the *p-value* is defined as “the smallest level of significance that would lead to a rejection of the null hypothesis”. According to Vardanega (2011), low *p-values* for a correlation provide strong evidence that there exists a correlation between the dependent and independent variable. The lower the *p-value*, the lower the probability that a similar regression with random sampling would result in a coefficient of determination R^2 at least as large as observed. If the *p-value* for a regression is 0.001 for an R^2 of 0.5, it means that there is a 1 in 1,000 chance that a similar regression with random sampling would result in an R^2 value that is at least as large as 0.50, making the regression statistically significant. Therefore, regressions with much

higher *p-values* have lower statistic significance. The *p-value* criterion utilised to determine the outliers was that the *p-value* < 0.01.

Using Student's t-distribution, the test statistic t_{st} is calculated as:

$$t_{st} = \frac{r \times \sqrt{n-2}}{\sqrt{1-r^2}} \quad (5.14)$$

where r is the square root of the coefficient correlation, R^2 which can vary from -1 to 1 and n is the number of data points used in the regression. Once t_{st} was calculated, the *p-value* was calculated using the TDIST function in Microsoft Excel that calculates the Student's t-distribution. According to Miles and Barnyard (2007), the *p-value* is calculated in Microsoft Excel with the TDIST function as follows:

$$p\text{-value} = \text{tdist}(t_{st}, \text{dof}, \text{tails}) \quad (5.15)$$

where *dof* is the number of the degrees of freedom that is greater or equivalent to 1 and *tails* is the number of tails for the distribution that must be either 1 (returning the one-tailed distribution) or 2 (returning the two-tailed distribution). Since a two-tailed distribution was utilised, $\text{dof} = n - 2$ and $\text{tails} = 2$. Utilising equations (5.14) and (5.15), the *p-values* for the fittings shown in Figure 5.35 were calculated. Based on the R^2 values for OWF 06 stage 2 and OWF 07 stage 2, the resulting *p-values* were 0.99 and 0.85 respectively. Since the *p-values* greatly exceeded 0.01, these fittings were considered as outliers, as shown in Figure 5.37.

Both power fittings to A_k/k_o vs. $\Delta\varepsilon_{pile}$ and $\Delta\theta$ curves have coefficients of determination that are very similar to each other. Though it is preferable to select A_k/k_o vs. $\Delta\varepsilon_{pile}$ that categorises strain with respect to diameter, D as compared to A_k/k_o vs. $\Delta\theta$ that categorises strain with respect to pile length, L , the A_k/k_o vs. $\Delta\theta$ fitting was selected for various reasons. Firstly, if A_k/k_o vs. $\Delta\varepsilon_{pile}$ was selected, then $\Delta\varepsilon_{pile}$ would have to be redefined based on marginal mudline displacement. Though it is possible to accurately estimate the marginal mudline displacement of experiments OWF 06 to OWF 08 as soil reaction data is available in conjunction with both laser displacement and MEMs readings, it is however not possible for experiment OWF 09 as no bending

moment readings are available due to the failure of the strain gauges. In addition, the estimation of bending moments above the mudline to calculate displacements is not suitable as there are no bending moment readings to confirm the vertical load conditions above the mudline and any assumptions made would introduce inaccuracies.

Another possible option to calculate the marginal mudline displacement is by assuming the pile is completely rigid with zero flexing. With this assumption, not only can rotation depth, d_{rot} be calculated utilising both laser & MEMs rotation measurements, the mudline displacement can also be trigonometrically calculated. However, there are issues that make this option unsuitable. As highlighted in Figure 5.5, the rotation depth at zero load was observed to be deeper relative to the rotation depth at peak load. In addition, even though the rotation depth at peak load calculated from “soil reaction” and “Laser & MEMs” were similar, the rotation depth at zero load between these two methods were significantly different, highlighting the limitation of the laser & MEMs readings methodology to accurately calculate the rotation depth at zero load.

Though soil reaction data is unavailable for OWF 09, marginal mudline displacement can be calculated by assuming the rotation depth remains constant from zero to peak load while utilising the peak load rotation depth from the laser and MEMs readings. However, this methodology will produce inaccurate estimates of k . An example is shown in Figure 5.39 that shows the difference between stiffness calculated with a changing rotation depth from zero load to peak load (taken from soil reaction) and a constant rotation depth which is taken at peak load. Marginal mudline displacement was calculated using the marginal laser readings 10 m above mudline. Even though the initial stiffness values are similar, the difference between both methods increases with increasing cycles, resulting in different A_k values that would significantly affect the validity of the A_k/k_o vs. $\Delta\varepsilon_{pile}$ fitting.

Considering the absence of bending moment curves to accurately estimate mudline displacement, the uncertainties of the vertical load condition and the inaccuracies that may be introduced by assuming the vertical load condition, and the inaccuracies

introduced by assuming a constant rotation depth (as shown in Figure 5.39), complete and accurate redefinition $\Delta\varepsilon_{pile}$ to mudline displacement for the A_k/k_o vs. $\Delta\varepsilon_{pile}$ fitting cannot be done. Therefore, the A_k/k_o vs. $\Delta\theta$ fitting was selected.

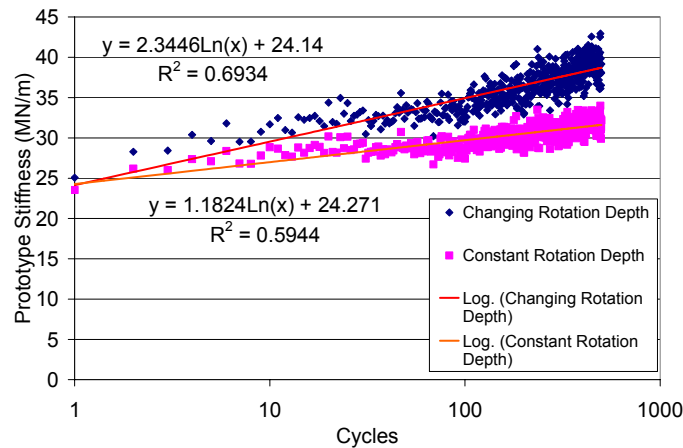


Figure 5.39 OWF 08 Stage 4 $\xi_b = 0.57$, $\xi_c = 0.10$ Monopile Secant Stiffness from Mudline Displacement Comparison between Changing and Constant Rotation Depth

To determine how accurate the A_k/k_o vs. $\Delta\theta$ fitting of Figure 5.37(b) was, the fitting was utilised to calculate A_k and then used in conjunction with equation (5.13) to estimate k . As shown in Figure 5.40, most of the load stages have a k_o (fitted secant stiffness at cycle 1) that is equal or similar to the measured k at cycle 1. However, some of the experimental stages have a k_o that is significantly higher than the measured k at cycle 1. k_o was hence utilised instead of the measured k at cycle 1 as usage of k_o produced much more accurate estimates that matched experimental observations. For consistency, k_o was utilised throughout the comparisons.

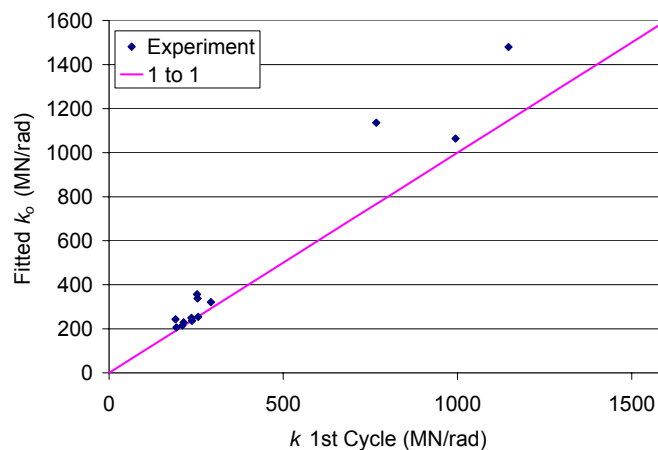


Figure 5.40 Fitted Secant Stiffness and Measured Secant Stiffness at Cycle 1

Comparisons of the estimates, $k_{equation}$ with the experimental observations, $k_{experiment}$ are shown in Figure 5.41. Comparison was not done with OWF 06 stage 2 and OWF 07 stage 2 as the data from these stages were determined as outliers as previously discussed. Since the cyclic experiments were not as extensive as those of LeBlanc et al. (2010b) and were carried out in succession instead of at zero locked in stress conditions, it is not possible to develop a methodology similar to equation of (5.10) of LeBlanc et al. (2010b) to estimate k_o . Considering the limitations, accurate estimation of cyclic secant stiffness will require one to estimate k_o from a monopile that has been subjected to at least a few cycles of cyclic load. In practice a prediction of behaviour during the first cycle of loading is almost irrelevant for a wind turbine, as lifetime behaviour will dominate performance (provided that the first cycle behaviour is not substantially weaker than subsequent behaviour).

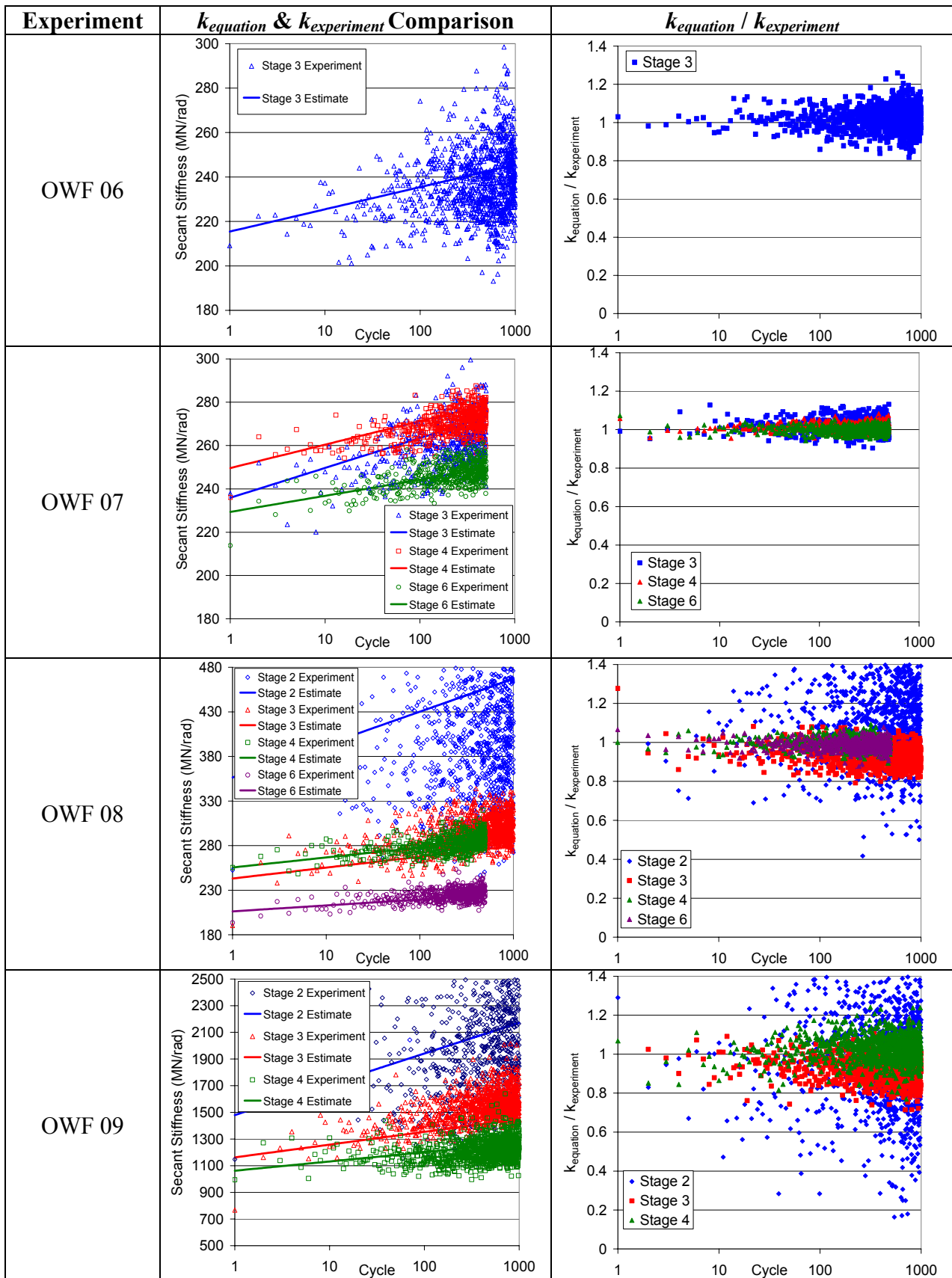


Figure 5.41 Secant Stiffness Comparison between Equation Derived vs. Experiment

As can be seen from Figure 5.41, k is accurately estimated by the usage of the A_k/k_o vs. $\Delta\theta$ fitting of Figure 5.37(b) and compares very well despite the scatter observed in stage 2 due to the high noise to signal ratio. Therefore, the comparison suggests that the A_k/k_o vs. $\Delta\theta$ fitting of Figure 5.37(b) is valid and can be used in conjunction with equation (5.13) to accurately estimate k in the stiffening regime. However, the fitting is only valid for monopile-soil systems that have not been significantly softened. As mentioned earlier, the monopile-soil system was significantly softened in OWF 09 stage 6 as a result of a 4.56 MN load applied prior to cyclic loading due to 2D-actuator trouble. If the fitting is utilised to estimate stiffness change of OWF 09 stage 6 as in Figure 5.42, the fitting would significantly underestimate k . This is due to the significant softening from the 4.56 MN load prior to cyclic loading. Based on the results, the fitting is only valid for monopile-soil systems that have not previously been significantly softened. It is hence only valid when the current loading pattern is the largest magnitude that the pile has experienced.

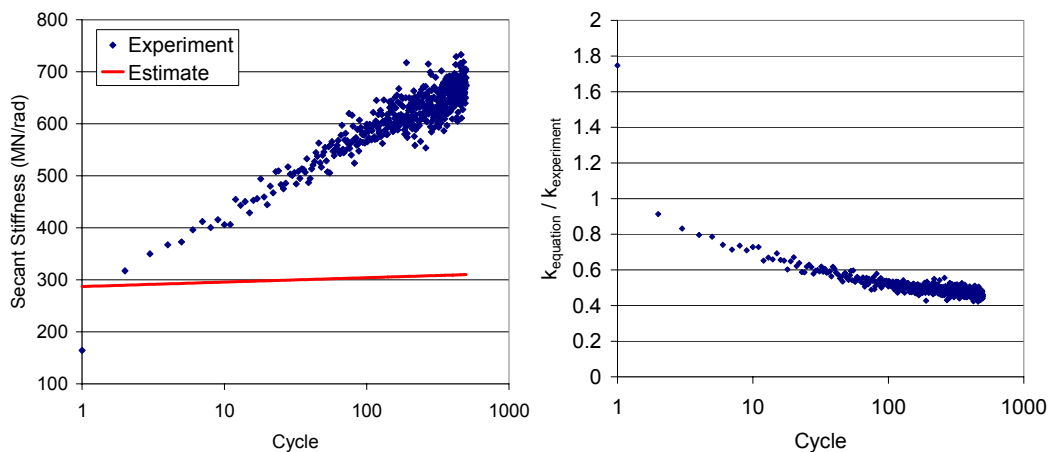


Figure 5.42 OWF 09 Stage 6 $\xi_b = 0.40$, $\xi_c = -0.39$ Secant Stiffness Comparison between Equation Derived vs. Experiment

5.6.3 Estimating Cyclic Stiffness of Softening Regime

As discussed in section 5.5.4, a range of reverse cyclic loads to a monopile-soil system that has previously accumulated locked in stresses will cause soil reaction reversal that destroys the locked in stresses within the first 100 cycles, softening the monopile-soil system. Once the stresses have been destroyed, the system will once again proceed to slowly lock in stresses and stiffen. Based on Table 5.2, only three stages of $\xi_c \approx -0.25$ cyclic loads were carried out for a $\xi_b = 0.61$, 0.62, and 0.44. With limited data, it is not possible to develop a comprehensive and fully validated

methodology to estimate the rate of softening experienced by a monopile-soil system with previously accumulated stresses under different ξ_b values. However, considering the ξ_b values of the cyclic load stage 4, it is possible to compare the rate of stiffness change between stiffening and softening regime for similar ξ_b .

Experiment	A_k (MN/rad per ln (N)) at Stage			Stage 5 A_k / Stage 4 A_k	
	4	5		1 st 100	Beyond 100
		1 st 100	Beyond 100		
OWF 07	3.956	-11.213	0.815	-2.835	0.206
OWF 08	5.320	-14.043	3.536	-2.640	0.665
OWF 09	26.265	-80.404	32.694	-3.062	1.245

Table 5.8 A_k Comparison between Stiffening and Softening Regimes for Similar ξ_b

The comparison of A_k between stages 4 and 5 as in Table 5.8 suggests that for similar ξ_b , the monopile-soil system softens at a rate 2.6 to 3 times faster than the stiffening rate of the stiffening regime within the first 100 cycles. Though the extent of softening is limited to 100 cycles, the degree that it softens relative to the stiffness of the 1st cycle is quite substantial.

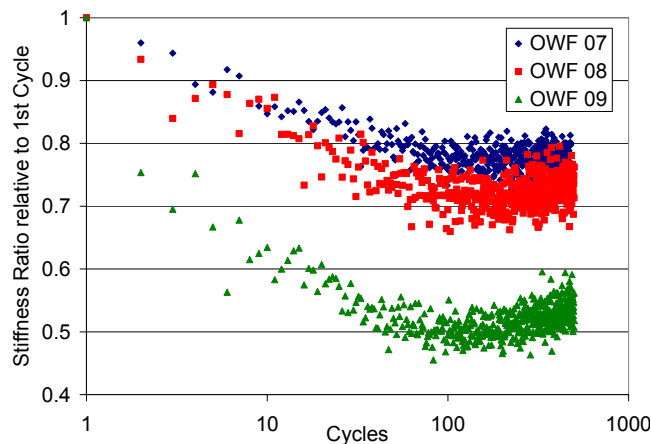


Figure 5.43 Stiffness Change Relative to 1st Cycle for Softening Regime

As shown in Figure 5.43, the 3.83 m monopile-soil system softens by 25% to 30% while the 7.62 m monopile softens by 50%. Based on Table 5.8, beyond 100 cycles, the system starts to stiffen at an A_k that is substantially less or slightly bigger than A_k of the stiffening regime. Since the stiffening behaviour is logarithmic in nature, marginal stiffening beyond 100 cycles reduces with increasing cycles, causing the system to stiffen at an increasingly reduced rate. Assuming the system was to soften

substantially as seen in experiment OWF 09, it would take millions of cycles of sustained reverse loading for the stiffness of the system to be restored to its original stiffness. However, this is unlikely to be the case in the field as cyclic loading is varied in nature. In summary, the results suggest that reverse cyclic loading of the characteristics mentioned in section 5.5.4 on a monopile-soil system with previously accumulated locked-in stresses can be extremely detrimental as it can significantly soften the system and reduce the system's natural frequency substantially.

5.6.4 Recommendation to Estimate Cyclic Stiffness

Based on the results, the following methodology is recommended to estimate the increase of k of monopile-soil systems due to the stiffening regime:

1. Determine an appropriate $\Delta\theta_o$ (radians) from zero load to peak load for the first cycle of cyclic load in question. This in turn will enable calculation of k_o .
2. Once an appropriate $\Delta\theta_o$ has been determined, utilise equation (5.16) as below to determine the rate of stiffness increase, A_k with respect to k_o .

$$\frac{A_k}{k_o} = 0.0008\Delta\theta_o^{-0.572} \quad (5.16)$$

3. Once A_k/k_o has been determined, estimate cyclic stiffness utilising the previously mentioned equation (5.13)

$$k_N = k_o \left(1 + \frac{A_k}{k_o} \ln(N)\right) \quad (5.13)$$

To estimate the softening rate, $A_{k \text{ soft}}$ due to the softening regime for cyclic loads with $\xi_b \geq \xi_{b \text{ prv}}$ on a system with previously accumulated locked in stresses, the following equation can be utilised:

$$A_{k \text{ soft}} = -\omega.A_k \quad (5.17)$$

where $2.6 \leq \omega \leq 3.0$. Once $A_{k \text{ soft}}$ has been calculated, the reduced stiffness in the first 100 cycles can be calculated by substituting A_k of equation (5.13) with $A_{k \text{ soft}}$.

5.7 Estimating Accumulated Rotations

5.7.1 Estimating Accumulated Rotations in Stiffening Regime

There are two ways to quantify accumulated rotations, exponentially as proposed by LeBlanc et al. (2010b) or logarithmically as proposed by Lin and Liao (1999). Exponential quantification of accumulated rotation was carried out to evaluate the suitability of this methodology. Based on LeBlanc et al.'s (2010b) model cyclic tests in sand, the accumulated rotation resulting from cyclic loading in sand can be quantified as:

$$\frac{\Delta\theta(N)}{\theta_s} = T_b(\xi_b, R_d)T_c(\xi_c) \cdot N^{0.31} \quad (5.18)$$

where $\Delta\theta(N)$ is the N th cycle cumulative net rotation from the first cycle, θ_s is the static pile rotation as shown in Figure 5.44. T_b and T_c are dimensionless functions that are dependent on load characteristics and relative density as shown in Figure 5.45. M in Figure 5.44 refers to applied bending moment whereas M_{max} and M_{min} are the maximum and minimum applied bending moments respectively.

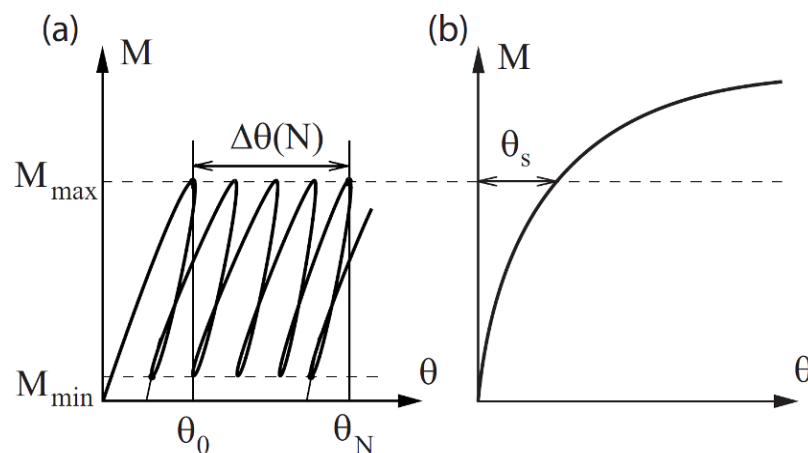


Figure 5.44 Accumulated Rotation Definition (adapted from LeBlanc et al., 2010b)

Based on Figure 5.45, accumulated rotation increases as ξ_b increases. This is expected as a greater load magnitude would induce greater displacements. In addition, for the same ξ_b , $-0.9 < \xi_c < 0$ produces greater accumulated rotation relative to $\xi_c = 0$.

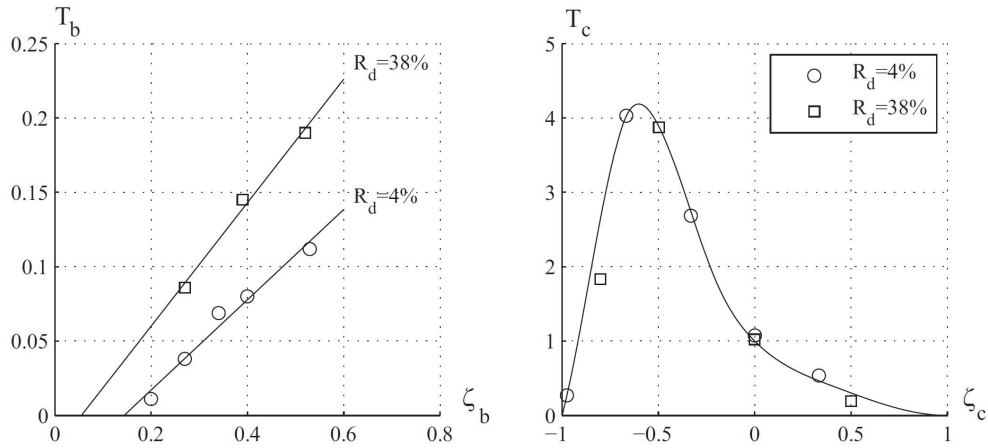


Figure 5.45 Functions Relating T_b and T_c to R_d , ξ_b , and ξ_c (LeBlanc et al., 2010b)

As in Table 5.2, cyclic tests of $\xi_c < 0$ were very limited and not carried out at the same ξ_b . Therefore, it was not possible to fully verify LeBlanc et al.'s (2010b) finding and develop an equation that fully accounts for ξ_c . As a result, general quantification of accumulated rotations due to the stiffening regime with respect to ξ_b was carried out. To determine if accumulated rotations could be quantified exponentially, accumulated rotations were quantified as:

$$\frac{\Delta\theta(N)}{\theta_o} = B.N^\eta \quad (5.19)$$

where θ_o is the peak load rotation of the first cycle and η is the average exponent resulting from the power curve fits to the experimental data. Since the stiff base layer of OWF 07 and OWF 08 experienced significant softening, it is highly likely that the stress-strain properties of the stiff base layer no longer behaved according to equation (4.5) by Vardanega et al. (2012) in section 4.4.1. Since no triaxial tests were carried out to measure the stress-strain properties of the softened base layers, accurate estimation of ε_c was not possible. Therefore, estimation of θ_s for experiments OWF 07 and OWF 08 via LPILE was not possible. As a result, θ_o , as shown in Figure 5.44 was utilised instead of θ_s . The average exponential power η was determined to be 0.348.

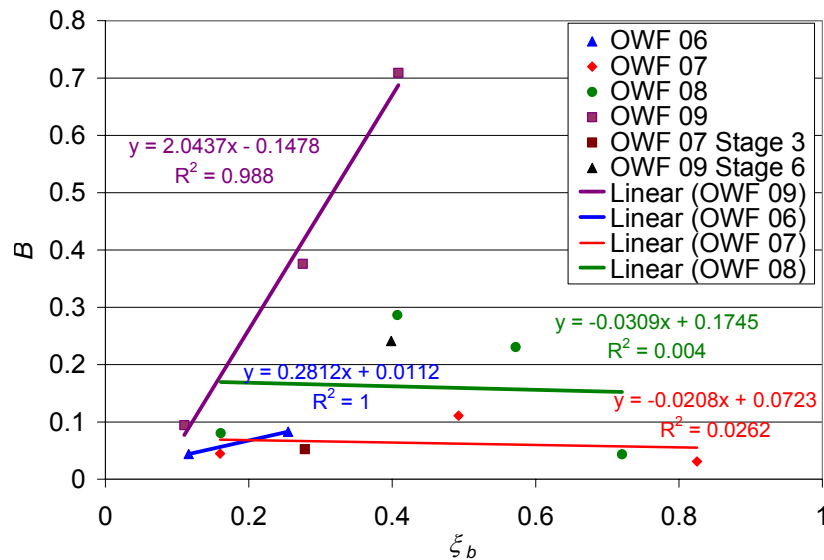


Figure 5.46 B as a Function of ξ_b

B was plotted against ξ_b and fitted with linear fittings with respect to each experiment as shown in Figure 5.46. Data from OWF 09 stage 6 ($\xi_b = 0.4$ and $\xi_c = -0.39$) and OWF 07 stage 3 ($\xi_b = 0.28$ and $\xi_c = -0.35$) were not considered in the fittings for various reasons. Firstly, the observed accumulated rotation behaviour was most likely compromised by previously applied loads of greater magnitudes. As in Figure 5.46, the B value from OWF 09 stage 6 of 0.24 is relatively much lower compared to the B value of 0.71 from OWF 09 stage 4 for ξ_b of 0.4. This is not possible as there cannot be two extremely different B values for the same ξ_b . In addition, the accumulated rotations observed in OWF 09 stage 6 may have been compromised. As mentioned at the end of section 5.6.2 and shown in Figure 5.42, due to 2D-actuator problems, the monopile was significantly softened in OWF 09 stage 6 since a $\xi_b = 0.837$ load was applied prior to the cyclic load which in turn compromised the secant stiffness data. Similar to OWF 09 stage 6, four cycles of $\xi_b = 0.404$, $\xi_c = 0$ load were applied prior to the cyclic loads of OWF 07 stage 3. Even though the load magnitude was relatively small and did not significantly affect the stiffness data resulting from the cyclic loads, the low rate of accumulated rotations observed suggest that the accumulated rotation behaviour was adversely affected by the larger magnitude loads applied prior to the cyclic loads.

Secondly, reverse cyclic loads of $\xi_c \approx -0.35$ are expected to cause greater accumulated rotations. According to LeBlanc et al. (2010b), cyclic loads of $\xi_c = -0.35$ for the same

for the same ξ_b , should accumulate rotations at a rate 2.7 times greater than $\xi_c = 0$. Similarly, Kirkwood and Haigh (2013) observed greater pile head accumulated rotations for $\xi_c = -0.37$. Considering that the accumulated rotation data was adversely affected by the larger magnitude loads applied prior to the cyclic loads and that literature suggests that the accumulated rotations for cyclic loads of $\xi_c \approx -0.35$ should be greater relative to $\xi_c = 0$ cyclic loads, data from OWF 09 stage 6 and OWF 07 stage 3 was not considered.

Based on Figure 5.46, data from experiments OWF 07 to OWF 08 are in conflict with the expectation of increasing accumulated rotation with increasing ξ_b . In addition, the coefficient of determination R^2 from the linear fits is extremely low, indicating that the fittings should not be considered. The data from experiment OWF 06 and OWF 09 (where $D = 7.62$ m) produces a high coefficient of determination linear fit that is in line with the expectation of increasing rate of accumulated rotation with increasing ξ_b . However, the slope of the linear fit for OWF 09 is 7.3 times bigger than that of OWF 06. Since the linear fitting results across the experiments were inconsistent, exponential quantification of accumulated rotations was deemed unsuitable.

Since exponential quantification was not suitable, logarithmic quantification of accumulated rotation was carried out. Similar to Lin and Liao (1999), accumulated rotation was quantified as:

$$\frac{\theta_N}{\theta_o} = 1 + j \ln(N) \quad (5.20)$$

where θ_N is the peak load rotation at the N th cycle, θ_o is the peak load rotation of the 1st cycle, and j is the dimensionless rate of accumulated rotation.

Similar to Figure 5.46, linear fits to each experiment was carried out as shown in Figure 5.47. In addition, similar to the exponential fits and for the same reasons mentioned previously, data from OWF 09 stage 6 and OWF 07 stage 3 was not considered. Based on Figure 5.46, the linear fittings to each experiment are in line with the expectation of increasing accumulated rotation with increasing ξ_b . In addition,

the slope of the linear fits for experiments OWF 06 to OWF 08 involving the 3.83 m pile diameter is similar to each other as shown in Figure 5.47.

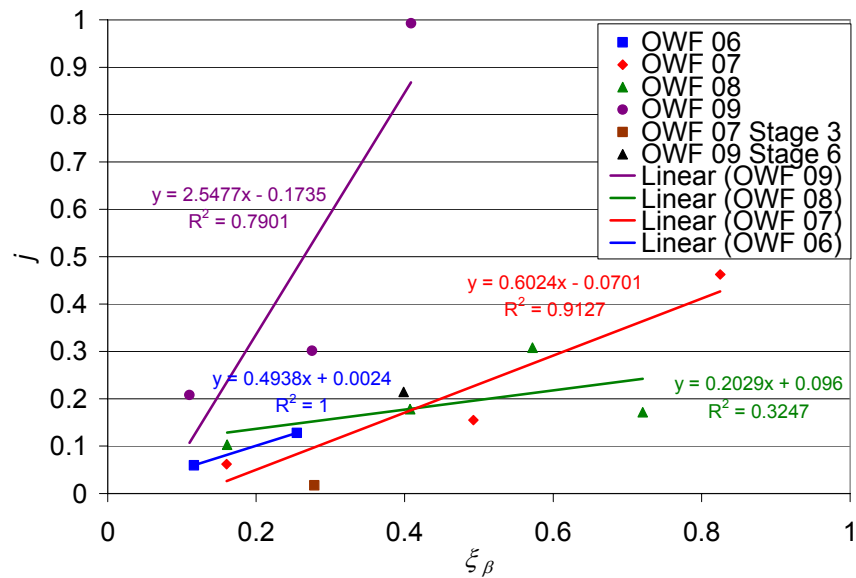


Figure 5.47 j Fittings as a Function of ξ_b for Respective Experiments

The slope of the OWF 09 linear fit is exceptionally high due to the exceptionally high rate of accumulated rotation observed in stage 4 where $\xi_b = 0.41$. Investigation into the data from OWF 09 stage 4 did not indicate issues with the logarithmic fit as the p -value < 0.01 . With limited data and no other experiments involving the 7.62 m diameter monopile, validation and comparison of the data from OWF 09 stage 4 was not possible. Therefore, more experiments involving the 7.62 m diameter should be carried out to ascertain the observation and to determine the cause behind the observation.

Since the working load of the wind turbines should range from $0.2 \leq \xi_b \leq 0.3$ (as shown in Figure 4.24, the monopile would have rotated 0.5° at mudline at $\xi_b \approx 0.5$), data from OWF 09 stage 4 was taken out of consideration from the fitting. In addition, since vertical load was free to act in OWF 09 due to the absence of the counterweight system, it is possible that the 7.62 m monopile experienced greater accumulated rotations rates relative to the 3.83 m monopile for the same ξ_b . Therefore, two separate linear fits were fitted across the data of OWF 09 and across the data of OWF 06 to OWF 08 as shown in Figure 5.48.

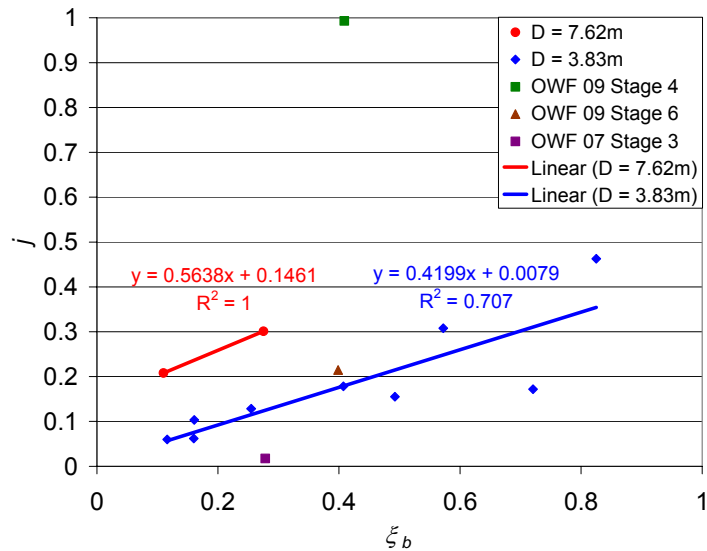


Figure 5.48 j Fittings as a Function of ξ_b by Pile Diameter

As shown in Figure 5.48, both linear fits produce relatively high coefficients of determination that adhere to the principle that accumulated rotation increases with increasing ξ_b . In addition, both fits have similar slopes, suggesting that the rate that j increases with respect to ξ_b is uniform with D . However, this is limited to $\xi_b \leq 0.3$. The fits also reinforce the suggestion that the 7.62 m monopile experienced greater accumulated rotations rates relative to the 3.83 m monopile for the same ξ_b due to the contribution of the vertical load. However, it is unlikely that the vertical load contributed to the high j value of OWF 09 stage 4 as the accumulated rotations from stage 2 and 3 amounted to approximately 0.36° . Therefore more experiments involving the 7.62 m diameter monopile have to be carried out to investigate the cause behind the high j values. Considering the difference in vertical load conditions between the linear fits, it is possible that the $D = 3.83$ m fitting is valid only under zero vertical load conditions and that it will translate upwards towards the $D = 7.62$ m fitting with the inclusion of vertical load above the mudline.

To determine the validity of the fittings and the logarithmic quantification of equation (5.20), accumulated rotations for both monopile diameters were estimated and compared to the experimental observations as shown in Figure 5.49. In general, the estimates ($\theta_{equation}$) are similar to the experimental observations ($\theta_{experiment}$), with estimates that either match the observations throughout the loading stage or slightly overestimate the accumulated rotations by 20% to 30% by the end of the loading stage.

For a few stages, the estimates are observed to overestimate the accumulated rotations in the first 100 cycles by 20% to 40%. This is due to the lower logarithmic rate of accumulated rotation in the first 100 cycles relative to the logarithmic rate of accumulation of rotation beyond 100 cycles. However, overestimation in the first 100 cycles is not an issue as the issue of greater concern is the accurate prediction of accumulated rotation in the long-term which would greatly exceed 100 cycles. The accumulated rotation is significantly overestimated by 60% in OWF 08 stage 6 where $\xi_b = 0.72$. This suggests that the linear fit is not suitable for ξ_b approaching 1.

Based on the comparison results, the linear fits of Figure 5.48, the lack of understanding behind the high j value in OWF 09 Stage 4, and that the working load of wind turbines ranges from $0.2 \leq \xi_b \leq 0.3$ (since the monopile would have rotated 0.5° at mudline at $\xi_b \approx 0.5$ as shown by Figure 4.24), the usage of the fittings should be limited $\xi_b \leq 0.3$. The results suggest that it is suitable to quantify accumulated rotations logarithmically using equation (5.20). The difference in j values between the linear fits and the absence of the counterweight system in OWF 09 suggests that vertical load is contributing to greater j values. This also suggests that the $D = 3.83$ m fitting is valid only under zero vertical load conditions and that it may translate upwards towards the $D = 7.62$ m fitting with the inclusion of vertical load above the mudline. Since vertical load is likely to contribute to accumulated rotations, the fitting from OWF 09 should be considered in design. In addition further research is necessary to determine how the fitting changes with vertical loads of varying magnitudes.

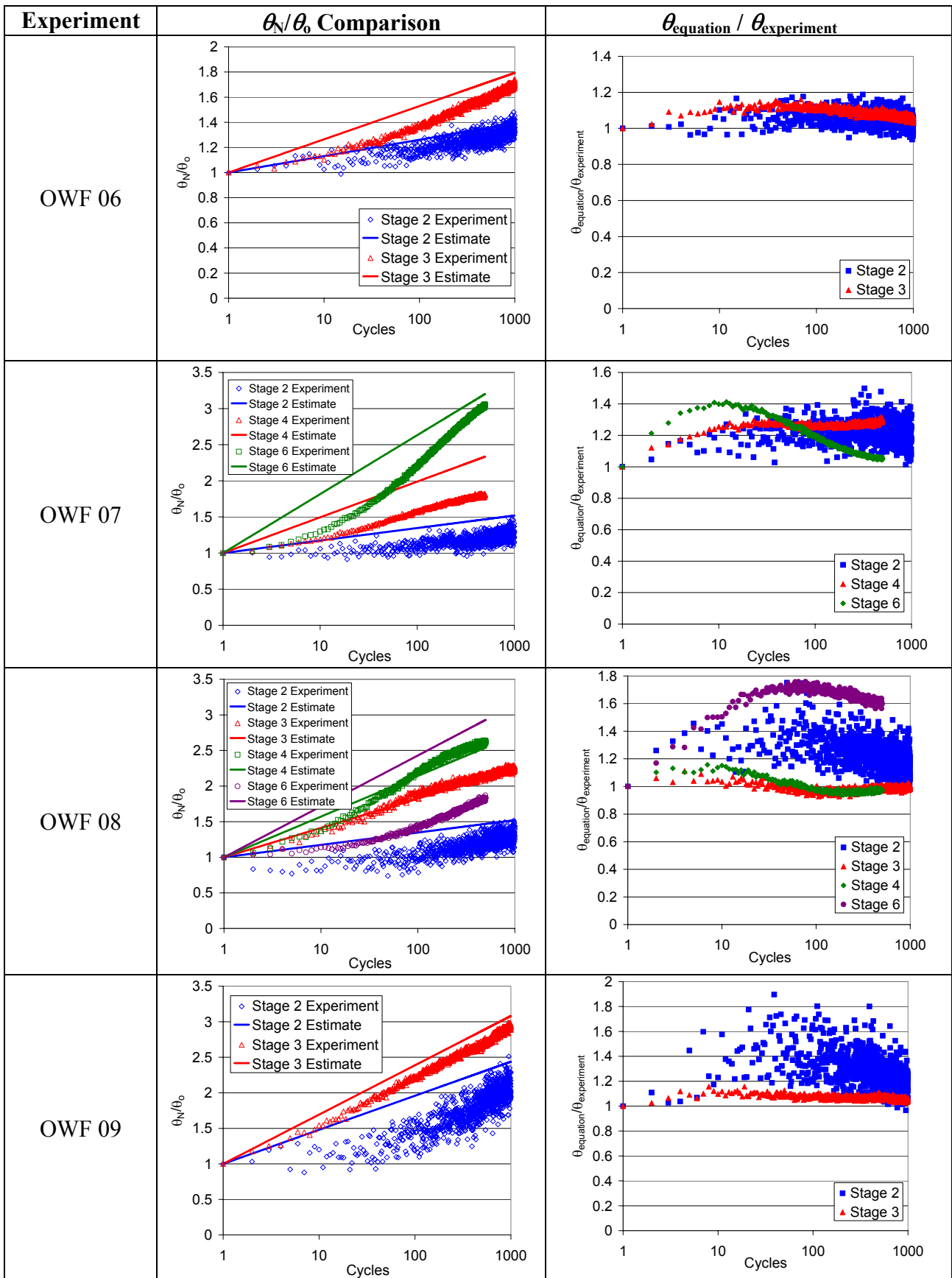


Figure 5.49 Accumulated Rotation Comparison between Equation Derived vs. Experiment

5.7.2 Estimating Accumulated Rotations in Softening Regime

Similar to section 5.6.3, due to the limited data, a comparison of accumulated rotation rates was carried out between stages 4 and 5 that had similar ξ_b . For the softening regime observed in stage 5, the j value for the first 25 cycles and beyond 25 cycles were considered separately as the behaviour between the two were very distinct as shown in Figure 5.50. Based on the comparison in Table 5.9, rotation accumulates at a low rate of 0.26 to 0.65 of that for the stiffening regime in the first 25 cycles. However, beyond 25 cycles, j greatly increases at a rate 3.12 to 3.73 times greater than that for the stiffening regime. This is due to the significant softening that took place in the first 100 cycles.

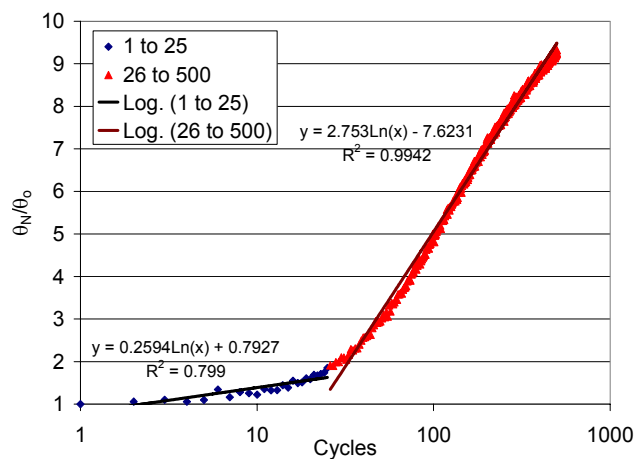


Figure 5.50 OWF 09 Stage 5 $\xi_b = 0.44$, $\xi_c = -0.27$ θ_N/θ_0 vs. Cycles

Experiment	<i>j</i> for Stage			Stage 5 <i>j</i> / Stage 4 <i>j</i>	
	4	5		1 st 25	Beyond 25
		1 st 25	Beyond 25		
OWF 07	0.155	0.100	0.558	0.645	3.596
OWF 08	0.308	0.097	1.150	0.315	3.734
OWF 09	0.993	0.259	3.101	0.261	3.123

Table 5.9 *j* Comparison between $\xi_c \approx 0$ and $\xi_c \approx -0.25$ for Similar ξ_b

As shown in Figure 5.50, it was observed that j was approximately constant from 25 to 500 cycles. This can be attributed to the logarithmic nature of stiffening beyond 100 cycles that causes marginal stiffening per cycle to reduce with increasing cycles as discussed in section 5.6.3. Based on the results, loading with $\xi_c \approx -0.25$ on a monopile-soil system with previously accumulated locked-in stresses which triggers the softening regime is extremely detrimental. Not only can it cause resonance due to

substantial softening, it also has the potential to cause excessive rotation that could exceed the maximum permanent rotation at mudline criteria of 0.5° (Achmus et al. , 2009) in the short term if ξ_b is sufficiently high. Considering the consequences that may result from the softening regime, the monopile may have to be designed to have a greater horizontal load capacity.

5.7.3 Recommendation to Estimate Cyclic Accumulated Rotations

Based on the results, the following methodology is recommended to estimate the accumulated rotations resulting from the stiffening regime for $\xi_b \leq 0.3$:

1. Determine θ_o (radians) from zero load to peak load for the first cycle of cyclic load in question for the desired ξ_b .
2. Once θ_o has been determined, utilise equation (5.21) as below to determine the rate of accumulated rotations, j .

$$j = 0.5638\xi_b + 0.1461 \quad (5.21)$$

3. Once j has been calculated, estimate accumulated rotations utilising the previously mentioned equation (5.20).

$$\frac{\theta_N}{\theta_o} = 1 + j \ln(N) \quad (5.20)$$

To estimate the rate of accumulated rotation due to the softening regime j_{soft} for cyclic loads with $\xi_b \geq \xi_{b \text{ prv}}$ on a system with previously accumulated locked in stresses, the following equation can be utilised:

$$j_{soft} = \psi j \quad (5.22)$$

where $3.1 \leq \psi \leq 3.7$. Once j_{soft} has been calculated, the accumulated rotations can be calculated by substituting j of equation (5.20) with j_{soft} .

5.8 Ground Surface Disturbance

According to Pender and Pranjoto (1996), cyclic lateral loading of piles in clay causes gapping, a process that forms an opening between the pile shaft and the surrounding soil. Based on their analysis, gapping leads to reduction in pile lateral stiffness. As discussed in section 3.6.7, a web camera was placed behind the monopile to record the soil deformation that took place at the mudline. To determine if gapping took place, the video recordings from this web camera were reviewed. Recordings from OWF 09 were not utilised as the size of the 7.62 m monopile completely blocked the view of the soil behind the monopile.

As exhibited by the example shown in Figure 5.51, the stiffening regime due to one-way loading was observed to cause little or no gapping to reduce the lateral stiffness of the monopile. Instead, the soil behind the monopile appears to experience soil deformation that results in the depression of the soil level and cracking. The extent of soil deformation behind the monopile was observed to extend further behind the monopile with increasing cycles and increasing load magnitude. The same observation was also made for the stiffening regime with $\xi_c \approx -0.35$ as shown in Figure 5.52.

The softening regime that was triggered by $\xi_c \approx -0.25$ cyclic loads was observed to influence the ground surface differently as shown in Figure 5.53. In the first 100 cycles, the soil behind the monopile was observed to remould itself. Some of the cracks from the prior $\xi_c \approx 0$ stages reduce in size while the other cracks appear to smoothen out, becoming either less visible or disappear. The ground surface soil also moves towards the monopile as it displaces forward. However, beyond 100 cycles, the soil remoulds itself differently. Firstly, the extent of deformation behind the monopile was observed to be much greater relative to $\xi_c \approx 0$ for the similar ξ_b . Since the view of the web camera is limited to approximately 30 mm, the extent of deformation directly behind the monopile as shown in Figure 5.53(c) is at least $2/3D$. In addition, the extent of deformation was observed to spread out laterally to the sides of the monopile. Secondly, the soil appears to experience greater deformations relative to the stiffening regime. Not only does the soil experience greater depressions in soil level, the soil also experiences many shallow thin cracks or deformation lines.

Stage	Beginning	End
<p style="text-align: center;">2 $(\xi_b = 0.16,$ $\xi_c = 0.01)$</p>		
<p style="text-align: center;">3 $(\xi_b = 0.41,$ $\xi_c = 0.05)$</p>		
<p style="text-align: center;">4 $(\xi_b = 0.57,$ $\xi_c = 0.10)$</p>		

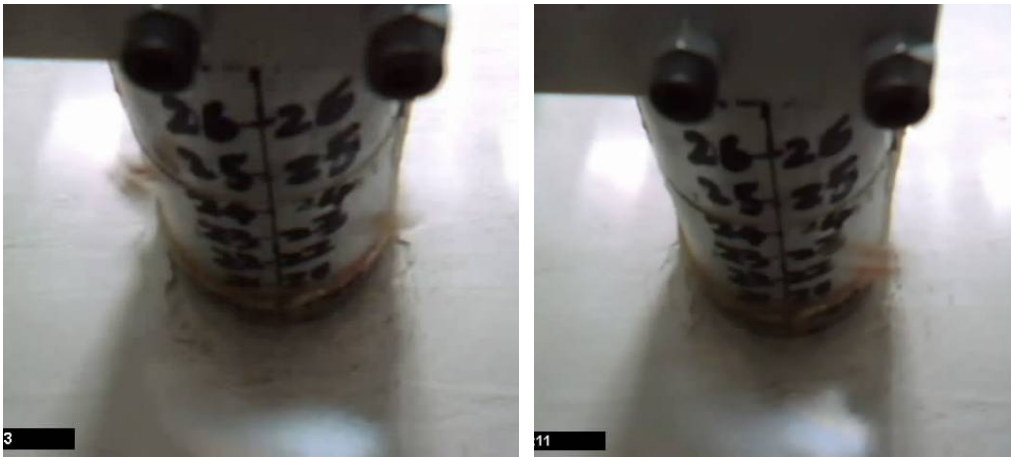
Figure 5.51 OWF 08 Stage 2 to 4 $\xi_c \approx 0$ Soil Deformation behind Monopile



(a) Beginning

(b) End

Figure 5.52 OWF 07 Stage 3 $\xi_b = 0.28$, $\xi_c = -0.35$ Soil Deformation behind Monopile



(a) Beginning

(b) 100th Cycle



(c) End

Figure 5.53 OWF 08 Stage 5 $\xi_b = 0.62$, $\xi_c = -0.25$ Soil Deformation behind Monopile

Based on the photos, little or no gapping was observed during the stiffening regime resulting from one-way loading and $\xi_c \approx -0.35$ cyclic loads and during the softening regime resulting from $\xi_c \approx -0.25$ cyclic loads. As a result, reduction in lateral stiffness resulting from gapping was not observed. Though soil deformation was observed to take place on the ground surface, the results from secant stiffness evaluation, accumulated rotations, and excess pore pressure behaviour suggest that soil deformation at the ground surface is not the main factor that dictates whether the system stiffens or softens. Instead, the soil *OCR*, the soil stress conditions and the excess pore pressure behaviour resulting from cyclic load are the main deciding factors.

5.9 Summary

The basis behind the analysis scope for the cyclic loading experiments and the undrained shear strength profiles utilised was explained to provide the foundation for the analysis. The filter frequency utilised was reported to provide evidence that phase-shifts did not occur across the instruments. The vertical and horizontal load conditions were verified to provide the basis behind the analysis that would follow. Verification of these conditions for the 7.62 m monopile show that the *p-y* curves in section 4.4.5 model the overall lateral response. However, the curves underestimate the ultimate soil reaction, p_u by 20% and is unable to accurately estimate the small strain stiffness. The verification of these conditions also suggests that pile toe shear force, F_{shear} increases at a 0.1 exponential power.

Two cyclic stiffness regimes were observed across the experiments, the stiffening regime and the softening regime. The stiffening regime was observed in experimental stages involving $\xi_c \approx 0$ and $\xi_c \approx -0.35$ cyclic loads whereas the softening regime was observed in experimental stages involving $\xi_c \approx -0.25$. Different aspects of both stiffening and softening regimes were discussed including bending moment at zero loads, evolution of secant rotational stiffness, *p-y* curve stiffness, and excess pore pressure behaviour across the monopile. Review of these aspects and review of the soil reaction profile at zero load suggests that cyclic loads of different characteristics (i.e. ξ_b and ξ_c) have effects on the soil stress conditions (i.e. accumulating or destroying locked in stresses) which in turn influences the excess pore pressure

behaviour which then dictates whether the stiffening or softening regime takes place. Considering that the cyclic loads applied in the experiments were not extensive in terms of load characteristics (i.e. three ξ_c values and $\xi_b \geq \xi_{b\text{ prv}}$), a framework outlining the cyclic load conditions that trigger the stiffening and softening regime was suggested. In addition to the framework, uncertainties over the exact ξ_c value that would cause the transition from stiffening to softening or from softening to stiffening regime for $\xi_b \geq \xi_{b\text{ prv}}$ magnitude loads under previously accumulated stress conditions were highlighted as an avenue for future research.

An exercise was carried out in LPILE to determine if quantification of the p - y curve stiffness was suitable to quantify the evolution of cyclic stiffness for both the stiffening and softening regimes. Results from the exercise suggests that quantification of p - y curve stiffness change via LPILE was unsuitable as the estimated rotation depths from LPILE significantly changed relative to the experimental rotation depths that remained relatively constant for the same experimental stage. The difference was attributed to the limitations of LPILE of not being able to capture the changes in locked in stresses and changes in mobilised soil reaction as a result of changes in locked in stresses. As a result, quantification of cyclic stiffness was done by evaluating secant stiffness.

Stiffness was observed to behave logarithmically in both stiffening and softening regimes. The stiffening rate of the stiffening regime was observed to decrease with increasing initial strain in the form of a power function. Since soil reaction curves were unavailable for $D = 7.62$ m, secant stiffness was quantified relative to strain evaluated with respect to pile length instead of pile diameter. Utilisation of the power fitting provided accurate estimates of the cyclic stiffness increase relative to the stiffening regimes observed across the experiments. The softening regime resulting from reverse loading of $\xi_c \approx -0.25$ on a system with prior locked in stresses was observed to be extremely detrimental due to the significant softening that takes place in the first 100 cycles. Taking into account the results, recommendations were made to estimate the variation of cyclic stiffness of both the stiffening and softening regimes.

Accumulated rotations for the stiffening regime were quantified logarithmically as exponential quantification did not match the expectation of increasing rate of accumulated rotations with increasing ξ_b . Fitting of the data from logarithmic quantification suggests that the rate of accumulated rotation may increase with increasing vertical load and is not dependent on pile diameter. However, since only one experiment involving the 7.62 m monopile was carried out with free acting vertical load, further research is recommended to verify the findings and to determine how the rate of accumulated rotation changes with vertical loads of varying magnitudes. Similar to findings pertaining to cyclic stiffness, the softening regime was also observed to be extremely detrimental as the rate of accumulated rotations from the softening regime was at most 3.7 times greater relative to the stiffening regime. As a result, the softening regime has the potential of causing excessive rotations that exceed the 0.5° mudline criteria (Achmus et al., 2009) in the short-term. Based on the results, recommendations were made to estimate the accumulated rotations resulting from both the stiffening and softening regimes.

Photos of soil deformation at mudline behind the monopile indicate little or no gapping took place to reduce the lateral stiffness. Soil deformation during the stiffening regime was observed to cause cracks and depression of the soil level. Soil deformation of the softening regime observed to be significantly different and resulted in soil deformations that extended behind the monopile to distances greater than the stiffening regime. Though soil deformation was observed to take place on the ground surface, the results from secant stiffness evaluation, accumulated rotations, and excess pore pressure behaviour suggest that soil deformation at the ground surface is not the main factor that dictates whether the system stiffens or softens. Instead, the soil *OCR*, the soil stress conditions and the excess pore pressure behaviour resulting from cyclic load are the main deciding factors.

CHAPTER 6

6. CONCLUSION

6.1 Introduction

Monopiles are expected to be heavily utilised as the foundations for future offshore wind turbines. Since most of the planned offshore wind farms in the UK are in the north and central parts of UK, there is a high probability that the monopiles will be founded in overconsolidated clays. Design of monopiles is carried out by utilising the p - y method and the criterion recommended by the DNV (2014) industry standard to construct p - y curves is the soft clay criterion by Matlock (1970). Though the criterion is well established in the offshore oil and gas industry, issues regarding its suitability to design monopiles have been raised. These include the suitability of the p - y curves derived from field tests on long flexible piles to design short rigid monopiles, the estimation of the initial pile-soil stiffness, and the shortcomings of the p - y curves for cyclic loading design.

Considering the issues above and the lack of research of monopiles in overconsolidated clays, centrifuge testing was carried out to study the response of monopiles subjected to monotonic and cyclic loads in different overconsolidated speswhite kaolin clay profiles. Triaxial testing was carried out to obtain the stress-strain properties of the speswhite kaolin under different overconsolidation ratios while LPILE analysis was carried out to analyse the lateral behaviour of the monopile. This chapter summarises the key findings of the thesis and provides recommendations for further research.

6.2 Static Loading

6.2.1 Analysis of Bending Moments

Soil reaction curves show that the monopile rotates at depth when laterally loaded, approximately at 70% of its embedded depth while displacement curves show that the

monopile behaved as a semi-flexible pile that flexes and rotates at depth, producing an undesirable toe-kick that in turn generated a shear force at the pile toe.

6.2.2 *p-y* Curves

Experimental results indicated that utilisation of the *p-y* curves based on the DNV (2014) design methodology greatly underestimated the lateral stiffness of the foundation, resulting in underestimation of the system's natural frequency. Based on the results, a monopile-wind turbine system designed as a “soft-stiff” structure according to the DNV design methodology in soil similar to overconsolidated speswhite kaolin would be 40% stiffer than estimated.

Though the DNV (2014) design methodology to construct *p-y* curves in clay based on Matlock's (1970) soft clay criterion was observed to significantly underestimate stiffness, various findings indicated that modification of the criterion was the best approach to characterise the experimental *p-y* curves. There are as follows:

- LPILE analysis utilising the DNV *p-y* curves produced similar bending moment curves to the experiments, implying that the correct lateral resistance profile is calculated from the DNV *p-y* curves.
- The underestimation in global initial stiffness suggests that while the stiffness distribution along the pile is broadly correct, the stiffness of all *p-y* curves should be increased.
- The reduced ultimate soil resistance at depths where $OCR \geq 4$ was well estimated by Matlock's (1970) criterion for heavily overconsolidated soils.
- On average, the experimental *p-y* curves increase at an exponential power of 0.29, slightly lower than Matlock's (1970) value of 1/3.
- Sullivan et al. (1980) and Gazioglu and O'Neill (1984) suggests that the constant to calculate the reference deflection at which half the ultimate soil reaction is mobilised, y_c can vary based on the soil and be lower than 2.5 (Matlock, 1970).

As a result, the DNV (2014) design methodology was modified and a recommendation was made based on the above findings. LPILE estimates based on the modified criterion corresponded very well with the experimental curves within the

maximum permanent rotation at mudline of 0.5° as specified by Achmus et al. (2009) and estimated the ultimate lateral load very well. However, the modified DNV methodology overestimated lateral stiffness beyond a permanent rotation at mudline of 1.0° . Therefore, the modified DNV methodology may be suitable for monopile wind-turbine designs but may be unconservative for applications where ultimate lateral stiffness is of greater importance such as in the design of anchor piles.

6.2.3 Pile Toe Shear Force

The shear force at the pile toe was observed to contribute little to the ultimate lateral resistance and the lateral stiffness of the 3.83 m diameter monopile as approximately 25% of the pile length below the rotation point mobilised less lateral resistance. The base shear was also observed to contribute to a slight increase in bending moments at depths close to the pile toe. However, the increase is well within the design capacity as design is dictated by the much larger moments closer to the soil surface. Considering the slight contribution to lateral resistance and stiffness and the limited effect it has on bending moments, the effects of base shear may not need to be considered in monopile design. However, its effects may have to be considered for much stubbier structures that have much larger widths and lower slenderness ratios. Despite the marginal effects of the pile toe shear force, an effort was made to characterise the base shear as it was observed to enhance the mobilisation of capacity at low displacements and affect bending moments to some extent. Similar to the p - y curves, the base shear was characterised to increase exponentially with displacement by powers ranging from 0.1 to 0.3.

6.2.4 Effect of Pile Diameter

The 7.62 m monopile was observed to have a deeper rotation depth relative to the 3.83 m monopile. Parametric analysis not only suggested that the pile toe shear force was responsible for pulling the rotation depth deeper, it also suggested that the base shear increases exponentially at a power of 0.1. The effect of base shear was greater on the 7.62 m monopile due to the magnitude that increases with diameter (increase of diameter by 2 increases base shear by 4, but only increases lateral resistance along the pile shaft by 2). Therefore, the results suggest that the effects of the base shear should be considered for stubbier structures that have much larger widths and lower slenderness ratios.

More research is necessary to improve the modified DNV methodology. Estimates of the modified methodology for the 7.62 m monopile relative to the experimental observations suggest that the modified methodology underestimates the ultimate soil reaction by 20% and greatly overestimates the initial stiffness of the system. Efforts made to soften the p - y curves were unsuccessful as the estimated load-displacement curves could not be matched with the experimental observations, suggesting the modified DNV methodology is unsuitable to evaluate small strain stiffness of larger diameter monopiles of lower slenderness ratios. However, the overall response was still well modelled. It is recommended that the experiment involving the 7.62 m monopile be carried out with functioning strain gauges. Not only can vertical load conditions be confirmed, additional data regarding the lateral behaviour of the 7.62 m monopile can be utilised to further improve the recommendations made regarding the modified DNV methodology to construct p - y curves and the methodology to characterise the pile toe shear force.

6.3 Cyclic Loading

6.3.1 Cyclic Stiffness Regimes

Two cyclic stiffness regimes were observed as a result of the cyclic loads applied. In the stiffening regime, monopile stiffness increased as a result of cyclic loads that contributed to the accumulation of locked in stresses which in turn influenced the soil stress conditions to produce excess pore pressure behaviour that resulted in stiffening. The stiffening regime also took place after previously accumulated locked in stresses were completely destroyed by reverse cyclic loads of $\xi_c \approx -0.35$ that caused soil reaction reversal above and below the rotation point. Under zero locked in stress conditions, the system can only proceed to accumulate locked in stresses. The softening regime was observed to take place when reverse cyclic loading of $\xi_c \approx -0.25$ caused the progressive destruction of locked in stresses of previously accumulated locked in stresses. As a result of the changes in soil stress conditions, the excess pore pressure behaviour changes to cause significant softening of the monopile-soil system within 100 cycles.

A framework that took into consideration the locked in stress conditions and the cyclic load characteristics (ξ_b and ξ_c) was developed based on the results from

experiments involving cyclic loads of limited load characteristics. In addition, uncertainties pertaining to the exact ξ_c value that would cause the transition from stiffening to softening or from softening to stiffening regime for $\xi_b \geq \xi_{b\text{ prv}}$ magnitude loads under previously accumulated stress conditions were brought up. Considering that the experiments involved cyclic loads of limited load characteristics and that there are uncertainties over the exact ξ_c value that would cause transition for stiffening to softening or vice-versa, future research involving cyclic loads of various characteristics can be carried out to address these issues.

6.3.2 Estimating Cyclic Stiffness

Stiffness changes in both stiffening and softening regime were observed to behave logarithmically. Based on the results, the rate of stiffness increase in the stiffening regime reduces with increasing strain. Comparison between the stiffening and softening regime suggests that the rate of softening of the softening regime for the same ξ_b is 2.6 to 3 times higher than the rate of stiffening of the stiffening regime. Therefore, in merely 100 cycles and in the short term, the softening regime could be extremely detrimental as it can cause excessive softening. Should the reverse loading that triggered the softening regime persist, it would take millions of cycles of sustained reverse loading for the stiffness of the system to be restored to its original stiffness. Though it is unlikely to be the case in the field as cyclic loading is varied in nature, designers have to be prepared and aware of the detrimental effects of the softening regime.

6.3.3 Estimating Accumulated Rotations

Accumulated rotations in both stiffening and softening regime were observed to be better quantified logarithmically as exponential quantification did not match the expectation of increasing rate of accumulated rotations with increasing ξ_b . Based on the experiment results, the results suggest that the rate of accumulated rotation in the stiffening regime increases with vertical load. However, more research has to be pursued as only one experiment involving free acting vertical load was carried out. Not only would further research be able to verify this, it would also provide findings that explain how accumulated rotation rates change with respect to vertical loads of varying magnitudes. The softening regime is extremely detrimental relative to the

stiffening regime. For the same ξ_b , the accumulated rotation rate of the softening regime was 3.1 to 3.7 times greater than the accumulated rotation rates of the stiffening regime. Therefore, in the short-term, the softening regime could potentially cause excessive accumulated rotations that could exceed the 0.5° mudline criteria (Achmus et al., 2009). Therefore, designers have to take into consideration the detrimental effects of the softening regime.

6.3.4 Implications of Stiffness Changes

The observed changes in p - y curve stiffness with cyclic loading will have implications for the overall stiffness of the foundation system. While the wind turbine system stiffness is dominated by the flexibility of the tower, these will still have a minor impact on the system natural frequency and should be considered in design.

6.3.5 Ground Surface Disturbance

Photos of soil deformation at the mudline indicate little or no gapping took place to reduce the lateral stiffness. The stiffening regime causes cracks and depression of the soil level whereas the softening regime resulted in soil deformations that extended behind the monopile to distances greater than the stiffening regime. Though soil deformation was observed to take place on the ground surface, the results from secant stiffness evaluation, accumulated rotations, and excess pore pressure behaviour suggest that soil deformation at the ground surface is not the main factor that dictates whether the system stiffens or softens. Instead, the soil OCR , the soil stress conditions and the excess pore pressure behaviour resulting from cyclic load are the main deciding factors.

6.4 Recommendations for Further Research

The research presented in this thesis has provided a better understanding of the lateral behaviour of monopiles under both static loading and cyclic loading in overconsolidated clays. However, the research has its limitations. Therefore, suggestions on further research are discussed as follows:

- The modified DNV methodology suggests that the constant to define the reference deflection, y_c varies based on the soil in question. This recommendation was made

based on the findings of Sullivan et al. (1980) and Gazioglu and O'Neill (1984). Since the tests were carried out in overconsolidated speswhite kaolin, further research should be carried out in different types of clay to ascertain the validity of the suggestion and to investigate how different soil properties affect the constant that defines reference deflection. This is of interest as the monotonic test results suggests that the accuracy of estimating the system stiffness is mainly dependent on the accuracy of the p - y curves.

- Validation of the modified DNV methodology on the 7.62 m monopile suggests that the modified DNV methodology has to be improved so that it can better estimate the initial stiffness of stubbier monopiles of larger diameters and lower slenderness ratios. Since the strain gauges on the 7.62 m monopile failed, centrifuge monotonic and cyclic experiments with functioning strain gauges should be carried out to ascertain the factors that contributed to the inaccurate estimations. Repetition of the experiment with functioning strain gauges will also provide an accurate picture of the vertical load condition and pile toe shear force conditions acting on the 7.62 m monopile. This will in turn provide the additional information necessary to improve the modified DNV methodology and possibly provide more information on the role of pile toe shear force on stubbier structures, how to better characterise it, and how it should be considered in design.
- Though a framework considering the locked in stress conditions and cyclic load characteristics was proposed, the framework is not comprehensive enough as it is based on test results resulting from cyclic loads of limited characteristics. In addition, there is uncertainty over the ξ_c that causes transition from the stiffening regime to the softening regime and vice-versa on a system with previously accumulated locked in stresses for load magnitudes that are $\xi_b \geq \xi_{b\text{ prv}}$. Therefore, further research involving cyclic loads of various characteristics should be carried out to further improve the proposed framework and to investigate the exact ξ_c that causes transition between the stiffening and softening regimes.
- Cyclic accumulated rotation analysis suggests that the vertical load above the soil surface contributes to higher accumulated rotation rates. Since the strain gauges on the 7.62 m monopile failed, it is recommended that the experiment be repeated with functioning strain gauges. In the case that the finding is proven to be true, it is recommended that the experiments be repeated with vertical loads of varying

magnitudes to quantify the influence of different vertical load magnitudes on cyclic accumulated rotation.

- Due to the limitations of the 2D-actuator, it was not physically possible to load the monopile at frequencies representative of the prototype frequencies experienced by a wind turbine. Therefore, the results from the cyclic tests may be limited to the long-term behaviour of monopiles under storm loadings. Considering this limitation, a much stronger and faster loading device capable of loading the monopile under free-head conditions should be developed so that the experiments can be repeated with representative prototype loading frequencies. This would also enable a greater number of cyclic loads to be applied onto the monopile in a shorter period of time. Since the monopile was loaded to a maximum of 1,000 cycles, it is of interest to repeat the experiments with a greater number of cycles to verify the validity of the findings and to assess the suitability of applying the findings beyond the tested 1,000 cycles.
- It would also be of interest to develop a device capable of multi-directional loading that can load the monopile under representative prototype frequencies in the centrifuge as findings from both Su et al. (2014) and Rudolph et al. (2014) suggests that multi-directional loading caused greater degradation to stiffness and significantly increased deformation relative to unidirectional loading. Should this device be developed, it would enable quantification of stiffness and accumulated rotation changes from multi-directional loading and provide the information necessary to further improve the design process.
- Considering the findings of Sullivan et al. (1980) and Gazioglu and O'Neill (1984) that suggests that different clay properties may influence the lateral behaviour of the monopile, it is possible that the cyclic load findings may be limited in application to clays similar to overconsolidated speswhite kaolin. Therefore, further cyclic load testing should be carried out in different types of clays to evaluate the difference in cyclic load response and to evaluate the appropriateness of applying the cyclic load findings from this dissertation to other types of clays.
- Considering that the results suggest that cyclic loading causes changes to the system stiffness, it is of interest to carry out natural frequency measurements on wind turbines that have been in operation for at least ten years and to compare these measurements to the estimates or measurements made when the wind

turbine was first installed. This would provide valuable information on how the system stiffness changes over time and in turn enable the design process to be improved. Comparisons can also be made with the findings to evaluate the validity of the findings.

- Finite element modelling calibrated against centrifuge or field test results would enable the development of models that could potentially accurately estimate the stiffness and accumulated rotations resulting from cyclic loads. If this can be carried out, the results from finite element modelling may provide more information to better explain the causes contributing to the observed centrifuge or field test results.

REFERENCES

- Aas, G., Lacasse, S., Lunne, T. & Høeg, K. (1986). Use of In Situ Tests for Foundation Design on Clay. *ASCE Specialty Conference In Situ '86: Use of In Situ Tests in Geotechnical Engineering*. Blacksburg. Reston: American Society of Engineers (ASCE). pp. 1-30.
- Abdel-Rahman, K. & Achmus, M. (2005). Finite Element Modelling of Horizontally Loaded Monopile Foundations for Offshore Wind Energy Converters in Germany. *International Symposium on Frontiers in Offshore Geotechnics*. Perth, Western Australia. 19 - 21 September. Leiden, The Netherlands: CRC Press/Balkema. pp. 391-396.
- Achmus, M., Albiker, J. & Abdel-Rahman, K. (2010). Investigations on the behavior of large diameter piles under cyclic lateral loading. *2nd International Symposium on Frontiers in Offshore Geotechnics*. Perth, Western Australia. 8 - 10 November. Leiden, The Netherlands: CRC Press/Balkema. pp. 471-476.
- Achmus, M., Albiker, J., Peralta, P. & tom Wörden, F. (2011). Scale effects in the design of large diameter monopiles. *EWEA*. Brussels. 14 - 17 March. pp. 326-328.
- Achmus, M., Kuo, Y.-S. & Abdel-Rahman, K. (2009). Behavior of monopile foundations under cyclic lateral load. *Computers and Geotechnics*, 36(5), pp. 725-735.
- Airey, D. W. (1984). *Clays in the circular simple shear apparatus*. Ph.D. Thesis, University of Cambridge.
- Al-Tabba, A. (1987). *Permeability and stress-strain response of Speswhite Kaolin*. Ph.D. Thesis, University of Cambridge.
- Allotey, N. & El Naggar, H. (2008). A numerical study into lateral nonlinear soil-pile response. *Canadian Geotechnical Journal*, 45(9), pp. 1268-1281.
- API (1978). *RP 2A: Recommended Practice for Planning, Designing and Constructing Fixed Offshore Platforms*. Washington, DC: American Petroleum Institute.
- API (2000). *API RP 2A-WSD, Recommended practice for planning, designing and constructing fixed offshore platforms- working stress design*. Washington, DC: American Petroleum Institute.
- API (2011). *RP 2 Geotechnical and Foundation Design Considerations*. Washington, DC: American Petroleum Institute.
- Ashford, S. A. & Juirnarongrit, T. (2005). *Effect of Pile Diameter on the Modulus of Subgrade Reaction*. Report No. SSRP-2001/22. San Diego: Department of Structural Engineering. University of California.

- Augustesen, A. H., Brødbæk, K. T., Møller, M., Sørensen, S. P. H., Ibsen, L. B., Pedersen, T. S. & Andersen, L. V. (2009). Numerical Modelling of Large-Diameter Steel Piles at Horns Rev. *12th International Conference on Civil, Structural and Environmental Engineering Computing*. Funchal, Madeira. 1 - 4 September. Kippen: Civil-Comp Press.
- Bathe, K.-J. (1996). *Finite Element Procedures*. Upper Saddle River, New Jersey: Prentice Hall.
- Bond, A. J., Hight, D. W. & Jardine, R. J. (1997). *Design of Piles in Sand in the UK Sector of the North Sea*. Offshore Technology Report OTH 94 457. London: Health and Safety Executive.
- Bransby, M. F. (1996). Difference between the load-transfer relationships for laterally loaded pile groups: Active p-y or passive p- δ . *Journal of Geotechnical Engineering*, 122(12), pp. 1015-1018.
- Briaud, J.-L., Smith, T. D. & Meyer, B. J. (1984). Using the Pressuremeter Curve to Design Laterally Loaded Piles. *15th Annual Offshore Technology Conference*. Houston, Texas. pp. 495-502.
- Brødbæk, K. T., Møller, M., Sørensen, S. P. H. & Augustesen, A. H. (2009). *Review of p-y relationships in cohesionless soil*. DCE Technical Report No. 57. Aalborg: Department of Civil Engineering, Aalborg University
- Broms, B. B. (1964a). The Lateral Resistance of Piles in Cohesive Soils. *Journal of the Soil Mechanics and Foundations Division*, 90(2), pp. 27-63.
- Broms, B. B. (1964b). Lateral Resistance of Piles in Cohesionless Soils. *Journal of the Soil Mechanics and Foundations Division*, 90(3), pp. 123-158.
- Brouwer, J. J. M. (2007). *In-situ soil testing*. Bracknell: iHS BRE Press.
- Brown, D. A. & Shie, C.-F. (1990). Three dimensional finite element model of laterally loaded piles. *Computers and Geotechnics*, 10(1), pp. 59-79.
- Budhu, M. & Davies, T. (1987). Nonlinear analysis of laterally loaded piles in cohesionless soils. *Canadian Geotechnical Journal*, 24(2), pp. 289-296.
- Byrne, B. W. & Houlsby, G. T. (2003). Foundations for Offshore Wind Turbines. *Philosophical Transactions of the Royal Society of London, Series A*, 361, pp. 2909-2930.
- Cabalar, A. F., Cevik, A. & Guzelbey, I. H. (2010). Constitutive modeling of Leighton Buzzard Sands using genetic programming. *Neural Computing and Applications*, 19(5), pp. 657-665.
- Carbon Trust (2008). *Offshore wind power: big challenge, big opportunity*. Report no. CTC743. London: Carbon Trust.
- Carter, D. P. (1984). *A non-linear soil model for predicting lateral pile response*. M.Eng. Thesis, University of Auckland.

- Carter, J. M. F. (2007). North Hoyle offshore wind farm: design and build. *Proceedings of the ICE - Energy*, 160(1), pp. 21-29.
- Cavallaro, A., Lanzo, G., Pagliaroli, A., Maugeri, M. & Lo Presti, D. C. F. (2003). A comparative study on shear modulus and damping ratio of cohesive soil from laboratory tests. *3rd International Symposium on Deformation Characteristics of Geomaterials*. Lyon, France. 22 - 24 September. The Netherlands: A.A. Balkema. pp. 257 - 266.
- Chung, S. F. & Randolph, M. F. (2004). Penetration resistance in soft clay for different shaped penetrometers. *2nd International Conference on Geotechnical Site Investigation*. Porto. 19 - 22 September. Rotterdam: Millpress. Vol. 1, pp. 671-677.
- Clegg, D. (1981). *Model Piles in Stiff Clay*. Ph.D. Thesis, University of Cambridge.
- Cuéllar, P., Baeßler, M. & Rücker, W. (2009). Ratcheting convective cells of sand grains around offshore piles under cyclic lateral loads. *Granular Matter*, 11(6), pp. 379-390.
- Darendeli, M. B. & Stokoe, K. H. (2001). *Development of a new family of normalized modulus reduction and material damping curves*. Geotechnical Engineering Report GD01-1. Austin: Department of Civil Engineering, University of Texas.
- DasyLab (2004). *DasyLab 8 user guide*. DasyLab.
- Dean, E. T. R. (2010). *Offshore Geotechnical Engineering: Principles and Practice*. London: Thomas Telford Ltd.
- Delft University of Technology, FUGRO & John Brown Hydrocarbons Ltd. (2003). *Design Methods for Offshore Wind Turbines at Exposed Sites*. Report no. SW-02181. Delft: Section Wind Energy, Delft University of Technology
- Department of Trade and Industry (2007). *Meeting the Energy Challenge, A White Paper on Energy*. London: The Stationary Office.
- DNV (1992). *DNV Classification Notes 30.4: Foundations*. Høvik: Det Norske Veritas.
- DNV (2014). *DNV-OS-J101: Design of Offshore Wind Turbine Structures May 2014*. Norway: Det Norske Veritas.
- DNV & Risø National Laboratory (2002). *Guidelines for Design of Wind Turbines*. 2nd ed. Copenhagen: DNV/Risø.
- Dobry, R., Vicente, E., O'Rourke, M. & Roesset, J. (1982). Stiffness and damping of single piles. *Journal of Geotechnical Engineering*, 108(3), pp. 439-458.
- Dobry, R. & Vucetic, M. (1987). Dynamic properties and seismic response of soft clay deposits. *International Symposium on Geotechnical Engineering of Soft Soils*. Mexico City. Vol. 2, pp. 51-87.

- Doherty, P., Gavin, K. & Casey, B. (2011). The Geotechnical Challenges Facing the Offshore Wind Sector. *Geo-Frontiers 2011: Advances in Geotechnical Engineering*. Dallas, Texas. 13 - 16 March. Reston: American Society of Civil Engineers. pp. 162 - 171.
- Dunnivant, T. W. & O'Neill, M. W. (1985). *Performance analysis and interpretation of a lateral load test of a 72- inch-diameter bored pile in overconsolidated clay*. Report no. UHCE 85-4. Houston: Department of Civil Engineering, University of Houston.
- Elkinton, C. N. (2007). *Offshore Wind Farm Layout Optimization*. Ph.D. Thesis, University of Massachusetts Amherst.
- Elmes, D. (1985). *Creep and viscosity of two kaolin clays*. Ph.D. Thesis, University of Cambridge.
- European Commission (2008). *Memo on the Renewable Energy and Climate Change Package*. Brussels: European Commission.
- Fan, C.-C. & Long, J. H. (2005). Assessment of existing methods for predicting soil response of laterally loaded piles in sand. *Computers and Geotechnics*, 32, pp. 274-289.
- Fannin, R. J. (1986). *Geogrid reinforcement of granular layers of soft clay – a study at model scale and full scale*. Ph.D. Thesis, Oxford University.
- Ffrench, R., Bonnet, D. & Sandon, J. (2006). Wind power; a major opportunity for the UK. *Proceedings of the ICE - Civil Engineering*, 158(6), pp. 20-27.
- Gazioglu, S. M. & O'Neill, M. W. (1984). Evaluation of p-y relationships in cohesive soils. *Analysis and design of pile foundations*. San Francisco, California. 1 - 5 October. Reston: American Society of Civil Engineers. pp. 192-213.
- Haiderali, A. (2012). *Numerical Modelling of Monopiles for Offshore Windfarms*. First Year Report. Cambridge: University of Cambridge.
- Haiderali, A., Cilinger, U. & Madabhushi, S. P. G. (2013). Lateral and Axial Capacity of Monopiles for Offshore Wind Turbines. *Indian Geotechnical Journal*, 43(3), pp. 181-194.
- Haiderali, A., Lau, B. H., Haigh, S. K. & Madabhushi, S. P. G. (2014). Lateral response of monopiles using centrifuge testing and finite element analysis. *8th International Conference on Physical Modelling in Geotechnics*. Perth, Western Australia. 14 - 17 January. Leiden, The Netherlands: CRC Press/Balkema. Vol. 2, pp. 743-749.
- Haigh, S. K. (2014). Foundations for offshore wind turbines. *8th International Conference on Physical Modelling in Geotechnics*. Perth, Western Australia. 14 - 17 January. Leiden, The Netherlands: CRC Pres/Balkema. Vol. 1, pp. 153-159.

- Haigh, S. K., Houghton, N. E., Lam, S. Y. & Wallbridge, P. J. (2010). Development of a 2D servo-actuator for novel centrifuge modelling. *7th International Conference on Physical Modelling in Geotechnics*. Zurich. 28 June - 1 July. Leiden, The Netherlands: CRC Press/Balkema. Vol. 1, pp. 239-244.
- Hearn, E. (2009). *Finite Element Analysis of an Offshore Wind Turbine Generator Monopile Foundation*. M.Sc. Thesis, Tufts University
- Heidari, M., Jahanandish, M., Naggar, H. E. & Ghahramani, A. (2014). Nonlinear cyclic behavior of laterally loaded pile in cohesive soil. *Canadian Geotechnical Journal*, 51(2), pp. 129-143.
- Hinz, P., Lesny, K. & Richwien, W. (2006). Prediction of monopile deformation under high cyclic lateral loading. *8th German Wind Energy Conference*. Bremen. 22 - 23 November.
- Idriss, I. M., Singh, R. D. & Dobry, R. (1978). Nonlinear Behavior of Soft Clays during Cyclic Loading. *Journal of the Geotechnical Engineering Division*, 104(12), pp. 1427-1447.
- IMERYS (2008). *SpeswhiteTM*. DAT002K. Par: IMERYS Performance & Filtration Minerals.
- Karthigeyan, S., Ramakrishna, V. & Rajagopal, K. (2007). Numerical Investigation of the Effect of Vertical Load on the Lateral Response of Piles. *Journal of Geotechnical and Geoenvironmental Engineering*, 133(5), pp. 512-521.
- Kim, K., Prezzi, M., Salgado, R. & Lee, W. (2008). Effect of Penetration Rate on Cone Penetration Resistance in Saturated Clayey Soils. *Journal of Geotechnical and Geoenvironmental Engineering*, 134(8), pp. 1142-1153.
- Kim, Y. & Jeong, S. (2011). Analysis of soil resistance on laterally loaded piles based on 3D soil-pile interaction. *Computers and Geotechnics*, 38(2), pp. 248-257.
- Kirkwood, P. & Haigh, S. K. (2013). Centrifuge Testing of Monopiles for Offshore Wind Turbines. *23rd International Offshore and Polar Engineering*. Anchorage, Alaska. 30 June - 5 July. Cupertino, California: International Society of Offshore and Polar Engineers. Vol. 1, pp. 126-130.
- Kirkwood, P. & Haigh, S. K. (2014). Centrifuge testing of monopiles subject to cyclic lateral loading. *8th International Conference on Physical Modelling in Geotechnics*. Perth, Western Australia. 14 - 17 January. Leiden, The Netherlands: CRC Press/Balkema. Vol. 2, pp. 827-831.
- Klar, A. & Osman, A. S. (2008). Load-displacement solutions for piles and shallow foundations based on deformation fields and energy conservation. *Géotechnique*, 58(7), pp. 581-589.
- Klinkvort, R. T. & Hededal, O. (2010). Centrifuge modelling of offshore monopile foundation. *2nd International Symposium on Frontiers in Offshore Geotechnics*. Perth, Western Australia. 8 - 10 November. Leiden, The Netherlands: CRC Press/Balkema. pp. 581-586.

- Klinkvort, R. T. & Hededal, O. (2013). Lateral response of monopile supporting an offshore wind turbine. *Proceedings of the Institute of Civil Engineers - Geotechnical Engineering*, 166(2), pp. 147-158.
- Kodikara, J., Haque, A. & Lee, K. (2010). Theoretical p-y Curves for Laterally Loaded Single Piles in Undrained Clay Using Bezier Curves. *Journal of Geotechnical and Geoenvironmental Engineering*, 136(1), pp. 265-268.
- Kodikara, J., Lee, K. Y. & Haque, A. (2006). Theoretical prediction of p-y curves for laterally loaded piles in clay. *Australian Geomechanics*, 41(4), pp. 69-77.
- Kühn, M. (2000). *Dynamics of Offshore Wind Energy Converters on Monopile Foundations - Experience from the Lely Offshore Wind Farm*. Engineering and Physical Sciences Research Council, Didcot, UK, EPSRC Workshop Report on OWEN (Offshore Wind Energy Network).
- Kühn, M. (2001). *Dynamics and design optimisation of offshore wind energy conversion systems*. Ph.D. Thesis, Delft University of Technology.
- Kühn, M., Cheng, P. W., Bergstrom, H., Dahlberg, J.-A., Duffy, J., Jacquemin, J., Thiringer, T., Passon, P. & Petterson, J. (2005). Utgrunden Offshore Wind Farm: Results of 5 Years of Operation and Research. *Copenhagen Offshore Wind*. Copenhagen. 26 - 28 October. pp. 1 - 10.
- Ladd, C. C. & Foott, R. (1974). New design procedure for stability of soft clays. *Journal of Geotechnical Engineering*, 100(7), pp. 763 - 786.
- Lam, S. Y. (2010). *Ground Movements due to Excavation in Clay: Physical and Analytical Models*. Ph.D. Thesis, University of Cambridge.
- Lau, B. H., Lam, S. Y., Haigh, S. K. & Madabhushi, S. P. G. (2014). Centrifuge testing of monopile in clay under monotonic loads. *8th International Conference on Physical Modelling in Geotechnics*. Perth, Western Australia. 14 - 17 January. Leiden, The Netherlands: CRC Press/Balkema. Vol. 2, pp. 689-695.
- LeBlanc, C. (2009). *Design of Offshore Wind Turbine Support Structures - Selected topics in the field of geotechnical engineering*. Ph.D. Thesis, Aalborg University.
- LeBlanc, C., Byrne, B. W. & Houlsby, G. T. (2010a). Response of stiff piles to random two-way lateral loading. *Géotechnique*, 60(9), pp. 715-721.
- LeBlanc, C., Houlsby, G. T. & Byrne, B. W. (2010b). Response of stiff piles in sand to long-term cyclic lateral loading. *Géotechnique*, 60(2), pp. 79-90.
- Lee, K. Y. (2005). *Numerical analysis of piles loaded laterally by structural forces or moving soil*. M.Eng.Sc. (Res) Thesis, Monash University.
- Lesny, K. & Hinz, P. (2007). Investigation of Monopile Behaviour under Cyclic Lateral Loading. *6th International Offshore Site Investigation and Geotechnics*

- Conference: Confronting New Challenges and Sharing Knowledge*. London. 11 - 13 September. London: Society for Underwater Technology. pp. 383-390.
- Lesny, K., Paikowsky, S. G. & Gurbuz, A. (2007). Scale Effects Lateral Load Response Large Diameter Monopiles. *Geo-Denver 2007: New Peaks in Geotechnics, Contemporary Issues in Deep Foundations*. Denver, Colorado. 18 - 21 February. Reston: American Society of Civil Engineers. pp. 1-10.
- Lesny, K. & Wiemann, J. (2006). Finite-Element-Modelling of Large Diameter Monopiles for Offshore Wind Energy Converters. *GeoCongress 2006*. Atlanta, Georgia. 26 February - 1 March. Reston: American Society of Civil Engineers. pp. 1-6.
- Leth, C. T. (2013). *Improved Design Basis for Laterally Loaded Large Diameter Pile: experimental based approach*. Ph.D. Thesis, Aalborg University.
- Li, Z., Haigh, S. K. & Bolton, M. D. (2010). Centrifuge modelling of mono-pile under cyclic lateral loads. *7th International Conference on Physical Modelling in Geotechnics*. Zurich. 28 June - 1 July. Leiden, The Netherlands: CRC Press/Balkema. Vol. 2, pp. 965-970.
- Lin, S.-S. & Liao, J.-C. (1999). Permanent Strains of Piles in Sand due to Cyclic Lateral Loads. *ASCE Journal of Geotechnical and Geoenvironmental Engineering*, 125(9), pp. 798-802.
- Ling, L. F. (1988). *Back analysis of lateral load tests on piles*. M.Eng. Thesis, University of Auckland.
- Lombardi, D., Bhattacharya, S. & Wood, D. M. (2013). Dynamic soil–structure interaction of monopile supported wind turbines in cohesive soil. *Soil Dynamics and Earthquake Engineering*, 49, pp. 165-180.
- Long, J. H. & Vanneste, G. (1994). Effects of Cyclic Lateral Loads on Piles in Sand. *ASCE Journal of Geotechnical Engineering*, 120(1), pp. 225-224.
- Lunne, T., Robertson, P. K. & Powell, J. J. M. (1997). *Cone Penetration Testing in Geotechnical Practice*. New York: Blackie Academic/Routledge Publishing.
- Madabhushi, S. P. G. (2014). *Centrifuge Modelling for Civil Engineers*. Boca Raton: CRC Press Taylor & Francis Group.
- Martin, C. M. & Randolph, M. F. (2006). Upper bound analysis of lateral pile capacity in cohesive soil. *Géotechnique*, 56(2), pp. 141-145.
- Matasović, N. & Vucetic, M. (1995). Generalized Cyclic-Degradation-Pore-Pressure Generation Model for Clays. *Journal of Geotechnical Engineering*, 121(1), pp. 33-42.
- Mathworks (1984). *MATLAB* (Version R2014a). Cambridge: MathWorks.
- Matlock, H. (1970). Correlation for Design of Laterally Loaded Piles in Soft Clay. *2nd Annual Offshore Technology Conference*. Houston, Texas. pp. 577-594.

- Matlock, H. & Reese, L. C. (1960). Generalized Solutions for Laterally Loaded Piles. *ASCE Journal of Soil Mechanics & Foundation Engineering*, 86(5), pp. 63-91.
- May, R. (2011). *Offshore Wind Farms in UK Waters: An Overview*, [Presentation to British Geotechnical Association and Engineering Group of the Geological Society]. 9 February. Ground Engineering Design and Construction for Off-shore Wind Farms. Institution of Civil Engineers, London.
- McCarthy, M. (2008). A revolution on the horizon: 7,000 more wind turbines. *The Independent*. [Online] 27 June 2008. Available from: <https://www.wind-watch.org/news/2008/06/27/a-revolution-on-the-horizon-7000-more-wind-turbines>. [Accessed: 8 January 2015].
- Meyer, B. J. & Reese, L. C. (1979). *Analysis of single piles under lateral loading*. Report no. FHWA/TX-79/38+244-1. Austin: Center for Transportation Research, University of Texas.
- Miles, J. & Barnyard, P. (2007). *Understanding and Using Statistics in Psychology: A Practical Introduction*. London: SAGE Publications Ltd.
- Mitrani, H. (2006). *Liquefaction Remediation Techniques for Existing Buildings*. Ph.D. Thesis, University of Cambridge.
- Montgomery, D. C., Runger, D. C. & Hubele, N. F. (2004). *Engineering Statistics (3rd Edition)*. New York: John Wiley & Sons.
- Mortenson, M. E. (1985). *Geometric modelling*. New York: John Wiley & Sons.
- Muir Wood, D. (1990). *Soil behaviour and critical state soil mechanics*. Cambridge: Cambridge University Press.
- New Civil Engineer (2014). *Largest monopiles from Dong Energy*. [Online]. Available from: <http://www.nce.co.uk/news/geotechnical/largest-monopiles-from-dong-energy/8665644.article>. [Accessed: 8 January 2015].
- Noordzee Wind, Shell & Nuon (2008). *Offshore Windfarm Egmond aan Zee General Report*. Report no. OWEZ_R_141_20080215. Noordzee Wind.
- O'Neill, M. W. & Dunnavant, T. W. (1984). *A Study of the Effects of Scale, Velocity, and Cyclic Degradability on Laterally Loaded Single Piles in Overconsolidated Clay*. Report no. UHCE 84-7. Houston: Department of Civil Engineering, University of Houston.
- Offshore Wind Industry (2013). *Colossus made out of steel*. [Online]. Available from: <http://www.offshorewindindustry.com/news/colossus-made-out-steel>. [Accessed: 12 January 2015].
- Ovesen, N. K. (1979). The scaling law relationship. *7th European Conference on Soil Mechanics and Foundation Engineering*. Brighton. Vol. 4, pp. 319-323.
- Pan, J. L., Goh, A. T. C., Wong, K. S. & Selby, A. R. (2002). Three-dimensional analysis of single pile response to lateral soil movements. *International*

- Journal for Numerical and Analytical Methods in Geomechanics*, 26(8), pp. 747-758.
- Pao, L. Y. & Johnson, K. E. (2009). A Tutorial on the Dynamics and Control of Wind Turbines and Wind Farms. *American Control Conference*. St. Louis, Missouri. 10 - 12 June. New York: Institute of Electrical and Electronics Engineer. pp. 2076-2089.
- Peck, R. B., Hanson, W. E. & Thornburn, T. H. (1974). *Foundation engineering*. New York: John Wiley & Sons.
- Pender, M. J. & Pranjoto, S. (1996). Gapping Effects during Cyclic Lateral Loading of Piles in Clay. *Eleventh World Conference on Earthquake Engineering*. Acapulco, Mexico. 23 - 28 June. Paper No. 1007. Oxford: Elsevier Science Ltd.
- Phillips, W. J. (1981). *Centrifuge lateral pile tests in clay. Tasks 2 and 3*. Exxon Production Research Corp.
- Potts, D. M. & Zdravkovic, L. (2001). *Finite element analysis in geotechnical engineering: theory*. London: Thomas Telford Ltd.
- Poulos, H. G. (1971). Behavior of laterally loaded piles: I - Single piles. *Journal of the Soil Mechanics and Foundations Division*, 97(5), pp. 711-731.
- Poulos, H. G. & Hull, T. (1989). The Role of Analytical Geomechanics in Foundation Engineering. *Foundation Engineering: Current Principles and Practices*. Evanston, Illinois. 25 - 29 June. Reston: American Society of Civil Engineers. Vol. 2, pp. 1578-1606.
- Pradhan, D. L. (2012). *Development of P-Y Curves for Monopiles in Clay using Finite Element Model Plaxis 3D Foundation*. M.Sc. Thesis, Norwegian University of Science and Technology.
- Pranjoto, S. & Pender, M. J. (2003). Gapping effects on the lateral stiffness of piles in cohesive soils. *7th Pacific Conference on Earthquake Engineering*. Christchurch, New Zealand. 13 - 15 February. Paper no. 096.
- Randolph, M. F. & Houlsby, G. T. (1984). The limiting pressure on a circular pile loaded laterally in cohesive soil. *Géotechnique*, 34(4), pp. 613-623.
- Rattley, M. (2011). *Small Strain Stiffness and the Dynamic Loading Response of Soil*, [Presentation to British Geotechnical Association and Engineering Group of the Geological Society]. 9 February. Ground Engineering Design and Construction for Off-shore Wind Farm. Institution of Civil Engineers, London.
- Reese, L. C., Cox, W. R. & Koop, F. D. (1975). Field Testing and Analysis of Laterally Loaded Piles on Stiff Clay. *7th Annual Offshore Technology Conference*. Houston, Texas. pp. 671-690.
- Reese, L. C. & Matlock, H. (1956). Non-Dimensional Solutions for Laterally Loaded Piles with Soil Modulus Assumed Proportional with Depth. *8th Texas*

- Conference on Soil Mechanics and Foundation Engineering*. Austin, Texas. pp. 1-41.
- Reese, L. C. & Van Impe, W. F. (2001). *Single Piles and Pile Groups under Lateral Loading*. Leiden, The Netherlands: Taylor & Francis/Balkema.
- Reese, L. C. & Welch, R. C. (1975). Lateral Loading of Deep Foundations in Stiff Clay. *Journal of the Geotechnical Engineering Division*, 101(7), pp. 633-649.
- Renewable Energy Focus (2009). *Renewable energy can reduce 20% of world goal for GHG emissions*. [Online]. Available from: <http://www.renewableenergyfocus.com/view/4766/renewable-energy-can-reduce-20-of-world-goal-for-ghg-emissions/>. [Accessed: 8 January 2015].
- Roscoe, K. H. & Burland, J. B. (1968). On the generalized stress-strain behaviour of wet clay. *Engineering Plasticity*. Cambridge. London: Cambridge University Press. pp. 535-609.
- Rudolph, C., Bienan, B. & Grabe, J. (2014). Effect of variation of the loading direction on the displacement accumulation of large-diameter piles under cyclic lateral loading in sand. *Canadian Geotechnical Journal*, 51(10), pp. 1196-1206.
- Schofield, A. N. (1980). Cambridge University geotechnical centrifuge operations. *Géotechnique*, 30(3), pp. 227-268.
- Schofield, A. N. (1981). Dynamic and earthquake geotechnical centrifuge modelling. *International Conference on Recent Advances in Soil Dynamics and Earthquake Engineering*. St Louis. 26 April - 3 May. Vol. 3, pp. 1081-1100.
- Schofield, A. N. & Wroth, C. P. (1968). *Critical State Soil Mechanics*. London: McGraw-Hill.
- Skempton, A. W. (1951). The Bearing Capacity of Clays. *Building Research Congress*. London. Division 1, Part 3, pp. 180-189.
- Skempton, A. W. (1954). Discussion: sensitivity of clays and the c/p ratio in normally consolidated clays. *Proceedings of the American Society of Civil Engineers*. Separate 478, pp. 19-22.
- Skempton, A. W. (1957). Discussion: further data on the c/p ratio in normally consolidated clays. *Proceedings of the Institution of Civil Engineers*. Vol. 7, pp. 305-307.
- Smith, M. G. (1993). *A laboratory study of the Marchetti dilatometer*. Ph.D. Thesis, Oxford University.
- Stern, N. (2007). *The Economics of Climate Change: The Stern Review*. Cambridge: Cambridge University Press.

- Stevens, J. B. & Audibert, J. M. E. (1979). Re-examination of p-y curve formulations. *11th Annual Offshore Technology Conference*. Houston, Texas. 30 April - 3 May. pp. 397-403.
- Stewart, D. P. & Randolph, M. F. (1991). A new site investigation tool for the centrifuge. *International Conference on Centrifuge Modelling - Centrifuge '91*. Boulder, Colorado. 13-14 June. Rotterdam, The Netherlands: A.A. Balkema. pp. 531–538.
- Su, D., Wu, W. L., Du, Z. Y. & Yan, W. M. (2014). Cyclic Degradation of a Multidirectionally Laterally Loaded Rigid Single Pile Model in Compacted Clay. *Journal of Geotechnical and Geoenvironmental Engineering*, 140(5), pp. 06014002.
- Sullivan, W. R., Reese, L. C. & Fenske, C. W. (1980). Unified Method for Analysis of Laterally Loaded Piles in Clay. *Numerical Methods in Offshore Piling*. London. London: Institution of Civil Engineers. pp. 135-146.
- Take, W. A. (2003). *The influence of seasonal moisture cycles on clay slopes*. Ph.D. Thesis, University of Cambridge.
- Take, W. A. & Bolton, M. D. (2003). Tensiometer saturation and the reliable measurement of soil suction. *Géotechnique*, 53(2), pp. 159-172.
- Terzaghi, K. (1955). Evaluation of coefficients of subgrade reaction. *Géotechnique*, 5(4), pp. 297-326.
- The Crown Estate (2013). *Round 3 Offshore Wind Site Selection at National and Project Levels*. London: The Crown Estate.
- Thiers, G. R. & Seed, H. B. (1968). Cyclic stress–strain characteristics of clay. *Journal of the Soil Mechanics and Foundations Division*, 94(2), pp. 558-569.
- Thomas, S. (1989). *Geotechnical investigation of UK test sites for the foundations of offshore structures*. Offshore Technology Report OTH 89 294. London: Department of Energy.
- Trochanis, A. M., Bielak, J. & Christiano, P. (1991). Three-Dimensional Nonlinear Study of Piles. *Journal of Geotechnical Engineering*, 117(3), pp. 429-447.
- Tuladhar, R., Maki, T. & Mutsuyoshi, H. (2008). Cyclic behavior of laterally loaded concrete piles embedded into cohesive soil. *Earthquake Engineering and Structural Dynamics*, 37(1), pp. 43-59.
- USACE (1990). *Settlement Analysis*. Washington, DC: United States Army Corps of Engineers.
- Vardanega, P. J. (2011). *Strength Mobilisation for Geotechnical Design & its Application to Bored Piles*. Ph.D. Thesis, University of Cambridge.

- Vardanega, P. J., Lau, B. H., Lam, S. Y., Haigh, S. K., Madabhushi, S. P. G. & Bolton, M. D. (2012). Laboratory measurement of strength mobilisation in kaolin: link to stress history. *Géotechnique Letters*, 2(January - March), pp. 9-15.
- Vesic, A. B. (1961). Beams on Elastic Subgrade and Winkler's Hypothesis. *5th International Conference on Soil Mechanics and Foundation Engineering*. Paris. 17 - 22 July. Paris: Dunod. Vol. 1, pp. 845-850.
- Vucetic, M. (1994). Cyclic Threshold Shear Strains in Soils. *Journal of Geotechnical Engineering*, 120(12), pp. 2208-2228.
- Vucetic, M. & Dobry, R. (1988). Degradation Marine Clays under Cyclic Loading. *ASCE Journal of Geotechnical Engineering*, 114(2), pp. 133-149.
- White, D. J., Gaudin, C., Boylan, N. & Zhou, H. (2010). Interpretation of T-bar penetrometer tests at shallow embedment and in very soft soils. *Canadian Geotechnical Journal*, 47(2), pp. 218-229.
- Wiemann, J., Lesny, K. & Richwien, W. (2004). Evaluation of Pile Diameter Effects on Soil-Pile Stiffness. *7th German Wind Energy Conference (DEWEK)*. Wilhelmshaven, Germany. October.
- Williamson, M. (2014). *Tunnelling Effects on Bored Piles in Clay*. Ph.D. Thesis, University of Cambridge.
- Wu, K., Chen, R. & Li, S. (2009). Finite Element Modeling of Horizontally Loaded Monopile Foundation of Large Scale Offshore Wind Turbine in Non-homogeneity Clay. *World Congress on Software Engineering*. Xiamen, Fujian. 19 - 21 May. Los Alamitos, California: IEEE Computer Society. Vol. 2, pp. 329-333.
- Zhang, C., White, D. & Randolph, M. (2011). Centrifuge Modeling of the Cyclic Lateral Response of a Rigid Pile in Soft Clay. *Journal of Geotechnical and Geoenvironmental Engineering*, 137(7), pp. 717-729.
- Zhou, H. & Randolph, M. F. (2009). Numerical investigations into cycling of full-flow penetrometers in soft clay. *Géotechnique*, 59(10), pp. 801-812.
- Zhu, B., Sun, Y. X., Chen, R. P. & Chen, Y.-M. (2014). Model tests on offshore monopile subjected to lateral monotonic and cyclic loading. *8th International Conference on Physical Modelling in Geotechnics*. Perth, Western Australia. Leiden, The Netherlands: CRC Press/Balkema. Vol 1, pp. 553-559.